NOVEL CARDIOVASCULAR MAGNETIC RESONANCE PHENOTYPING OF THE MYOCARDIUM

PhD Thesis

Dr Laura-Ann McGill

Imperial College London
National Heart and Lung Institute
CID: 00817170

Supervisors: Professor Dudley J Pennell,
Professor David N Firmin & Dr Sanjay Prasad

I would like to dedicate this work to my family, my partner Oscar, and dear friend Sharon, whose unwavering support and encouragement was central to the completion of this project. And also to the patients and volunteers who offered their valuable time in the name of cardiovascular research.

Declaration of Originality

This thesis is the product of my own research and writing; any data reproduced from additional sources has been appropriately referenced.

Copyright Declaration

The copyright of this thesis rests with the author and is made available under a Creative Commons Attribution Non-Commercial No Derivatives licence. Researchers are free to copy, distribute or transmit the thesis on the condition that they attribute it, that they do not use it for commercial purposes and that they do not alter, transform or build upon it. For any reuse or redistribution, researchers must make clear to others the licence terms of this work

ABSTRACT

INTRODUCTION

Left ventricular (LV) microstructure is unique, composed of a winding helical pattern of myocytes and rotating aggregations of myocytes called sheetlets. Hypertrophic cardiomyopathy (HCM) is a cardiovascular disease characterised by left ventricular hypertrophy (LVH), however the link between LVH and underlying microstructural aberration is poorly understood. In vivo cardiovascular diffusion tensor imaging (cDTI) is a novel cardiovascular MRI (CMR) technique, capable of characterising LV microstructural dynamics non-invasively. In vivo cDTI may therefore improve our understanding microstructural-functional relationships in health and disease.

METHODS AND RESULTS

The monopolar diffusion weighted stimulated echo acquisition mode (DW-STEAM) sequence was evaluated for in vivo cDTI acquisitions at 3Tesla, in healthy volunteers (HV), patients with hypertensive LVH, and HCM patients. Results were contextualised in relation to extensively explored technical limitations. cDTI parameters demonstrated good intra-centre reproducibility in HCM, and good inter-centre reproducibility in HV. In all subjects, cDTI was able to depict the winding helical pattern of myocyte orientation known from histology, and the transmural rate of change in myocyte orientation was dependent on LV size and thickness. In HV, comparison of cDTI parameters between systole and diastole revealed an increase in transmural gradient, combined with a significant re-orientation of sheetlet angle. In contrast, in HCM, myocyte gradient increased between phases, however sheetlet angulation retained a systolic-like orientation in both phases. Combined analysis with hypertensive patients revealed a proportional decrease in sheetlet mobility with increasing LVH.

CONCLUSION

In vivo DW-STEAM cDTI can characterise LV microstructural dynamics non-invasively. The transmural rate of change in myocyte angulation is dependent on LV size and wall thickness, however inter phase changes in myocyte orientation are unaffected by LVH. In contrast, sheetlet dynamics demonstrate increasing dysfunction, in proportion to the degree of LVH. Resolving technical limitations is key to advancing this technique, and improving the understanding of the role of microstructural abnormalities in cardiovascular disease expression.

THESIS SUMMARY

The following is a summary of the achievements and observations outlined in this thesis:

Healthy Hearts

Successful recruitment and application of the DW-STEAM sequence

This work demonstrates the successful application of a novel in vivo DW-STEAM cDTI sequence and represents the second largest published cohort of healthy volunteer data to date.

Normal values for B_{main} 350 sequence

In healthy volunteers, normal value ranges were established for each of the quantitative cDTI parameters, at a diffusion weighting of B_{main} 350s/mm^2.

Relation between helix angle gradient and measures of LV size

On assessment of innate heterogeneity, the rate of change of transmural helix angles, i.e. the helix angle gradient (°/mm), was found to be inversely related to body surface area, LV cavity size and LV wall thickness. These associations persisted when the helix angle gradient was expressed as a % wall thickness.

Confirmation of theory of sheetlet re-orientation in systole

These data include the first published study of in vivo human sheetlet orientations in systole and diastole. Sheetlet orientations were determined from the secondary eigenvector angle. These data provide further confirmation of the theory of radial sheetlet re-orientation as a mechanism of systolic radial thickening.

Hypertrophic Cardiomyopathy

Assessment of disarray with cDTI fractional anisotropy

This work established that myocardial disarray could not be detected non-invasively, in hypertrophy cardiomyopathy patients, using fractional anisotropy derived from in vivo DW-STEAM with a diffusion weighting of B_{main} 350s/mm^2.

Detection of aberrant sheetlet re-orientations in hypertrophic cardiomyopathy

In patients with hypertrophic cardiomyopathy, diastolic sheetlet orientations, assessed via the secondary eigenvector, were found to be significantly more radially orientated than healthy volunteers, with less angular mobility between systole and diastole. This novel observation provides a potential explanation for diastolic impairment observed in HCM, and for the degree of myocardial hypertrophy.

Subsequent, combined assessment of sheetlet mobility in healthy volunteers, patients with hypertension and hypertrophic cardiomyopathy, demonstrated a significant inverse correlation with LV wall thickness, thereby implying aberrant sheetlet orientation is not specific to HCM. In addition, this raises the question as to whether reduced diastolic sheetlet mobility is the cause of the consequence of left ventricular hypertrophy.

Technical development

Application of the B_{main} 750 in vivo DW-STEAM sequence

In tandem sequence development work demonstrated that a diffusion weighting of B_{main} 750s/mm^2 conferred greater myocardial diffusivity than B_{main} 350s/mm^2. Following application of this sequence, in healthy volunteers, the superior diffusivity was found to enable the detection of innate transmural heterogeneity of cellular organization via fractional anisotropy. Repeat study with a higher solution sequence excluded partial voluming as a potential contributor. These data have since been independently replicated.

Tables

Table 3.1: Left ventricular summary data from 120 patients aged 20-80yrs (41).

Table 3.2: Quoted values for longitudinal strain measures in healthy subjects by CMR & echo (100).

Table 8.1: List of Gadolinium compounds based on structure, charge, kinetic stability and reported cases of NSF (426).

Table 9.1: Baseline patient characteristics (432).

Table 9.2: Fractional anisotropy results from the initial study from each patient (432).

Table 9.3: Mean diffusivity results from the initial study (432).

Table 9.4: Helix angle values for the initial study (432).

Table 9.5: Fractional anisotropy reproducibility demonstrating minimal variance between scans (432).

Table 9.6: Reproducibility analysis of mean diffusivity (432).

Table 10.1: Results from phantom validation of the monopolar DW-STEAM sequence conducted at Oxford (372).

Table 10.2: Baseline subject characteristics.

Table 10.3: Fractional anisotropy in systole and diastole.

Table 10.4: Regional mean diffusivity in systole and diastole.

Table 10.5: Regional Helix angle gradient in systole and diastole.

Table 10.6: Regional E2A in systole and diastole and regional E2A mobility.

Table 10.7: Phasic FA and MD data from Stoeck et al.

Table 11.1: Baseline subject characteristics.

Table 11.2: Characteristics of the HCM cohort.

Table 11.3: Further analysis of E2A data based on LVH (H) and LGE (LG).

Table 12.1: Baseline demographics and CMR characteristics of the 3 cohorts.

Table 12.2: HCM cohort characteristics.

Table 12.3: Septal-lateral intra-cohort comparison of fractional anisotropy.

Table 12.4: Inter-cohort comparison of fractional anisotropy.

Table 12.5: Inter-cohort comparison of mean diffusivity.

Table 12.6: Inter-cohort comparison of helix angle gradient.

Table 12.7: Inter-cohort comparison of the secondary eigenvector angle.

Table 13.1: Regional fractional anisotropy.

Table 13.2: Regional mean diffusivity

Table 13.3: Regional eigenvalues

Table 13.4: Regional signal to noise ratio

Figures

Figure 2.1: Graph of mean mammalian arterial pressure (37, 38).

Figure 2.2: Anatomical drawings of sheep hearts at various stages of dissection (1)

Figure 2.3: Five successive phases of the unwinding of the ventricular myocardial band (53).

Figure 2.4: Photomicrographs showing myocyte angles in successive sections taken from a heart in systole (2).

Figure 2.5: Schematic representation of the discreet bands within a sarcomere (73).

Figure 2.6: Histological image of cardiomyocyte structure with haematoxylin and eosin staining (77).

Figure 2.7: Scanning electron micrographs of canine left ventricle (4).

Figure 2.8: High resolution extended volume confocal microscopy images of rat left ventricle sections with three dimensional reconstruction (84).

Figure 2.9: Histological photo of 2 observed sheetlet populations in a section from sheep left ventricle (7).

Figure 3.1: Illustration of LV longitudinal, radial and circumferential strain and apical and basal rotation (96).

Figure 3.2: Example illustration of the derivation of myocyte (fibre) and cross-myocyte (fibre) axes using CMR (100).

Figure 3.3: Sliding filament theory.

Figure 4.1: cDTI reconstruction of canine myocyte architecture at different transmural depths (83).

Figure 4.2: cDTI derived sheetlet orientation from Harrington et al (5).

Figure 4.3: Example of in vivo cDTI acquisition of myocardial fibre orientation in the lateral wall of the left ventricle in a healthy volunteer (154).

Figure 4.4: Two dimensional representation of sheetlet dynamics adapted from Harrington et al. (5)

Figure 5.1: Illustration of the sarcomeric proteins and their interactions (68).

Figure 5.2: CMR images of different HCM morphologies.

Figure 5.3: Examples of late gadolinium enhancement in HCM.

Figure 5.4: Histological specimens from a patient with a diagnosis of HCM (167).

Figure 5.5: Nuclear and myofibrillar abnormalities in HCM (167).

Figure 5.6: Myocardial sections with Mallory-Heidenhain staining at x160 magnification (188).

Figure 5.7: In vivo cDTI images in HCM from Tseng et al (297).

Figure 6.1: Diagram of the CMR system components (300).

Figure 6.2: Precession of hydrogen ions.

Figure 6.3: Illustration of an RF pulse.

Figure 6.4: T1 recovery after a 90degree RF pulse.

Figure 6.5: The application of the slice select gradient (Gs).

Figure 6.6: Pulse sequence diagram showing the timing of the relevant gradients in relation to the RF pulse (300).

Figure 6.7: Illustration of a spin echo sequence.

Figure 6.8: Single shot echo planar imaging illustration.

Figure 6.9: Cine imaging illustration.

Figure 6.10: Illustration of phase contrast velocity mapping.

Figure 6.11: Illustration of T1 recovery after a 180° inversion pulse.

Figure 6.12: Example of volumetric assessment by thresholding.

Figure 6.13: Myocardial gadolinium distribution (313).

Figure 6.14: Characteristic patterns of late gadolinium enhancement (315).

Figure 6.15: bSSFP image of the aorta at 3Tesla.

Figure 7.1: Illustration of Brown's early description of diffusion.

Figure 7.2: Representation of free diffusion displacement.

Figure 7.3: Illustration of diffusion modulation at the cellular level (331).

Figure 7.4.1: Spin echo sequence with application of diffusion sensitizing gradients.

Figure 7.4.2: Spin echo sequence with application of diffusion sensitizing gradients.

Figure 7.5: Illustration depicting the parameters used in calculating the diffusion weighting of a sequence.

Figure 7.6: Illustration of diffusion weighted cerebral imaging (331).

Figure 7.7: Anisotropy and Isotropy

Figure 7.8: Representation of diffusion in 2 dimensions derived from a 2x2 tensor.

Figure 7.9: Graphic representation of diffusion in 3D (arbitrary units).

Figure 7.10: Representation of the eigensystem reference frame for the diffusion ellipsoid.

Figure 7.11: Illustration of the shape of the diffusion ellipsoid at increasing FA values.

Figure 7.12: Cerebral white matter tractograms from the Human Connectome Project dataset (357).

Figure 7.13: A sample of papillary muscle and adjacent myocardium imaged with diffusion tensor imaging (358).

Figure 7.14: First published in vivo diffusion weighted image of the myocardium (359).

Figure 7.15: Diffusion weighted images of perfused ex vivo rat hearts (141).

Figure 7.16: Helix angle, at progressive myocardial depths from the endocardium (360).

Figure 7.17: Histograms of the tertiary eigenvector intersection angle pooled from 7 canine hearts (85).

Figure 7.18: Illustration of potential intra-voxel myolaminae orientation.

Figure 7.19: Transmural helix angle at basal, mid and apical ventricular levels from Chen et al (12).

Figure 7.20: Changes in helix angle between diastole and systole (13).

Figure 7.21: Histologically derived sheetlet angles in diastole and systole (12).

Figure 7.22: Short axis view through the mid ventricle in a rat heart demonstrating myocyte and sheetlet orientations in systole and diastole (13).

Figure 7.23: A: Example of a mouse heart imaged with diffusion spectroscopy (145).

Figure 7.24: DSI tractography of the anterior epicardial surface of a mouse heart (318).

Figure 7.25: Short axis section through the mid ventricle of a hamster with heart failure (393).

Figure 7.26: Illustration of cDTI angular calculations (385).

Figure 7.27: Mid ventricular short axis cDTI acquisition (367).

Figure 7.28: Different components of laminar function as proposed by Dou et al (372).

Figure 7.29: Comparison of myocyte orientation in systole and diastole derived from cDTI tractography (155).

Figure 7.30: The Stejskal-Taner spin echo sequence.

Figure 7.31: Monopolar diffusion weighted stimulated echo sequence (DW-STEAM).

Figure 7.32: Bipolar diffusion weighted stimulated echo sequence proposed by Dou et al.

Figure 7.33: Bipolar diffusion weighted, velocity compensated, spin echo sequence proposed by Gamper et al.

Figure 7.34: Bipolar diffusion weighted, second order motion corrected, spin echo sequence proposed by Stoeck et al.

Figure 7.35: Gelatin phantom diffusion-deformation experiment (366).

Figure 7.36: Representation of the Reese et al. theory of acquired strain artefacts in monopolar diffusion sequences (394).

Figure 7.37: Illustration of myocardial diffusion imaging with the monopolar STEAM sequence (395).

Figure 7.38: In vivo cardiac cycle 'sweet spots' (387).

Figure 7.39: Illustration of the impact of b value and noise on diffusion weighting signal intensity. Adapted from Jones et al (406).

Figure 8.1: Monopolar diffusion weighted stimulated echo sequence (DW-STEAM) adopted by the Royal Brompton Hospital.

Figure 8.2: BH and NAV images from an example patient (19).

Figure 8.3: Three-dimensional visualisation of the tensor information derived from both NAV and BH sequence protocols (19).

Figure 8.4: Examples of diffusion weighted images from in vivo cDTI acquisitions.

Figure 8.5: Customised cDTI analysis platform.

Figure 8.6: Rejection of bad frames. Each average for each phase encoding step was reviewed. Poor quality frames were manually rejected.

Figure 8.7: Each average for each direction are co-registered, adjusting for inplane motion.

Figure 8.8: Manual thresholding the myocardium.

Figure 8.9: Surrounding structures such as the diaphragm and chest wall are manually excluded from the image.

Figure 8.10: Edge pixels and papillary muscles with a vertical/non-helical axis are visualised in white are excluded from the analysis.

Figure 8.11: A red dot is placed in the mid myocardium adjacent to the superior RV insertion point.

Figure 8.12: Diagram illustrating how helix angle (E1A) and E2A values were calculated for each voxel. Reproduced from Ferreira, Kilner, McGill et al (395).

Figure 8.13: Example of volumetric assessment using bSSFP cines.

Figure 8.14: Illustration of magnitude (top panel) and phase sensitive inversion recovery (PSIR). Adapted from Ferreira et al. (419).

Figure 8.15: Patterns of myocardial late enhancement

Figure 8.16: Example of full width half maximum analysis (430).

Figure 8.17: Royal Brompton Hospital CMR safety checklist.

Figure 9.1: Example of patient with a highly reproducible dataset (422).

Figure 9.2: Patient with the least reproducible dataset out of 10 patients (422).

Figure 9.3: Cardiac diffusion tensor data from an example HCM patient (422).

Figure 9.4: Bland-Altman plots for global FA and MD and HA plots per transmural layer (422).

Figure 9.5: Line plots of the mean global HA values for the initial and repeat studies in for the endo, meso and epicardial layers for all 10 subjects (422).

Figure 10.1: Bland-Altman plots of Oxford (O) and Brompton (B) initial inter-centre reproducibility (372).

Figure 10.2: Comparison of ROIs drawn at the Brompton and Oxford (372).

Figure 10.3: Colour scaled systolic and diastolic FA and MD maps in an example patient (427).

Figure 10.4: Bullseye plot of the average helix angle per LV regional wall and transmural layer in both systole and diastole (427).

Figure 10.5: 3D representation of primary eigenvector, helix angle data in diastole and systole (427).

Figure 10.6: Data from the interventricular septum of an example patient represented in super quadric glyphs (427).

Figure 11.1: Three dimensional visualization of the primary eigenvector (E1) helix angle (HA) and secondary eigenvector angle (E2A) (395).

Figure 11.2: Histograms of myocardial HA values in HCM and control cohorts in both cardiac phases 395).

Figure 11.3: Histograms of E2A in systole and diastole for both cohorts (395).

Figure 11.4: Scatter plots showing the absolute E2A in systole and diastole (395).

Figure 12.1: Parameter maps for FA, MD, HA and E2A from an example subject in each cohort.

Figure 12.2: Scatter plots of fractional anisotropy in systole and diastole.

Figure 12.3: Scatter plots of mean diffusivity in systole and diastole.

Figure 12.4: Superquadric glyphs representing the whole tensor, per pixel, in an example patient in both cardiac phases.

Figure 12.5: Comparative transmural helix angles for all three cohorts.

Figure 12.6: Scatter plots with regression line for systolic (left) and diastolic HAG (right) in all subjects against maximum LV wall thickness.

Figure 12.7: Scatter plots of the secondary eigenvector angle in systole and diastole.

Figure 12.8: Scatter plots with regression line for systolic (left) and diastolic (right) E2A in all subjects against maximum LV wall thickness.

Figure 12.9: Scatter plots of secondary eigenvector angle mobility.

Figure 12.10: Scatter plot with regression line for E2A mobility in all subjects against maximum LV wall thickness.

Figure 13.1: Short axis transmural maps in an example subject, at increasing b values (440).

Figure 13.2: Plot of DTI signal (S)/signal minus diffusion weighting (S0) against sequence diffusion weighting, or b value (440).

Figure 13.3: Comparison of mean diffusivity (MD), fractional anisotropy (FA) and helix angle gradient (HAG) values at increasing b values.

Figure 13.4: FA maps in an example subject at increasing b values (440).

Figure 13.5: HA maps from an example patient with A: bmain=350s/mm2, bref=135s/mm2 and B: bmain=750s/mm2, bref=150s/mm2.

Figure 13.6: Comparison of transmural helix angle line profiles from an example subject against data from Streeter et al.

Figure 13.7: Typical examples of fractional anisotropy maps (441).

Figure 13.8: Mean diffusivity map from an example subject with a narrowed scale to emphasis differences (441).

Figure 13.9: Colour Bullseye maps showing the significant heterogeneity in the distribution of FA, MD, SNR and e1-e3 (441).

Figure 13.10: HA, FA, MD and SNR maps for 2 subjects at standard resolution (2.8x2.8x8mm2) and higher resolution (1.9x1.9x6mm2) (441).

Figure 14.1: Comparison of fractional anisotropy and the mode of anisotropy (447).

Abbreviations

ADC	Apparent diffusion coefficient
ASH	Asymmetrical septal hypertrophy
BH	Breath hold
BSA	Body surface area
bSSFP	Balanced steady state free precession
cDTI	Cardiovascular diffusion tensor imaging
CMR	Cardiovascular magnetic resonance
CoV	Coefficient of variation
DTI	Diffusion tensor imaging
DW-STEAM	Diffusion weighted stimulated echo activation mode
$\varepsilon_1\, \varepsilon_2\, \varepsilon_3$.	Primary, secondary and tertiary eigenvectors
ECG	Electrocardiograph
EDV	End diastolic volume
EF	Ejection fraction
EPI	Echo planar imaging
ESV	End systolic volume
E2A	Secondary eigenvector angle
FA	Fractional anisotropy
FOV	Field of view
GRAPPA	Generalised auto-calibrating partially parallel acquisitions
GRE	Spoiled gradient echo
$\lambda_1\, \lambda_2\, \lambda_1$	Primary, secondary and tertiary eigenvalues
HA	Helix angle
HAG	Helix angle gradient
HCM	Hypertrophic cardiomyopathy

HTN	Hypertension
LGE	Late gadolinium enhancement
LV	Left ventricle
LVH	Left ventricular hypertrophy
MD	Mean diffusivity
MWTd	Maximal wall thickness in diastole
NAV	Navigator
PSIR	Phase sensitive inversion recovery
RF	Radiofrequency
ROI	Region of interest
RV	Right ventricle
SD	Standard deviation
SENSE	Sensitivity encoding
SNR	Signal to noise ratio
SPAMM	Spatial modulation of magnetisation
TE	Time to echo
TR	Time to repeat
TT	Trigger time
VMB	Ventricular myocardial band

Table of Contents

CHAPTER 1: OBJECTIVES **30**

CHAPTER 2: LEFT VENTRICULAR STRUCTURE **33**

2.1: Macroscopic Left Ventricular Anatomy **33**

2.1.1: Introduction 33

2.1.2: Cardiothoracic Anatomy 33

2.1.3: Trabecular Myocardium 33

2.1.4: Evolution of Compact Myocardium 34

2.1.5: Myocardial Adaptation 35

2.2: Left Ventricular Myocyte Organisation **36**

2.2.1: Introduction 36

2.2.2: Helical Myocyte Arrangement 36

2.2.3: Myocardial 'Muscle Bands' 39

2.2.4: The Ventricular Myocardial Band Theory 40

2.2.5: A Bioengineering Perspective 42

2.3: Microscopic Left Ventricular Anatomy **44**

2.3.1: Introduction 44

2.3.2: Sarcomeric Structure 44

2.3.3: Cardiomyocyte Structure 45

2.3.4: Structural Arrangement of Cardiomyocytes and Myocardial Connective Tissues 47

2.3.5: Cross Myocyte Myolaminar Structure - Myocardial 'Sheetlets' 47

CHAPTER 3: LEFT VENTRICULAR MECHANICS **51**

3.1: Global Left Ventricular Mechanics **51**

3.1.1: Introduction 51

3.1.2: Left Ventricular Ejection Fraction 51

3.2: Axial Left Ventricular Mechanics **52**

3.2.1: Introduction 52

3.2.2 Longitudinal Strain 53

3.2.3: Circumferential Strain 55

3.2.4: Radial Strain 55

3.2.5: Ventricular Torsion 56

3.3: Local Myocyte and Cross Myocyte Mechanics 56

3.3.1: Introduction 56

3.3.2: Left Ventricular Myocyte Axis 57

3.3.3: Cross-Myocyte Mechanics 58

3.4: Sarcomeric & Myocyte Mechanics 58

3.4.1: Introduction 58

3.4.2: Sarcomeric Mechanics 59

3.4.3: Myocyte Mechanics 60

CHAPTER 4: CONTEMPORARY IMAGING TECHNIQUES AND MYOLAMINAR MECHANICS 61

4.1: Introduction 61

4.2: Non-Invasive Structural Imaging with Cardiac Diffusion Tensor Imaging 61

4.2.1: Introduction 61

4.2.2: Ex Vivo Assessment of Myocyte Orientation 62

4.2.3: Ex Vivo Assessment of Myolaminae 63

4.3.4: Assessement of Myocyte Orientation Dynamics 64

4.3.5: Assessment of Myolaminar Dynamics 65

CHAPTER 5: HYPERTROPHIC CARDIOMYOPATHY – MICROSTRUCTURAL ABERRATION AND LEFT VENTRICULAR HYPERTROPHY 68

5.1: Introduction 68

5.2: Hypertrophic Cardiomyopathy Incidence and Genetics 68

5.3: Macroscopic Phenotype **70**

5.3.1: Left Ventricular Hypertrophy 70

5.3.2: Left Ventricular Outflow Tract Obstruction 72

5.3.3: Marcroscopic Scars with Late Gadolinium Enhancement 72

5.4: Microstructural Phenotype **75**

5.4.1: Introduction 75

5.4.2: Disarray 75

5.4.3: Intra-Myocyte Abnormalities & Vascular abnormalities 77

5.4.4: Myocardial Fibrosis 79

5.5: Myocardial Mechanics **81**

5.5.1: Introduction 81

5.5.2: Sarcomeric Mechanics 81

5.5.3: Ventricular Mechanics 82

5.6: Adverse Clinical Events **84**

5.6.1: Introduction 84

5.6.2: Sudden Cardiac Death 84

5.6.3: Heart failure 85

5.6.4: Arrhythmia 85

5.7: HCM Phenocopies **86**

5.7.1: Introduction 86

5.7.2: Hypertensive Heart Disease 86

5.7.3: The Athletic Heart 87

5.8: Diagnosis **88**

5.9: Management **89**

5.10: Future Directions & Diffusion Tensor Imaging **90**

CHAPTER 6: CARDIOVASCULAR MAGNETIC RESONANCE IMAGING **94**

6.1: Introduction **94**

6.2: CMR System Components 94

6.3: Basic Physics **96**

6.3.1: Hydrogen Precession 96

6.3.2: Radiofrequency Excitation and Magnetic Strength 97

6.6.3: Relaxation and Recovery 98

6.3.4: Gradients 100

6.3.5: k-space and Image Formation 101

6.4: Signal to Noise Ratio **103**

6.6: Cardiovascular Magnetic Resonance Pulse Sequences and Image Contrast **104**

6.6.1: Introduction 104

6.6.2: Spin Echo 105

6.6.3: Stimulated Echo Acquisition Mode 106

6.6.4: Gradient Echo 106

6.6.5: Cine Imaging 108

6.6.6: Phase Contrast Velocity Mapping 109

6.6.7: Myocardial Tagging 110

6.6.8: Gadolinium Contrast & Inversion Recovery 111

6.7: Clinical Applications of Cardiovascular Magnetic Resonance **112**

6.7.1: Introduction 112

6.7.2: Tissue Characterisation 112

6.7.3: Functional Assessment 113

6.7.4: Late Gadolinium Enhancement Imaging 114

6.7.5: T1 Mapping and Extracellular Volume Quantification 116

6.8: 3 Tesla Cardiovascular Magnetic Resonance **117**

6.8.1: Introduction 117

6.8.2: Advantages 117

6.8.3: Disadvantages 119

CHAPTER 7: CARDIOVASCULAR DIFFUSION TENSOR IMAGING 121

7.1: Introduction 121

7.2: Diffusion 121

7.2.1: Diffusion Displacement 122

7.2.2: Free (Gaussian) Diffusion 123

7.2.3: In Vivo Diffusion – Apparent Diffusion Coefficient 123

7.3: Diffusion Weighted Magnetic Resonance Imaging 124

7.3.2: Diffusion Weighting – the 'b valve' 127

7.3.3: The Diffusion Equation 128

7.3.4: Contemporary Clinical Applications 128

7.4: Diffusion Tensor Magnetic Resonance Imaging 130

7.4.1: History of Sequence Development 130

7.4.2: Isotropic v Anisotropic Diffusion 130

7.4.3: The Diffusion Tensor Model 131

7.4.4: The Diffusion Tensor Ellipsoid 133

7.4.5: The Eigensystem 134

7.4.6: Diffusion Tensor Imaging Parameters & Clinical Applications 135

7.5: Development of Cardiovascular Diffusion Tensor Imaging 139

7.5.1: History of development 139

7.5.2: Cardiovascular Diffusion Tensor Imaging Histological Validation 141

7.5.3: Review of Cardiovascular Diffusion Tensor Imaging Studies 144

7.5.4: In vivo Cardiovascular Diffusion Tensor Imaging Sequences 163

7.5.5: Practical Considerations & Sequence Optimisation 172

7.5.6: Limitations and Artefacts 174

CHAPTER 8: METHODS 179

8.1: In vivo Cardiovascular Diffusion Tensor Imaging Sequence Development at the Royal Brompton Hospital 179

8.1.1: Introduction 179

8.1.2: Monopolar STEAM Sequence Development 179

8.1.3: Comparison of Breath Hold and Navigator Acquisitions 180

8.1.4: Comparison with Previous Literature 183

8.1.5: Summary 184

8.3: In vivo Diffusion Weighted Stimulated Echo Acquisition Mode (DW-STEAM) Sequence Implementation 184

8.3.1: Introduction 184

8.3.2: Cardiovascular Magnetic Resonance Imaging Hardware 184

8.3.3: DW-STEAM Acquisition Protocol 185

8.3.4: DW-STEAM Scanning Observations and Protocol Developments 186

8.3.5: Diffusion Tensor Imaging Analysis 189

8.4: Assessment of Left Ventricular Volumes, Function and Mass 201

8.4.1: Introduction 201

8.4.2: Acquisition 201

8.4.3: Analysis 201

8.5: Assessment of Focal Myocardial Fibrosis: Late Gadolinium Enhancement Imaging 202

8.5.1: Introduction 202

8.5.2: Acquisition 205

8.5.3: Analysis 205

8.6: Safety in the Scanner Environment 207

8.7: Statistics 209

RESULTS **210**

CHAPTER 9: REPRODUCIBILIY OF IN VIVO CARDIOVASCULAR DIFFUSION TENSOR IMAGING IN PATIENTS WITH HYPERTROPHIC CARDIOMYOPATHY **210**

9.1: Introduction **210**

9.2: Methods **211**

9.2.1: Patient Recruitment 211

9.2.2: Ethical Approval 211

9.2.3: Image Acquisition 211

9.2.4: Diffusion Tensor Analysis 212

9.2.5: Functional, Volumetric and Late Gadolinium Enhancement Image Analysis 213

9.2.6: Statistical Analysis 213

9.3: Results **214**

9.3.1: Study Population 214

9.3.2: Quantitative Parameter Results 218

9.3.3: Reproducibility 221

9.4: Discussion **225**

9.5: Limitations **227**

9.6: Conclusion **227**

CHAPTER 10: INNATE HETEROGENEITY OF CARDIOVASCULAR DIFFUSION TENSOR IMAGING PARAMETERS IN HEALTHY VOLUNTEERS **229**

10.1: Introduction **229**

10.2: Methods **233**

10.2.1: Study population 233

10.2.2: Ethical Approval 233

10.2.3: Image Acquisition 233

10.2.4: Image Analysis 234

10.2.5: Functional and Volumetric Analysis 235
10.2.6: Statistical Analysis 235
10.3: Results 236
10.3.1: Study Population 236
10.3.2: Global and Regional cDTI Results 237
10.3.3: Relationship Between Subject Anthropometrics and cDTI Parameters 242
10.3.3.2: Mean Diffusivity 244
10.3.3.4: Secondary Eigenvector Angle 245
10.4: Discussion 245
10.4.1: Global and regional analysis 245
10.4.2: Phase Specific Differences in cDTI Parameters 247
10.4.3: Relation Between Subject Anthropometrics and cDTI Parameters 248
10.5 Limitations 249
10.6 Conclusion 250
CHAPTER 11: INVESTIGATION OF LAMINAR MECHANICS IN HYPERTROPHIC CARDIOMYOPATHY 251
11.1: Introduction 251
11.2: Methods 252
11.2.1: Study population 252
11.2.2: Ethical Approval 252
11.2.3: Image Acquisition 252
11.2.4: Diffusion Tensor Analysis 253
11.2.5: Functional, Volumetric and Late Gadolinium Enhancement Image Analysis 254
11.2.6: Quantitative and Statistical Analysis 254
11.3: Results 255

11.3.1: Subject Characteristics 255

11.3.2: Diffusion Tensor Visualisation 256

11.3.3: Diffusion Tensor Quantification 258

11.3.3.1: Helix Angle 258

11.3.3.2: Secondary Eigenvector Angle 259

11.4: Discussion 262

11.5: Limitations 263

11.6: Conclusion 264

CHAPTER 12: COMPARISON OF CARDIOVASCULAR PARAMETERS IN PATIENTS WITH HYPERTROPHIC CARDIOMYOPATHY, HYPERTENSION AND CONTROLS ... 265

12.1: Introduction 265

12.2: Methods 266

12.2.1: Study Population 266

12.2.2: Ethical Approval 267

12.2.3: Image Acquisition 267

12.2.4: Diffusion Tensor Analysis 268

12.2.5: Functional, Volumetric and Late Gadolinium Enhancement Image Analysis 268

12.2.6: Quantitative and Statistical Analysis 269

12.3: Results 269

12.3.1: Subject Characteristics 269

12.3.2: Regional Intra-Cohort Comparisons 271

12.3.3: Inter-cohort Comparison of cDTI Parameters 272

12.3.3.4: Secondary Eigenvector Angle 279

12.4: Discussion 282

12.4.1: Study Cohort 282

12.4.2: Regional Intra-Cohort Comparisons 283

12.4.3: Inter-Cohort Comparison of cDTI Parameters 284

12.4.3.2: Mean Diffusivity 284

12.4.3.3: Helix Angle and Helix Angle Gradient 285

12.4.3.4: Secondary Eigenvector Angle and Mobility 285

12.5: Limitations 285

12.6: Conclusion 286

CHAPTER 13: NEW INSIGHTS INTO TRANSMURAL MYOCARDIAL HETEROGENEITY REVEALED BY DIFFUSION WEIGHTING OPTIMISATION 287

13.1: Introduction 287

13.2: Methods 293

13.2.1: Study Population 293

13.2.2: Image Acquisition 293

13.2.3: Diffusion Tensor Analysis 294

13.2.4: Statistical Analysis 294

13.3: Results 295

13.3.1: Helical Angle 295

13.3.2: Fractional Anisotropy 297

13.3.3: Mean Diffusivity 298

13.3.4: Eigenvalues 299

13.3.5: Signal to Noise Ratio 301

13.3.6: Higher Resolution Imaging 303

13.4: Discussion 305

13.4.1: Comparison with Previous Work 305

13.4.2: Influence of Microstructure on FA and MD Measurements 305

13.4.3: Influence of SNR on FA and MD Measurements 306

13.4.4: Influence of Resolution, Partial Voluming and ROIs on FA and MD Measurements 307

13.4.5: Influence of Strain on FA and MD Measurements 307

13.5: Conclusions 308

CHAPTER 14: CONCLUSIONS AND FUTURE DIRECTIONS 310

14.1: Summary 310

14.2: Technical Developments 310

14.3: Inferring Myocardial Structure From Quantitative In Vivo Cardiovascular Diffusion Tensor Imaging 311

14.3.1: Myocardial Fibrosis Via Mean Diffusivity 311

14.3.2: Myocardial Organisation Via Fractional Anisotropy 311

14.3.3: Myocyte Orientation Via Helix Angle 312

14.2.4: Sheetlet Orientation Via The Secondary Eigenvector 313

14.4: Interpretation of Hypertrophic Cardiomyopathy Myo-architecture From In Vivo Cardiovascular Diffusion Tensor Imaging 313

14.5: Conclusion 314

14.6: Future Directions 315

14.6.1: Development of 3D Strain Sequence and Assessment of Strain Artefacts 315

14.6.2: Evaluation of The Second Order Motion Correction Bipolar Spin Echo Sequence.. 315

14.6.3: Evaluation of Alternative Measures of Anisotropy 315

14.6.4: Evaluation of Myocyte and Sheetlet Orientations in Dilated Cardiomyopathy 316

References 317

Appendix 348

1. Prizes Awarded For This Work 348

2. First Author Publications Arising From This Research 348

3. Additional Publications **349**

4. Abstracts **349**

Personal Contribution to Thesis **349**

Supervision **350**

Acknowledgements **350**

Funding **350**

Permissions **351**

CHAPTER 1: OBJECTIVES

The left ventricle (LV) has a unique structure to facilitate contraction in multiple planes. Unlike other striated muscles, left ventricular myocytes are arranged in a winding helical arrangement, rotating from a left-handed orientation in the epicardium, to a circumferential orientation in the mesocardium, on to a right-handed orientation in the endocardium (1-3). LV myocytes are also sub-divided in small groups, called sheetlets (4-8), which together with their subdividing shear layers are referred to a myolaminae. Sheetelets are reported to function as individual contractile units, with a significant role in the genesis of cardiac contraction (9-13), however contemporary imaging techniques are limited in their ability to characterise microstructural dynamics in vivo.

Hypertrophic cardiomyopathy is an inheritable cardiovascular disease characterised by LV hypertrophy (LVH). The clinical course in majority of HCM patients is benign, however an important subset are at risk of complications, including heart failure and sudden cardiac death (14). Histological studies demonstrate the presence of myocyte 'disarray' (15-17), but the prevalence of disarray and relation to disease expression, in real world HCM populations, is unknown. The origin of LVH is also poorly understood, with no demonstrable relation to disarray (18). A better understanding of the link between LV microstructural abnormality and disease expression may improve risk stratification and diagnostic algorithms.

Cardiovascular diffusion tensor imaging (cDTI) is a novel cardiovascular magnetic resonance (CMR) technique, capable of interrogating myocardial microstructure non-invasively. The technique is in its developmental stage, however the event of clinical 3Tesla CMR scanners has improved sequence capabilities. Our department recently implemented the monopolar diffusion weighted stimulated echo acquisition mode (DW-STEAM) sequence at 3Tesla, demonstrating good intra-centre reproducibility of quantitative parameters in healthy volunteers (19). The aim

of this thesis is therefore to evaluate the monopolar DW-STEAM sequence in healthy volunteers and patients with hypertrophic cardiomyopathy.

The following objectives were determined for this thesis:

1. Technical Development of the In Vivo cDTI Technique

This thesis was conducted in tandem with sequence development work. Together these projects aimed to improve the understanding of technical limitations and advance the technique through innovation.

2. Assessment of Intra-centre Reproducibility in Patients with Hypertrophic Cardiomyopathy

Reproducibility of cDTI in HCM patients cannot be assumed from healthy volunteer data. Monopolar DW-STEAM acquisitions are technically complicated, and patient factors may impact on reproducibility.

3. Assessment of Inter-centre Reproducibility in Healthy Volunteers

Measures of quantitative cDTI parameters are highly varied across the literature; investigation of contributing technical factors is required. Assessment of inter-centre reproducibility will encourage measurement standardisation and highlight technical discrepancies.

4. Investigation of Innate Heterogeneity of cDTI Parameters in Healthy Volunteers

To date in vivo cDTI studies in healthy volunteers have comprised of small cohorts. The relation between quantitative parameters and subject anthropometrics is unknown. Establishing the innate heterogeneity of micro-structure, inferred from cDTI, is essential for the interpretation of results in HCM.

5. Comparison of Myocyte and Sheetlet Orientations in Hypertrophic Cardiomyopathy and Healthy Volunteers

cDTI offers the unique opportunity to assess myocyte and sheetlet dynamics in vivo. Understanding the contribution of these structures to LV function in health, and disease expression in HCM, may advance our understanding of pathophysiological mechanisms.

6. Comparison of cDTI Parameters in in Hypertrophic Cardiomyopathy, Hypertension and Controls

cDTI has the potential to differentiate HCM from healthy volunteers and other aetiologies of LVH. Evaluating cDTI parameters in HCM, hypertension and healthy cohorts will determine its diagnostic utility and may offer new insights into the link between microstructural abnormalities and disease expression.

In summary this thesis aims to explore the potential for in vivo cDTI in the assessment of microstructural dynamics in health and disease.

CHAPTER 2: LEFT VENTRICULAR STRUCTURE

2.1: Macroscopic Left Ventricular Anatomy

2.1.1: Introduction

The left ventricle is the most complex structure of the heart which has proven remarkably resistant to analysis of functional anatomy. Numerous investigators, from wide range of specialties, have contributed their views on its structure; however there remains a lack of consensus. In recent years, considerable advances in histological and imaging techniques have added a new perspective to this field and re-ignited the debate.

2.1.2: Cardiothoracic Anatomy

In health, the adult left ventricle (LV) measures between 9-12cm in length (20) with a shape described as a truncated ellipsoid (21). The LV forms the cardiac apex and a considerable portion of the diaphragmatic surface of the heart. In its short axis, the left ventricle is largely circular, with the septal component of the LV curving outwards towards the RV (22); however in vivo this circularity is attenuated by inferior wall flattening, as it rests on the diaphragm (23).

2.1.3: Trabecular Myocardium

Within the LV cavity the endocardial surface is characterised by a meshwork of trabeculations which are particularly prominent at the apical third. The presence and extent of ventricular trabeculation has been a matter of interest in recent years. Left ventricular 'non-compaction' (LVNC) is a cardiomyopathy characterised by an extensive layer of trabecular myocardium and thin/ absent compact layer combined with heart failure and malignant arrhythmias (24). A number of studies have proposed diagnostic criteria for LVNC based on imaging measures of the trabecular layer and ratios of compact to non-compact myocardium (25-27). Excessive

trabeculation has also been described in other cardiomyopathy phenotypes (28) and congenital heart disease (29), however recent population studies suggest that hypertrabeculation exists within the spectrum of normality (30), with ethnic dependent variation and increased prevalence in the context LV loading conditions (31). What truly constitutes 'excessive' trabeculation is therefore debatable.

2.1.4: Evolution of Compact Myocardium

Beneath the trabecular endocardial layer lies the compact myocardium. Some anatomists have argued that, in its early stages, the fetal left ventricle is spongiform and composed entirely of trabeculae (32). However Professor Robert Anderson and colleagues at University College London, dispute this theory, instead proposing that the compact layer is present at all stages, developing and thickening over time into its highly structured format (33, 34). Prof Anderson therefore has therefore argued that 'non-compaction' represents a misnomer as it implies that the condition is a consequence of trabeculae failing to compact, however there is no embryological evidence to support this theory of compact myocardial development (34). He does concede that the exact process and triggers for the genesis of compact myocardium are poorly described, however there is some evidence that ventricular loading conditions are important (35).

The LV morphological diversity observed across different species also appears to give support to loading conditions & LV stress as a driver for compact myocardium. In fish species alone, LV myocardium ranges from a spongiform arrangement in the minute zebra fish, to the highly compact myocardium of the tuna fish (33, 36). Mammalian hearts are morphologically similar with increasing cardiac mass, and compact myocardium, in proportion to body mass, with a relative cardiac mass of approximately 0.5% (37). The giraffe heart is particularly interesting as it is required to generate blood pressures of almost twice that of other mammals to maintain cerebral perfusion, yet retains a relative cardiac mass of 0.5% (figure 2.1)(37, 38). This is

achieved by significant left ventricular hypertrophy within a relatively smaller heart, with a near linear relationship between the thickness of the LV compact layer and neck length, such that a compact wall thickness of around 6cm is reported in the average adult giraffe (39).

Figure 2.1: The mean arterial pressure (MAP) of the giraffe is twice as high as that of human and other mammalian MAP (A). The relative weight, however, is similar as that of man and other mammals. All data

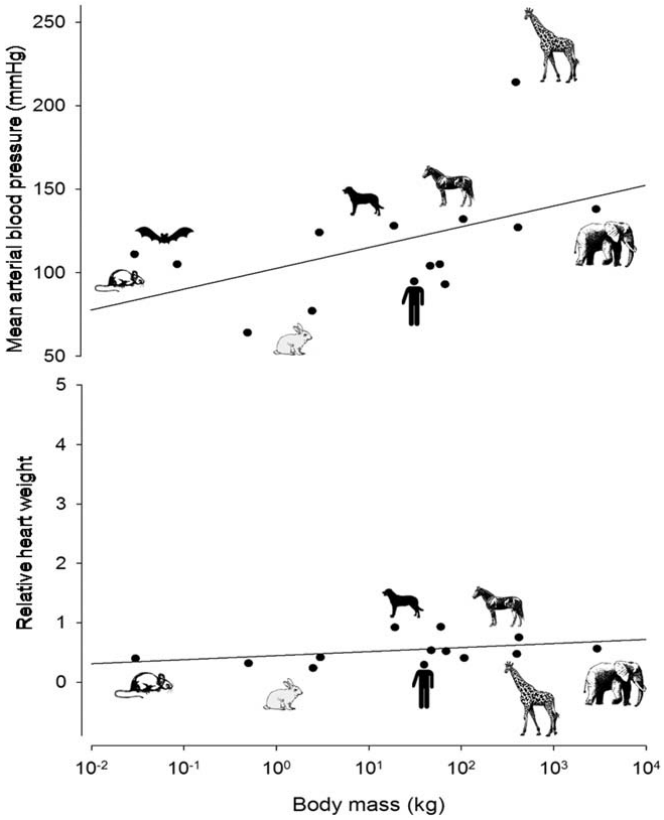

except for the giraffe are from Seymour and Blaylock (2000) (37, 38).

2.1.5: Myocardial Adaptation

In keeping with other mammalian hearts, the chamber size and mass of the human LV is dictated by body mass, and increases in line with growth throughout childhood (40). In adulthood the left ventricle has an estimated mass per body surface area of 74 ± 8.5g/m^2 (95% CI: 58, 91) in men; and 63 ± 7.5g/m^2 (95% CI: 48, 77) in women (41). The distribution of LV mass displays marked regional variation, decreasing from the base of the ventricle to the apex, with maximal wall thickness at the basal septum and minimum wall thickness at the apical cap (42, 43). As with skeletal muscle, in adulthood the myocardium retains the ability to adapt in response to

physiological demands. In the case of aerobic, endurance training, the LV adapts to increase stroke volume through ventricular chamber enlargement and mild eccentric hypertrophy. In contrast, resistance training results in concentric hypertrophy of the compact myocardium in the absence of chamber enlargement(44, 45).

2.2: Left Ventricular Myocyte Organisation

2.2.1: Introduction

The composition of the compact layer of the left ventricle myocardium has been the subject of innumerable studies, however its structure is still debated. This section describes theories of myocyte composition and its controversies.

2.2.2: Helical Myocyte Arrangement

Anatomical reports of LV myoarchitecture can be traced as far back as the 17th century, but in 1864 a Scottish pathologist called James Bell Pettigrew published a detailed account of macroscopic structure that remains relevant today (1). Pettigrew built on concepts originally proposed by Lower (1669), Senac (1749), Wolff (1780-1792), Gerdy (1823) and Ludwig (1849), and described the LV as 'so unusual, so perplexing, that it has long since been considered as forming a kind of Gordian knot in anatomy' (1). He embarked on a process of methodical calf and sheep heart dissection, the results of which won the Senior Anatomy Gold Award at Edinburgh University, and have been reproduced in drawings for his paper (Figure 2.2) (1). He identified visible, rounded strands of muscle travelling in parallel to one another, which he referred to as 'fibres', and noted that the connective tissues binding the muscle fibres were easily overcome by boiling, thus facilitating stripping of the muscle during dissection. He described the existence of 7 transmural layers, at increasing depth from epicardium to the endocardium, in which the fibres gradually change orientation with reference to the local wall plane. Fibres in the outer, epicardial

three layers were found to run from 'left to right downwards', otherwise known as left-hand helix, with gradually decreasing angulation from a vertical to horizontal orientation. The fourth layer was shown to have a circumferential, or horizontal orientation, and the final three, endocardial layers, ran in a 'right to left upwards' direction, also known as a right-handed helix, with increasing angulation towards the vertical (1). Pettigrew also asserted that the external, left-handed epicardial fibres spiral continuously to form the internal, right-handed endocardial fibres, such that fibres located in layers 1, 2 and 3 were continuous with layers 5, 6 and 7 respectively. He attributed the gradual apical thinning of the ventricle to the increasing height of the spiral continuations, i.e. layers 1 and 7 spiral at the apex, layers 2 and 6 above the apex, 3 and 5 higher still, with the 4th layer terminating above (1, 3).

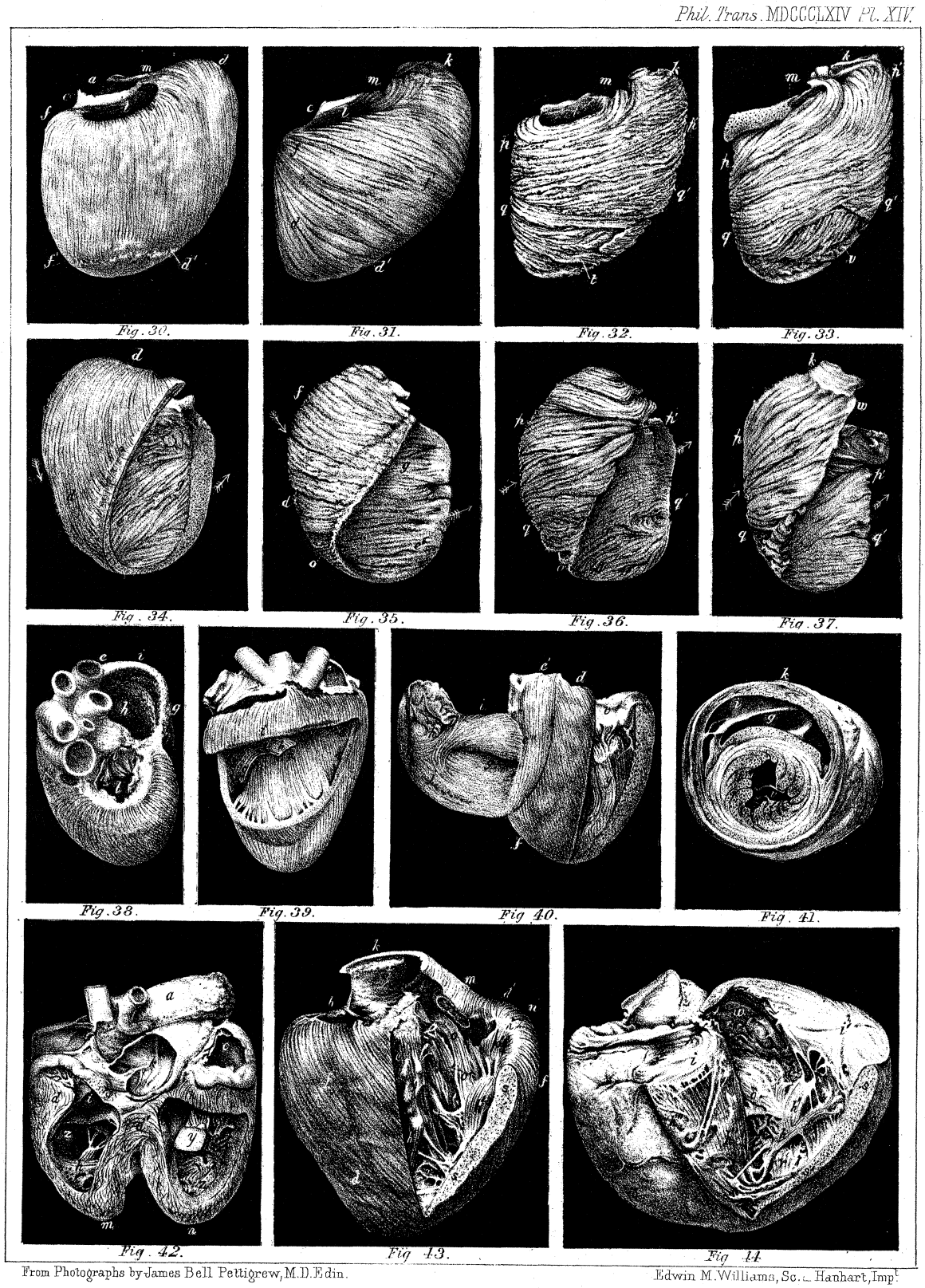

Figure 2.2: Anatomical drawings of sheep hearts at various stages of dissection. The top 8 pictures depict the cardiac 'fibre' orientation during gradual stripping of the muscle layers. It shows fibres winding anticlockwise in the epicardium, circumferentially in the midwall and clockwise in the endocardium (1).

Towards the end of the 19th century, Krehl performed a similar analysis and emphasised the presence of the circumferential myocytes identified by Pettigrew. He referred to them as the 'Triebwerkzeug', a rough translation of this: trieben – drive and werkzeug – tool, reveals that he theorized an important role cardiac contraction (46).

2.2.3: Myocardial 'Muscle Bands'

In the early 20th century growing interest brought new theories regarding LV myoarchitecture. Investigators were still reliant on dissection and believed that, like skeletal muscle, the LV was composed of long fibres, or bands of muscle, which could be located with the correct dissection plane. MacCallum dissected embryo porcine hearts and described a continuous fibrous skeleton originating from the ventricular base and terminating within the papilliary muscles (47). Mall, MacCallum's teacher, built on this concept and described distinct tracts labelled 'bulbo-spinal', which coincided with circumferential fibres, and 'spino-spiral', which wound in a figure of 8 making the helical pattern of the epi and endocardium (48), however he conceded that his theory did not apply 'equally well to all portions of the ventricular wall'. In 1956 Lev and Simkins adopted a 'modified MacCallum-Mall technique' but were unsuccessful in their attempt to reproduce the reported cleavage plane between bulbo- and spino-spiral tracts, and instead proposed the myocardium comprised of three fascicles: epicardial, mid wall and endocardial (49). In 1965 Grant published a critical review of the MacCallum approach, asserting that such theories were flawed in their assumption that the myocardium was composed discreet muscle bundles. He referred to the myocardium as a 'syncytium' and illustrated its branching composition with a network of connections in numerous directions. He also highlighted that the dissector could easily influence the interpretation through the size of the segments studied and by following preconceived pathways (50).

2.2.4: The Ventricular Myocardial Band Theory

Subsequent analyses of macroscopic anatomy can broadly be divided into proponents and opponents of the myocardial bundle or band theory. The most noteworthy proponent was Torrent-Guasp, a Spanish cardiothoracic surgeon, who conceived the theory and whose work continues to shape opinion. During his surgeries he directly observed cardiac contraction and firmly believed that the ability of the left ventricle to suck blood into its cavity during diastole was evidence that diastole, like systole was an active as opposed to passive process. In the 1950s, during his fourth year of medical studies at Salamanca University, Torrent-Guasp began a quest to explain this theory through cardiac dissection. After 25 years of study he concluded that both the right and left ventricles are formed from a continuous ventricular myocardial band (VMB) that could easily be unwrapped via a natural cleavage planes (51-53). He proposed that the band was activated sequentially during the cardiac cycle, with activation of the terminal portion accounting for 'diastolic sucking'. The initial evidence to support this claim was the reproducibility of the dissection and his assertion that sequential contraction of the descending and ascending limbs of the apical loop explained forceful reciprocal twisting observed by cardiothoracic surgeons during operative procedures (figure 2.3) (51-53). His work gained international recognition and in 2002 The National Institute of Health in Bethesda held a multidisciplinary workshop to debate his theory and examine supporting electrophysiological and imaging evidence. In 2005, the year of his death, in his final publication Torrent-Guasp boldly claimed that the 'ancient enigma of myocardial architecture is finally solved' (53).

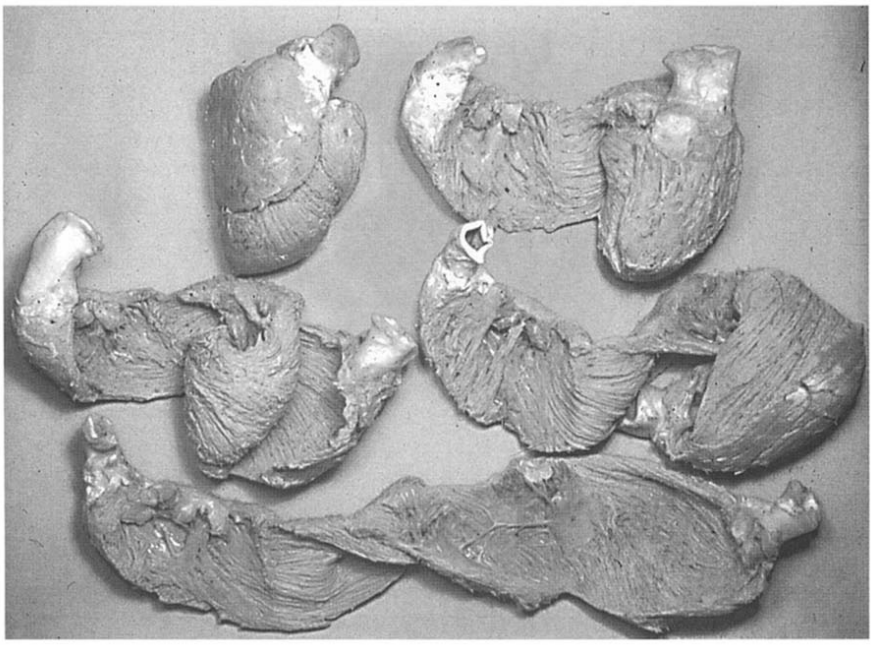

Figure 2.3: Five successive phases of the unwinding of the ventricular myocardial band. In the first specimen (upper left) the band appears in its normal position, as it is in the intact heart. In the last specimen (bottom) the band is fully unwound (51).

Support for the VMB theory remains today; Buckberg a UCLA based academic cardiothoracic surgeon and contributing author on Torrent-Guasp's later works, has continued to develop the concept. His contribution includes evidence from contemporary imaging studies such as DTI, CMR tagging, echocardiography tissue velocity, and sonomicrometer recordings which confirm the helical structure of LV, and rotational and twisting mechanics central to the hypothesis (54-57). However the VMB theory has attracted significant opposition. Among the most vocal critics being Professors Lunkenheimer and Anderson, who in 2005 published reviews in the European Journal of cardiothoracic surgery to counterbalance those from Torrent-Guasp and Buckberg in the same journal (46, 58). The debate was somewhat heated with Anderson referring to the publications of his academic adversaries as 'diatribes' (46) and Lunkenheimer described the situation as an 'enigmatic states of affairs' (58). Their criticisms included the crude nature of the manual dissection that, as Grant had previously commented, could create artefactual cleavage planes. They also cited embryological (33), electrophysiological and diffusion tensor imaging

studies (59) in conjunction with classic dissection which contradicted the VMB theory (46, 58, 60). Other notable critics include Greenbaum, a Royal Brompton based collaborator. He countered the work of Torrent-Guasp with his own dissections and histology, but stated that both techniques were still inadequate to draw final conclusions regarding LV structure (3). He emphasised the regional heterogeneity of the myocardium and the presence of circumferentially orientated myocytes in the septum, a fact denied by VMB supporters, and concluded that models based on simple, uniform structure could not explain LV function (3).

2.2.5: A Bioengineering Perspective

Alongside Pettigrew, Streeter is arguably one of the most influential researchers in LV myoarchitecture. Streeter and colleagues were the first to introduce objective quantitative analysis of myocardial structure marking a significant change in direction from the qualitative analysis undertaken by anatomists, towards a new bioengineering perspective concerned with mechanics and functional modelling (2, 10, 61-64). In his initial work, samples were taken at 1mm transmural intervals in contracted pig hearts, the results demonstrated smooth transition in myocyte angulation with no evidence of distinct muscle layers and minimal regional heterogeneity and he concluded the myocardium was more appropriately regarded as a 'continuum' than as discreet muscle bundles (61). More extensive work followed in canine hearts arrested in systole and diastole, with analysis of tissue wedges taken from a T shaped specimen of the LV free wall, with the terminal portion of the T extending to the LV apex. In this instance, greatest change in transmural myocyte angulation was observed at the apex, with a near linear change in angulation through the midwall. In contrast, the more basal samples had a sigmoid shaped graph of depth v myocyte angle, with the greatest change in the epi and endocardium, and reduced rate of change in the midwall (figure 2.4), a finding that was later replicated by Greenbaum et al. (3). When comparing myocyte angles in systole and diastole, the shape of the

graphs remained the same with systolic uniformly increased fibre angles by approximately 7° near the base, and 19° near the apex (2).

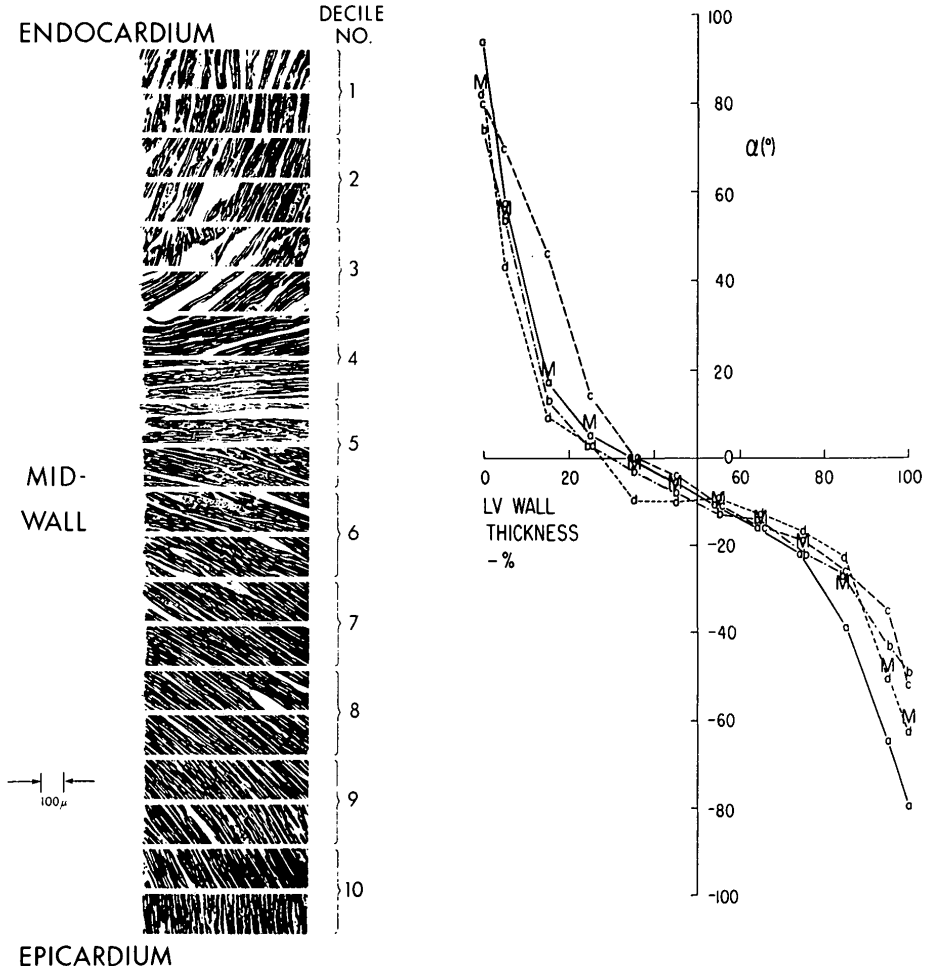

Figure 2.4: The left-hand picture is a sequence of photomicrographs showing myocyte angles in successive sections taken from a heart in systole. The sections are parallel to the epicardial plane. Myocyte angle is +90° at the endo- cardium, running through 0° at the midwall to -90° at the epicardium. The sequence of numbers refers to deciles of wall thickness.

The right-hand picture depicts the angles determined from 4 transmural samples with M representing the mean. Zero percent thickness represents the subendocardium and 100% the subepicardium. Myocyte angles were observed to decrease sharply in the outer most subpeicardium and subendocardium with reduced angular rate of change in the mid-wall (2).

Since Streeter a number of bioengineers have tackled the subject of macroscopic LV anatomy, reaching a general consensus with regards to the progressive helical arrangement of myocytes (4, 65, 66). Proponents of the VMB theory remain but are outnumbered by those who believe the evidence is to the contrary. In Chapter 4 the impact of new technologies on our understanding of LV functional anatomy will be discussed.

2.3: Microscopic Left Ventricular Anatomy

2.3.1: Introduction

In recent years, arguably the most significant advances in our understanding of myocardial mechanics have come from analysis of microstructural and ultrastructural anatomy.

2.3.2: Sarcomeric Structure

The fundamental structural and functional unit of contraction in both skeletal and cardiac muscle is the sarcomere. The sarcomere is a specialised cytoskeletal structure, which serves as the motor unit of the myocyte. The importance of sarcomeric protein interactions in cardiac health has been highlighted in recent years by the association of a growing number of sarcomeric protein mutations with cardiomyopathies (67, 68). Each sarcomere is composed of a highly ordered array of contractile proteins with an alternating thick (diameter: 10-12nm, length: 1.65μm) and thin (diameter: 5-7nm, length: 1.0μm) filaments (69). The highly organised arrangement of partially overlapping myofilaments creates a characteristic band-like appearance which is delineated laterally by Z lines, and the midline by thin M lines (figure 2.5) (69-71). At either side of the Z line is the I (isotropic) band, a region comprised solely of thin filaments and thus comparatively light. In contrast, the adjacent A (anisotropic) band is dark and reflects the alignment of multiple thick filaments; at its centre is the H zone is a narrow light region that is relatively devoid of myosin cross bridges (figure 2.5)(67, 68, 72).. Using high-resolution microscopy, observations of the sarcomeric band pattern lead to the breakthrough in understanding of the behaviour of myofibrillar proteins during contraction (70, 73, 74).

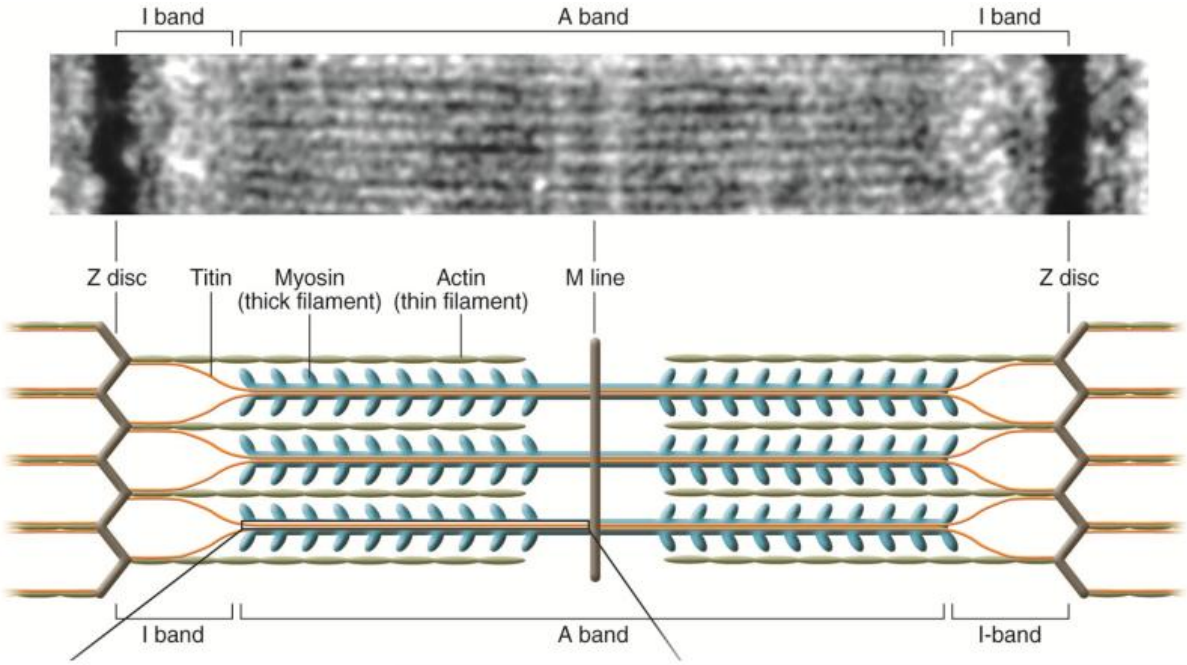

Figure 2.5: Schematic representation of the sarcomere. The M band marks the middle of the sarcomere; the A band is made of parallel overlapping thick and thin filaments and includes a central H zone where the thick filament is devoid of myosin cross bridges; the I band marks where there are only thin filaments; and the z discs mark the lateral borders of the sarcomere (72).

2.3.3: Cardiomyocyte Structure

Vertebrate cardiac sarcomeres at rest are ~2.0-2.5μm in length and are arranged longitudinally, in a repeating pattern, into rod like muscular units called myofibrils. Myofibrils are further grouped together into individual myocytes; human myocytes are estimated to be ~130-160μm in length and μm in cross sectional diameter (fixed with isotonic solution & wax embedded) (75, 76). Compared to skeletal myocytes, cardiomyocytes are predominantly mononucleate, with a higher density of mitochondria ensuring low fatigability. Cardiomyocytes insert end-to-end thus ensuring efficient contraction through axial alignment of the contractile apparatus and, unlike skeletal myocytes, possess a number of side branches, which interconnect with neighbouring cells (46, 65). Cardiomyocytes branch at relatively acute angles, connecting in 3 dimensions with cells running parallel, as a result a predominant myocyte long and short axes can be identified (figure 2.6) (65). The terminal portion of myocytes and their branches form a series of projections and depressions that are bound to adjacent myocytes through intercalated discs. These

connections provide structural integrity, via desmosomes, and create an electrochemical myocardial syncytium by facilitating rapid and coordinated transmission of electrical impulses through porous gap junctions (65). Ventricular myofibrils are encased externally by a membranous sarcolemma, which invaginates to form T-tubules, rich in ion channels responsible for excitation-contraction coupling. Ventricular myocyte t-tubules are bigger than skeletal, but less numerous, forming a diad with terminal cisterna of the sarcoplasmic reticulum (77, 78). An extensive network of fibrous connections surrounds the myocyte complex, such that the myocardium has been referred to as a complex fibrous continuum (65).

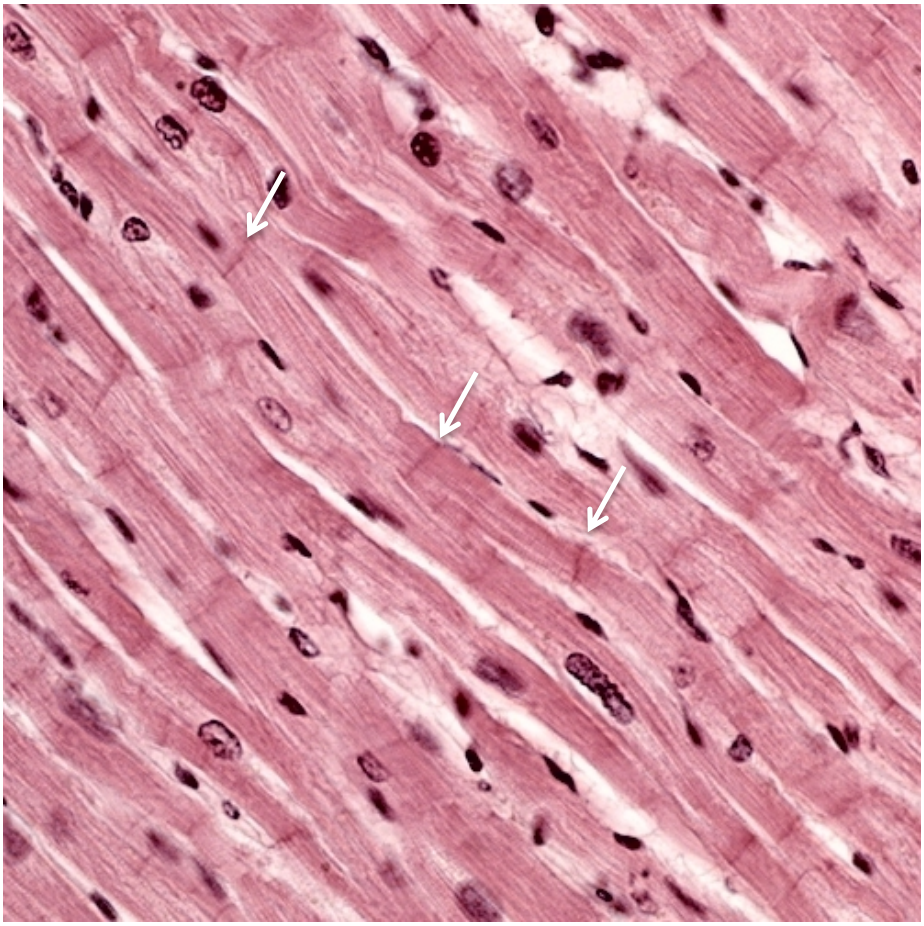

Figure 2.6: Histological image of cardiomyocyte structure with haematoxylin and eosin staining. Cardiomyocytes run parallel to one another and are joined, via intercalated discs (arrows), in a random branching pattern. Cardiomyocytes are mononucleate with sarcomeres arranged longitudinally for efficient contraction (79).

2.3.4: Structural Arrangement of Cardiomyocytes and Myocardial Connective Tissues

The myocardium is a complex mixture of fluid, myofibrillar and elastic components, with intra and extracellular fluid estimated to account for ~90% of the myocardium. The microscopic arrangement of cardiomyocytes and their connective tissues has been a subject of significant interest in recent years. Around the late 1970s/early 80s electron microscopy studies brought new insights into the connective tissue network of the left ventricle (65, 80, 81). A detailed description of the collagen hierarchy was given by Robinson (81-83), who categorised the appearances using skeletal muscle terminology; although the appropriateness of this system, beyond trabeculae and papilliary muscle, has been questioned (65):

1. The first layer is the **endomysium**, which surrounds each myocyte connecting them to adjacent myocytes via and array of 'collagen struts', 120-150nm in length, woven around the Z-bands of the myofibrils (4, 65, 80-83).
2. The **perimysium** is described as a network of longer collagen fibres, which loosely connect groups of three or more myocytes into discreet bundles (figure 2.7)(4, 80). This structure appears to be unique to the myocardium and differs in trabeculae and papilliary muscles, where long, coiled fibres up to 10μm have been described (83). The perimysial spaces also facilitate autonomic innervation and the passage of blood vessels.
3. The **epimysium** surrounds the ventricular mass and protects the entire structure from destructive degrees of stress (46).

2.3.5: Cross Myocyte Myolaminar Structure - Myocardial 'Sheetlets'

The significance of perimysial and myocyte bundle structure has been a subject of great interest to those attempting to unravel the complexity myocardial contraction. Early anatomical & histological analyses focused primarily on the orientation of myocytes along their long axes, which lie in a plane tangential to the epicardial surface (2, 3, 61, 64). However the perimysium permits further subdivisions of the myocardium in planes oblique to the epicardial wall, ie. the

cross myocyte plane. These subdivisions, or cleavage planes, were initially highlighted by Spotnitz, who demonstrated visible gaps in transversely sectioned rat hearts (10). Subsequent histological investigations, applying techniques such as electron microscopy and confocal microscopy, have revealed the ventricular myocardium is divided into branching sheets or 'sheetlets', 4-5 myocytes thick, held tightly together by perimysial collagen (figure 2.7) (4-6, 11, 13, 84-87).

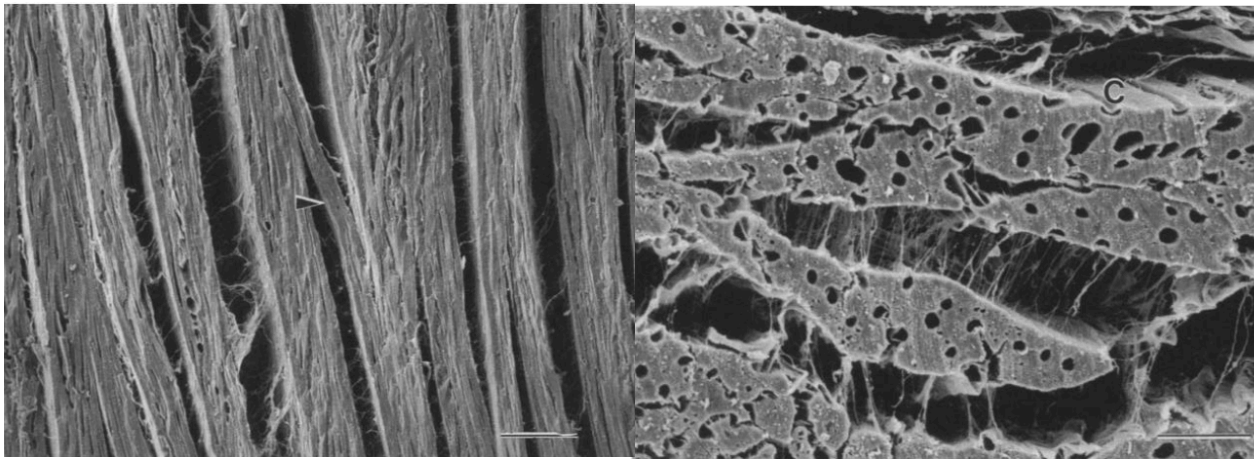

Figure 2.7: Scanning electron micrographs of canine left ventricle. The left-hand picture is from the tangential surface of the myocytes at a scale of 100μm. It illustrates the layered structure, branching myocytes (indicated by the black arrow) and the collagen fibres between the sheets. The right-hand picture is from the transverse surface of the myocytes at a scale of 25 μm. In this image the perimysial collagen can be visualised between myocardial sheets and surface capillaries (marked with C) (4).

Adjacent sheets are held by looser connections with resulting gaps which are proposed to function as 'shear layers' (5, 7, 9, 10, 13). Together the network of sheetlets and interspersing shear layers are referred to as **myolaminae**. Studies of the electrical properties of the heart support this anatomical interpretation, with 3 distinct left ventricular propagation directions identifiable, which coincide with microstructural axes defined by myolaminae (88, 89).

Initially Le Grice et al. proposed that cleavage planes were long radial septations, spanning continuously from the epicardium to endocardium (4), but subsequent contributions from this

group and others suggest that myolaminae are highly discontinuous throughout the midwall and endocardium and absent in the subepicardium where the perimysium is organised in long chords (figure 2.8) (5, 86, 90).

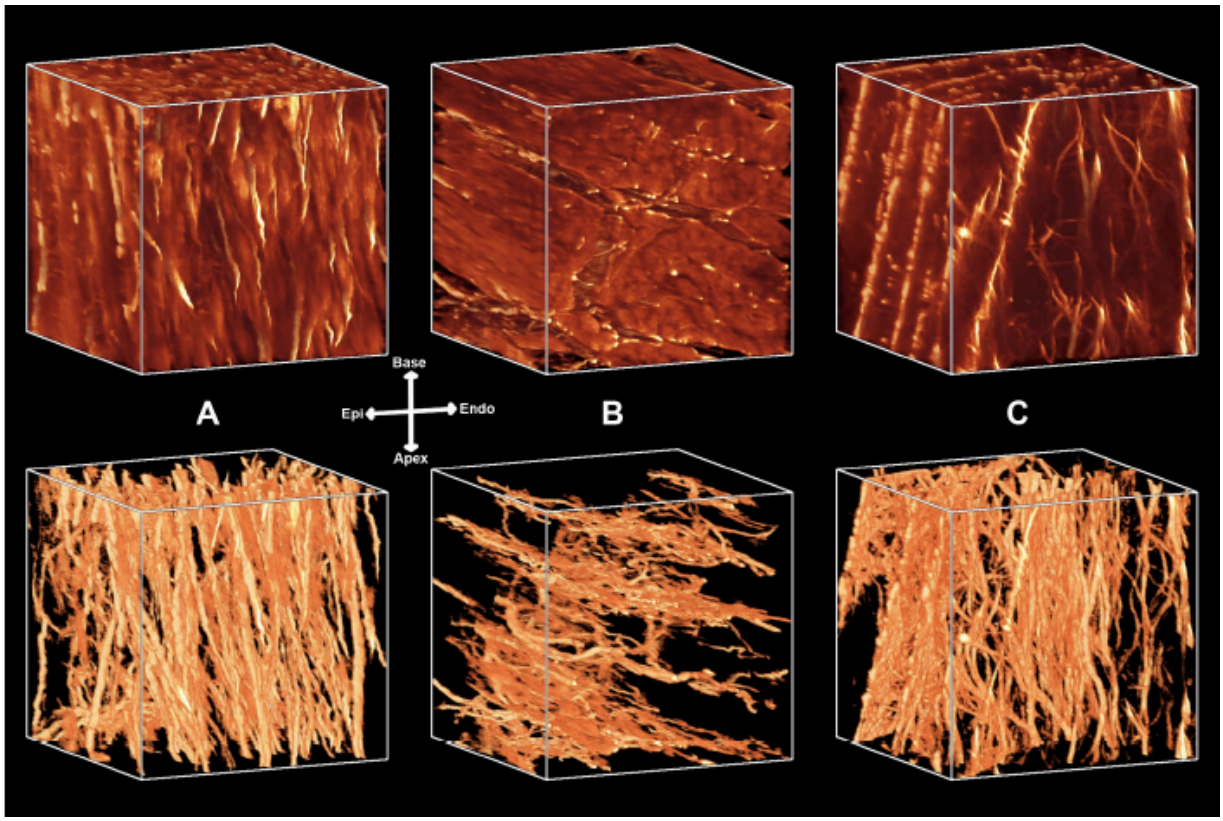

Figure 2.8: High resolution extended volume confocal microscopy images of rat left ventricle sections with three dimensional reconstruction. The top images show myocytes and collagen together and bottom row shows collagen only. Subepicardial sections in column A show long wavy chords of perimysial collagen with sparse interconnections. Within the midwall sections in column B groups of myocytes are surrounded by sheets of collagen giving rise to cleavage planes. In column C subendocardial perimysial collagen is similar in arrangement to the midwall but with a higher concentration of sheets (86).

Later work suggested that sheetlets in fact exist in two distinct transmural populations, at right angles to one another, raising questions of their role in cardiac mechanics (figure 2.9) (7, 8, 91).

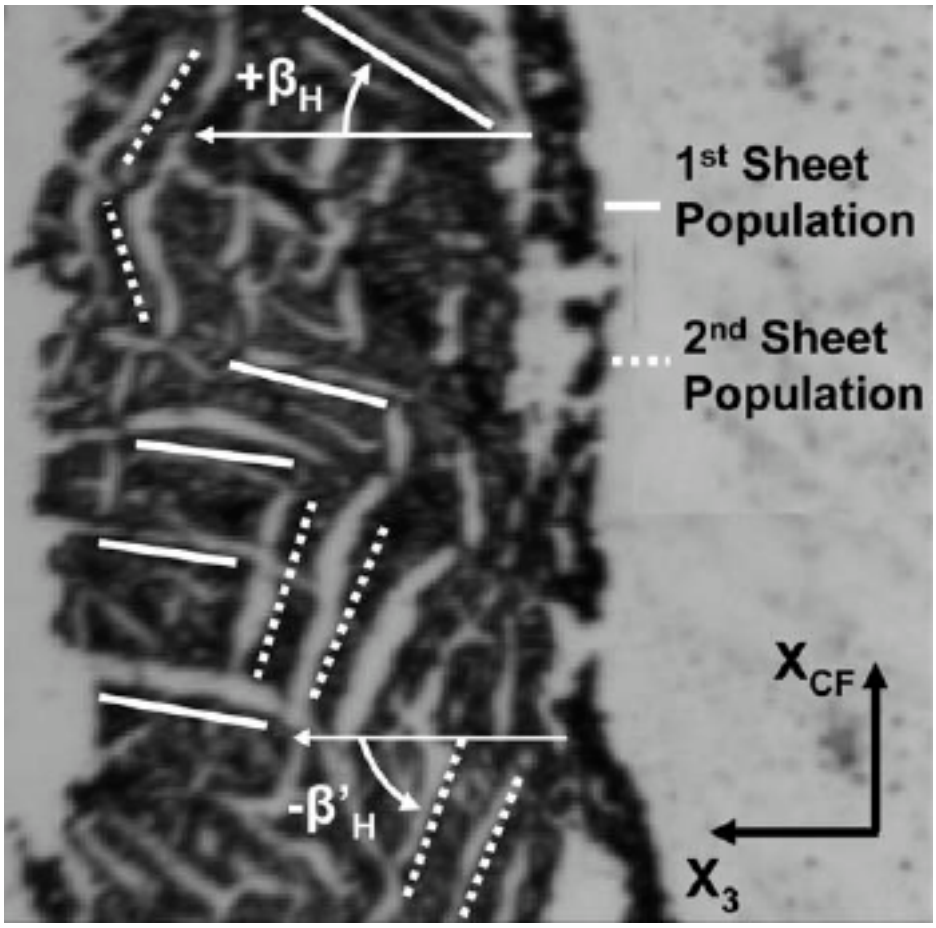

Figure 2.9: Histological photo of 2 observed sheetlet populations in a section from sheep left ventricle. The section is longitudinal and the fibre axis points out of the page towards the reader, XCF represents the cross-fibre plane and X3 the perpendicular local axis. Sheetlet populations are demarcated with solid and dashed lines and their angulation is shown projected onto the X3 axis (7).

In recent years, arguably the most considerable contributions to this field have come from contemporary imaging techniques, such as diffusion tensor imaging (DTI), which have enabled the non-destructive interrogation of myolaminar dynamics during cardiac contraction (Chapter 4)(7, 13, 92). An improved understanding of myolaminae may in turn open new lines of investigation into structural-functional relationships in myocardial disease processes.

CHAPTER 3: LEFT VENTRICULAR MECHANICS

3.1: Global Left Ventricular Mechanics

3.1.1: Introduction

This chapter discusses the myocardial function that arises from the unique anatomy of the left ventricle. The complexity of left ventricular architecture is reflected in its mechanics as the relatively straightforward time-dependent and length-dependent features of skeletal muscle mechanics are not observed in the heart. The identification of sheetlets and shear layers has brought renewed interest in the mechanics of contraction and new technologies have offered a new perspective.

3.1.2: Left Ventricular Ejection Fraction

The mammalian LV is a highly efficient pump, which delivers a variable cardiac output in response to physiological demands. Normal resting cardiac output around 5 L/min in a 70kg person and is the product of heart rate and the volume of blood ejected with each cardiac contraction. Ejection of blood from the ventricle is the result of a reduction in intra-cavity volume between systole and diastole. The advent of high spatial and temporal resolution imaging techniques, such CMR and echocardiography, have enabled accurate assessment of LV volumetric data. With each beat the volume of blood ejected from the heart is the stroke volume (ml), which is also expressed as a percentage of the starting diastolic volume, known as the ejection fraction (EF). As with LV mass, LV volumes and EF are dependent on body surface area (BSA) and gender (41, 93). The average measures of cardiac chamber and function in adult men and women, as assessed by CMR are given in table 3.1.

	All	Males	Females
EDV [mL]	142 ± 21	156 ± 21	128 ± 21
	(102, 183)	(115, 198)	(88, 168)
EDV /BSA [mL/m^2]	78 ± 8.8	80 ± 9	75 ± 8.7
	(60, 95)	(63, 98)	(57, 92)
ESV [mL]	47 ± 10	53 ± 11	42 ± 9.5
	(27, 68)	(30, 75)	(23, 60)
ESV/BSA [mL/m^2]	26 ± 5.1	27 ± 5.5	24 ± 4.7
	(16, 36)	(16, 38)	(15, 34)
SV [mL]	95 ± 14	104 ± 14	86 ± 14
	(67, 123)	(76, 132)	(58, 114)
SV/BSA [mL/m^2]	52 ± 6.2	53 ± 6.1	50 ± 6.2
	(40, 64)	(41, 65)	(38, 63)
EF [%]	67 ± 4.6	67 ± 4.5	67 ± 4.6
	(58, 76)	(58, 75)	(58, 76)
Mass [g]	127 ± 19	146 ± 20	108 ± 18
	(90, 164)	(108, 184)	(72, 144)
Mass/BSA [g/m^2]	69 ± 8.1	74 ± 8.5	63 ± 7.5
	(53, 84)	(58, 91)	(48, 77)

Table 3.1: Left ventricular summary data from 120 patients aged 20-80yrs (mean±SD, 95% confidence intervals) EDV: end diastolic volume, ESV: end systolic volume, BSA: body surface area, SV: stroke volume, EF: ejection fraction (41).

In general CMR measures of ejection fraction are greater than those reported by echo, however the techniques are largely in agreements with regards to the lower limit of normal: Echo 55% (94), CMR 57% (41). In vivo, therefore, the normal functioning ventricular cavity reduces in size by ≥55% in systole.

3.2: Axial Left Ventricular Mechanics

3.2.1: Introduction

End systolic geometry is the end result of a number of complex morphological changes encompassing myocardial shortening and thickening (95). Both shortening and thickening can be quantified by measuring regional strain, which is expressed as a fractional or percentage change of the original dimension, such that positive strains represent thickening and negative strains represent shortening (96, 97). Contemporary imaging techniques express strain in 3 perpendicular axes defined by the global geometry of the LV: radial, circumferential and longitudinal. A fourth measure of systolic function is ventricular rotation or torsion, which is bi-phasic, occurring in a clockwise direction at the ventricular base and an anti-clockwise direction

at the ventricular apex during systole and reversing in diastole(when viewed from the apex). Rotation is more pronounced at the apex due to a relative lack of local structural constraints (figure 3.1).

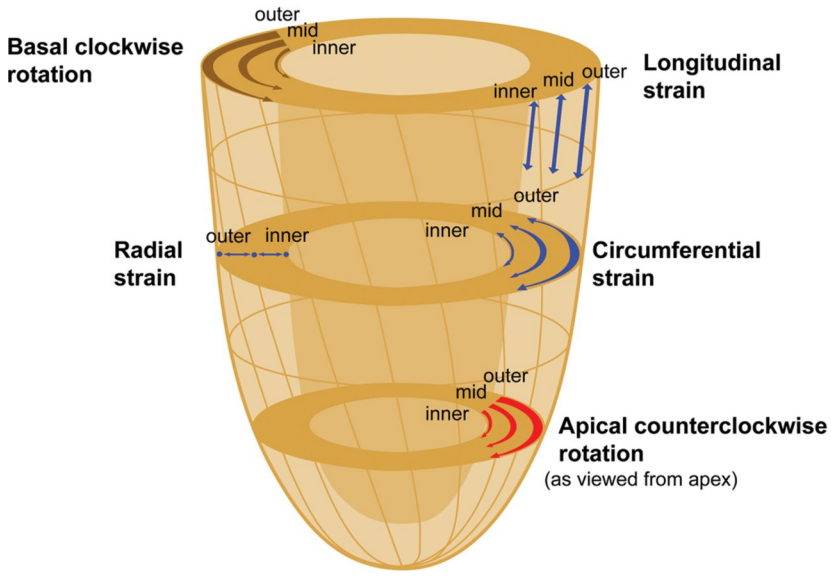

Figure 3.1: Illustration of LV longitudinal, radial and circumferential strain and apical and basal rotation (98).

3.2.2 Longitudinal Strain

The left ventricle shortens along its long axis during contraction and in vivo is assessed by measuring the apical decent of the mitral valvular annulus. Both CMR and echo measures of longitudinal function are predominantly taken from the apical 4-chamber view (40, 93, 99-101), however measures are also reported from the apical 2 and 3-chamber views (93, 102). Analysis methods include manual measurement of distance travelled by the mitral annulus reported in millimetres, or expressed as a percentage of ventricular length to give strain, in addition to automated techniques based on feature tracking (93, 100, 103, 104). In light of the variety of measures used and inter and intra-observer variability, there are a number of quoted values in healthy hearts, however estimates of strain range between 12 and 21% (table 3.2).

Four chamber longitudinal strain measurement	**CMR**	**Echo**
Mitral annular descent (mm):	Maceria et al (41):	Doesch et al (105):
Septal	15±3.4	
Lateral	17±3.7	
Average		14.3±1.8
Feature tracking global longitudinal strain (%)	Onishi et al (100):	Onishi et al (100):
	-14.1±6.8	-12.0±5.6
	Andre et al (93):	Caselli et al (106):
	-19.2±3.6	-19.4±2.3
		Farsalinos et al (102):
		-17.9 to -21.4

Table 3.2: Quoted values for longitudinal strain measures in healthy subjects by CMR & echo. Farsalinos et al. quotes the range of global longitudinal strain across different echo machine vendors (102).

Longitudinal strain is directly correlated with global LV systolic function (107-111) and displays regional variation with greater strain in the lateral and inferior walls to the septal and anterior (41, 112). CMR feature tracking recently found strain to be greater in women than men (93), however both echo and CMR report little gender difference in measures of mitral annular descent (110, 113). Longitudinal function declines with age (93), but appears to be unaffected by athletic training (106). Although EF is the preferred measure of LV systolic function, in patients with hypertrophic cardiomyopathy, longitudinal function was found to be correlated with the degree of fibrosis (105) and a predictor of adverse events (104). It has also been reported as a predictor of myocardial recovery post aortic valve replacement (103), and an early marker of LV systolic impairment (110, 114) coronary artery disease (115) and chemotherapy related cardiotoxicity (116).

3.2.3: Circumferential Strain

During contraction the left ventricular subendocardial and subepicardial radii reduce in size, which expressed as circumferential strain. Estimates of global circumferential strain in healthy human hearts range between -16 and -25% (40, 93, 99-101, 112). Circumferential strain is greater at the endocardium than the epicardium and increases from the base of the ventricle to the apex, and is greater in the anterior and lateral walls than inferior and septal walls (40, 101). Global circumferential strain declines with age, is greater in women than men, and displays ethnic differences with greater strain in people of Asian descent than African-American descent (93, 101). Although less sensitive than longitudinal strain, reduced circumferential strain has been reported as an early marker of coronary artery disease (115).

3.2.4: Radial Strain

Radial myocardial wall thickening, or strain, is arguably the most studied aspect of left ventricular mechanics. Radial strain is the greatest of the axial left ventricular strains and in fixed canine hearts has been estimated at between 20-30% (63). From in vivo human data, the majority of global estimates from CMR and echo ranging between 30 - 60% (93, 99, 101, 117), but with some reports as high as 88% (118). Radial strain decreases from the ventricular base to the apex and is greater in the anterior and lateral walls compared to the septal and inferior walls (101, 112). Men have greater radial strain than women and, in contrast to longitudinal and circumferential strain, radial strain increases with age (93).

The transmural heterogeneity of radial strain has been a subject of interest to those investigating ventricular mechanics. Before the event of high temporal & spatial resolution imaging with CMR & echo, investigators placed radio-opaque markers at increasing transmural depths in anaesthetised animal hearts (9, 66, 119). The results have been corroborated by contemporary in vivo canine imaging and revealed a transmural gradient in radial strain increasing from the epicardium (25.5±0.6%) to the endocardium (43.3±0.1%) (120). Radial strain is also sensitive to

cardiovascular disease processes with impairment demonstrated in the context of myocardial ischaemia (121), diabetes (122) and pre-eclampsia (123).

3.2.5: Ventricular Torsion

In addition to the axial strain components of LV mechanics, during contraction, the ventricle rotates in a clockwise direction at the base, and an anti-clockwise direction at the apex, with ventricular 'torsion' defined as the difference between the two (figure 3.1) (124). This has been described as a wringing motion and was first quantified in humans with the aid of surgically implanted radio-opaque markers (125) and more recently with echo and CMR (96, 124, 126-128). Ventricular torsion is thought to arise from contraction of helically arranged myocytes and is significantly greater at the apex (~10°) compared to the base (~3°), and at the endocardium compared to the epicardium (96, 128). Supporters of Torrent-Guasp's Ventricular Myocardial Band theory have proposed that the forceful reciprocal ventricular twisting observed during open chest surgery is proof of the existence of the VMB (46, 53). Ventricular torsion declines with age (129) and impaired torsion has been demonstrated in patients with dilated cardiomyopathy (130) and coronary artery disease (131), whereas greater than normal torsion but has been reported in patients with hypertrophic cardiomyopathy (132).

3.3: Local Myocyte and Cross Myocyte Mechanics

3.3.1: Introduction

In addition to left ventricular deformation along artificially defined geometric axes, ventricular mechanics can also be described in relation to histological planes defined by the local myocyte, or 'fibre' axis (figure 3.2).

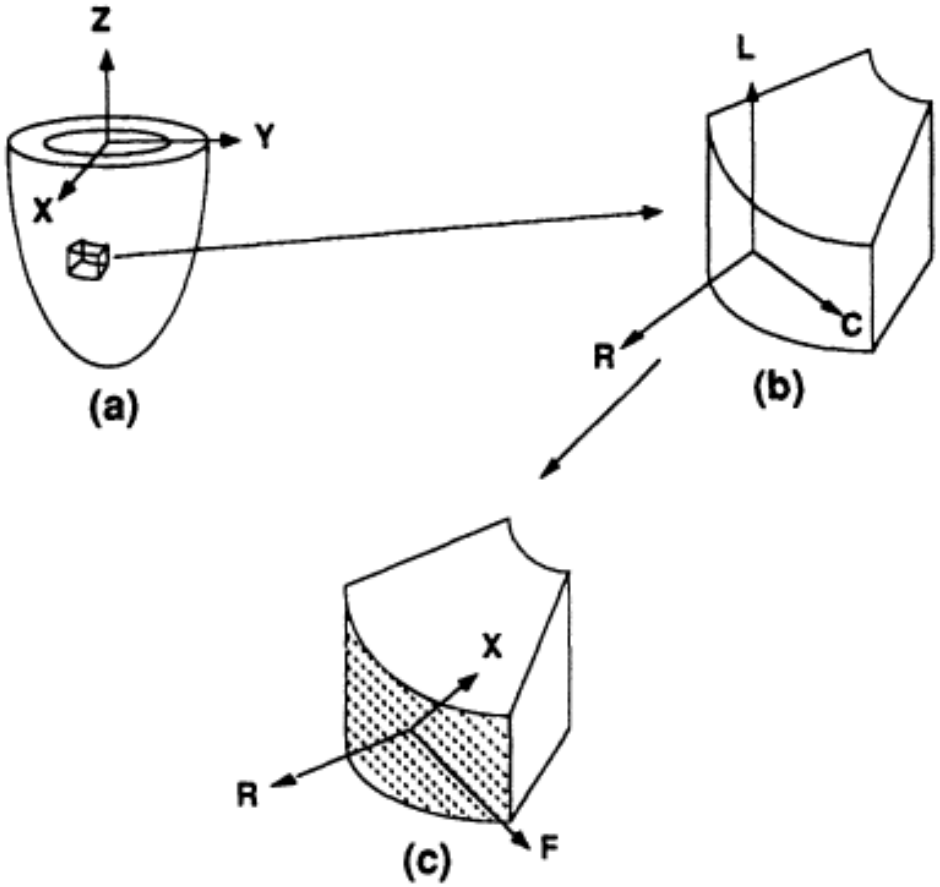

Figure 3.2: Example illustration of the derivation of myocyte (fibre) and cross-myocyte (fibre) axes using CMR. In figure (a) the axial xyz magnetic coordinates are shown. From these axes the standard LV geometric axes are obtained (b): L represents the long axis of the ventricle, R the transmural radius and C the circumferential plane which lies in a tangent to the surface of the ventricle. In (c) fibre angulation data is superimposed on to the surface of the tissue cube (broken lines). The circumferential-longitudinal plane is then rotated to around R to align the fibre direction (F), with the cross-myocyte direction (X) defined as perpendicular to the radial-fibre plane (120).

3.3.2: Left Ventricular Myocyte Axis

In vivo myocyte shortening occurs along the long axis of cells due to the longitudinal arrangement of sarcomeres. Streeter et al. studied the change in myocyte angulation between diastole and systole and found a uniform increase in angles by approximately 7° near the base, and 19° near the apex (2), with the discrepancy attributed to torsion (95). In vivo myocyte axis strain was initially studied by imaging transmural radio-opaque beads (11, 66, 133, 134) and subsequently via CMR tagging (120) with histologically derived myocyte angulation superimposed (figure 3.2).

In each case myocyte long axis strain was estimated at ~-8% with no significant difference from the epicardium to the endocardium.

When myocyte long axis strain is interpreted within the context of observed axial strains, it is clear that LV mechanics cannot be explained by the angulation or shortening of myocytes in the sarcomeric axis alone. Myocyte long axis strains are relatively minor and largely uniform and therefore appear to offer little explanation for the magnitude and heterogeneity of myocardial deformation.

3.3.3: Cross-Myocyte Mechanics

In contrast to the minimal changes observed along the myocyte long axis, mechanics in the perpendicular, or cross-myocyte axis (figure 3.2), show greater transformations. Sarcomeres are aligned with the myocyte long axis; sarcomeric and myocyte shortening is therefore only possible in this direction, however, in vivo, cross-myocyte shortening, or negative strain, is also observed (9, 11, 66, 120, 133). Moreover, the heterogeneity observed in transmural radial strains is mirrored in cross-myocyte mechanics, with minor cross-myocyte shortening at the epicardium (-0.6%±0.5%) compared to extensive endocardial shortening (-25±0.6%) (120). As this phenomenon cannot be explained by contraction at the myocyte level, it suggests a potential role for myolaminar sheetlets and shear layers (9, 10, 119, 120).

3.4: Sarcomeric & Myocyte Mechanics

3.4.1: Introduction

Global left ventricular contraction is the culmination of a number of complex contractile processes ranging from the ultrastructural to macroscopic level. Understanding ventricular mechanics therefore requires an appreciation of the relationship between these elements.

3.4.2: Sarcomeric Mechanics

At the ultra-structural level, sarcomeric contraction is the result of interaction between actin and the cross-bridges on myosin filaments and is referred to the as the 'sliding filament theory'. Observations of the sarcomeric band pattern during contraction revealed narrowing of the I bands and H zone, with constant length of the A band (62, 68, 73). Depolarisation of the cardiomyocte cell membrane results in calcium release from the sarcoplasmic reticulum, which binds with troponin exposing the myosin binding sites on actin. The myosin heavy chain head then interacts with actin, forming a cross-bridge, and with release of ADP pulls actin towards the M-band. Subsequent hydrolysis of bound ATP then releases the cross-bridge therefore allowing the cycle to repeat. Consequently sarcomeric shortening occurs despite preservation of actin and myosin filament length, hence the sliding filament theory (figure 3.3)(68, 69, 73).

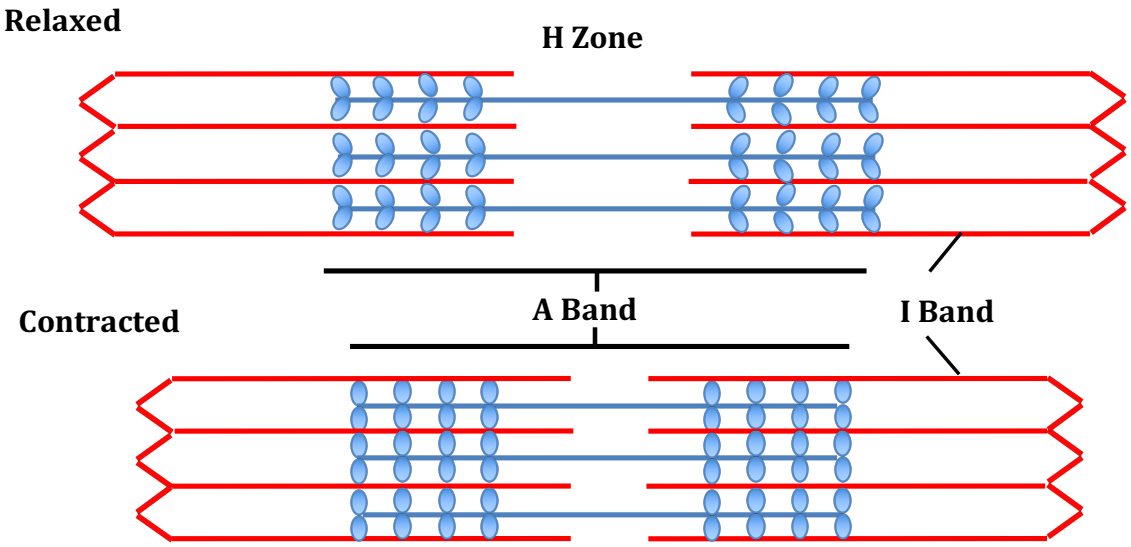

Figure 3.3: Sliding filament theory: During contraction actin-myosin cross bridges form and myosin heavy chain heads (blue) pull actin filaments (red) towards the H zone. The I bands and H zone thus shorten resulting in sarcomeric shortening.

Sarcomere length and the force of cardiac contraction are inextricably linked. The Frank-Starling law states that cardiac stroke volume is dictated by the volume of blood filling the heart (135). Within the left ventricle blood stretches the cardiac wall, and thus the sarcomeres, such that increasing blood volumes result in more forceful contraction. Length-tension studies of cardiac

sarcomere suggest that a resting length ~2.2μ is optimal for myofilament overlap, with a 10% reduction in sarcomere length resulting in 30% decrease in active tension and estimates of maximum sarcomeric contraction of around 15% (69). Active tension rapidly declines at resting lengths greater than ~2.2μ, due to availability of fewer cross-bridges, this provides the explanation for the reduced systolic contraction observed in patients with heart failure and ventricular dilatation (136).

3.4.3: Myocyte Mechanics

Sarcomeric shortening directly translates to myocyte shortening. Myocytes are bound by cell walls and connective tissues, thus sarcomeric shortening will also result in myocyte thickening, estimated to be approximately ~8% (9). Interpreting this within the context of axial mechanics, the extensive radial wall thickening observed therefore cannot be attributed to myocyte thickening alone. As with the discrepancy observed in cross-myocyte mechanics, it is clear that another contributing force exists, which myolaminar structures may play a role (9).

CHAPTER 4: CONTEMPORARY IMAGING TECHNIQUES AND MYOLAMINAR MECHANICS

4.1: Introduction

The previous chapter highlights the discrepancy that exists between systolic changes at the cardiomyocyte level (~15% shortening, ~8% thickening) compared to those observed in the left ventricle in vivo (~12-21% shortening, ~30-60% thickening) and suggests a potential role for myolaminar sheetlets and shear layers. Advanced histological techniques, such as high-resolution confocal microscopy, have offered improved visualisation of the myocardial fibre & myolaminar architecture and aided the development of theories regarding their role in LV mechanics (4, 6, 9, 10, 84, 86), however, histological analysis is limited by the fact it is both destructive and static and cannot assess the dynamic behaviour of microstructures in vivo. CMR (Chapter 6) is the gold standard technique for in vivo imaging of myocardium; in additional to quantification of left ventricular size, function and regional strains it can also enable tissue characterisation of the myocardium (137-140). Nonetheless, like histology, CMR has limitations, and in its current clinical form cannot provide information regarding the behaviour of myolaminae.

4.2: Non-Invasive Structural Imaging with Cardiac Diffusion Tensor Imaging

4.2.1: Introduction

Cardiac diffusion tensor imaging cDTI (Chapter 7) is a novel MRI technique, which is capable of interrogating myocardial microstructures non-invasively. It has brought new insights into the role of myocardial structures in both health and disease and the first technique to permit assessment of myolaminar dynamics in vivo

4.2.2: Ex Vivo Assessment of Myocyte Orientation

Early cDTI work in ex vivo hearts established its ability to depict myocyte orientation, validating it against histology (141-143). Since then numerous studies have unanimously confirmed the winding helical arrangement of myocytes that Pettigrew illustrated many years ago (19, 59, 142-151).

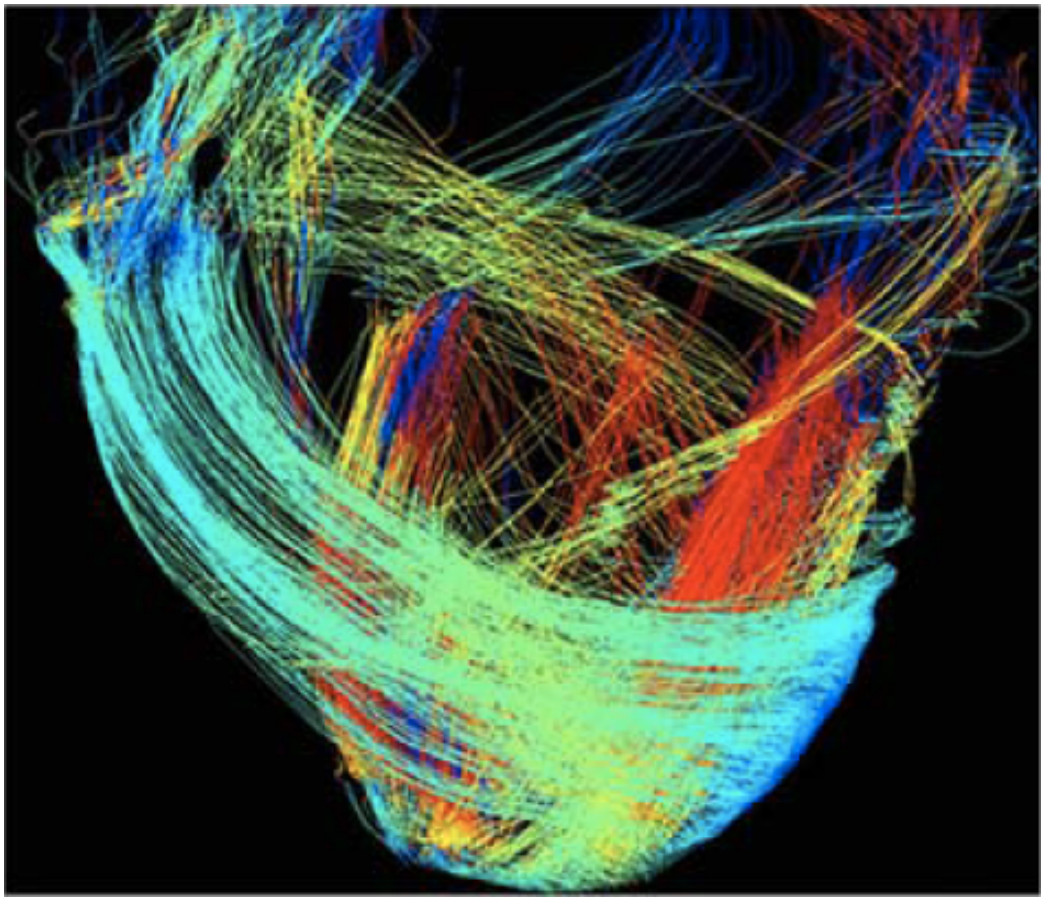

Figure 4.1: cDTI reconstruction of canine myocyte architecture at different transmural depths. Left-handed subepicardial myocytes are highlighted in blue and right-handed subendocaridal myocytes in red. The helical pattern of myocyte orientation matches Pettigrew's original drawings (85).

Despite the wide spread academic agreement over the helical arrangement of myocytes, the emergence of cDTI has yet to lay the VMB debate to rest. Vocal VMB opponents, Anderson and Lunkenheimer, were the first to utilise cDTI to support their position in the publication by Schmid et al. (59). This work studied porcine hearts and the authors commented that the results proved

'the ventricular mass is arranged as a complex three-dimensional mesh of tangential and intruding fibres' with 'no support for the concept of a 'unique myocardial band''. However their paper was followed by a predictably critical editorial from Buckberg who challenged their interpretation stating: 'This paper amplifies the sustained effort from Lunkenheimer and Anderson to show that the ventricular band concept of Torrent-Guasp is wrong'. In 2013 Spanish VMB proponents provided a supporting cDTI study (148). The authors took advantage of the technical developments that had occurred by this time and with advanced post-processing reconstructed individual 'fibres', which were said to illustrate the band from beginning to end.

4.2.3: Ex Vivo Assessment of Myolaminae

In 1998 Scollan et al. observed that in addition to demonstrating ventricular myocyte orientation, cDTI was also able to depict myolaminae (144). Other investigators made similar observations and Tseng et al. obtained histological validation (5, 12, 85, 145, 152, 153). As with the original histological descriptions of myolaminae, cDTI measures initially indicated the presence of a predominant transmural sheet population. Chen at al. reported that sheetlets in the base of the ventricle had a predominantly positive angulation and a predominantly negative orientation at the apex (12). However subsequent analyses with both cDTI and high resolution MRI have indicated that sheetlets exist in 2 populations transmurally angulated at ~90° to one another (7, 13, 85, 154). Harrington et al. found sheetlets, in the lateral wall at mid ventricular level were angulated at ~45° in the epicardium, ~ -45° in the mid wall, returning to ~45° in the endocardium, with the reverse pattern observed in the anterior wall (figure 4.2)(5).

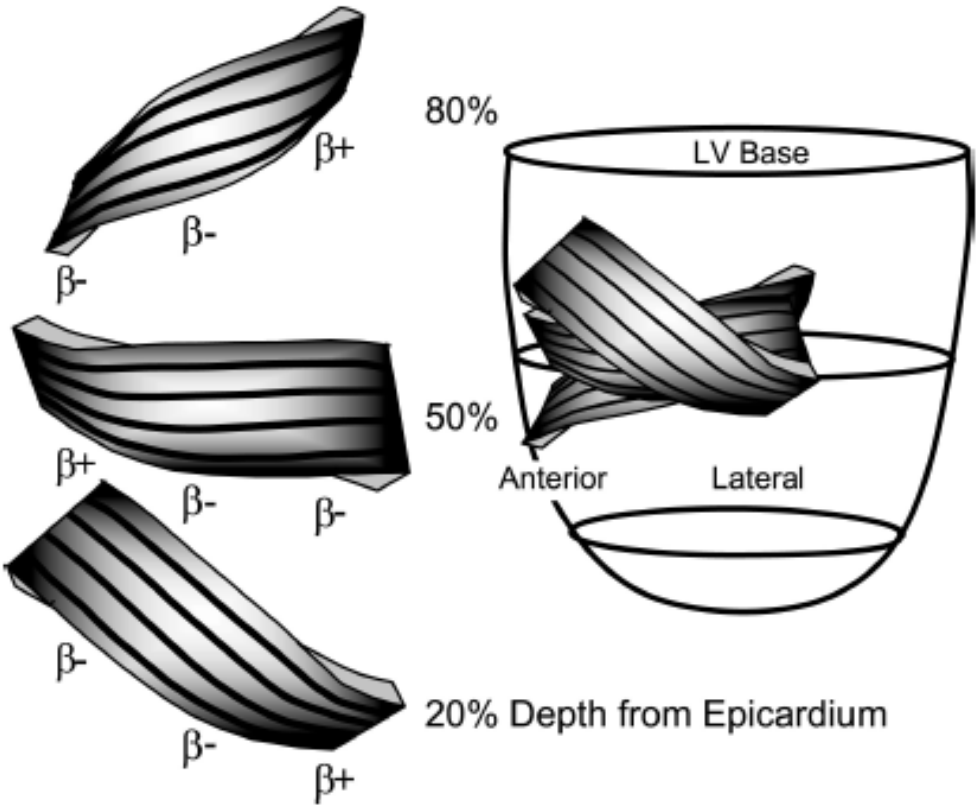

Figure 4.2: cDTI derived sheetlet orientation from Harrington et al. (5). β+ sheetlets are clustered around +45°, β- sheetlets are clustered around -45°. orientation was found to be dependent on transmural and regional location. From top to bottom sheetlets are depicted at 80%, 50% and 20% transmural distance from the epicardium respectively. From left to right sheetlets are represented from the anterior to lateral walls of the left ventricle. In the anterior wall sheetlets are orientated as β-, β+ and β- at decrease depth from the epicardium, with the reverse pattern in the lateral wall. Sheetlets in the middle are uniformly β-.

4.3.4: Assessement of Myocyte Orientation Dynamics

Although cDTI is uniquely capable of interrogating microstructures in ex vivo hearts noninvasively, its major advantage is the dynamic assessment of microstructures in living hearts. One of the first dynamic in vivo studies was conducted by Dou et al. who found a small but significant shift in myocyte angulation towards a more longitudinal orientation at both the endocardium and epicardium in systole (151). This result has since been replicated in further in vivo studies (figure 4.3)(150, 155) and Chen et al. reported similar findings in rat hearts which were chemically induced into diastolic and systolic states (12). Although later studies were discrepant (13, 92) the general consensus remained that, as Streeter et al. (2) had previously

suggested, changes in myocyte angulation were relatively minor within the context of ventricular thickening and shortening in vivo. Histologists and bioengineers had theorised for some time that the additional function arose of reorganisation of myolaminar structures (8-11, 60, 65, 66, 91, 120, 156).

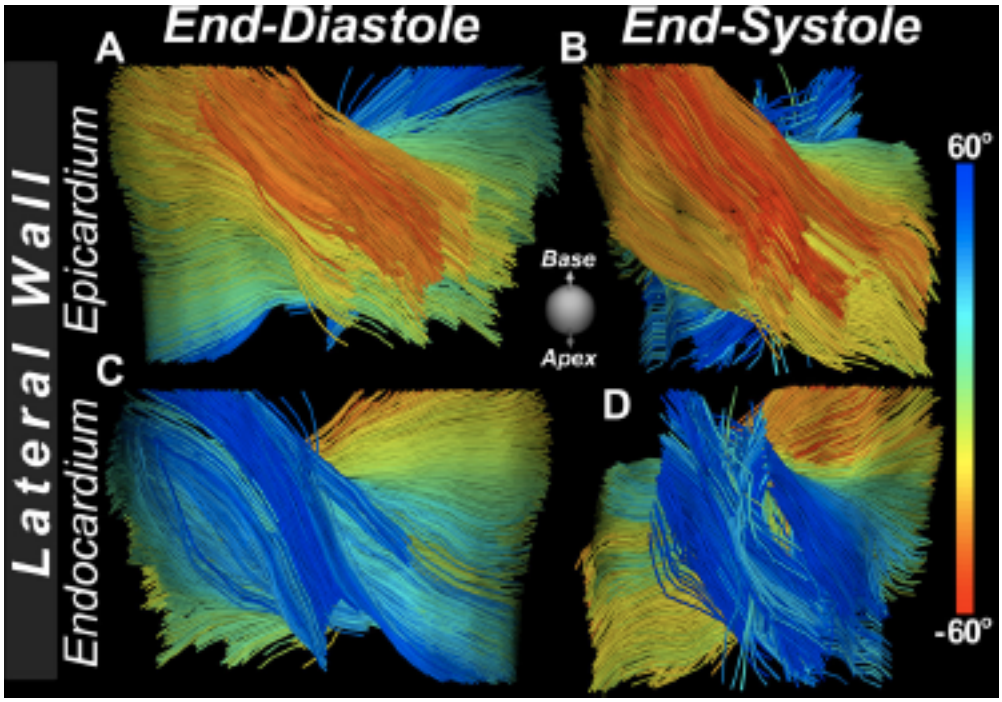

Figure 4.3: Example of in vivo cDTI acquisition of myocardial fibre orientation in the lateral wall of the left ventricle in a healthy volunteer. The data has been reconstructed to represent the continuity of fibres from base to apex and fibres are colour coded according to angulation. Images A and C display fibres in diastole and images B & D fibres in systole. Images A & B are the epicardial view and images C &D are the endocardial view. From diastole to systole fibres are relatively more longitudinal in both the epicardium (more red) and the endocardium (more blue) (155).

4.3.5: Assessment of Myolaminar Dynamics

Dynamic study of sheetlets with cDTI has significantly contributed to the understanding of their role in left ventricular function. In the in vivo study by Dou et al. sheetlets were observed to obtain a relatively more radial (horizontal) orientation in systole compared to a more longitudinal (vertical) orientation in diastole (151) with Chen et al. reporting similar findings in rat myocardium (12). In an Langendorff experiment Hales et al. provided further confirmation and

demonstrated an increase in the angle between the two transmural sheetlet populations, from 86±6° in diastole to 108±5° in systole (13).

The apparent ability of sheetlets to re-orientate during the cardiac cycle offers an explanation for the additional radial thickening and ventricular shortening observed in vivo. An illustration of how radial reorientation of sheetlets may translate to ventricular shortening and wall thickening is given in figure 4.4 (5). It has been proposed that the shear layers between sheetlets allow them to slide past one another along their cleavage planes. During contraction sheetlets can then slide to re-orientate from being vertically stacked in diastole to being aligned side by side, i.e. more radial, in systole (5, 9). This has the dual effect of longitudinal shortening and radial thickening, thus offering an explanation for the origin of the missing component of cardiac contraction. As it is thought that there are two transmural sheetlet populations at ~90° to one another, this mechanism has been likened to an accordion, with the greater angulation between sheetlet populations in systole comparable to expansion of an accordion's bellows (figure 4.4)(5).

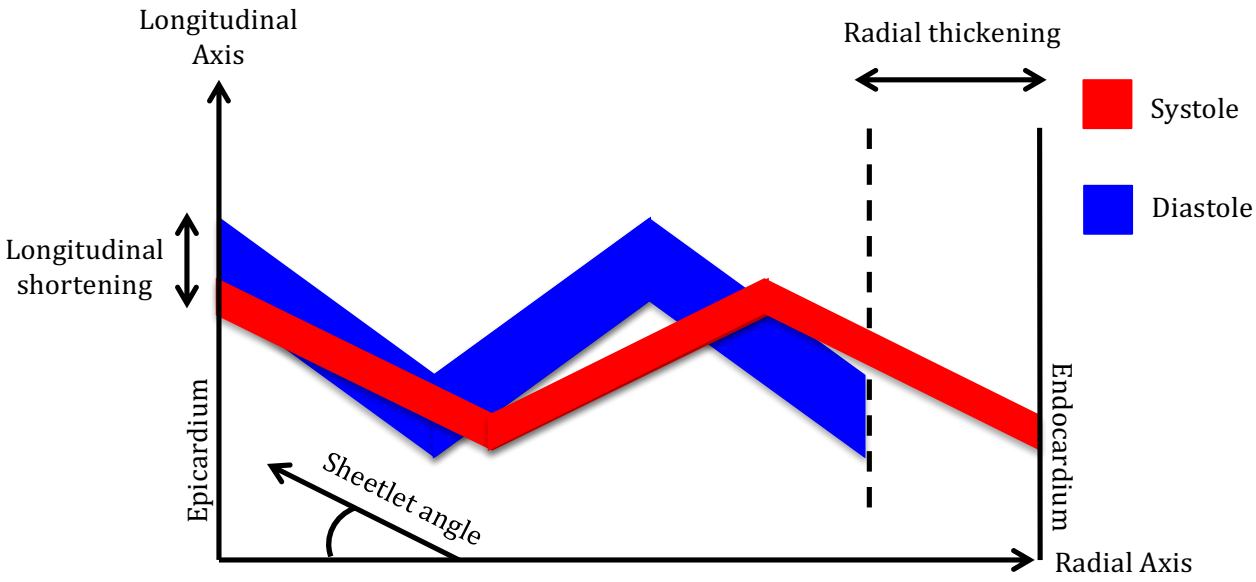

Figure 4.4: Two dimensional representation of sheetlet dynamics adapted from Harrington et al. (5). The myocyte long axis is out of the page towards the reader, the vertical axis and horizontal axes represent the ventricular long axis and radial axis respectively. The red line represents sheetlets in systole and the blue line diastole. In systole sheetlets realign becoming more horizontal in orientation. As sheetlets exist in 2 populations in opposing directions, the effect is like an accordion with a reduction in longitudinal height and increase in radial thickening.

Presently there are few in vivo studies of myocardial fibre architecture and myolaminar dynamics. Since the original studies from ~1995-2006 there have been considerable developments in CMR scanner technology, cDTI sequences and post processing techniques, cDTI may therefore provide new insight into the role of these microstructures in LV function. Specifically questions remain with regards to the normal variation of these structures both at the ventricular level and across the population, moreover the relationship between the in vivo myocardial microarchitecture and cardiovascular disease processes has yet to be addressed.

CHAPTER 5: HYPERTROPHIC CARDIOMYOPATHY – MICROSTRUCTURAL ABERRATION AND LEFT VENTRICULAR HYPERTROPHY

5.1: Introduction

Cardiac Diffusion Tensor Imaging has already shed new light on myocardial mechanics in healthy hearts, however its potential to advance our understanding of structural-functional relationships in disease is of particular interest. Hypertrophic cardiomyopathy is genetic cardiac muscle disorder with unique macro and microstructural features. Genetic mutations of sarcomeric proteins are reported to translate to myocyte 'disarray' at histology, which in turn leads to marcoscopic asymmetrical left ventricular hypertrophy. Until recently micro-architectural studies have been limited to biospies and autopsy specimens; cDTI offers the ability to interrogate myocyte orientation and myolaminar structures non-invasively and correlate these findings with macroscopic phenotypes.

5.2: Hypertrophic Cardiomyopathy Incidence and Genetics

Hypertrophic cardiomyopathy (HCM) affects 1 in 500 of the population and is a global condition with similar prevalence across continents and ethnicities (14, 157). It has been described in patients of all ages, however diagnosis predominantly occurs in the 5th decade, with a slight male predominance (158, 159). HCM is inheritable with predominantly autosomal dominant transmission, presently around 1,500 mutations in 11 genes have been identified which code for sarcomeric proteins within the thick and thin myofilaments (158, 159). The majority of these mutations (~75%) affect either β-myosin heavy chain (MYH7) or myosin binding protein C (MYBPC3), less common mutations involve troponin T (TNNT2), troponin I (TNNI3), α-

tropomyosin (TPM1), α-myosin heavy chain (MYH6), the myosin light chains (MYL2, MYL3) and actin (ACTC) (figure 5.1) (68, 158-161).

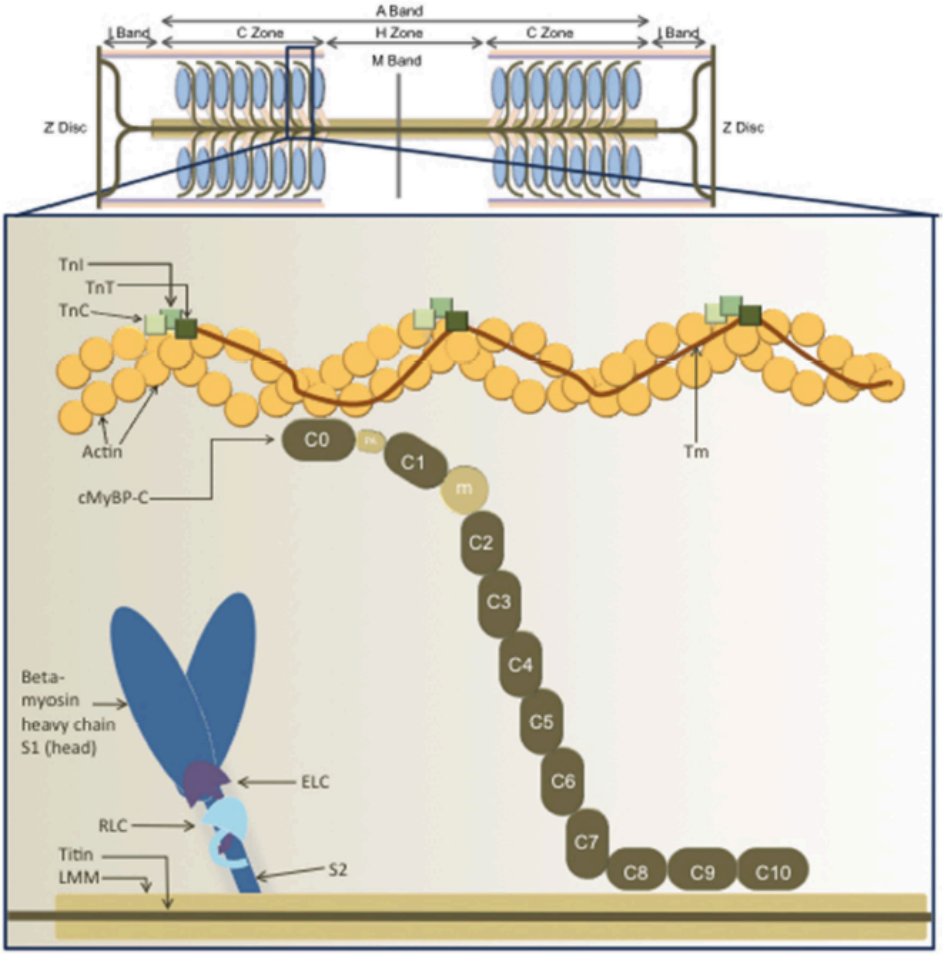

Figure 5.1: Illustration of the sarcomeric proteins and their interactions. cMyBP: cardiac myosin binding protein C; TnI, TnT, TnC: troponin I, T and respectively; Tm: tropomyosin; ELC: essential myosin light chain; RLC: Regulatory myosin light chain; LMM: Myosin heavy chain's light meromyosin (68).

HCM can also occur as part of the disease spectrum in a number of genetic conditions such as Noonan's syndrome, Fredreich's ataxia and storage diseases such as Anderson-Fabry disease (14, 158, 160, 162). Despite significant advances in genetic testing, pathogenic mutations are not always identified in probands. Success is dependent upon the sequencing technique used, with estimates of around 50-65% in cases with a family history, and 20-40% in cases of new unexplained LVH (158, 159, 161, 163). Moreover HCM genetics are complex as disease

expression is heterogeneous both between and within families (160). The increasing utilisation of genetic testing in family screening has also led to the recognition of a subset of patients who are gene positive, but lack the HCM phenotype. Modifier genes and environmental factors therefore play an important, yet undefined role in disease development (160, 164-166). When available, a genetic diagnosis is an invaluable screening tool for family members, however genetics alone are insufficient to establish a diagnosis in index cases. Further work is required to understand genotype-phenotype relations in HCM.

5.3: Macroscopic Phenotype

5.3.1: Left Ventricular Hypertrophy

HCM is characterised macroscopically by left ventricular hypertrophy (LVH) (defined as a maximal wall thickness ≥15mm, or ≥13mm with a family history) in the absence of loading conditions such as aortic stenosis or hypertension (14). Average wall thickness is 21-22mm, however it can exceed 30mm and in rare occasions may measure up to 50mm (157, 167). The hypertrophy is usually asymmetrical, the most common morphology being asymmetrical septal hypertrophy (ASH), however a number of morphologies have been described including apical and mid-ventricular hypertrophy (figure 5.2).

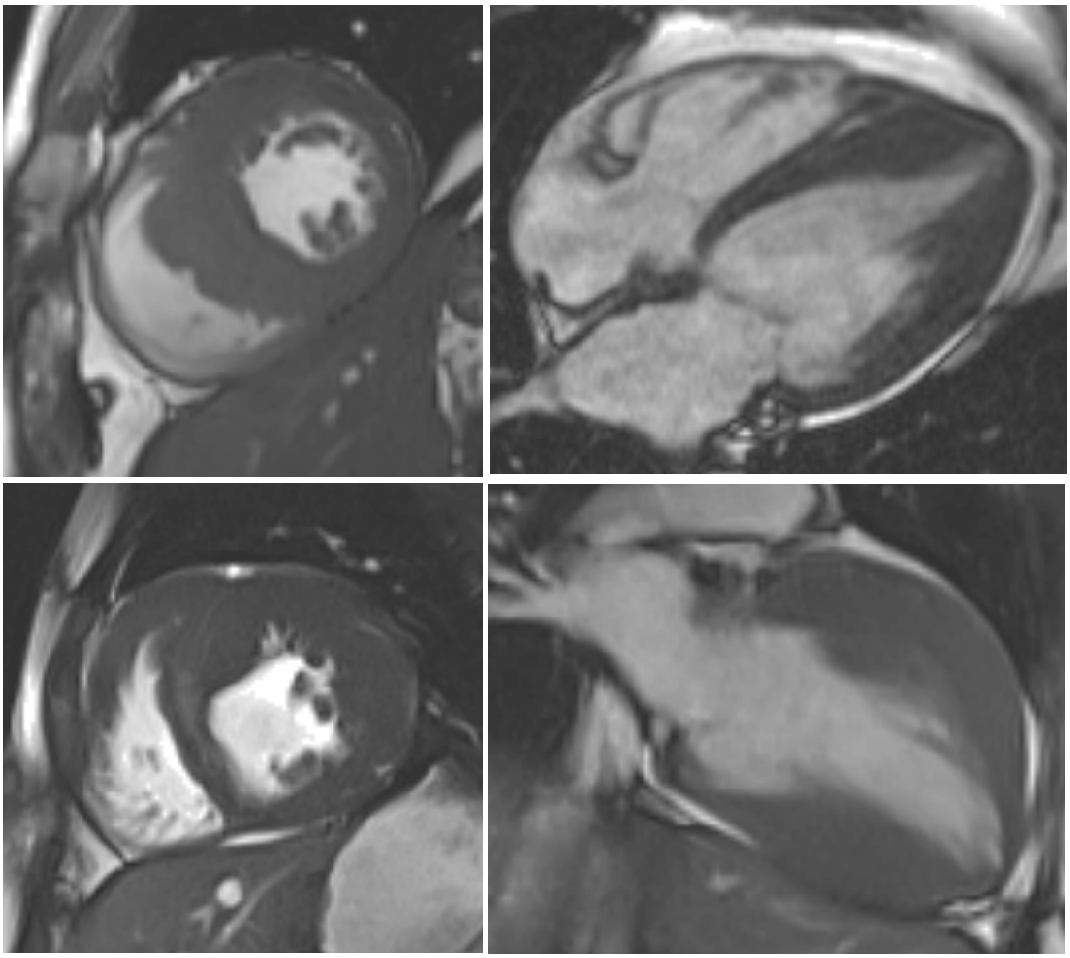

Figure 5.2: CMR images of different HCM morphologies. A: Classical asymmetrical septal hypertrophy. B: Apical hypertrophy C: Anteroseptal, anterior and lateral hypertrophy in additional right ventricular hypertrophy D: Anterior and inferior hypertrophy.

Truly symmetric hypertrophy is rare (14, 159, 168). No obvious association between genotype and LV morphology has been identified, however wall thickness is greater, on average, in gene positive patients (21mm v 19.3mm) (158, 164). In addition to LVH, other macroscopic abnormalities are associated with HCM including right ventricular hypertrophy, myocardial crypts, papillary muscle abnormalities, mitral valve leaflet elongation and left atrial dilatation (159, 169, 170). In HCM the left ventricular cavity is typically small, however a dilated ventricle may be present in cases with progressive disease.

5.3.2: Left Ventricular Outflow Tract Obstruction

Another key feature of HCM is left ventricular intra-cavity obstruction, which is present in approximately 30% of cases at rest and up to 60% of patients during exercise (14, 171, 172). In the context of ASH morphology, left ventricular outflow tract obstruction results from contact between the hypertrophied septum and mitral valve apparatus, which moves anteriorly in systole (173, 174). Factors contributing to obstruction include mitral valve elongation and papillary muscle abnormalities, severe LVH and aortoseptal angulation (171, 175). In mid ventricular HCM, significant hypertrophy can result in direct muscular apposition in systole, with mid cavity obstruction and apical aneurysm formation (159, 176).

5.3.3: Marcroscopic Scars with Late Gadolinium Enhancement

Macroscopic myocardial scars are an additional feature of HCM. Non-invasive imaging of replacement fibrosis with late gadolinium enhancement CMR (LGE) (Chapter 6) has greatly contributed to the understanding of these lesions, which are estimated to be present in up to 80% of patients (177). Moon et al. and Iles et al. demonstrated a significant relationship between histological collagen and the extent of LGE; myocardial segments containing >15% collagen were more likely to display LGE (178, 179). Clinical observations have revealed that rather than being confined to the septum, the location of LGE fibrosis follows the pattern of LVH morphology (figure 5.3).

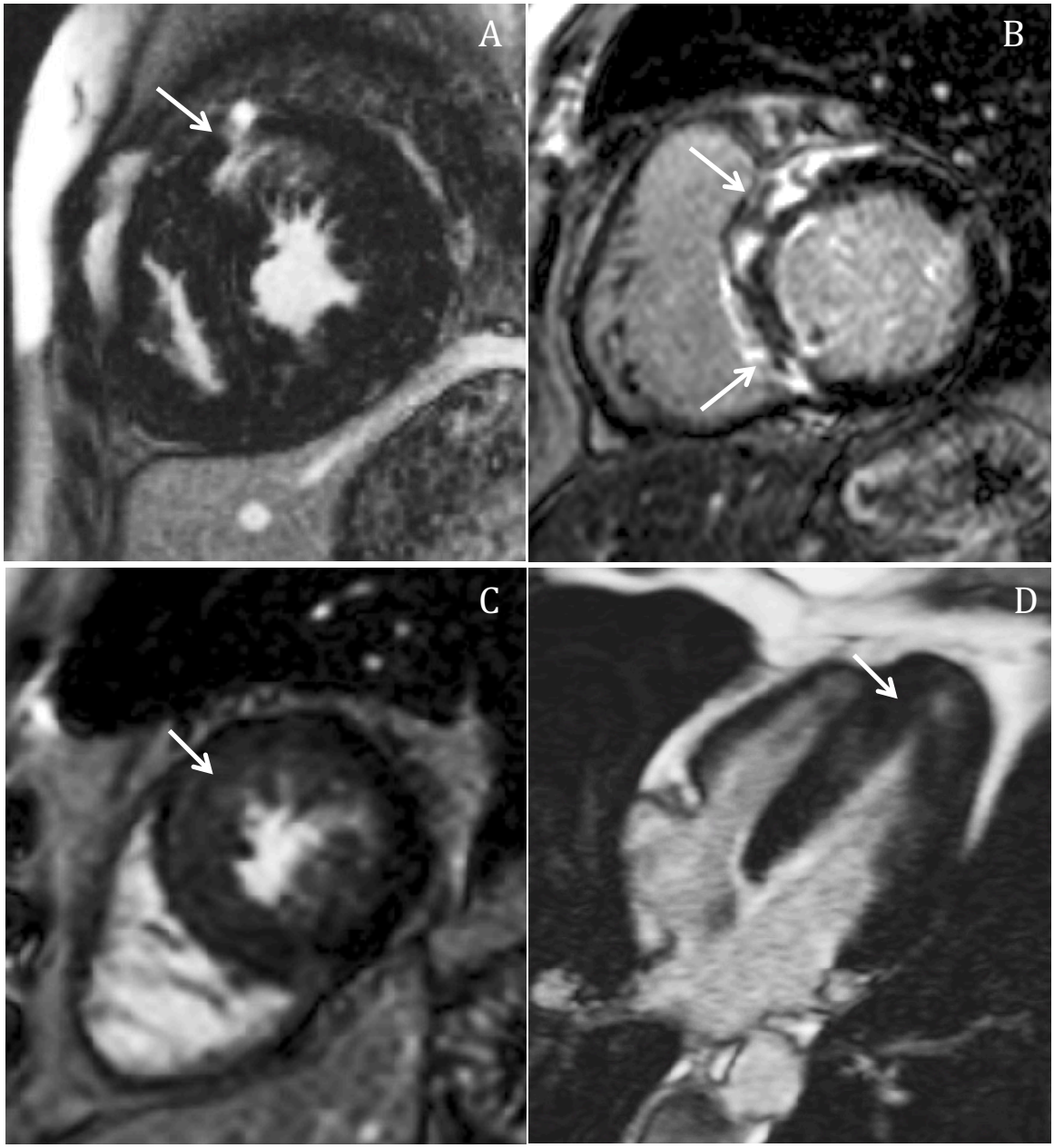

Figure 5.3: Examples of LGE in HCM. A) RV insertion point and anteroseptal enhancement. B) Extensive patchy septal enhancement. C) & D) subtle diffuse apical enhancement.

However LGE is not specific to HCM, Rudolph et al. found LGE was a feature of LVH regardless of the cause and concluded it was a marker of LV remodelling (180). Characteristic patterns of LGE are now recognised in a number of conditions therefore improving the diagnostic accuracy of clinical CMR (181). LGE carries prognostic significance in dilated cardiomyopathy, Gulati et al. demonstrated that mid wall LGE was an independent predictor of all cause mortality and sudden

cardiac death (182). A number of studies have investigated the link between myocardial LGE and clinical outcomes in HCM, however due to the relatively low event rate in this population establishing clear associations has been challenging. Both Moon et al. and O'Hanlon et al. from the Royal Brompton Hospital found that the presence of LGE was associated with progressive disease and risk factors for sudden death (177, 183). Building on the work from these studies, Ismail et al. studied over 700 patients with HCM and found the extent, but not presence of LGE, was a univariate predictor of sudden death and cardiovascular mortality, however on multivariable analysis this effect was lost after adjustment for LV ejection fraction (184). A meta-analysis of pooled data from over 1000 patients found the presence of fibrosis, as detected by LGE, correlated with cardiovascular death, in particular heart failure death, and all cause mortality, there was also a trend towards a correlation with sudden death and aborted sudden death, but this did not reach significance (185). More recently, in the largest study of just under 1300 patients, Chan et al. found sudden death events (sudden death or aborted sudden death) occurred in direct relation to the extent of LGE, with >15% myocardial LGE conferring a 2-fold increase risk of events in patients previously assessed as low risk (186). The same group emphasised the findings of Ismail et al., that the presence of LGE, specifically LGE limited to the RV insertion points, was a benign feature with no association to adverse events (187).

5.4: Microstructural Phenotype

5.4.1: Introduction

Although many patients with HCM display an overt phenotype, the morphology can be subtle with mild LVH. Patients may also have additional risk factors for LVH, such as hypertension. In this situation the absence of an identifiable genetic mutation or clear family history, can present a diagnostic challenge for the clinician. The ability to identify HCM from its micro-architecture may therefore improve the identification of affected patients

5.4.2: Disarray

5.4.2.1: Histological Appearance

Although the cardiology community at large regards histological disarray as pathognomic, the micro-architectural appearance of HCM has courted a degree of controversy akin to the ventricular myocardial band. In his original paper Teare described the histological features in a case series of patients with septal hypertrophy and a history of sudden death (188). He likened the septal hypertrophy to tumour and reported a 'bizarre arrangement of bundles of muscle fibres running in diverse directions and separated by connective tissue and clefts', in addition to hypertrophy of individual muscle cells (188). A number of histological studies followed which either described or quantified the disorganised myocardial appearance, which became known as 'disarray' (189-193). In 1979 Maron et al. offered the largest study of that time, comprising of 54 HCM specimens (194). He described 4 different patterns of disarray visible at magnifications ranging from x40 to x130, from either transverse or longitudinal sections. In general disarray was characterised as a disorganised myocardial appearance where myocytes are either parallel or obliquely orientated with interspersed collagen in a pinwheel or herringbone configuration (figure 5.4) (168, 194).

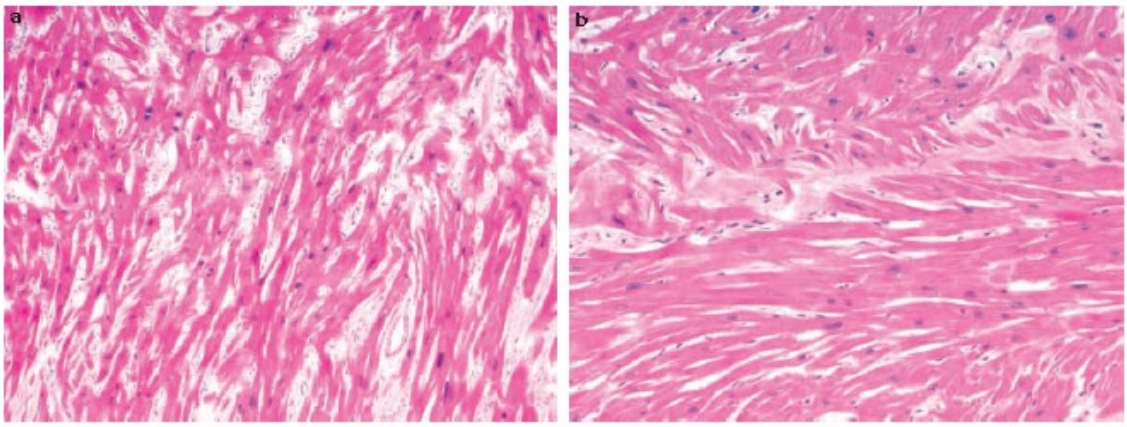

Figure 5.4: Histological specimens from a patient with a diagnosis of HCM. Examples of myocyte disarray are illustrated with myocytes arranged obliquely and perpendicularly around foci of interstitial collagen in a) pinwheel or b) herringbone pattern (168).

The majority of reports of disarray have focused on the ventricular septum (15, 188, 194, 195), however there are also reports of disarray within the ventricular free wall (15, 18) and circumferentially throughout the ventricle (18, 189, 196). Around the time of these reports it became widely accepted within the cardiology community that the presence of disarray was pathognomic of HCM. This generated a degree of academic controversy a number of publications emerged questioning its specificity (189, 192, 193, 197-200). Disarray has since been described in normal hearts (190, 197, 199), in hypertensive heart disease (199, 200), aortic stenosis (189), fetal hearts (192, 200) and in congenital heart diseases (162, 192, 201). Notable critics include Ross and Streeter who suggested that disarray could arise from the intrinsic heterogeneity of local fibre orientation (202). Becker and Garuso investigated this idea further by repeating analysis of tissue blocks in different orientations illustrating that, by Maron's criteria, it changed the interpretation in 52 out of 60 blocks (193). In addition they observed that disarray was a particularly frequent finding in the endocardium, the ventricular apex and right ventricular insertion points of healthy hearts.

5.4.2.2: Diagnostic utility

There remains a lack of consensus regarding the utility of disarray in the diagnosis of HCM. Disarray is reported to be present in only 50% of samples taken from the ventricular septum

(189, 194, 197). Maron and associates have stressed that it is the total quantity rather than the presence of myocardial disarray that is important (16, 18, 190, 194). At least four papers have reported disarray in >20% of the total myocardium sampled in HCM patients (15, 168, 189, 203). Maron et al. maintain that ≥5% of septal disarray is sufficiently sensitive and specific for a diagnosis (15, 17), however others have challenged this claiming that at least 10% is required (168, 204). Despite disagreements over quantitative diagnosis at autopsy, it is generally acknowledged that myocardial disarray is a feature of HCM. Nonetheless its lack of complete specificity renders the detection, via endocardial biopsy, insufficient to confirm or exclude the diagnosis in vivo.

5.4.2.3: Clinical Relevance

The clinical relevance of disarray is also uncertain. Maron et al. reported that disarray was unrelated to the degree of hypertrophy (18). It has been postulated that disarray may serve as a substrate for arrhythmia. Varnava et al. studied the relation between disarray and other phenotypic features and found it was greater in non-dilated hearts, areas with evidence of ischaemia and in young patients with a history of sudden death (196, 205). In subsequent work they reported severe disarray within specimens from young patients with the Troponin T mutation and a history of sudden death (206). Similarly McKenna et al. reported severe disarray in a family with a history of sudden death, but interestingly in the absence of increased myocardial mass (207). Both drew the conclusion that disarray was potentially the pathological substrate for sudden death, however autopsy sample bias for a cardiovascular mode of death makes it difficult to interpret the findings within the context of real world HCM.

5.4.3: Intra-Myocyte Abnormalities & Vascular abnormalities

In addition to abnormalities of the inter-myocyte structure, intra-myocytes abnormalities are also observed. HCM myocytes are hypertrophied; exact measurements vary however one report

estimated average human HCM myocyte cross sectional diameter as 15.8μm, compared to 14.3μm in hypertrophied hypertensive hearts, and 12.6μm in normal myocardium (formalin fixed preparation) (203). In health myocyte diameter increases from the subepicardium to the subendocardium with the same pattern observed in hypertensive hearts (203, 208). In contrast, Hoshino et al. reported greatest myocyte diameter in the midwall of the hypertrophied septum in HCM (203). They also found myocytes were larger in areas of disarray compared to normal architecture, raising questions as to whether myocyte hypertrophy acts as a substrate for disarray or vice versa.

In normal myocardium myocyte nuclei are central and singular, whereas in HCM nuclei may be numerous and are often pleomorphic and hyperchromatic (figure 5.3). Aberrant myofibrillar architecture has also been demonstrated via electron microscopy, with oblique and perpendicular intracellular orientation. This is referred to as myofibrillar disarray, and as with inter-cellular disarray is not specific to HCM (figure 5.5) (209).

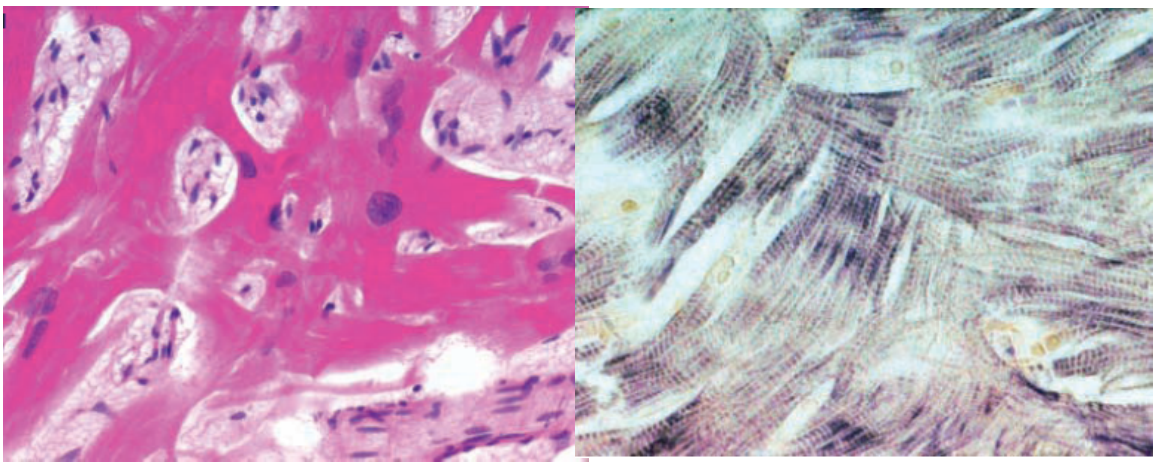

Figure 5.5: Left-hand image: Nuclear abnormalities in HCM with multiple nuclei per cell, nuclear pleomorphism and hyperchromasia. Right-hand image: myofibrillar disarray with oblique and perpendicular myofibrils within the same cell (168).

Abnormalities of the microcirculation are also recognised in HCM. Intra-luminal narrowing, due to vessel wall thickening, is predominantly observed in areas of hypertrophy (210). Vessel wall thickening has been attributed to proliferation of endothelial cells, or intimal components such

as smooth muscle cells and collagen, and is associated with myocardial micro-infarctions (210, 211). Vascular abnormalities are reportedly more frequent in areas of myocardial fibrosis (211), however Varnava et al. identified normal vessels in fibrotic regions as well as abnormal vasculature in areas devoid of fibrosis (196). Microvascular ischaemia at rest, as assessed with CMR perfusion, is an independent risk factor for malignant arrhythmia (212). The frequency of abnormal vasculature in dilated HCM also implicates micro-perfusion abnormalities in ventricular dilatation (211).

5.4.4: Myocardial Fibrosis

5.4.4.1: Histological Patterns of Fibrosis

Myocardial fibrosis is a characteristic feature of HCM and is characterised by expansion of the interstitial collagen compartment. In HCM histological fibrosis is described in four distinct forms: microscopic scars, perivascular fibrosis, interstitial fibrosis and finally plexiform fibrosis, which occurs in conjunction with disarray (figure 5.6) (189).

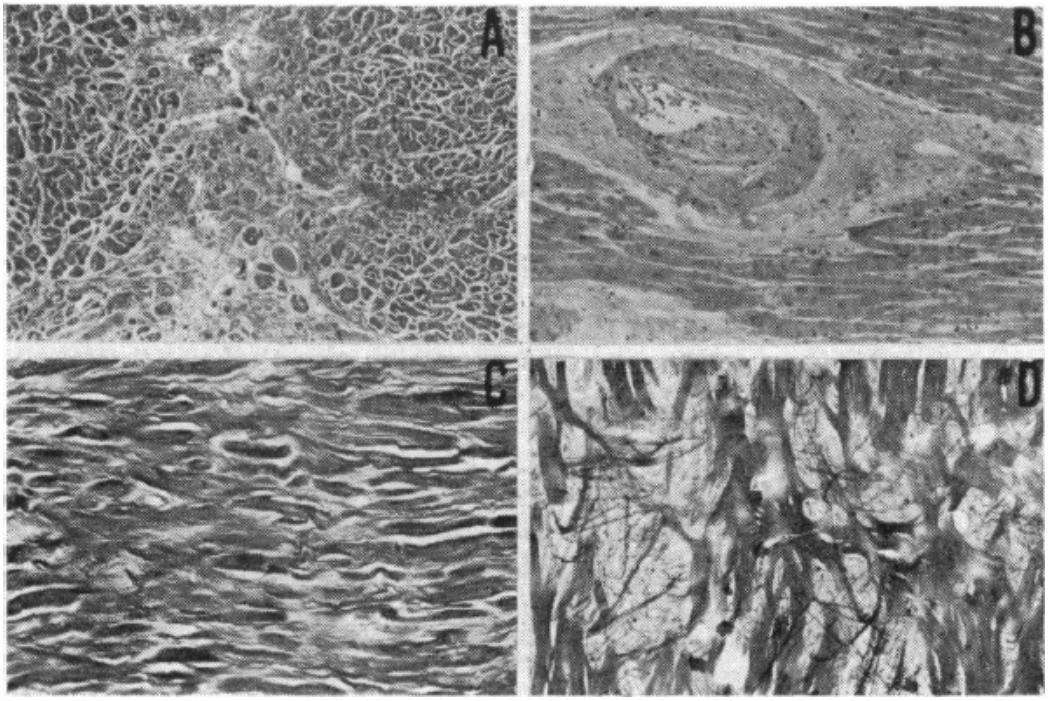

Figure 5.6: Myocardial sections with Mallory-Heidenhain staining at x160 magnification. A: microscopic scars, B: perivascular fibrosis, C: interstitial fibrosis and D: plexiform fibrosis with evidence of disarray (189).

Numerous histological studies have identified an increase in fibrosis compared to normal hearts (189, 198, 204, 208, 213) and patients with hypertensive heart disease (204, 213). On histological examination, fibrosis is present in all myocardial walls but is greatest in the septum in the case of ASH hypertrophy morphology (204, 208, 213). Plexiform fibrosis is the most common subtype identified, with the other subtypes occurring more frequently in dilated cardiomyopathy and severe aortic stenosis (189). Fibrosis is more prevalent in male HCM hearts, is an early feature in children and young adults with a history of sudden death, and expands in line with growth through to adulthood (196, 213). In terms of its clinical relevance, Varnava et al. demonstrated a positive correlation between histological fibrosis and malignant arrhythmia and premature death from heart failure (205).

5.4.4.2: Diffuse Fibrosis Detected with T1 Relaxometry

In addition to the detection of overt, macroscopic fibrosis with CMR late gadolinium enhancement, CMR T1 relaxometry techniques have been applied to detect diffuse fibrosis (179). T1 values in have been shown to positively correlate with LV myocardial mechanics in HCM (214), however, in line with earlier ex vivo studies, in vivo diffuse fibrosis is less prevalent in HCM than patients with severe aortic stenosis (215) and dilated cardiomyopathy (214). Despite this, the detection of diffuse fibrosis may play a role in identifying subclinical HCM, Ho et al. found that gene positive patients both with and without LVH had a greater degree of diffuse fibrosis than healthy controls (216).

The overall message is that HCM is not just a disease of the sarcomere, but also the connective tissues. Myocardial fibrosis is an integral component of the HCM phenotype, however a greater understanding of the link between genetic mutations and phenotypic expression is required.

5.5: Myocardial Mechanics

5.5.1: Introduction

In addition to macroscopic and microscopic aberration, HCM hearts also display disordered mechanics insinuating a link between the two.

5.5.2: Sarcomeric Mechanics

There are conflicting reports regarding the mechanism by which sarcomeric mutations translate to an HCM phenotype. One theory is that the mutations result in structural or functional alterations, which affect saromeric integrity: Watkins et al. reported reduced contractile performance in quail myotubes with troponin T mutations (217); Lankford et al. studied slow twitch skeletal muscle fibres in patients with missense β-myosin heavy chain mutations and found reduced velocity and force of contraction (218); and Marian et al. found that cat myofibrils expressing a troponin T mutations also has impaired contractility (219). Supporters of the impaired contractility theory propose that myocardial hypertrophic is a compensatory mechanism arising from cell stress and the release of mitotic and trophic factors (220, 221).

The alternative theory is that HCM mutations result in a gain of function: Gomes et al. reported increased calcium sensitivity of troponin in stripped fibres with a troponin I mutation (222); Pinto et al. reported similar findings following troponin C mutations (223); and Belus et al. observed increased force of contraction within myofibrils with the a β-myosin heavy chain mutation (224). Supporters of the gain of function theory propose that HCM is the result of the excessive energy use of sarcomeres (224). In reality, given the heterogeneous nature of HCM, multiple pathophysiological mechanisms are likely to contribute.

5.5.3: Ventricular Mechanics

5.5.3.1: Systolic Mechanics

The LV ejection fraction is typically elevated in HCM, however this is the consequence of reduced LV cavity size rather than heightened systolic function. The LV morphological heterogeneity in HCM has led to conflicting reports regarding regional and global function. Despite this there is general agreement that longitudinal strain is impaired regardless of morphology (104, 225-231) correlated with the degree of hypertrophy(232). Longitudinal strain has also been demonstrated as an independent predictor of adverse events (104, 229). In contrast circumferential strain may be enhanced (227, 230) or impaired (228, 231, 232) with the suggestion that circumferential strain is greater in basal segments in the asymmetrical septal phenotype (230). LV rotation and torsion can be both increased (225) or decreased (228); and radial function may be preserved (14) or decreased (225, 229, 232). Heterogeneity in transmural strain has also been reported with a gradient of increasing strain from the subepicardial to the subendocardium (233, 234).

Aletras et al. investigated the relation between replacement fibrosis, as assessed by LGE, and regional LV strain in HCM (234). Regions of myocardium with confluent and diffuse LGE had significantly reduced circumferential shortening and radial thickening. However regions of hypertrophy without LGE had similar strain abnormalities, with an inverse relationship between the severity of LVH and the degree of radial myocardial thickening (strain).

Dass et al. investigated the relation between diffuse fibrosis, as measured by T1 mapping, and mid myocardial circumferential LV strain in HCM (214). Circumferential strain (shortening) was directly correlated with T1 relaxation time, such that strain was poorer in areas of greater fibrosis. T1 relaxation times were also elevated in hypertrophied myocardium in the absence of LGE, suggesting that fibrosis, in its diffuse form, may play a significant role in HCM mechanics. However these findings were challenged in a more recent paper, albeit with a smaller cohort,

which found no difference in the T1 relaxometry values in myocardium devoid of LGE in HCM compared to normal myocardium (235).

The relation between sarcomeric mutations and LV mechanics has also been investigated. Geske et al. studied echocardiography measures of longitudinal strain in gene positive and gene negative HCM (236). Patients with an identifiable sarcomeric mutation had lower basal septal strain, although when gene positive and gene negative patients with the same morphology were compared there was no difference. In line with Aletras et al.'s findings, strain was positively correlated with wall thickness (234). Germans et al. also studied circumferential strain in gene positive patients without the HCM phenotype and found, compared to controls, gene carrier status was an independent determinant of peak systolic circumferential strain (237).

5.5.3.2: Diastolic Mechanics

One of the characteristic features of HCM is diastolic dysfunction. Diastolic impairment is an important pathophysiological consequence as it is limits exercise tolerance and leads to heart failure (238). A number of factors contribute to diastolic impairment in HCM, either through reduced diastolic filling or impaired relaxation. Reduced ventricular filling arises from a reduction in LV chamber size and impaired ventricular compliance as consequence of fibrosis (176, 239). Ventricular relaxation is impaired due to prolonged ventricular contraction in the context of left ventricular outflow tract obstruction, microvascular ischaemia and delayed actin-myosin dissociation resulting from elevated calcium(239, 240).

Diastolic impairment is an early feature of HCM and may be present before the onset of LVH in gene positive individuals (237, 241, 242). There is some evidence to suggest that diastolic impairment is more severe in patients with ASH morphology, in particular the reverse septal curvature configuration (243, 244), however other reports suggest the degree of hypertrophy,

the patient's age and the presence of outflow tract obstruction are more important determinants (233, 245). In some cases diastolic impairment may dominate the clinical picture, manifesting as a restrictive cardiomyopathy (176). Restrictive physiology carries an adverse prognosis, with an increased risk of sudden cardiac and heart failure related death (246, 247).

5.6: Adverse Clinical Events

5.6.1: Introduction

HCM can be present at birth (248, 249), but in the majority of cases LVH develops, often asymptomatically, through childhood and adolescence (157, 250, 251). The majority of patients with HCM run a benign clinical course, with diagnosis occurring as an incidental finding or following family screening. However an important subset are at risk of serious adverse events such as heart failure, arrhythmia and sudden cardiac death, with an estimated annual incidence of cardiovascular mortality of 1-2% (159, 176, 252).

5.6.2: Sudden Cardiac Death

Sudden cardiac death is a devastating consequence of HCM and in many cases is the first manifestation of the disease. It remains the leading cause of sudden death in athletes and in the general population under 30 years of age (159, 252, 253). Despite showing a predilection for younger patients, the risk of sudden cardiac death persists into mid-life, but is rare over 60 years (254). The mode of sudden death in HCM is predominantly malignant ventricular arrhythmia, which can occur with every day activities but is also precipitated by physical exertion (253, 255, 256). A number of clinical risk factors have been identified including a family history of sudden death; LVH >30mm (although the effect is attenuated over >35mm); a history of syncope; left ventricular outflow tract obstruction; non-sustained VT; severe left atrial dilatation; and a fall in blood pressure with exercise (14, 159, 257, 258). Studies have also suggested and adverse prognosis associated with specific mutations such as MYH7-ARGR403Q and TNNT2-ARG92GLN (221, 259-263), however, as previously discussed, there is often marked heterogeneity of both

inter and intra-family expression of disease and contradictory studies with regards to specific mutations have been reported (166). In post mortem studies of HCM, disarray was identified as occurring more frequently in cases of sudden death compared to heart failure (205, 206).

5.6.3: Heart failure

Around 50% of patients with HCM experience heart failure symptoms. This is primarily due to restrictive physiology, owing to the small ventricular cavity and diastolic impairment with preserved systolic function (264). Left ventricular outflow tract obstruction and atrial fibrillation also exacerbate symptoms (265). Progressive heart failure has been reported to affect up to 17% of patients and is associated with declining ventricular function (264). This is often referred to as 'burnt out HCM' as occurs in conjunction with ventricular dilatation and wall thinning. The risk of heart failure increases with age and is the consequence of progressive ventricular fibrosis (177, 183, 205).

5.6.4: Arrhythmia

Atrial fibrillation (AF) is the most common arrhythmia associated with HCM, with an estimated prevalence of 22% (266). Left atrial size is a significant predictor of AF as are factors predisposing to atrial dilatation such as mitral regurgitation, diastolic impairment and left ventricular outflow tract obstruction (266, 267). In addition to worsening symptoms, AF carries a significant risk of thromboembolism, with an annual incidence of 3.8% (266). In the absence of symptoms, significant left atrial dilatation should therefore be met with a high index of suspicion for AF, with a low threshold for treatment to mitigate the thromboembolic risk.

Non-sustained ventricular tachycardia is a common finding on ECG monitoring in HCM. Its prevalence increases with age and is correlated with wall thickness and the presence of fibrosis (14, 183, 184). Non-sustained ventricular tachycardia is a risk factor for sudden death, especially

when initiated by exercise (14, 253, 258). It is theorised that the arrhythmia originates from disordered electrical function of the myocardial due to the presence of fibrosis and / or disarray.

5.7: HCM Phenocopies

5.7.1: Introduction

In clinical practice establishing a diagnosis of HCM can be difficult as patients may have additional risk factors for LVH which can act as phenocopies. As the definition of HCM does not stipulate a primary myocardial genetic pathology, LVH resulting from these conditions also falls under the HCM umbrella. Correct diagnosis in this context is vital to ensure appropriate specialist care as the clinical consequences are often multisystem and other organ pathologies may dominate.

5.7.2: Hypertensive Heart Disease

Hypertension is a known cause of LVH affecting approximately 30% of the adult population in mid life, and HCM patients are not exempt. A recent meta-analysis suggests that hypertension affects approximately 23% of sarcomeric mutation positive HCM patients and 42% of patients without an identifiable mutation (158). Hypertension generally causes concentric LVH, however most data suggest that LVH >15mm is rare in Caucasian patients with moderate hypertension (176, 268). By contrast hypertensive LVH in black patients is common and, although usually concentric, may also present with prominent septal hypertrophy (176).

In addition to LVH, hypertensive heart disease can mimic HCM in a number of ways. Hypertensive LVH is associated with diastolic dysfunction and is a common cause of heart failure with preserved EF (269). Systolic mechanics are also often abnormal with reduced longitudinal strain (270). Both histology and CMR demonstrate an increase in diffuse and replacement fibrosis (180, 204, 271). Focal areas of LGE (replacement fibrosis) have been reported as twice as common in

men and four times as common in women with sustained hypertension compared with normotensive patients (271). In hypertensive heart disease elevated diffuse fibrosis is directly related to the degree of LVH and is associated with adverse LV remodelling and declining EF (204, 271, 272). Myocyte disarray is also present in necropsy studies of hypertensive heart disease, however most studies agree the amount of disarray is considerably less than observed in hypertrophic cardiomyopathy (168, 197).

Differentiating HCM from hypertensive LVH is important to ensure that at risk patients are identified and family members are screened, however assessments with contemporary investigations are often inconclusive. Improved diagnostic tools are therefore required.

5.7.3: The Athletic Heart

Another HCM phenocopy is the athletic heart. Cardiac physiological adaptations are normally confined to professional/ elite level sports people, however extreme endurance sports are increasing in popularity amongst amateurs. As in the normal heart, LV mass and wall thickness in the athletic heart are dependent upon gender and body surface area. Ethnic differences are also observed, with a higher prevalence and greater severity of LVH reported in black athletes (273). There is general consensus that endurance training leads to a greater increase in LV cavity size compared to strength training, however controversy exists with regards to the incidence of LVH (44, 45, 274-278). Numerous studies have described eccentric LVH, in line with LV cavity enlargement, with normal LV wall thickness, in response to endurance training (44, 45, 274, 279, 280). By contrast, strength training was originally reported to result in disproportionate concentric hypertrophy, with normal LV cavity dimensions (274, 281). More recent reports have challenged this theory (45, 275, 276, 282-284) with the greatest increase in wall thickness alternatively reported in so called 'high isotonic and isometric' sports such as rowing, canoeing and endurance cycling (283). Nonetheless, although studies generally agree on relative increase in wall thickness compared to sedentary controls, reports of true LVH >12mm amongst elite

athletes are rare, with estimates of around 1.5-1.7% (275, 283, 285). However, a much greater incidence was recently reported in athletically trained army recruits, with LVH of ≥13mm in 23%, with an asymmetrical morphology in 10% (43). The incidence of LVH amongst amateur sport enthusiasts remains unknown.

Differentiating HCM from the athletic heart again requires a multi-modality approach. CMR phenotyping can assist by demonstrating a normal-elevated LV cavity size, low-normal EF and elevated stroke volume (286). In young athletes, LGE is suggestive of cardiomyopathy, however this is less useful in veteran athletes as one small study indicated an increase in LGE compared to controls (287). Echocardiographic determinants of diastolic and systolic mechanics are normal in the athletic heart (288), but athletically trained HCM patients have more normalised mechanics than sedentary patients, therefore assessment may be equivocal (289).

Identifying HCM amongst athletes is especially important in light of the risk of malignant arrhythmia during competitive sport (253). As a result, sports associations around the world have introduced screening programs to improve detection and mitigate risk. However screening programs are imperfect and there are wide implications for both false positives and false negatives. Improved diagnostics are required to correctly identify affected patients.

5.8: Diagnosis

The diagnosis of HCM is a complex process based on the patients' history, family history and genetic profile (where available) combined with ECG and imaging results. Based on European guidance, a diagnosis in adulthood can be made under the following conditions(14):

- LV wall thickness of ≥15mm in one or more myocardial segments measured by any imaging modality (CMR, echocardiography, CT) in the absence of loading conditions such as hypertension/ aortic stenosis.

- LV wall thickness of 13-15mm in combination with one or more of the following: a genetic mutation consistent with HCM, positive family history, symptom profile consistent with HCM, ECG or additional imaging features consistent with HCM.

CMR offers accurate assessment of LV morphology, combined with tissue characterisation and perfusion analysis. Characteristic patterns of LVH and fibrosis can help to differentiate HCM from other phenocopies, however, in the clinical setting, echocardiography is the preferred modality for the assessment of LV outflow tract obstruction and diastolic function (14). However, to date there is no absolute discriminatory test for HCM, the presence of a genetic mutation can confirm the diagnosis, but its absence does not exclude it. Myocardial biopsy is reserved for when an alternative diagnosis, such as myocardial infiltration, is suspected and is of little use in confirming HCM. In practice, in an age of finite resources, establishing a diagnosis can be costly requiring multiple investigations, hospital visits, and in some cases repeat imaging over time. Diagnostic uncertainty also carries significant implications for patients and their families. Improved imaging techniques could therefore help to streamline diagnostic algorithms and improve patient management.

5.9: Management

The majority of patients with HCM have benign disease, with no therapeutic requirements. Where necessary therapy is individualised and aimed at managing symptoms, reducing outflow tract obstruction and mitigating the risk of sudden death. CMR can guide therapeutic strategies by quantifying the severity of LVH, the extent of fibrosis and the presence of perfusion defects. Temporal imaging with echo and CMR also permits the detection of declining systolic function, which is managed with standard prognostic heart failure medications (14). As with the diagnosis of HCM, risk stratification for sudden death is a complex, multifaceted process. Those deemed to be of moderate or high risk are managed with an implantable cardioverter defibrillator (290).

CMR phenotyping forms part of the risk assessment, however improved risk stratification is necessary to ensure the adequate sensitivity and specificity of this process.

Despite decades of research, treatment strategies in HCM are still based on small cohort studies or clinical experience and are targeted towards symptom control rather than disease modification. Barriers to discovering disease modifying therapies are complex and include the heterogeneity of the condition, the low event rate and the perceived rarity of the condition by the pharmaceutical industry (291). An improved understanding of the link between genetic mutations, myocyte abnormalities and HCM phenotypes is required to drive treatment innovations.

5.10: Future Directions & Diffusion Tensor Imaging

The link between microstructural abnormalities and the expression of HCM phenotypes is not completely understood. Necropsy studies are biased towards severe disease and cases of sudden death, and therefore do not represent 'real world' HCM. CMR measures have advanced the knowledge of morphological phenotypes and the presence of both diffuse and replacement fibrosis, however the importance of disarray in disease expression and adverse events remains unanswered.

Cardiovascular Diffusion tensor imaging (Chapter 7) may offer new insights into microstructural pathology in HCM. In addition to non-invasive characterisation of myocardial fibre and sheetlet orientation, it offers the ability to assess architectural organisation through the measure of 'fractional anisotropy', which may reflect disarray. This technique therefore offers the potential to directly assess the relationship between disarray and CMR measures of disease expression such as LVH, fibrosis and LV mechanics.

Using a technique similar to diffusion tensor imaging, CMR diffusion spectrum imaging, Wang et al. assessed fibre organisation in a mouse model of HCM (homozygous MYBPC3 knockout) (292).

Wild type mice displayed a smooth transition in transmural helical angle, from a left-handed helix in the epicardium to a right-handed helix in the endocardium. In contrast, the MYBPC3 knockout mice showed a lack of fibre coherence in midwall and subendocardium, which was interpreted as disarray.

Nguyen et al. performed diffusion weighted imaging in HCM patients, this permits assessment of myocardial diffusivity (freedom of water), but not structural orientation. Results demonstrated an excellent correlation between LGE derived fibrosis and diffusivity, thus the authors concluded that diffusion weighted imaging could serve as a contrast free alternative to LGE in this cohort (293).

In 2006 Tseng et al. performed the first in vivo cDTI study in HCM; they imaged 5 patients with HCM and 5 healthy volunteers in conjunction with strain imaging (294). Transmural myocyte orientation was determined from the 'helix angle' and myocardial organisation assessed via fractional anisotropy. Strain was calculated using the local fibre coordinate system to determine fibre, cross-myocyte and radial strains. Despite the small sample size they demonstrated significantly reduced fractional anisotropy, interpreted as greater disarray, in the LV septum of HCM patients compared to LV free wall. Abnormalities in helical angulation were also reported, with more longitudinally orientated fibres detected in HCM hearts (figure 5.7). All measures of septal strain were reduced, including myocyte long axis and cross-myocyte components, however the correlation between cross-myocyte strain (sheetlet direction) and fractional anisotropy was greatest, implying that disarray may impede myocardial sheetlet reorientation.

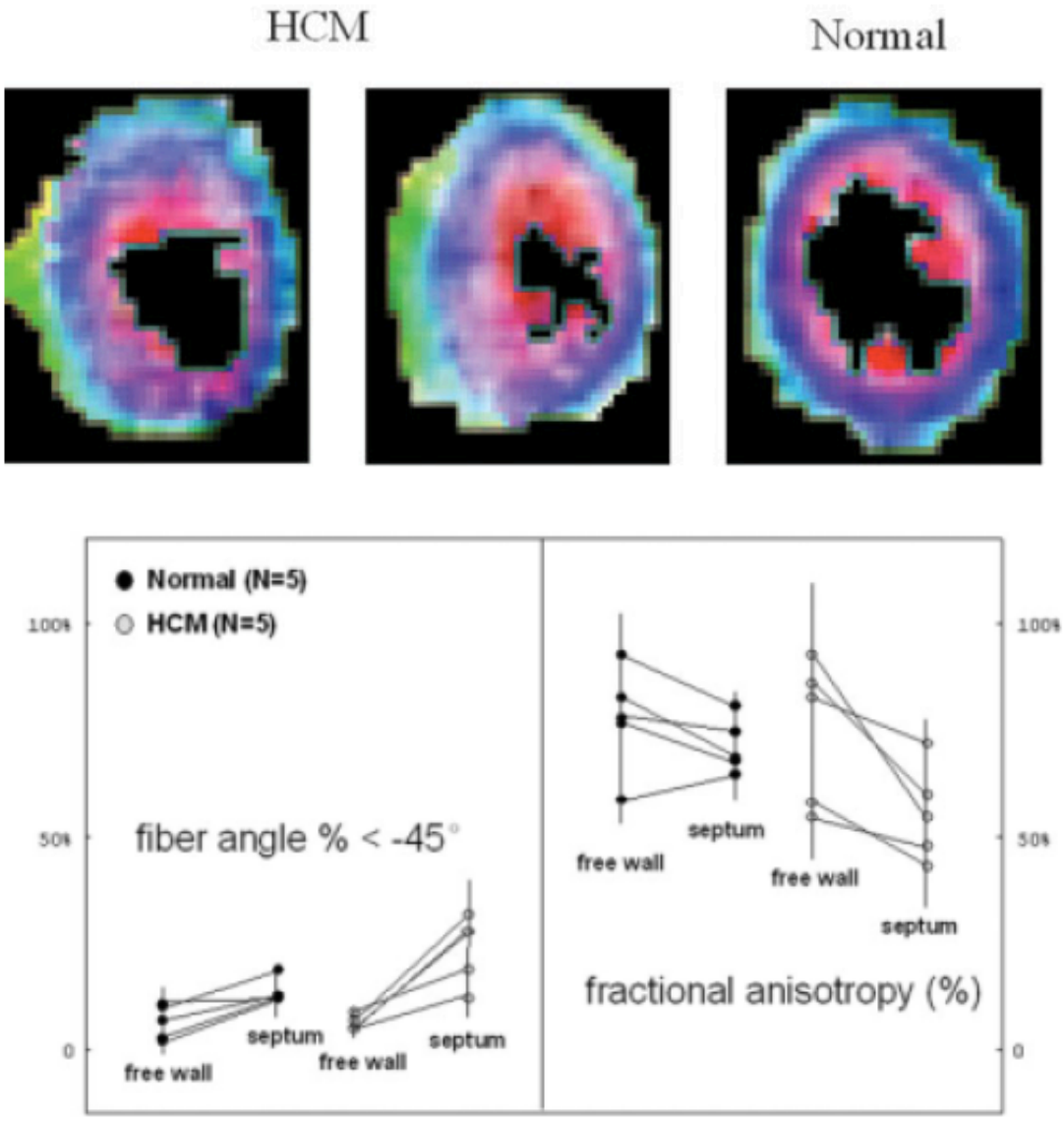

Figure 5.7: Images and data from Tseng et al. (294). The top panel depicts helical angulation in 2 HCM hearts and one healthy volunteer. Green denotes negative, or left-handed myocytes, blue indicates neutral, or circumferentially orientated myocytes and red positive, or right-handed myocytes. A greater proportion of green and red myocytes (longitudinal) are observed in the HCM hearts. The bottom left panel demonstrates a greater proportion of myocytes with a helical angle <-45° in the septum of the HCM cohort. The bottom right panel demonstrates comparatively reduced septal fractional anisotropy in the HCM cohort, therefore implying the presence of disarray.

Since the work of Tseng et al. the arrival of 3Tesla CMR scanners and sequence development have improved in vivo cDTI capabilities. Further investigation is required to determine the feasibility of this technique, however there is significant potential for cDTI in this condition. The ability to

detect disarray non-invasively could potentially stream line diagnostic algorithms, differentiating HCM from phenotype mimics. cDTI parameters may offer novel insights in the link between structural pathology mechanical abnormalities, and may even provide new methods of risk stratifying patients.

CHAPTER 6: CARDIOVASCULAR MAGNETIC RESONANCE IMAGING

6.1: Introduction

CMR is a clinically established, non-invasive imaging technique, which has become the standard reference for assessing several aspects of cardiac structure and function. Technical advances have led to a rapid expansion in clinical indications for CMR and the number of scans performed per centre is steadily growing (295). The relatively recent introduction of high field clinical scanners, such as 3Tesla, has opened the door to advanced imaging techniques, further expanding CMR capabilities. This chapter describes the basic physics principles of CMR, contemporary clinical applications and advantages of 3Telsa imaging (296-299).

6.2: CMR System Components

The basis of CMR is the detection of RF signals emitted from hydrogen ions within a magnetic field. Three types of magnetic field exist within a CMR scanner which are generated by dedicated coils (figure 6.1)(297):

1. **Main Magnetic Field**: The main magnetic coil wraps round a large cylindrical hollow core to form a strong electro-magnetic field orientated along the bore of the magnet. The strength of the magnet dictates the operating field strength, denoted by B_o, which is measured in units of Tesla. Most clinical CMR scanners operate at 1.5 Tesla, which is approximately 30,000 times the earth's magnetic field. Imaging is conducted with patients placed within the bore of the magnet and the direction of B_o defines the Z-axis in the orthogonal x,y,z coordinate system. The main magnetic field is constant and safety precautions must be observed at all times before entering the room.
2. **Magnetic Field Gradients**: Mounted inside the main magnet coil are the gradient coils which modify the magnetic field in the x, y and z directions. The magnetic field gradients can be rapidly switched on and off which permits spatial localisation and slice selection.

3. **Radiofrequency (RF) Magnetic Field**: The RF transmitter coil is mounted inside the gradient coil and produces the RF magnetic field. This field, known as B_1, has a much smaller amplitude (micro Tesla) than B_0 and its frequency is dictated by the main magnetic field (128MHz at 3T). The RF field is applied perpendicular to B_0 to rotate the magnetisation into the x-y plane and establish the coherent precession of hydrogen spins required for signal generation.

RF electromagnetic signals are emitted from hydrogen ions as a consequence of relaxation. These signals are detected by receiver coils, comprised of loops of wire, placed directly over the patient's chest. Contemporary CMR receiver coils consist of an array of up to 128 coils (300). All CMR components are connected to a computer which stores and reconstructs images and allows the operator to control the imaging process.

Figure 6.1: Diagram of the CMR system components: a) Location of the main magnetic, gradient, RF

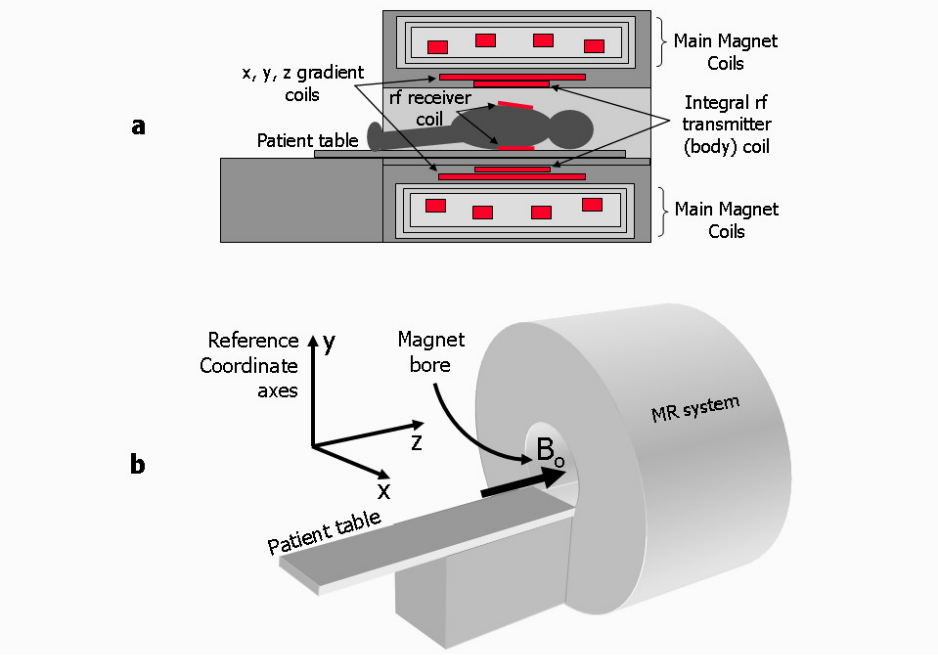

transmitter and receiver coils. b) Arrangement of the Mx,y,z coordinate system and B_o in relation to the bore of the magnet **(297)**.

6.3: Basic Physics

6.3.1: Hydrogen Precession

The human body is predominantly comprised of water and fat which are abundant in hydrogen ions. The hydrogen nucleus (^1H) consists of a single proton, and is thus positively charged, and spins to create a small magnetic field, known as a magnetic moment. The magnetic moments alignment is random, however when placed in a large magnetic field (B_o), the proton magnetic moments tend to align with the magnetic field to create a net magnetisation, known as M_o. Due to the interaction of the magnetic moment and the magnetic field, the magnetic moments actually precess (rotate) around B_0 (figure 6.2).

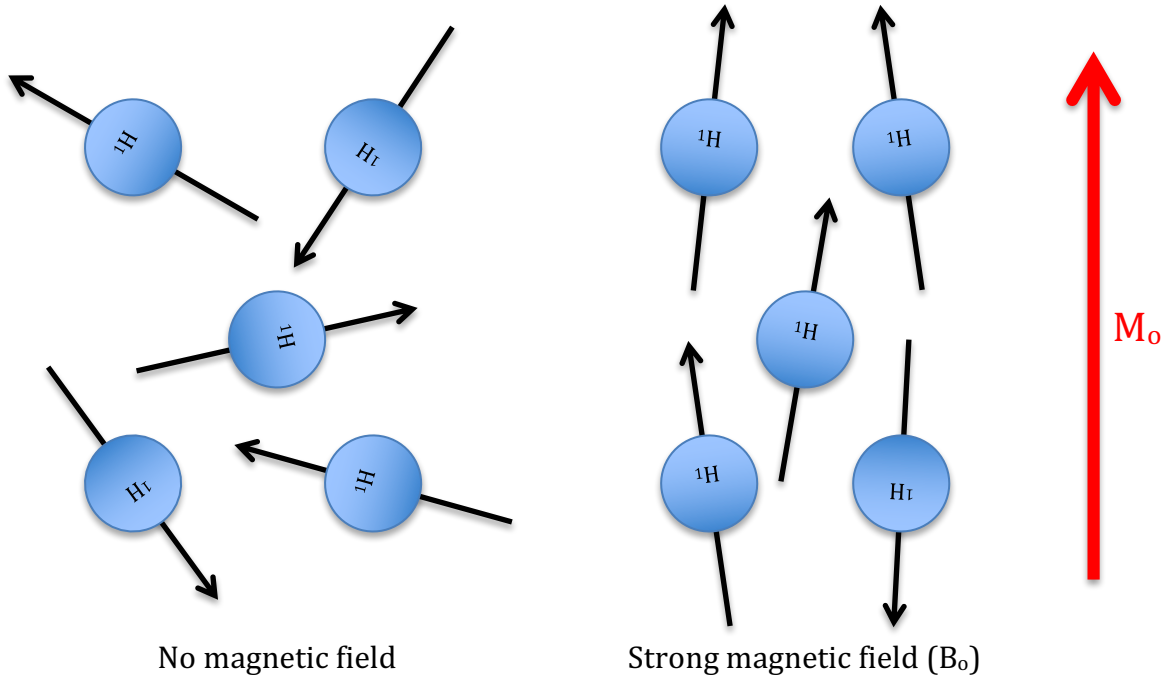

Figure 6.2: In the absence of magnetisation hydrogen ions precess at random. When placed in a strong magnetic field (B_o) proton precession aligns with the magnetic field to create a net magnetisation (M_o).

6.3.2: Radiofrequency Excitation and Magnetic Strength

Within the strong magnetic field net magnetisation aligns with the longitudinal (M_z) coordinate and individual hydrogen ions precess around B_0 at the same frequency, however their position (phase) in the transverse (M_{xy}) axis is random. In order to generate MR signal, proton precession must be coherent in phase and contain a component in the M_{xy} plane. To achieve this the RF magnetic field (B_1) must be applied perpendicular to B_o at the exact precessional frequency of the hydrogen ions. This is referred to as the Larmor frequency (ω_o) and is dictated by the a strength of B_o in the Larmor equation:

$$\omega_o = \gamma \times B_o$$

The constant γ is referred to as the gyromagnetic ratio and the hydrogen ion has the value of 46MHz/Tesla. Thus in a 1.5Tesla and 3Tesla CMR scanner the Larmor frequency is 64MHz and 128MHz respectively. Inhomogeneity of the B_o field results in hydrogen ions with different Larmor frequencies which may not be excited by the RF magnetic field. Metal implants are one cause of inhomogeneity, which result in image artefact, however this property can also be exploited to permit slice selection through application of the gradient magnetic field.

RF pulses of the correct frequency energise protons and deflect them away from their equilibrium position in the M_z plane into the M_{xy} plane. The angle of deflection from M_z is referred to as the flip angle (α) and has a range of 0-180°. The energy of the RF pulse, which is a product of both its amplitude and duration, dictates the deflection angle, with the greatest energy required to flip to 180° (figure 6.3)

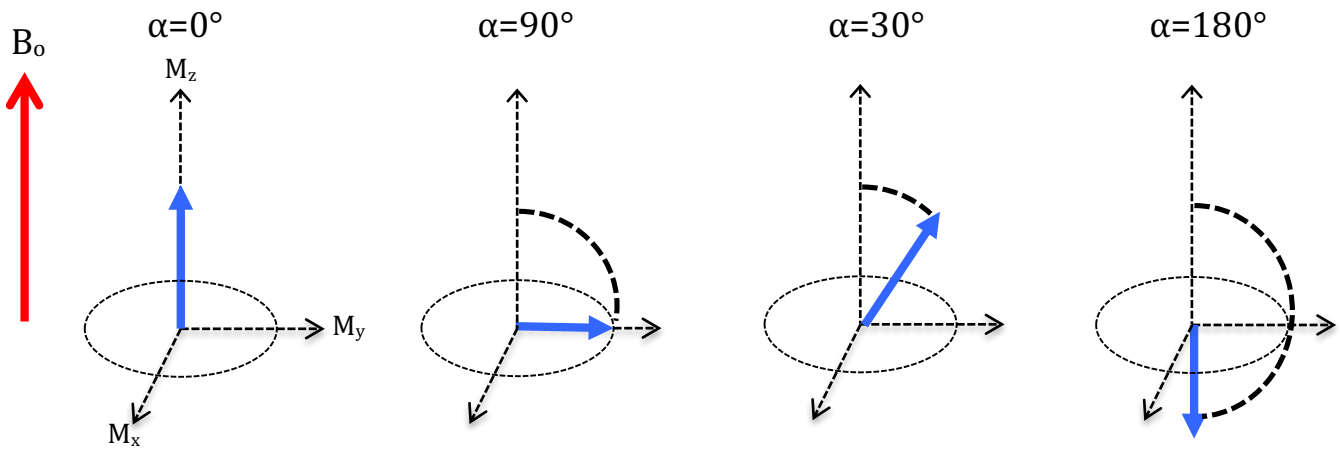

Figure 6.3: In the absence of an RF pulse net magnetisation lies only in the M_z plane. A flip angle of 90° transfers the net magentisation from the M_z into the M_{xy} plane. A flip angle of 30° stores magnetisation in both the M_z and M_{xy} planes. A flip angle of 180° is called an inversion pulse and inverts the magnetisation from the positive M_z axis to the negative M_z axis with no magnetisation in the M_{xy} plane.

6.6.3: Relaxation and Recovery

Once the RF pulse is switched off the only magnetic field remaining is the B_o field. The hydrogen protons therefore lose the stored RF energy and return to the equilibrium position with net magnetisation in the M_z plane and loss of coherence in the M_{xy} plane. This process called free induction decay (FID) and results in an oscillating magnetic field, which is detected by the receiver coil. The loss of net magnetisation in the M_{xy} axis occurs by two independent processes: T1 recovery (also called relaxation) and T2 relaxation and forms the basis of MR imaging.

6.3.3.1: T1 Recovery

The return of proton spin equilibrium to the longitudinal M_z axis is called T1 recovery. This is also known as 'spin-lattice relaxation'. Recovery is exponential and dictated by the tissue specific T1 constant, defined as the time taken for 63% recovery of longitudinal magnetisation, which is a function of B_0 amplitude. A long T1 gives slow recovery and short T1 gives fast recovery. In recent years assessment of T1 relaxometry has been utilised to detect diffuse myocardial fibrosis and differentiate between cardiovascular disease aetiologies (301). Estimates of myocardial T1 vary

but is roughly between 900 and 1100ms at 1.5Tesla and between 1100 and 1300ms at 3Tesla (40) (figure 6.4).

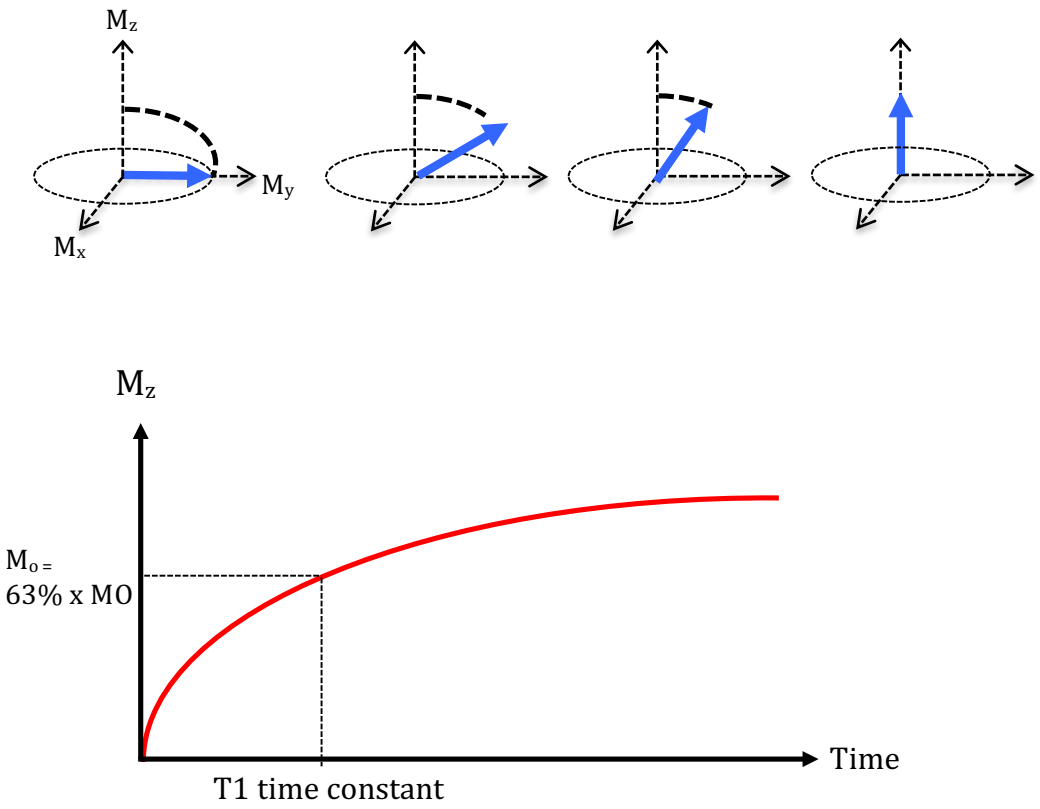

Figure 6.4: T1 recovery after a 90degree RF pulse: Return of equilibrium to the Mz axis is exponential and dictated by the strength of B_o and the tissue specific T1

6.3.3.2: T2 Relaxation

T2 relaxation is caused by loss of proton phase coherence in the transverse plane. After the removal of the RF pulse, over time the protons gradually move out of phase with one another. This is in part due to the interaction of the individual proton magnetic fields (magnetic moments) affecting the spin of neighbouring protons and is thus also referred to as spin-spin relaxation. The rate at which net magnetisation is lost (protons dephase) in the M_{xy} axis is dictated by the time constant T2, which is defined by the time taken for 63% of the signal to decay. T2 is always shorter than T1, with normal myocardial T2 estimated between 50 and 55ms at 1.5Tesla and 45ms at 3Tesla (302). A second factor influencing transverse decay is inhomogeneities in the B_0 field.

Inhomogeneities increase the speed at which protons dephase by varying the proton Larmor frequency and creating spins which are 'off resonance'. The sum of the effect of magnetic field non-uniformities and T2 is referred to as T2* and is a useful parameter to detect the presence of myocardial iron in transfusion dependent anaemias (303).

6.3.4: Gradients

Spatial encoding of MRI signals is required to generate images. This is achieved by manipulating the main magnetic field with gradient magnetic fields in the x, y and z directions.

6.3.4.1: Slice selection (M_z)

Slice selection is achieved by applying a slice select gradient (G_{ss}) in one direction at the same time as the RF pulse. This creates a linear magnetisation gradient, with a range of Larmor frequencies. Slice selection can therefore be achieved by limiting the bandwidth of the RF pulse so that only protons within a given slice will be excited.

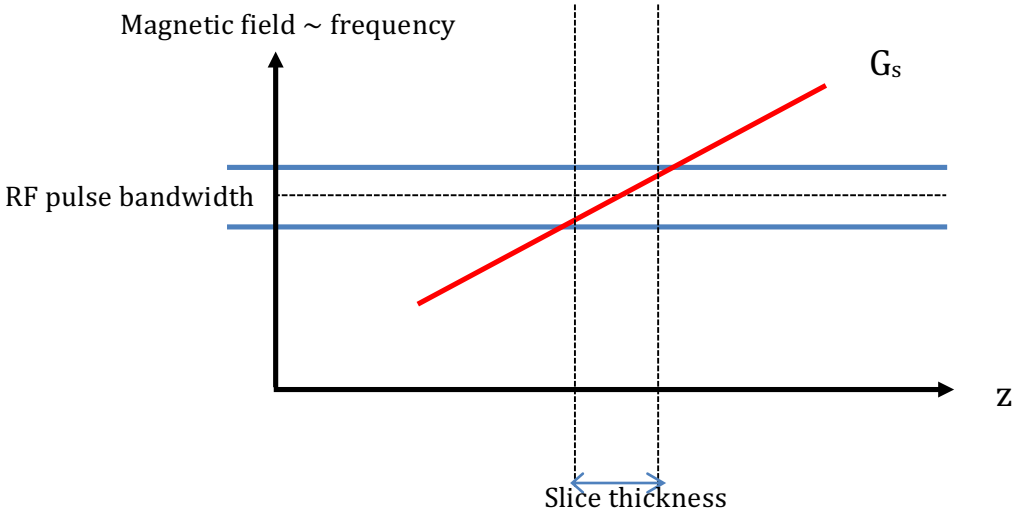

Figure 6.5: The application of the slice select gradient (G_s) creates a linear gradient in M_z. Slice selection is achieved by setting the RF pulse frequency bandwidth to the Larmor frequency range within the slice.

6.3.4.2: Frequency Encoding

To establish spatial localisation within the slice a frequency encoding gradient (G_F) is applied along one axis. The Larmor frequency of the protons will therefore depend on their position. The frequency encoding gradient is applied during the signal measurement, known as the read out, and the position of the signal is effectively encoded within the Larmor frequency.

6.3.4.3: Phase Encoding

Prior to the frequency encoding gradient a short phase encoding gradient (G_P) is applied along the axis perpendicular to the frequency encoding direction. Again during the application of the gradient the Larmor frequency of the protons will be dependent on their position along the axis. When the gradient is switched off, the protons at the stronger end of the gradient have gained more phase than those at the weaker end. The location in phase encode direction is therefore encoded in the phase offset. Unlike slice select and frequency encoding, phase encoding is repeated multiple times with different phase encode gradient strengths. The larger the phase encoding gradient, the greater the range in phase offsets. The combination of multiple phase encodings are required to determine the location in the phase encode direction.

6.3.5: k-space and Image Formation

The above steps are combined to locate the CMR signal in three dimensions (figure 6.6). The time interval between each repeat of the pulse sequence is known as the repetition time, TR. The signal emitted is called an 'echo' and contains both phase and frequency encoding information. This raw data from multiple signal measurements is combined to create 'k-space'. Each phase encoding step generates one line of data within k-space, where the co-ordinate k_x is determined by the relative time that the data was collected during the frequency encoding gradient. Each phase

encoding step moves along k_y. The central line of k-space (k_y =0) represents the echo from when the phase encoding gradient was zero and the periphery when then phase encoding gradient was high. High spatial frequency contributions are found at the periphery of k-space and low spatial contributions at the centre. The field of view (FOV) and resolution in both directions are determined by the spacing of the points and the maximum extent of k-space sampled in each direction respectively. The FOV and resolution in the frequency encoding direction is determined by the receiver bandwidth and the slope of the frequency encoding gradient. The FOV of the image in k_x is inversely related to the space between each of the data points and the resolution is determined by the maximum phase encode gradient. Although MR images are viewed in two dimensions, each point in the image contains signal from a voxel which has 3 dimensions, defined by x resolution, y resolution and slice thickness. The received signal is analysed using a two dimensional Fourier transform. The transform interprets the frequencies and phase offsets contained within each echo and reconstructs the MR signal into a visual image.

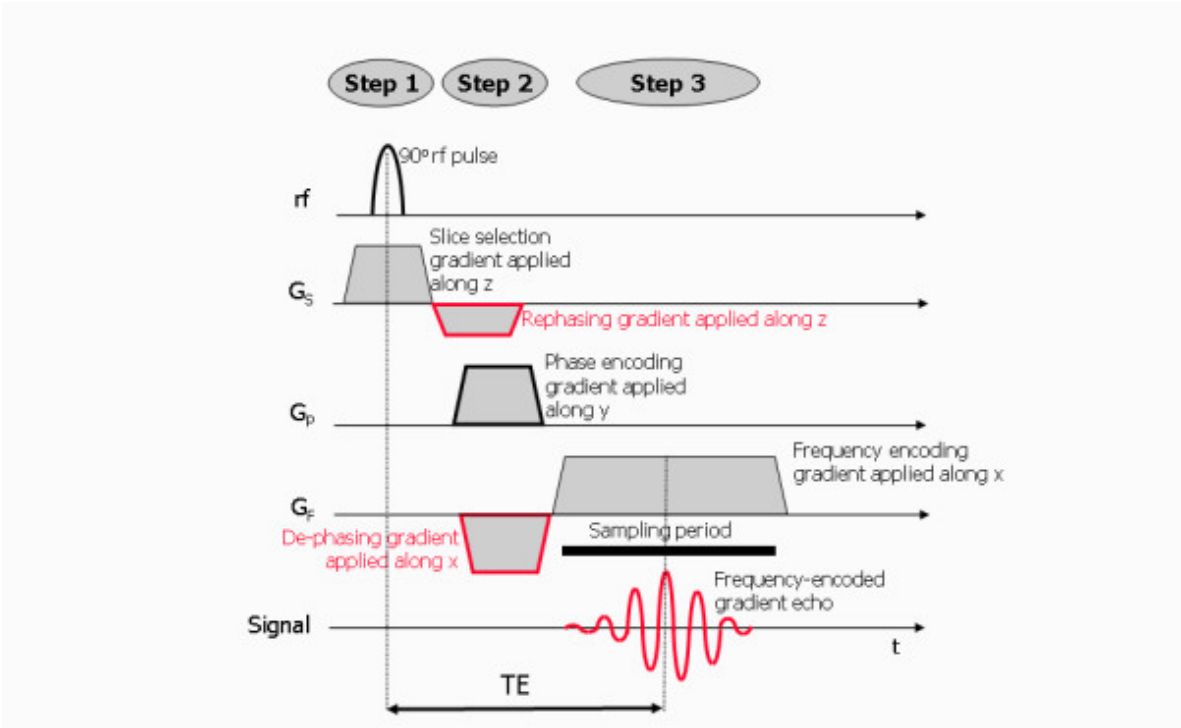

Figure 6.6: Pulse sequence diagram showing the timing of the relevant gradients in relation to the RF pulse. These amount to an MR echo which is sampled at the echo time, TE. Additional gradients, shown in red, are required to ensure that any de-phasing caused by the slice select and frequency encoding gradients are cancelled out by TE (297).

6.4: Signal to Noise Ratio

Every MR voxel contains a mixture of signal and noise. Image noise consists of random electrical fluctuations and can come from a number of sources. The signal to noise ratio is the ratio of these contributions:

$$SNR = signal / noise$$

SNR increases with increasing voxel volume and phase encoding steps and decreases as the receiver bandwidth increases. Therefore increases in SNR are at the expense of resolution, image acquisition time and the size of the field of view.

6.5: Reducing Scan Time

The acquisition time of each image is a product of the time to repeat of the sequence (TR) and the number of phase encoding steps (N_p). An increase in resolution along k_y and therefore the number of phase encoding steps, increases the scan time:

$$\text{Acquisition time} = TR \times N_p$$

In conventional imaging k-space is filled with equally spaced parallel lines along the k_x axis, this is know as a Cartesian acquisition. In this method k-space is either filled from the centre in alternate lines outwards or from one end of k-space to the other.

Scan time can be reduced by employing techniques which permit under sampling of k-space. Parallel imaging is a technique that makes use of the spatial distribution of the receiver coils to provide additional information with regards to the location of the signal origin. K-space is under sampled with fewer phase encoding lines by a reduction factor R, such that for half the original phase encoding lines R=2. The increased in the space between the lines would normally create an aliased image (i.e. the left side of the gap folds into the right and vice versa), however the additional spatial information afforded by the multiple receiver coils is used to fill these areas of

k-space. Reconstruction of this information requires knowledge of the variation in signal intensity in relation to the distance from each coil element and the sensitivity of the coils to the signal. A low resolution reference image in which only the central lines of k-space are acquired is used to measure the coil sensitivity profiles (298). A number of techniques exist including SENSE (sensitivity encoding) (304) and GRAPPA (Generalised auto-calibrating partially parallel acquisitions) (305) with differences between vendors. The timing of the reference acquisition is dependent upon the parallel imaging technique used with acquisition prior to parallel imaging in SENSE and as part of the acquisition in GRAPPA and modified SENSE (mSENSE). Reconstruction calculations are then either performed in the image space (SENSE) or in k-space (GRAPPA). Because parallel imaging techniques reduce the number of phase encoding steps the reduction in acquisition time is at the expense of SNR.

6.6: Cardiovascular Magnetic Resonance Pulse Sequences and Image Contrast

6.6.1: Introduction

Conventional CMR imaging is based on the ability to create contrast between neighbouring tissues by exploiting their characteristic T1 and T2 timings. This is achieved by using pulse sequences with varying amounts of T1 and T2 weighting. In addition to the signal weighting, the signal intensity in each voxel is dependent on a number of factors including: the strength of the main magnetic field (greater signal intensity afforded by higher field strengths); the proximity of the voxel to the receiver coil (signal intensity is inversely related to distance); and other factors such as particle flow or diffusion within the voxel.

6.6.2: Spin Echo

In vivo magnetic field inhomogeneities causes rapid signal decay via T2*. Spin echo sequences mitigate this loss by applying a 180° pulse after the initial 90° RF pulse. This re-establishes phase coherence in the M_{xy} plane therefore reversing the effect of field inhomogeneities on spin-spin interactions (T2*). The timing of the refocusing pulse is required is at exactly half the echo time (TE) i.e. TE/2. The echo time is the point at which the signal echo is at its peak and can be manipulated by the timing of the refocusing pulse. The result is that FID occurs as a consequence of T2 and T1 decay.

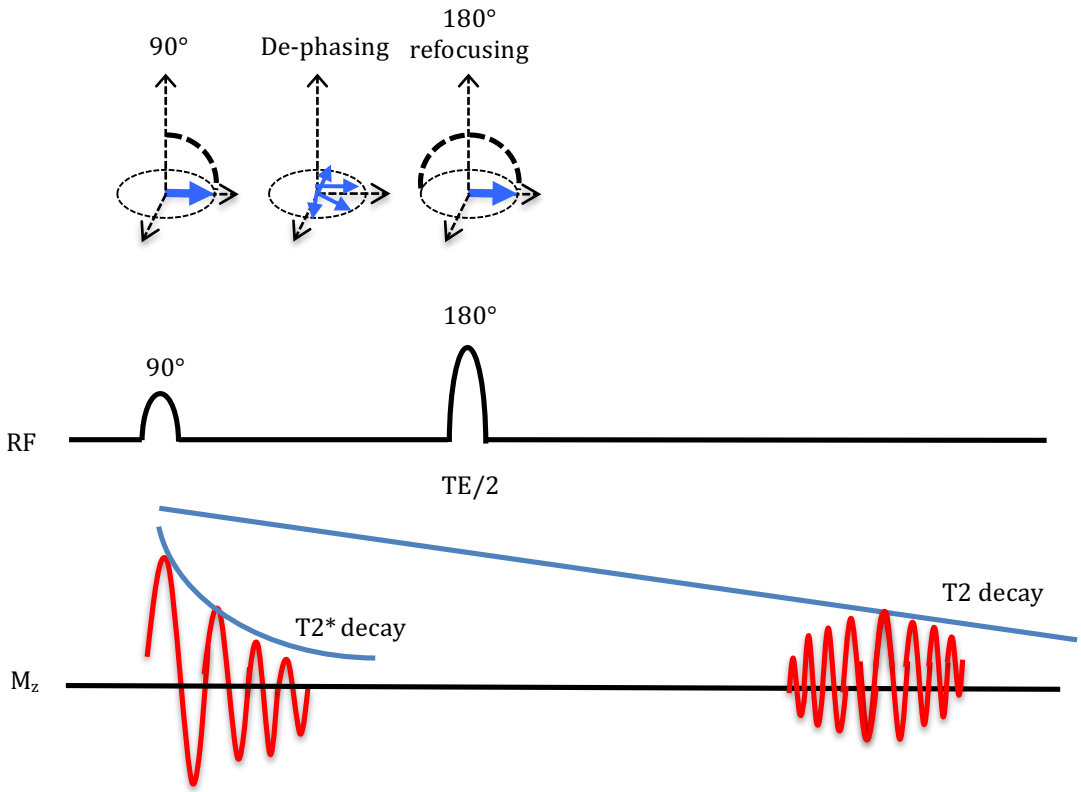

Figure 6.7: Illustration of a spin echo sequence. An initial 90° tips the magnetisation into the M_{xy} plane. Rapid de-phasing occurs due to field inhomogeneities (T2*). A refocusing 180° pulse re-establishes phase coherence at exactly half the echo time (TE/2).

T1 weighting is applied to spin echo sequence by adopting a short echo time (TE) and sequence repeat time (TR). Shortening the TE reduces the time for de-phasing and therefore reduces the dependence of the signal contribution on T2. Shortening the TR increases T1 contrast by reducing the time for longitudinal recovery within tissues with a long T1, such as fluid, therefore reducing the signal intensity. Conversely a T2 weighted image is created by sampling at relatively long TE,

therefore allowing the signal intensity to be dictated by the T2 weighting of the image. This is coupled with a long TR which allows adequate time for equal T1 recovery within all the tissues. In T2 weighted images the rapid loss of signal in tissues with a short T2, such as muscle, reduces the signal intensity compared to tissues with a long T2, such as fluid. During spin echo sequences fast flow blood within blood vessels and cardiac chambers will move out of the slice before the refocusing pulse, the new blood which replaces this space will not have been excited and therefore will not contribute any signal, this is known as 'black blood' imaging.

6.6.3: Stimulated Echo Acquisition Mode

The stimulated echo acquisition mode (STEAM) sequence is similar to spin echo but lacks the 180° pulse (306). Instead the 180° pulse is split into two separate 90° pulses, which combined have the same effect as refocusing pulse. This sequence type is utilized in diffusion imaging and will be discussed in the next chapter (Chapter 7).

6.6.4: Gradient Echo

Gradient echo imaging combines an RF pulse with an imaging gradient. After the initial RF pulse de-phasing occurs in the x-y plane, a gradient is then applied which dephases the magnetisation. A second gradient is then applied in the opposite direction to reverse the de-phasing, bringing the proton spins back to coherence at the TE. During this process signal decay is governed by T2* and is therefore the TE is shorter than in spin echo sequences.

6.6.4.1: Balanced Stead-State Free Precession

Numerous versions of gradient echo pulse sequences are used in clinical practice, but most functional CMR imaging is conducted with a variant called balanced steady state free precession (bSSFP). In this sequence the sequence repetition time is very short. The very short TR means that recovery of magnetisation in the M_z plane is incomplete and is thus carried over to the next RF pulse. A series of repetitions are conducted with alternating positive and negative flip angles

(e.g. +60° and -60°) that bring the signal to steady state and increase the strength of the signal (greater SNR) compared to a single sequence. Unlike spin echo sequences the speed and lack of a refocusing pulse in an bSSFP imaging sequence permits signal from blood, making this a 'bright blood' acquisition. One limitation of this sequence is its sensitivity to off resonance B_o field inhomogeneities, which more pronounced at higher field strengths i.e. 3T.

6.6.4.2: Echo Planar Imaging

Echo planar imaging (EPI) is another example of a gradient echo sequence that is employed to reduce scanning time. After an RF pulse multiple de-phasing and re-phasing gradients are applied to produce multiple gradient echoes therefore rapidly increasing the number of phase encoding lines acquired. The simplest version of this sequence is the single shot EPI which acquires all the echoes required to cover k-space after a single RF pulse. Short phase encoding gradients are applied between alternating positive and negative frequency encode gradients to acquire the data as quickly as possible. The amplitude of the signal diminishes with each echo due to T2* decay (figure 6.8). EPI can be combined with parallel imaging techniques to reduce scan time further still (307).

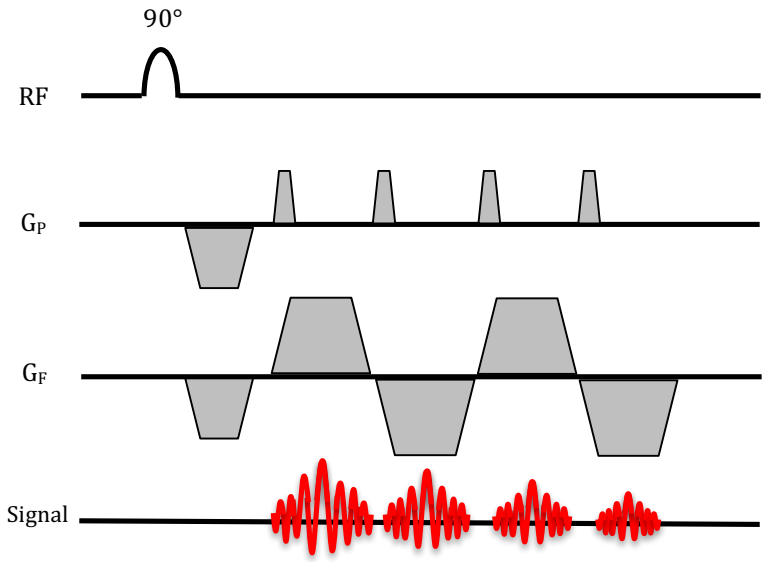

Figure 6.8: Single shot echo planar imaging illustration. After a single RF pulse multiple de-phasing and re-phasing gradients are applied to refocus the protons and produce multiple echoes. The echoes reduce in amplitude over time due to T2* decay.

6.6.5: Cine Imaging

Determining the contractile function of the heart is the crux of CMR imaging. Cine imaging requires multiple frame acquisitions throughout the cardiac cycle which are played in a loop to create a movie. ECG gating is used to define the beginning and end of the cardiac cycle, the RR interval is then divided into phases, with each phase representing an image frame. The full k-space for each frame is built up over a number of heartbeats. Cine imaging requires a short TR time as a number of images are acquired in a single RR interval, gradient echo sequences such as bSSFP are therefore used.

The assignment of data to a specific cardiac phase can be conducted either prospectively or retrospectively. Prospect gating is usually reserved for patients an irregular heartbeat. Data collection is triggered by the R wave and the number of subsequent phases determined by the shortest RR interval. After the final phase a short gap is left to permit detection of the next R wave, the resulting cine therefore plays with a slight jump between the end of the movie and the start of the next loop. In restrospective gating a data is collected continuously until k-space is filled for all phases (usually 25 but can be set lower to reduce scan time). In this instance the heart rate

recording is used to determine which phases coincide with the R wave. The data collected is then retrospectively assigned to a cardiac phase and will only work when there are minimal variations in the RR interval.

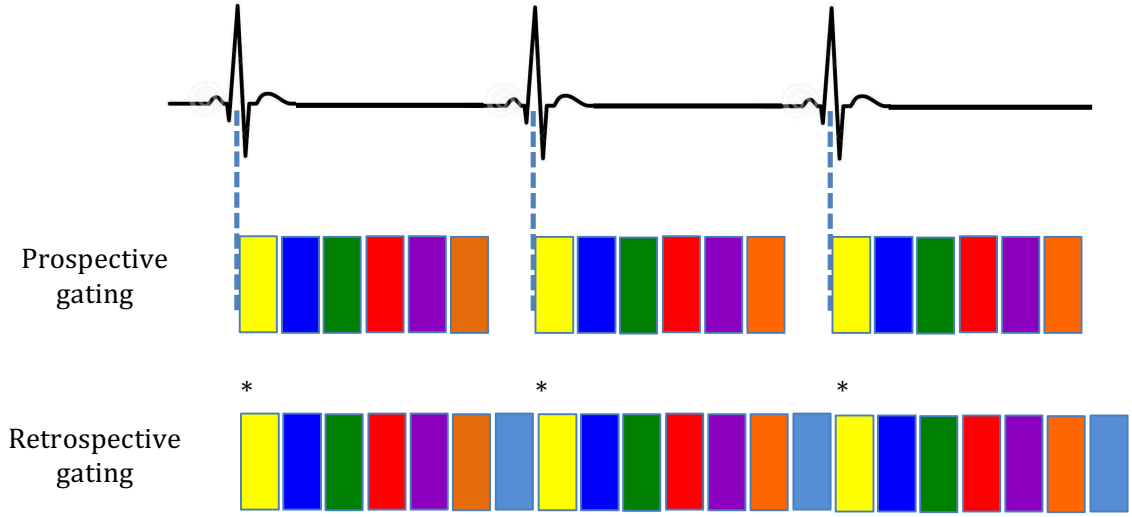

Figure 6.9: Cine imaging: Data collection is assigned prospectively and triggered by the R wave in prospective gating. A small gap is left at the end of data collection to allow for detection of the next R wave. Data is acquired throughout the cardiac cycle in retrospective gating and phases are assigned based on an average of the RR interval.

6.6.6: Phase Contrast Velocity Mapping

Spoiled gradient echo pulse sequences are sensitive to the presence of flow and can be exploited to calculate blood flow velocity (296, 298). During spoiled gradient echo sequences two gradients of opposite signs (bipolar) are applied along the same direction to mitigate against dephasing of the MRI signal arising from the slice select or frequency encoding gradients. For stationary spins both gradients are received equally and thus cancel one another out however, in the case of flowing blood, spins have moved along the gradient and complete reversal of the initial gradient is not achieved. The result is a phase shift which is directly proportional to the velocity of blood (figure 6.10).

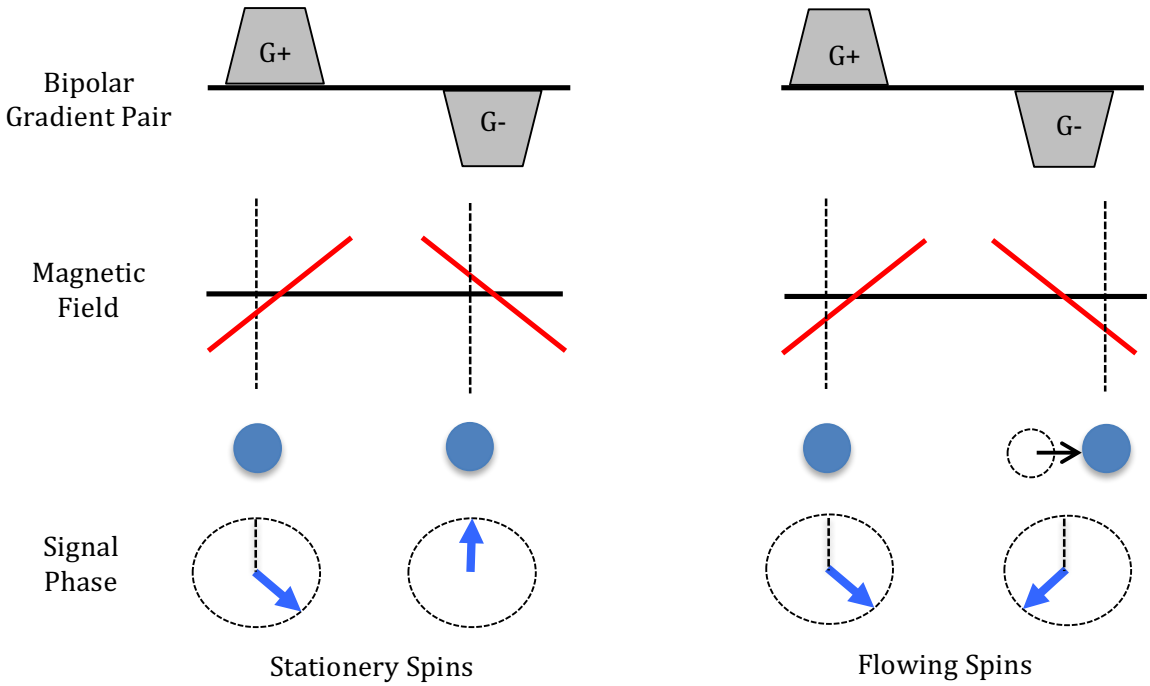

Figure 6.10: Illustration of phase contrast velocity mapping. In the context of stationery spins bipolar gradients of opposite polarity lead to equal dephasing and rephasing of transverse spins. Flowing spins move position along the second gradient such that the dephasing of the first gradient is not reversed. The extent of the phase shift is equal to the velocity of the flow.

To interpret blood flow velocity in a certain direction, consecutive acquisitions are acquired at different flow sensitivities, with flow sensitivity determined by the amplitude, duration and time between the bipolar gradient pair. The phase maps from the two acquisitions are then subtracted from one another to give pixel-wise velocity encoded phase shifts.

6.6.7: Myocardial Tagging

Cine imaging is employed to detect bulk cardiac motion for global functional assessment; in contrast myocardial tagging permits detection of intra-myocardial motion. This is achieved by applying a pattern of 'tags' to the myocardium that deform as the heart contracts. One technique is spatial modulation of magnetisation (SPAMM) where a series of non-selective RF pulses are combined with a series of gradient pulses called modulation gradients. The more non-selective gradients and modulation gradients used the sharper the definition of the lines (308, 309). The sequence is triggered by the R wave and creates a pattern of excited and non-excited myocardium

such as zebra pattern lines, or more commonly a grid of boxes. By tracking tag displacement throughout the cardiac cycle myocardial strain can be computed. In particular tagging allows assessment of circumferential strain which is not apparent on cine imaging.

6.6.8: Gadolinium Contrast & Inversion Recovery

Contrast in CMR acquisitions is dependent on proton density, T1, T2 and T2* relaxation characteristics of the tissues. This contrast can be manipulated by administering agents which alter these characteristics. The most commonly used compounds are gadolinium based. Gadolinium ions are toxic but can be chelated to create compounds that can be safely injected and are renally excreted. Gadolinium is paramagnetic and will therefore emit a magnetic field in the presence of the main magnetic field; this changes the Larmor frequencies of adjacent protons. The main effect this has is to shorten T1, with a much smaller effect on T2 & T2*. The magnetic field of gadolinium has a short range and will therefore only affect the protons in its immediate vicinity. Gadolinium shortens T1 in proportion to the concentration of the agent and the native T1 of the tissue.

The administration of gadolinium can be combined with T1 weighted sequences to enhance image contrast. Frequently, the sequence of choice in this instance is called 'inversion recovery'. Inversion recovery uses a non-selective 180° RF pulse which tips all of the magnetisation into the negative z-axis. Recovery of longitudinal magnetisation toward +z then has to recover through 0 and takes much longer. Image acquisition can then be timed such that tissues containing gadolinium and therefore have a short T1 emit a high intensity signal while other tissues emit little or no signal; this is called the inversion time (TI). Image contrast can be further enhanced by timing data acquisition to coincide with the point that a tissue has recovered longitudinal magnetization back to zero and therefore will not emit any signal, this is referred to as the null

point. Data is then typically collected using a gradient echo sequence and requires multiple heart beats for a full data set (figure 6.11).

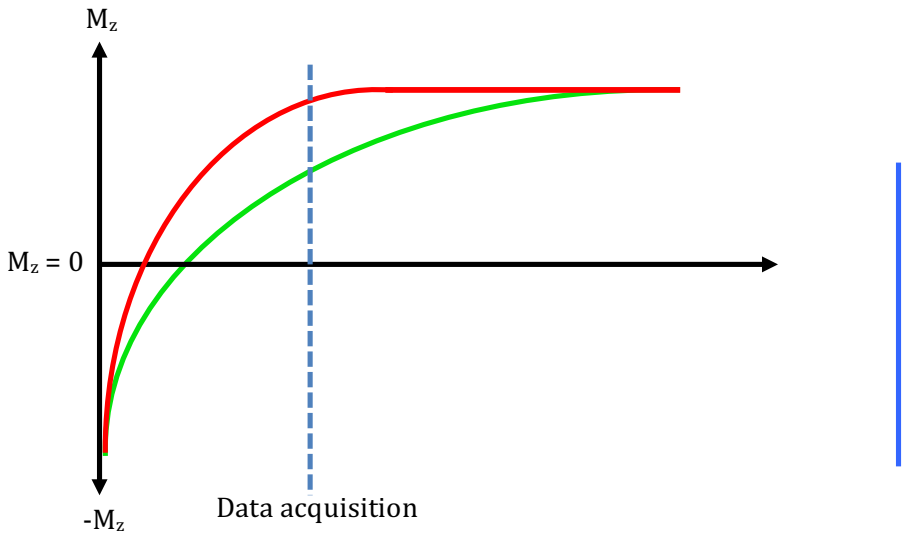

Figure 6.11: Illustration of T1 recovery after a 180° inversion pulse. The red line represents tissues containing gadolinium with a short T1, the green line represents tissues with an intermediate T1 and the blue line represents a tissue which is has reached zero longitudinal magnetization at the time of data acquisition and is therefore 'nulled'.

6.7: Clinical Applications of Cardiovascular Magnetic Resonance

6.7.1: Introduction

CMR has many advantages over other imaging modalities in light of its high spatial resolution, unique tissue characterising capabilities and lack of ionising radiation. A standard examination combines multiple sequences to build a complete picture of cardiac structure and function. These tools have enabled a wealth of CMR based research over the years, which has contributed to our understanding of cardiovascular diseases processes and shape our clinical practice.

6.7.2: Tissue Characterisation

Gradient echo sequences are used to establish patient localisation with the scanner and obtain basic structural guidelines to plan subsequent images (scouts). T1 and T2 weighted spin echo

techniques are then used to expose intrinsic tissue characteristics and build contrast between adjacent structures for visual assessment.

6.7.2.1: In Vivo T1 Recovery

T1 recovery is dependent up size of the molecule the hydrogen ion is attached to. Large molecules have a long T1 as they inhibit the movement of hydrogen ions and delay recovery. In contrast hydrogen ions in fat are relatively uninhibited and oscillate close to the Larmor frequency giving fat one of the lowest T1 values in vivo. Hydrogen ions within water tumble at speeds greater than the Larmor frequency, which also reduces energy exchange resulting in a high T1, however the T1 of water is reduced when in close proximity to larger molecules, i.e. muscle proteins.

6.7.2.2: In Vivo T2 Relaxation

The T2 of free water is also long as water molecules are sufficiently far apart to inhibit spin-spin interactions. Conversely water bound to tissues, i.e. myocardium, has a higher incidence of spin-spin interactions and therefore a lower T2. When the myocardial water content increases due to inflammation or oedema the T2 will increase, this property is exploited in clinical imaging to diagnosis pathologies such as myocarditis and sarcoidosis.

6.7.3: Functional Assessment

bSSFP cine imaging is widely considered the gold standard technique for assessment of cardiac volumes and function and the lack of ionising radiation permits safe repeat/ follow up imaging. Volumetric data can be compared to standard references values adjusted for BSA (40, 41). Cines are acquired in a contiguous short axis stack with additional long axis images used to define valve planes. The blood pool area is then defined in systole and diastole for each slice and the total

volume computed. The blood pool can be defined manually by drawing or by thresholding (figure 6.12).

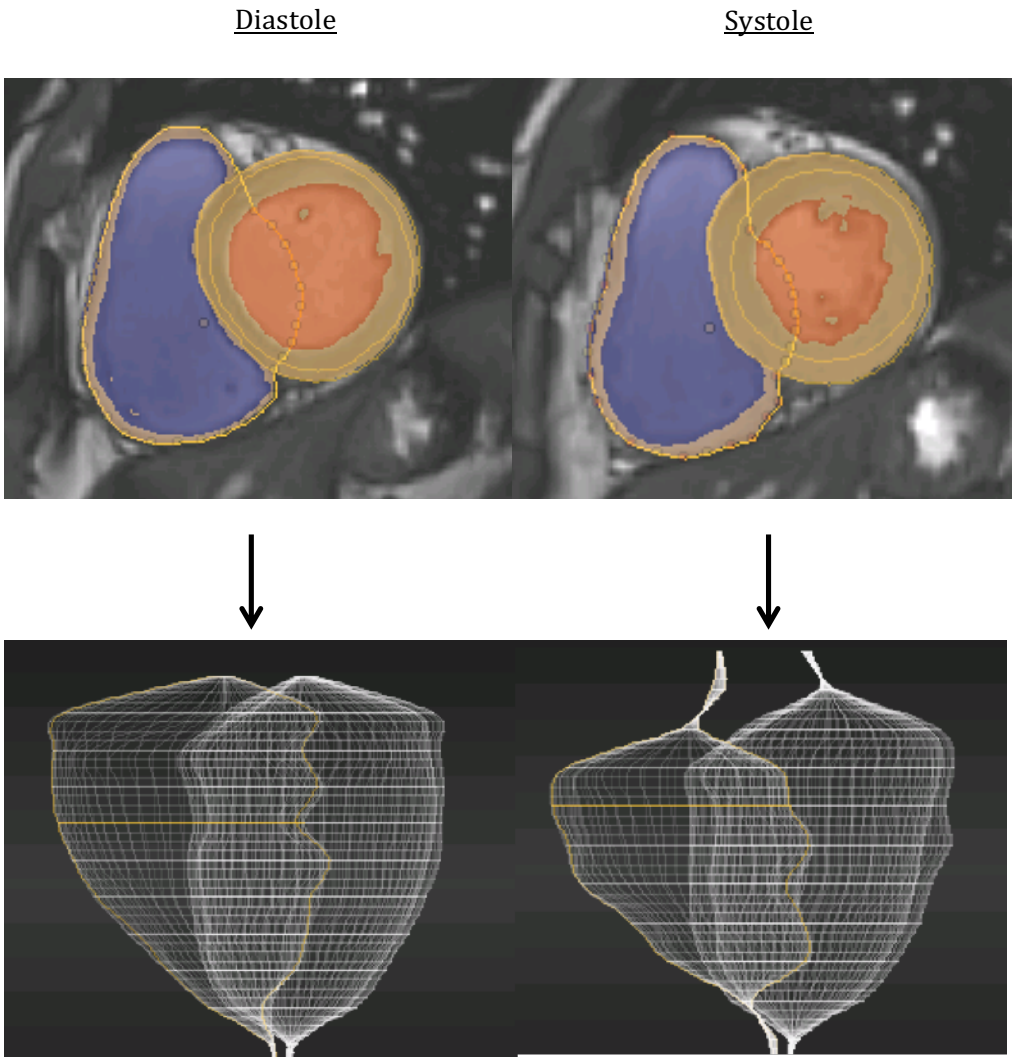

Figure 6.12: Example of volumetric assessment by thresholding. The blood pool is defined in systole and diastole. Full biventricular volumes are calculated by combining contiguous slices. Images obtained from CMR Tools software, (Cardiovascular Imaging Solutions, London, UK).

6.7.4: Late Gadolinium Enhancement Imaging

LGE is arguably one of the most important innovations in non-invasive cardiovascular imaging. When injected, gadolinium contrasts agents are extra cellular and unable to cross intact cell membranes. In normal myocardium myocytes are tightly packed, with an estimated extracellular space of around 25-28% therefore leaving minimal space for gadolinium accumulation (40).

However, in the early stages of infarction, the integrity of myocyte cell membranes is lost and gadolinium collects within the intracellular space. In established infarcts or myocardial scars myocytes are replaced by collagenous fibrosis, expanding the extracellular space, resulting in a high gadolinium concentration figure (6.13)(310).

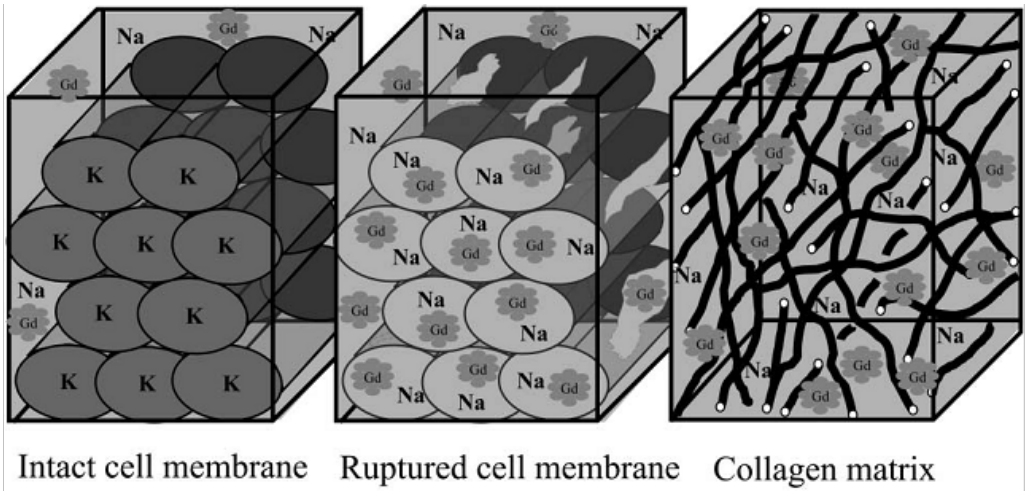

Figure 6.13: Following gadolinium injection voxels imaging healthy myocardium are packed tightly with myocytes resulting in low gadolinium concentration. Following acute infarction cell membranes become permeable and gadolinium becomes concentrated intracellularly. In regions of replacement fibrosis myocytes are replaced with collagen thereby expanding the extracellular space and permitting a high gadolinium concentration (310).

High concentrations of gadolinium lead to a pronounced shortening of regional T1. In combination with T1 weighted inversion recovery sequences, gadolinium enhancement is therefore an effective diagnostic tool for acute infarction and replacement fibrosis (178, 311). Contrast with healthy myocardium can be optimised by timing data acquisition (TI) to coincide with when healthy myocardium is passing through the null point. In light of the poor vascularity of infarcted and fibrotic regions, sufficient time (~15 mins) must also be allowed for gadolinium to disperse, hence the name LGE. Characteristic patterns of LGE are now recognised in a number of conditions including HCM, dilated cardiomyopathy and amyloid (312) (figure 6.14). As a result LGE imaging is now a standard in routine clinical examinations.

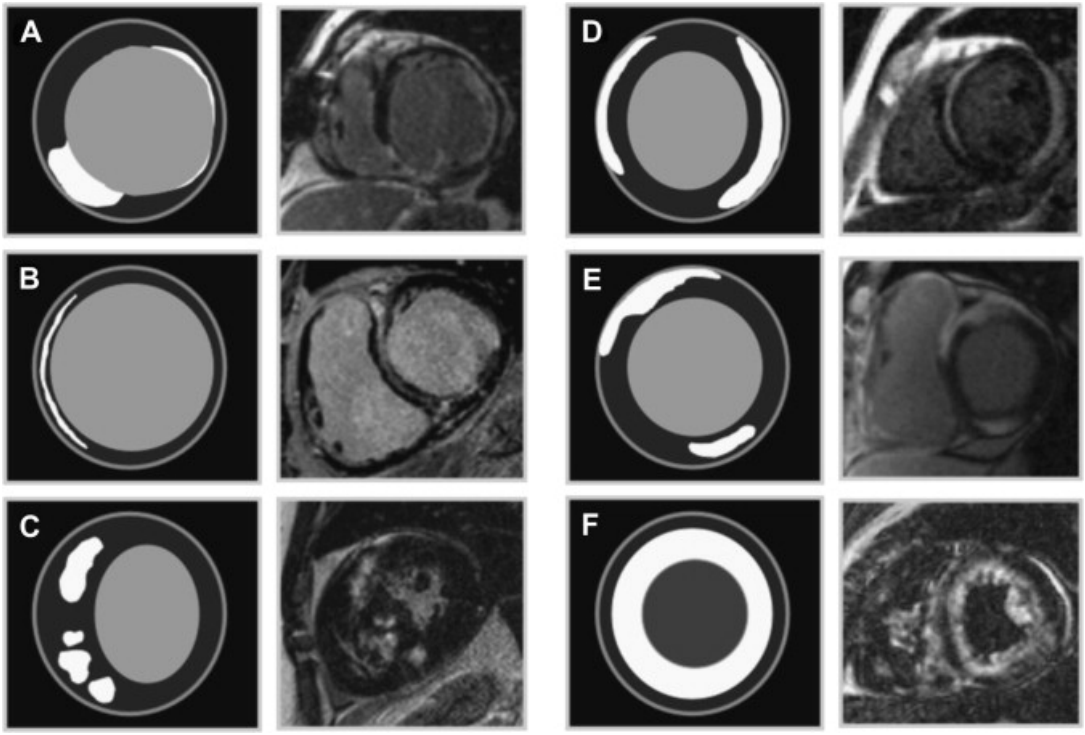

Figure 6.14: Characteristic patterns of late gadolinium enhancement. A) Transmural inferoseptal and subendocardial lateral wall enhancement due to myocardial infarction. B) Dilated cardiomyopathy with midwall enhancement of the interventricular septum. C) Hypertrophic cardiomyopathy with patchy enhancement within of the hypertrophied septum. D) Subepicardial enhancement of the lateral wall and mid wall enhancement of the interventricular septum following viral myocarditis. E) Dense subepicardial enhancement of the anteroseptal and inferior walls due to sarcoid infiltration. Additional enhancement of the right ventricular myocardium. F) Diffuse global, subendocardial enhancement of both the left and the right ventricle combined with nulling of the blood pool characteristic of amyloidosis (312).

6.7.5: T1 Mapping and Extracellular Volume Quantification

In recent years a wealth of research has analysed the relation between voxel-wise T1 and myocardial disease processes. LGE permits qualitative visual assessment of regional myocardial replacement fibrosis, however the technique is less useful for the detection of diffuse fibrosis as gadolinium concentrations are relatively low. Highly sensitive T1 weighted sequences which combine multiple inversion pulses, such as Modified Look Locker Inversion recovery (MOLLI) and Shortened MOLLI (shMOLLI), can be used to quantify voxel-wise T1 values. These values can be visually represented as a myocardial map with colour coding according to the T1 value. Following injection of gadolinium, myocardial T1 values will fall in direct proportion to the degree of diffuse myocardial fibrosis i.e. extracellular volume expansion. Native and post contrast T1 maps can therefore be compared to quantify the extracellular volume (ECV). ECV is elevated

in chronic aortic stenosis (215), cardiac amyloidosis and to a lesser degree in HCM and dilated cardiomyopathy (313). Further work is required to establish the link between diffuse fibrosis and clinical outcomes.

6.8: 3 Tesla Cardiovascular Magnetic Resonance

6.8.1: Introduction

3Tesla scanners have been approved for whole body scanning by the Food and Drug Administration since 2001. The advantages of high field scanning have been realised in relation to cerebrovascular imaging, where 3Tesla scanners are commonplace. However, the uptake of 3Tesla CMR scanners has been slower in light of technical difficulties specific to cardiovascular imaging. The following is a review of the advantages and disadvantages of 3Tesla CMR (314-316).

6.8.2: Advantages

6.8.2.1: Greater Signal to Noise Ratio

At 3Tesla the increase in B_0 increases the net magnetisation, which lead to a theoretical two-fold increase in SNR compared to 1.5Tesla. Greater SNR increases voxel-wise signal intensity, improving the ability to differentiate between adjacent tissues. This can also translate to greater resolution as voxel size can be reduced whilst maintaining 1.5Tesla SNR. Techniques operating with low SNR at 1.5T stand to benefit the greatest from 3Tesla. Perfusion imaging is one example which requires a short acquisition time and low spatio-temporal resolution. The improved resolution afforded by 3Tesla is associated with reduced dark ring artefacts (317) and greater diagnostic accuracy of significant coronary stenoses (317). Parallel imaging is another low SNR technique, with signal loss in proportion to the reduction factor; 3Tesla therefore improves the feasibility of this technique with resulting savings in acquisition time. SNR gains also open the door to novel techniques with inherently poor SNR which have been impractical at 1.5Tesla. The

most noteworthy are diffusion tensor and diffusion weighted CMR, where 3Tesla has brought renewed interest and a rapid increase in published research (19, 150, 318, 319).

6.8.2.2: Increased Larmor Frequency

The resonant frequency increases linearly with increasing field strength. Frequency separation is therefore greater between proton containing compounds such as fat and water. This improves the specificity of fat saturation pulses with less cross suppression of water. Greater separation also translates to greater dispersion of spectral peaks, which combined with enhanced resolution, has improved the feasibility of CMR spectroscopy (320).

6.8.2.3: Increased T1 recovery time

At 3Tesla the T1 of most tissues is increased compared to 1.5Tesla, due to greater B_o magnetisation. During tagging sequences, such as SPAMM, this results in decreased tag fading with improvements in strain analysis (321). Following injection of gadolinium, increased separation between myocardial T1 and regional gadolinium enhancement improves delineation of regional replacement fibrosis. Contrast MR angiography also benefits from greater T1 separation with improved suppression of background tissues improved quality imaging (322).

6.8.3: Disadvantages

6.8.3.1: B_o field inhomogeneities

Within the main magnetic field, differences in the magnetic susceptibility between adjacent tissues result in B_o inhomogeneities. Inhomogeneities are most evident in areas with large susceptibility differences, such as lung and myocardium. Field variations increase linearly with field strength and are thus exacerbated at 3Tesla (314, 323). Cine imaging with bSSFP is particularly sensitive to B_o inhomogeneities, which manifest as 'dark band' artefacts. Increasing the TR moves artefacts further away from the field of view, however this is at the expense of SNR (315, 324). The severity of artefacts can be reduced by 'shimming' over the FOV to improve local B_0 homogeneity or by setting a frequency offset to move the dark band out of the FOV (6.15)(325).

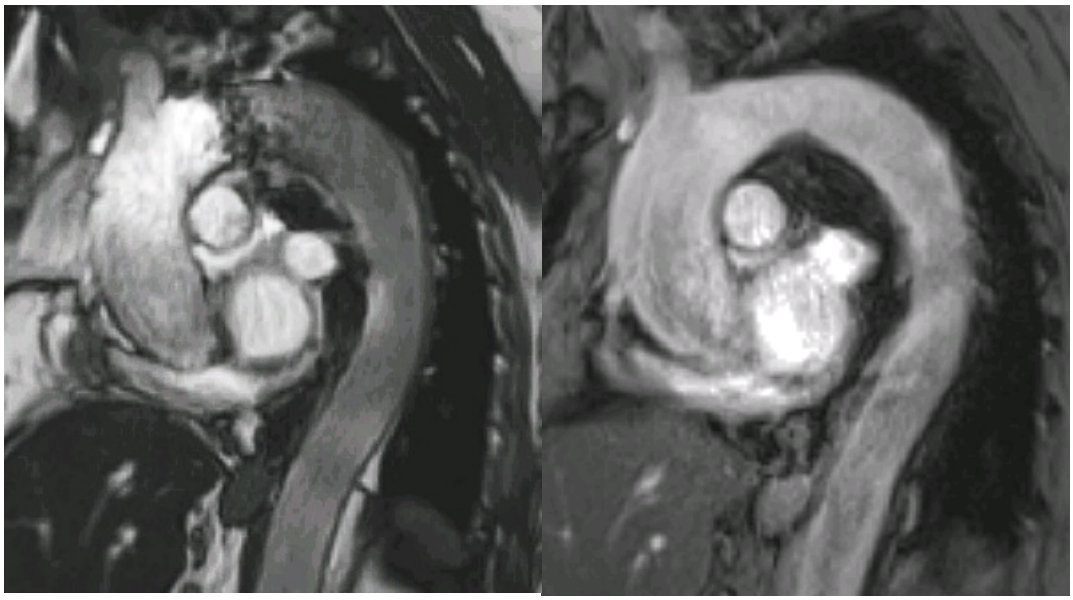

Figure 6.15: bSSFP image of the aorta at 3Tesla. In the initial image a dark band artefact is seen within the middle of the arch, degrading image quality. Image quality is subsequently improved by frequency shimming over the region of interest.

6.8.3.2: Increased Radiofrequency Power

RF pulses induce small electric currents as a result of energy absorption; this is referred to as the specific absorption rate (SAR). SAR rises in direct proportion the RF power and safe limits are set for SAR to protect the patient against injury as a result of excessive heating. At 3Tesla the frequency of the RF pulse increases as a direct consequence of the increase in B_o. As the frequency increases the power required to deliver a given flip angle increases by the square of the increase in B_0 therefore, for a given sequence, the SAR will be increased by four fold at 3Tesla compared to 1.5Tesla (314, 326). Sequences with large flip angles (≥90°) i.e. spin echo, and sequences with rapid sequential pulses i.e. bSSFP, may therefore have to be modified to ensure safe SAR limits are not exceeded. Modifications include reducing the flip angle and are at the expense of SNR.

Over the years, a wealth of knowledge and experience of operating at 3Tesla has improved confidence in reducing artefacts and mitigating SAR increments. Consequently the advantages of high field imaging are being increasingly realised, with a steady rise in the number of 3Tesla CMR scanners. At the Royal Brompton Hospital we are exploring the opportunities afforded by 3Tesla CMR in the interrogation of myocardial structural-functional relationships in health and disease. The following chapter discusses the basics of cardiac diffusion tensor imaging, its clinical applications and studies to date.

CHAPTER 7: CARDIOVASCULAR DIFFUSION TENSOR IMAGING

7.1: Introduction

Conventional CMR techniques build image contrast based on T1 and T2 relaxation times, with tissue contrast unsurpassed by other imaging modalities. However current CMR techniques provide little information regarding the architectural arrangement and dynamics of sub-voxel structures. In vivo cardiovascular diffusion tensor magnetic resonance imaging (cDTI) is an advanced technique with the potential for novel characterisation of myocardial microarchitecture. This chapter discusses the basic principles of diffusion tensor imaging, validation in myocardium, contemporary clinical applications, and in vivo cDTI sequences.

7.2: Diffusion

Diffusion describes the random movement, or walk, of particles in a liquid or gas. This arises from multiple collisions between atoms or molecules and is also referred to as Brownian motion, after Robert Brown, who has been credited with its description. Brown was a botanist who reported the phenomenon in 1827 in relation to the microscopic fluctuations of pollen grains trapped in water (figure 7.1) (327). In the early 20th century Einstein independently described Brownian motion and provided the link between the observed motion and the presence of atoms.

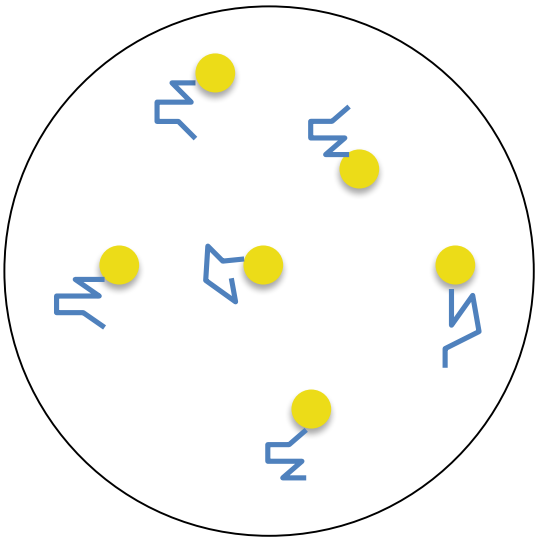

Figure 7.1: Illustration of Brown's early description of diffusion: Pollen grains display random fluctuations in water.

7.2.1: Diffusion Displacement

Einstein recognised that it was impossible to predict the trajectory of an individual particle, but the average 'displacement' of a sufficiently large number of diffusing particles could be calculated. He deduced that the square of the average displacement is proportional to the time given for diffusion and the 'diffusion coefficient' of the medium (328, 329):

$$(X^2) = q_i t D$$

Where (X^2) is the average square of the distance travelled, q_i is a numerical constant dependent on the number of dimensions (2 for 1 dimension, 4 for 2 dimensions and 6 for 3 dimensions), t is time and D is the diffusion coefficient. The diffusion coefficient quantifies the freedom of a particle to diffuse and is dependent on the size of the particle, the viscosity of the solvent and temperature. For example, the diffusion coefficient of water in water (the self-diffusion coefficient) at 25° is $2.3 \times 10^{-3} mm^2/sec$ (330). Thus, based on the equation, the greater the diffusion coefficient the greater the probability that the particles will have displaced from their starting point.

7.2.2: Free (Gaussian) Diffusion

When molecules are free to diffuse, the displacements form a Gaussian distribution, where zero is the peak, and the probability of diffusing a given distance is the same in all directions (figure 7.2) (328):

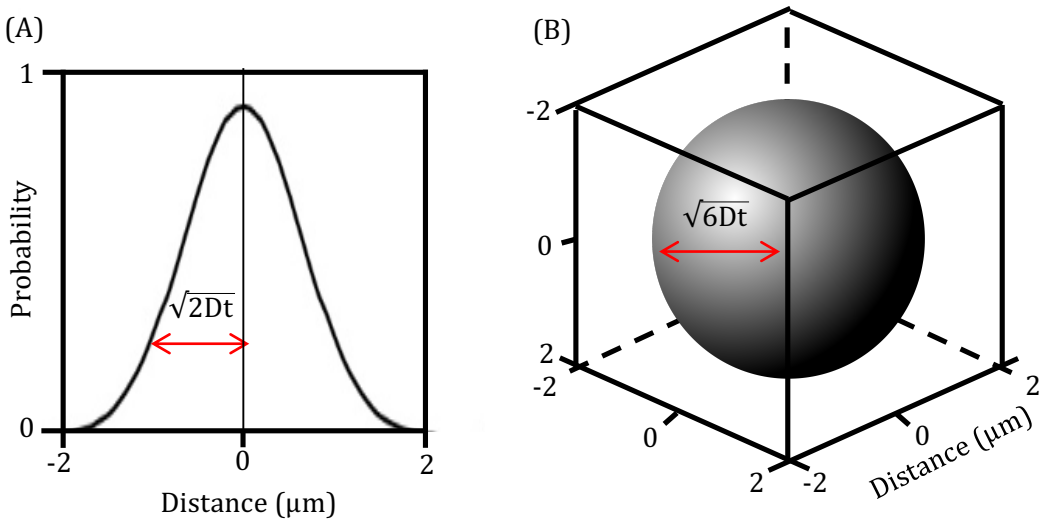

Figure 7.2: Representation of free diffusion displacement in: A) One dimension: The peak diffusion probability is zero and the distribution of displacement probability is Gaussian, calculated by $\sqrt{2Dt}$. B) Three dimensions: The probability of displacement is equal in all directions and the root mean square is spherical, calculated by $\sqrt{6Dt}$ (328).

In the case of a cube of free water at 25°, the mean square of displacement in a given direction, over 100msec, is 20µm (i.e. the sphere has a radius of 20µm) (329).

7.2.3: In Vivo Diffusion – Apparent Diffusion Coefficient

Unlike free water, at the cellular level, diffusion of in vivo water is limited by the local cell architecture. Within biological tissues diffusion behaviour can be modulated by three broad mechanisms (figure 7.3) (328, 331):

- **Restriction**: The diffusion of water which is confined to a certain space is under restriction (332). This is the case for intracellular water bound by impermeable cell walls, such that diffusion becomes a function of the cell geometry.

- **Hindrance**: Diffusion within the extracellular space is impeded by cell walls and other tissue structures. In contrast to restricted diffusion there are no boundaries, however diffusion is slower in comparison to free diffusion as it has to navigate fixed obstacles.
- **Barriers**: Diffusion from the extracellular to the intracellular space occurs across permeable cell membranes. Diffusion is slowed as it traverses the membranes which act as porous barriers.

Within biological tissues the diffusion of water is therefore less that than self-diffusion coefficient. The root mean square of diffusion is tissue specific and a direct function of the tissue architecture; this is referred to the apparent diffusion coefficient (ADC) (329).

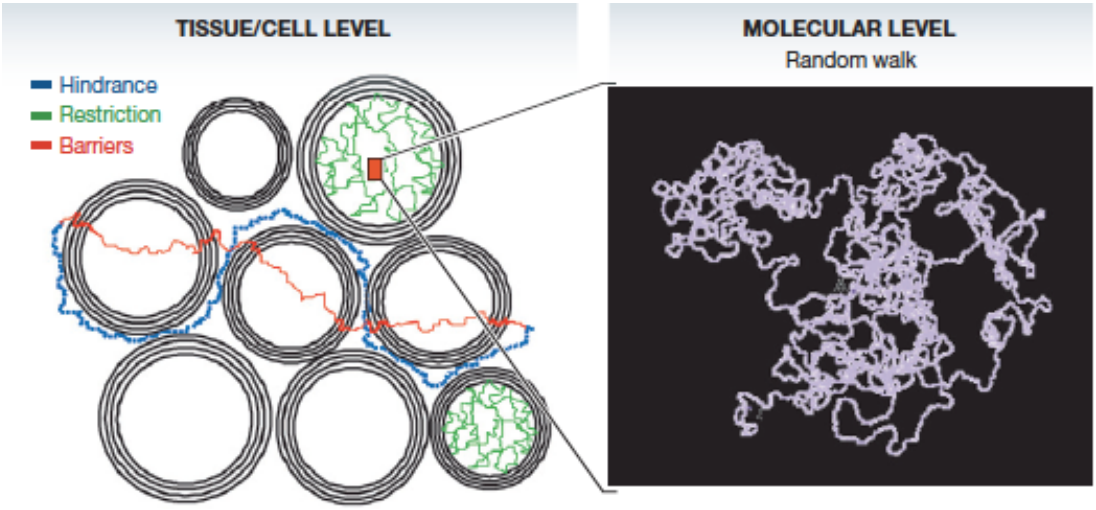

Figure 7.3: Illustration of diffusion modulation at the cellular level occurring due to hindrance, restriction and cell barriers. In comparison molecular level diffusion displays a random walk due to collisions with atoms and molecules (331).

7.3: Diffusion Weighted Magnetic Resonance Imaging

7.3.1: History of sequence development

In 1950 Hahn developed the spin echo MRI sequence. During the initial work with this sequence he observed MRI signal attenuation which he attributed to dephasing protons as a consequence of diffusion (333). Carr and Purcell subsequently proposed that the spin echo sequence could be further sensitized to diffusion (334). They deduced that the addition of a high magnitude gradient

could generate sufficient phase changes, between adjacent protons, such that water diffusion was encoded into the sequence. Further development of the diffusion sequence was undertaken by Stejskal & Tanner who devised the format still widely used today (335). They proposed the incorporation of 2 pulsed, high magnitude diffusion sensitising gradients. The first gradient is described as the 'diffusion winding' gradient and is applied after the initial 90° pulse that introduces a linear phase offset. The signal is then refocused by the spin echo 180° pulse, following which the second diffusion 'unwinding' gradient is applied with same magnitude as the winding gradient. In the case of stationary protons, they will receive both the winding and unwinding gradients, with return to phase coherence and no effect on the signal magnitude (figure 7.4.1). However, randomly diffusing protons will receive the initial winding gradient, but will have displaced by the time of the unwinding gradient and will therefore experience a difference amount of phase unwinding. This results in incomplete cancellation of the initial phase offset, with loss of phase coherence. When the phase of the many protons present within an imaging voxel is averaged, the differing phases, due to different displacements, of the randomly diffusing water molecules results in signal cancellation and attenuation of the MR signal. Proton diffusion is therefore detected as a signal loss (figure 7.4.2).

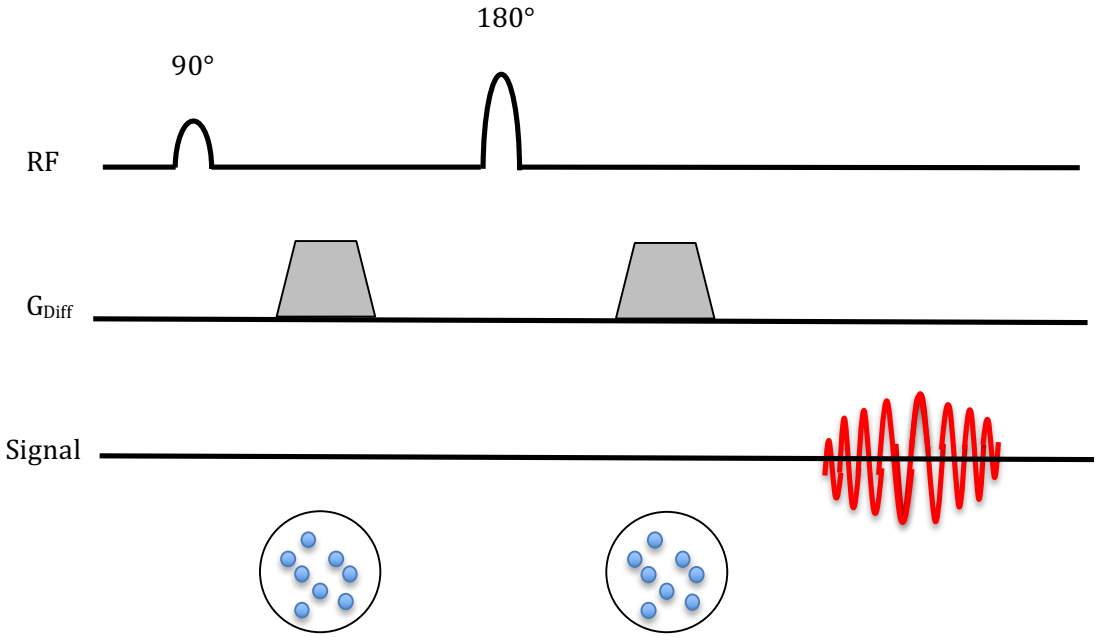

Figure 7.4.1: Spin echo sequence with application of diffusion sensitizing gradients. In the case of stationery water, protons receive both the winding and unwinding gradients with no modulation of the emitted signal

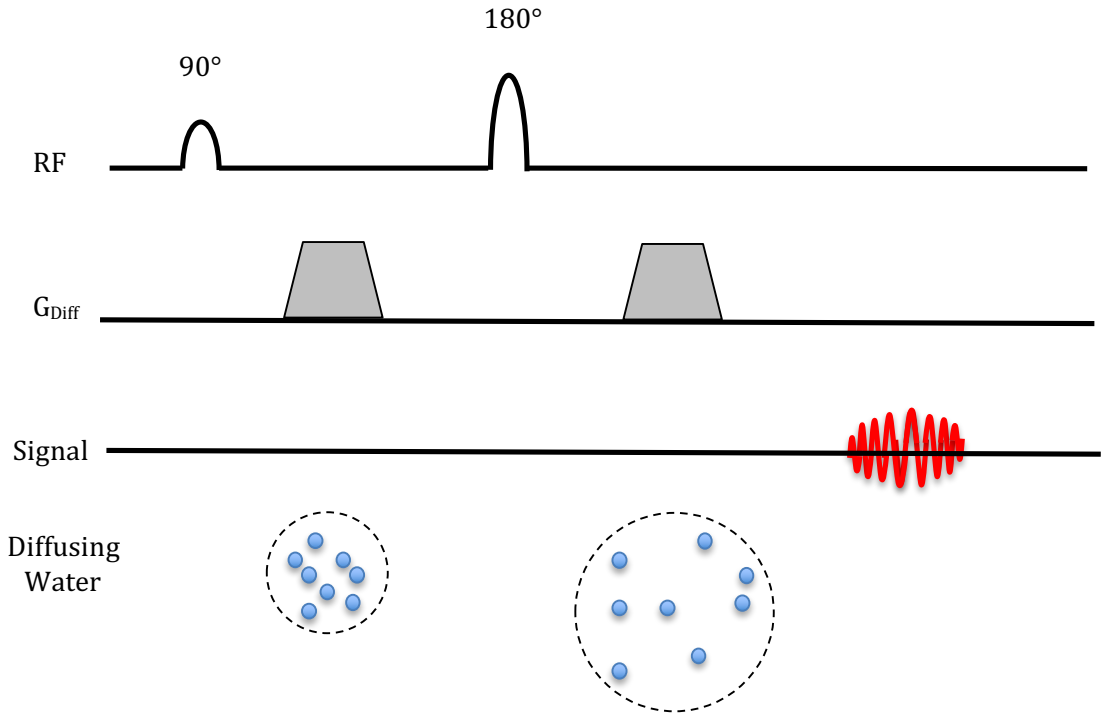

Figure 7.4.2: Spin echo sequence with application of diffusion sensitizing gradients. In the case of diffusing water, protons receive the winding gradients but have displaced by the time of the unwinding gradient, as a result the CMR signal is attenuated by an amount determined by the distance diffused by the water molecules.

7.3.2: Diffusion Weighting – the 'b valve'

The diffusion sensitivity of a given sequence is related to strength and timing of the diffusion sensitizing gradients (winding and unwinding). The degree of diffusion weighting is referred to as the 'b value' or 'b factor' after Dennis Le Bihan, who sought to differentiate diffusion gradient terminology from that of traditional imaging gradient pulses (329). The b value is approximately defined by the following equation (335):

$$b = (\gamma G \delta)^2(\Delta - \delta/3)$$

Where γ is the gyromagnetic ratio, G is the gradient magnitude, δ is the duration of the gradient pulse and Δ is the time between winding and unwinding pulses, the b value is typically measured in units of s/mm^2 (figure 7.5). The optimal b value is dependent on a number of factors including the MR field strength and the composition of the imaged structure, with typical in vivo values ranging from 0-1000s/mm^2.

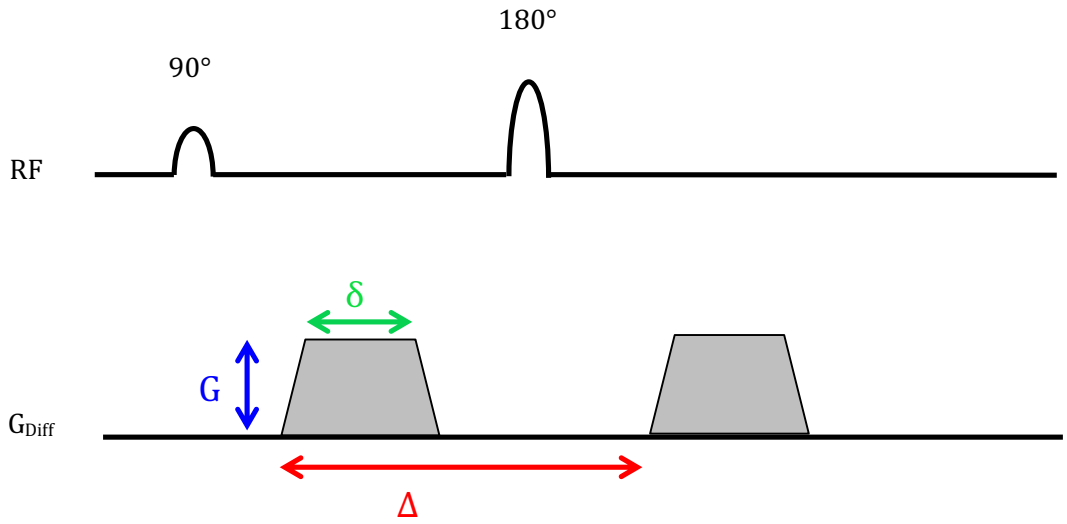

Figure 7.5: Illustration depicting the parameters used in calculating the diffusion weighting of a sequence, known as the b value. As described in the equation above, the diffusion weighting is directly related to the magnitude, of the gradient pulses (G), the duration of the pulses (δ) and the length of time between the winding and unwinding gradients (Δ).

7.3.3: The Diffusion Equation

In order to quantify diffusion a minimum of 2 MR signals are required (328, 335). The first is the diffusion attenuated MR signal (S) resulting from a diffusion sensitised spin echo sequence, the second is the baseline signal without the addition of diffusion sensitive gradients (S_0). The relationship between the signals is defined by (335):

$$\frac{S}{S_o} = \exp^{(-b.ADC)}$$

Where b is the b value, or diffusion weighting of the sequence, and ADC is the apparent diffusion coefficient. Hence there is an exponential relationship between the diffusion signal and the ADC. By rearranging the equation the tissue specific intra-voxel ADC can therefore be derived by from the S_o and S images as follows:

$$ADC = \frac{\log (S_0/S)}{b}$$

7.3.4: Contemporary Clinical Applications

The ADC is a direct function of the cellular environment, it is therefore hypothesised that early pathological changes may be detected through alterations in ADC.

7.3.4.1: Acute Stroke: Diffusion Weighted v Perfusion Weighted Imaging

The potential for enhanced tissue characterisation from diffusion-weighted imaging was first realised in cerebral imaging. In the 1980s Denis Le Bihan had the idea of mapping local ADC measures as a method of providing additional MRI contrast (331). In 1990 Moseley et al. reported a marked reduction in molecular diffusion within the ischaemic cerebrum of cats (336). This arises from disruption of cell membrane Na^+/K^+ homeostasis leading to cytotoxic oedema and

diffusion restriction (low ADC) (336). Interest in diffusion imaging therefore grew, and around the same time Le Bihan moved to the National Institute of Health in Bethesda where he encountered Robert Turner, an Echo Planar Imaging (EPI) expert. The addition of EPI to diffusion imaging sequences markedly reduced both imaging time and movement artefacts, thereby establishing a clinically feasible imaging protocol (337). Diffusion weighted MRI was consequently propelled from research status to potential diagnostic tool, as subsequent in vivo imaging in acute stroke patients confirmed Moseley et al.'s animal work, with hyper-intense signal in diffusion weighted imaging from areas of acute infarction due to diffusion restriction (331). This technical development of this protocol coincided with the event of a novel drug treatment for stroke called recombinant tissue plasminogen activator (rtPA), which offered the potential to prevent the debilitating effects of stroke by dissolving vessel occluding thrombus. Diffusion weighted imaging (DWI) was thus combined with perfusion weighted imaging (PWI) to define the region of PWI-DWI mismatch, known as the penumbra. The penumbra is the area of cerebrum which is ischaemic, but not yet infarcted, and thus potentially salvageable by rtPA (figure 7.6).

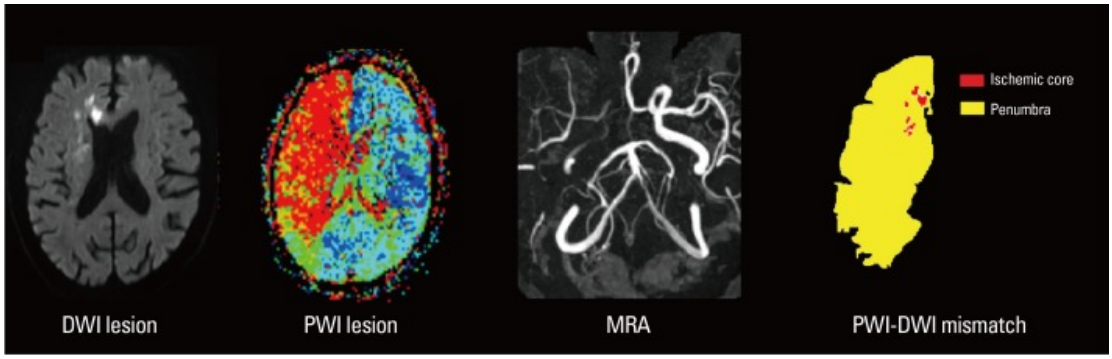

Figure 7.6: PWI-DWI mismatch: The DWI image identifies the area of the cerebrum already infarcted as a hyper-intense lesion. PWI highlights the total area of ischaemic cerebrum at risk of infarction. An MR angiogram (MRA) identifies the occluded vessel – the middle cerebral artery. By quantifying the PWI-DWI mismatch the area of potentially salvageable cerebrum identified (331).

7.4: Diffusion Tensor Magnetic Resonance Imaging

7.4.1: History of Sequence Development

In 1990, while working on diffusion weighted neuronal imaging, Moseley et al. observed variation in the received image according to the orientation of the diffusion-weighted gradient (338). Diffusion weighted images are acquired from gradients applied in a single direction, however the importance of gradient orientation had not previously been considered. Cortical and subcortical grey matter showed minimal signal variation with changing direction, however white matter of both the cerebrum and spinal chord displayed significant directional dependence. When the diffusion-sensitizing gradient was applied in parallel to the white matter, signal loss was greater in comparison to a gradient applied perpendicularly. This property was attributed to the linearity of the white matter neurons, also referred to anisotropy.

7.4.2: Isotropic v Anisotropic Diffusion

Isotropic is term used to describe the diffusion of free water, which is unrestricted and unhindered. The term is derived from the Greek isos (equal) and tropos (way), meaning uniform in all directions i.e. spherical. However, when water is diffusing through a linear cell type, such as a neurone or myocyte, diffusion occurs maximally along the long axis of the cell, and least along its short axis. This is the opposite of isotropy and is therefore defined as anisotropic (figure 7.7).

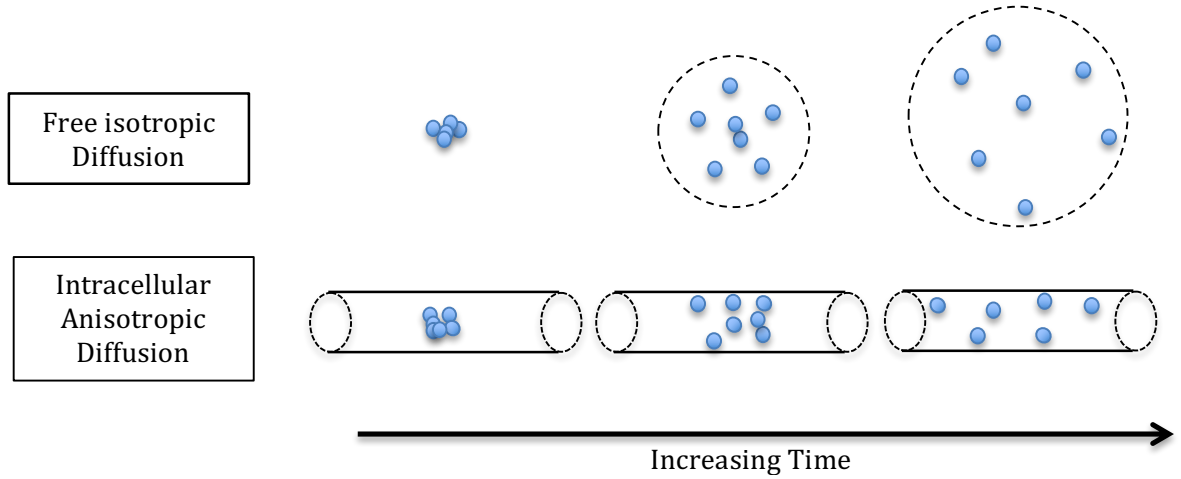

Figure 7.7: Free diffusion is unrestricted and lacks direction, this thus isotropic. Intracellular diffusion is restricted along the short axis of the cell greater than the long axis and is therefore anisotropic.

7.4.3: The Diffusion Tensor Model

Given the directional dependence of signal from anisotropic tissue tyoes, unidirectional diffusion imaging is insufficient to accurately characterise the ADC. The more ordered the tissue is the more the measured ADC will depend on the direction of the diffusion-sensitizing gradient. Le Bihan's group recognised that this directional dependency could also be exploited to determine the orientation of neurones within the brain, with the direction of greatest diffusion coinciding with the cell long axis (339). To acquire directional information a more complex method is therefore required to characterise diffusion within each voxel. Assuming Gaussian diffusion, simple anisotropic diffusion can be described by the diffusion tensor (328, 340). This is a symmetric matrix of numbers which for 2D diffusion has 2x2 elements and for 3D diffusion has 3x3 elements:

$$\mathbf{ADC} = \begin{bmatrix} D_{xx} & D_{xy} & D_{xz} \\ D_{xy} & D_{yy} & D_{yz} \\ D_{xz} & D_{yz} & D_{zz} \end{bmatrix}$$

7.4.3.1: Diagonal Tensor Components

The diagonal components of the above tensor matrix (D_{xx}, D_{yy} and D_{zz}) correspond with the displacements along the three orthogonal MRI scanner axes (x,y and z). D_{xx}, D_{yy} and D_{zz} are always positive, as diffusion is never stationary, and the ADC is always positive. Assuming only passive processes contribute to the measured diffusion, the maximum possible value for each diagonal component is the self-coefficient of water and the minimum is always 0. The sum of the three diagonal elements reflects the total diffusivity of the tensor multiplied by 3 (328, 341).

7.4.3.2: Off Diagonal Tensor Components

In contrast the off diagonal components, e.g. D_{xy}, reflect the correlation (covariance) of displacements between those axes i.e. x and y, rather than a direct measurement of diffusion along that axis. All off diagonal elements are always smaller than the largest diagonal element. The presence of correlation between axes corresponds with a non-zero value for the corresponding tensor component. If all the off diagonal components are zero, then the principle direction of diffusion is either aligned with one of the orthogonal axes, or diffusion is isotropic. Perfect correlation between axial displacements, implies that diffusion is greatest at 45° to both axes (figure 7.8).

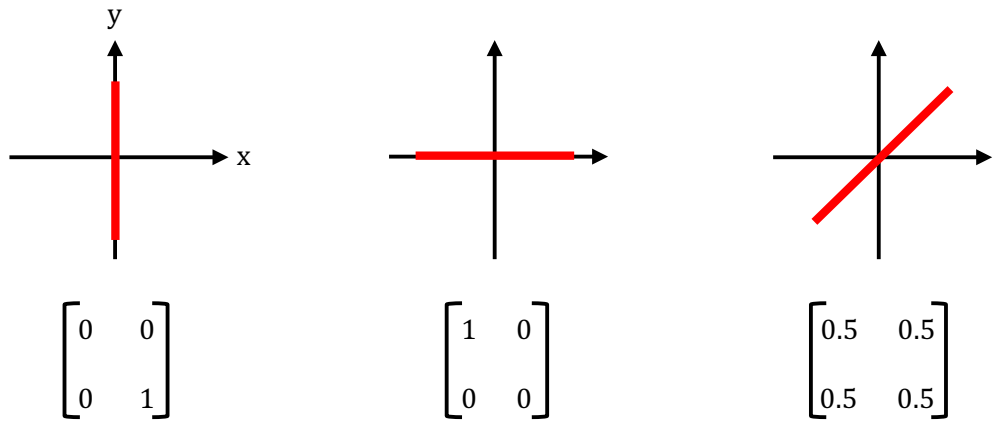

Figure 7.8: Representation of diffusion in 2 dimensions derived from a 2x2 tensor. If there is one unit of diffusion solely located along the y-axis then Dyy=1 and the other axes =0. If there is one unit of diffusion solely located along the x-axis then Dxx=1 and other axes =0. If there is one unit of diffusion equidistant from both the x and y-axis (45°) then all coordinates =0.5. Adapted from Kingsley et al.(341).

7.4.3.3: Solving the Diffusion Tensor

Le Bihan and colleagues illustrated that a series of diffusion-weighted images can be used to calculate the diffusion tensor (328, 340). The tensor model assumes that diffusion is Gaussian and is thus symmetrical with identical elements above and below the diagonal. The tensor therefore contains 6 unknown elements:

$$\begin{bmatrix} D_{xx} & D_{xy} & D_{xz} \\ D_{xy} & D_{yy} & D_{yz} \\ D_{xz} & D_{yz} & D_{zz} \end{bmatrix}$$

As *n* simultaneous equations are required to solve *n* unknown variables, a minimum of six diffusion-weighted images (plus six non-diffusion-weighted images) are required, in non-collinear and co-planar directions, to solve a 3x3 tensor. The degree off diffusion-weighted signal attenuation in a given direction is proportional to the diffusivity. The diffusion tensor is then estimated from log transformed diffusion-weighted signals using linear regression.

7.4.4: The Diffusion Tensor Ellipsoid

When 3-dimensional diffusion is isotropic (all off diagonal tensor elements are zero) the diffusion within that voxel can be represented graphically with a sphere. For anisotropic diffusion the equivalent graphic forms an ellipsoid, reflecting the fact that diffusion has a dominant direction (figure 7.9).

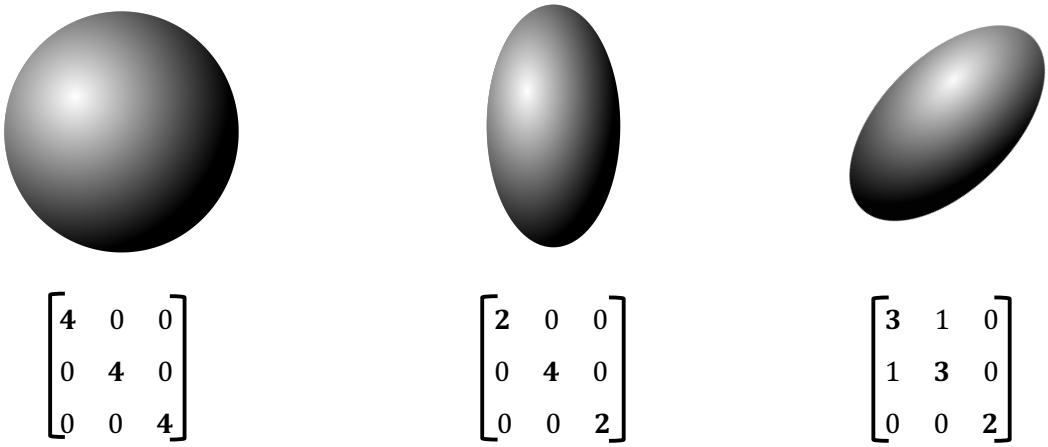

Figure 7.9: Graphic representation of diffusion in 3D (arbitrary units). For isotropic diffusion all diagonal elements are equal and all off diagonal elements are zero. In the case of anisotropic diffusion, where the principle diffusion direction is aligned with the y-axis, all off diagonal elements are zero and D_{yy} is greater than D_{xx} and D_{zz}. When diffusion is greatest along the xy axis, D_{xy}=1, D_{xx}=D_{yy} and D_{zz} < D_{xx} and D_{yy}.

7.4.5: The Eigensystem

The shape and orientation of each diffusion ellipsoid is defined by a reference frame called the 'eigensystem'. Within this system 3 orthogonal ellipsoid axes are defined by the eigenvectors: ε_1 ε_2 and ε_3. The magnitude, or length of each vector represents the squared distance diffused within a given time, t and is defined by the corresponding eigenvalue: λ_1, λ_2 and λ_3, where λ_1 has the greatest magnitude and λ_3 the least. As diffusion displacement distance is proportional to the square root of the diffusivity, the ellipsoid axes are scaled to the square root of the eigenvalues (figure 7.10).

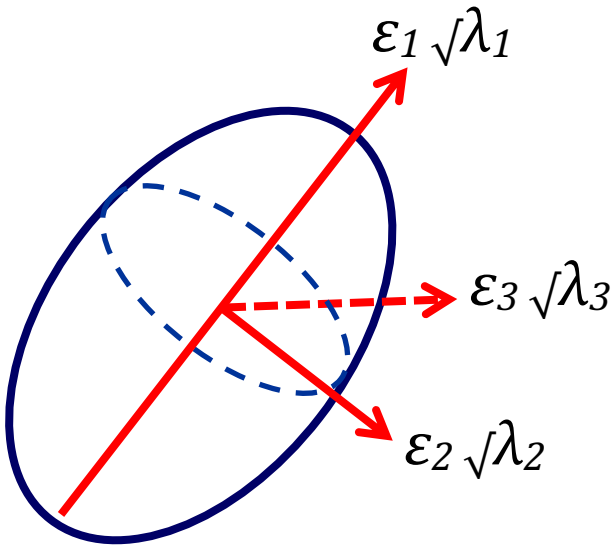

Figure 7.10: Representation of the eigensystem reference frame for the diffusion ellipsoid. The orientation of the ellipsoid is represented by the vectors ε_1 to ε_3. The magnitude of each vector is represented by the corresponding eigenvalue where λ_1 is the greatest and λ_3 the least. The shape of the ellipsoid is scaled to the diffusion distance along each eigenvector, which is equal to the square root of the eigenvalues.

7.4.6: Diffusion Tensor Imaging Parameters & Clinical Applications

From the eigensystem a number of quantitative parameters can be derived which permit novel tissue characterisation.

7.4.6.1: Mean Diffusivity (ADC)

The diffusivity of a substance can be quantified with a number of parameters. In vivo the intra-voxel ADC, or mean diffusivity (MD) (mm^2/s), is calculated from the sum of the eigenvalues divided by 3:

$$MD\ (ADC) = \frac{\lambda_1 + \lambda_2 + \lambda_3}{3}$$

The MD is higher in less structured, high water content tissues, compared to organised, tissue dense structures (342, 343). The tissue specific MD is affected by a number of pathological processes which affect the water content of tissue, or which alter the degree of diffusion

hindrance, restriction or barrier integrity (344). This includes acute stroke, as previously discussed, where MD is lowered due to diffusion restriction as a consequence of cytotoxic oedema (336). In contrast MD is greater than normal in established cerebral infarcts where tissue integrity is lost (345).

7.4.2.4: Fractional Anisotropy

The degree of diffusion anisotropy within a voxel can be quantified with a number of parameters. The most commonly adopted measure is fractional anisotropy (FA), which measures the fraction of the diffusion tensor that is anisotropic. FA is calculated as follows (328, 346):

$$FA = \sqrt{\frac{3}{2}} \sqrt{\frac{(\lambda_1 - (\lambda))^2 + (\lambda_2 - (\lambda))^2 + (\lambda_3 - (\lambda))^2}{\lambda_1^2 + \lambda_2^2 + \lambda_3^2}}$$

Where (λ) is the MD of the tensor. FA is independent of orientation and being a fraction has a range of 0 to 1, where 0 is completely isotropic and 1 is completely anisotropic (figure 7.11).

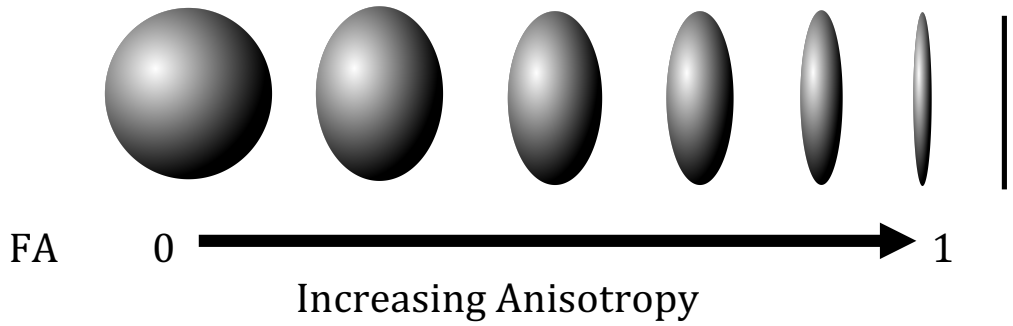

Figure 7.11: Illustration of the shape of the diffusion ellipsoid at increasing FA values. At an FA of zero the ellipsoid is perfectly isotropic. At an FA of 1 the ellipsoid is perfectly linear.

Although FA confers no directional information, it quantifies the degree to which diffusion is directionally dependent. For example, the FA of free water is zero whereas the FA of water

restricted linearly within a straw is closer to 1. In the context of in vivo cerebral imaging, the FA of less structured tissue, such as grey matter, is therefore lower than the FA of more linearly arranged tissue such as white matter (336, 346). Quantitative assessment of white matter anisotropy via FA has been utilized to investigate number of physiological a pathological processes (347). In newborn and premature infants, white matter anisotropy has been demonstrated to increase in line with age related axonal myelination (348). Conversely white matter FA has been shown to decrease in neurodegenerative disease processes such as multiple sclerosis (349), Alzheimer's disease (350) and CADASIL (351). FA therefore has the potential to serve as a novel diagnostic tool.

7.4.2.5: Tensor Orientation – Primary Eigenvector Tractography

DTI has the unique ability to interrogate structural orientation in vivo. In anisotropic cells and tissues, diffusion occurs preferentially along the dominant structural axis or long axis. In DTI acquisitions this corresponds with the largest ellipsoid eigenvector, otherwise known as the primary eigenvector (λ_1) (332, 336, 340, 352). The optimal method for representing primary eigenvector data has been a matter for debate, however the most widely recognised method is tractography (328, 347, 352-355). Tractography aligns the primary eigenvector of adjacent voxels, allowing visualisation of the trajectory of in vivo structures. The primary eigenvector from each voxel is represented, ignoring the secondary and tertiary data; the resulting graphic is therefore a stick. The stick represents the orientation of the primary eigenvector only, ignoring the magnitude, such that the resulting graphic traverses the entire length of the voxel, permitting end-to-end connections with adjacent voxels. A variety of computational methods are employed to generate tractograms, however the overriding principle involves streamlining of adjacent vectors to create smooth pathways (352). In order to project further 3D information into a 2D image, tractograms are colour coded according to their orientation in x,y,z coordinates (356). The

result is visually stunning images which have been particularly successful at illustrating cerebral white matter tract trajectories (figure 7.12)

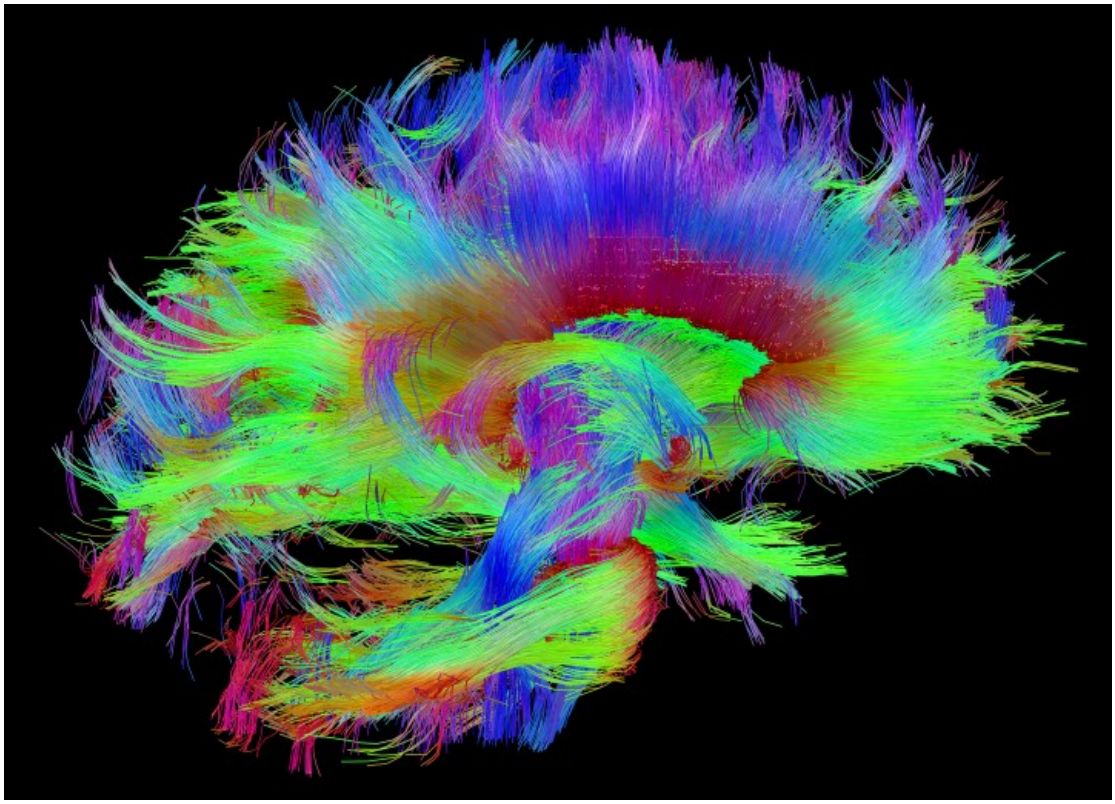

Figure 7.12: Cerebral white matter tractograms from the Human Connectome Project dataset. The image is colour coded by direction: Red, green blue=x, y, z (357).

7.4.2.6: Full Tensor Visualisation – Superquadric Glyphs

In order to improve visualisation and understanding of derived 3D tensor information, each voxel can be represented with an object called a superquadric glyph (358). Like the diffusion ellipsoid the shape of the glyph is dictated by the eigensystem, however the glyph offers better edge definition and visual appreciation of anisotropy. As with tractography glyphs can be colour coded to reflect the orientation of the primary eigenvector or the degree of anisotropy (figure 7.13).

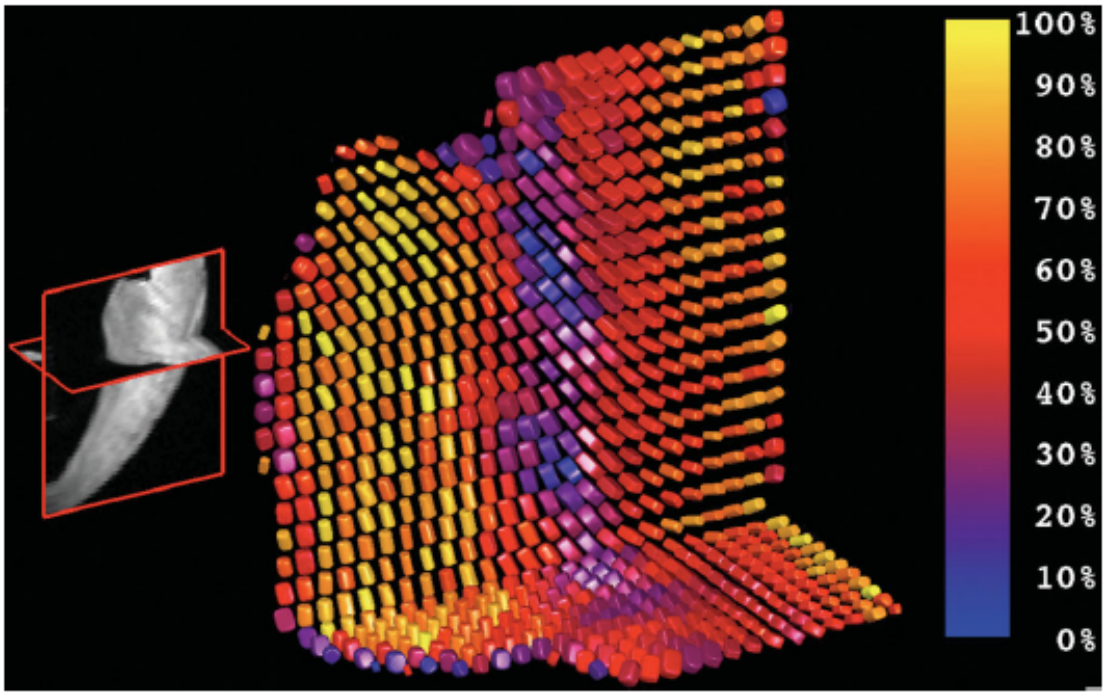

Figure 7.13: A sample of papillary muscle and adjacent myocardium imaged with diffusion tensor imaging. Each voxel is represented by a superquadric glyph which reflects the degree of anisotropy (yellow more anisotropic, blue more orthotropic). Voxels at the edge of the sample (epicardial and endocardial) are comparatively more anisotropic than the mid wall (358).

7.5: Development of Cardiovascular Diffusion Tensor Imaging

7.5.1: History of development

In comparison to cerebral diffusion imaging, in vivo cardiovascular diffusion imaging has been slow in uptake and development due to the significant technical challenges faced. Estimation of myocardial diffusion displacements, on the order of micrometres, is complicated by bulk cardiac motion, on the order of millimetres, arising from cardiac contraction and respiration. In 1994 Edelman et al. developed a sequence protocol capable of mitigating against these issues, which resulted in the first in vivo human diffusion weighted images (359). They acquired images at increasing b values, in 3 orthogonal axes defined by the true cardiac axes. The authors reported marked directional variation in interventricular septal ADC, with lower estimates from gradients applied along the ventricular short axis compared to the long axis. This observation was attributed to the natural anisotropy of the myocardium's helical arrangement (359) (figure 7.14).

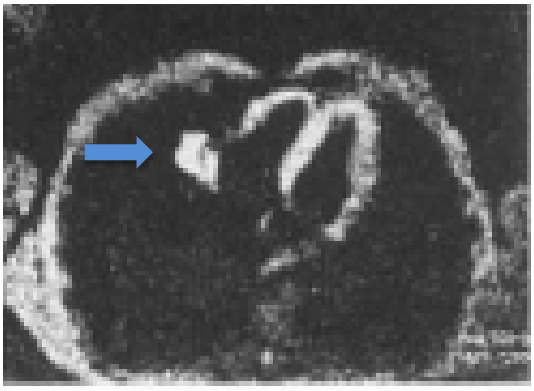

Figure 7.14: First published in vivo diffusion weighted image of the myocardium, (b= 385s/mm^2). ADC map aligned with the ventricular long axis. The volunteer has an incidental pericardial cyst (arrow) which has a higher ADC than the adjacent myocardium (359).

The theory of myocardial diffusion anisotropy was confirmed by Garrido et al. who acquired images in perfused, ex vivo rat hearts (7.15).

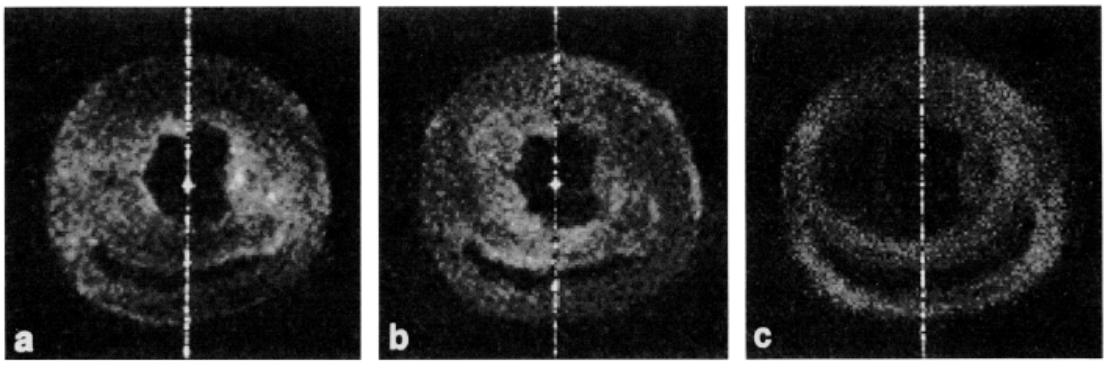

Figure 7.15: Diffusion weighted images of perfused ex vivo rat hearts acquired with sensitising gradients along the x (a), y (b) and z (c) axes. In c, when the gradient is applied along the cardiac long axis both the LV endocardium and epicardiam are dark in keeping with increased diffusion within longitudinally arranged myocytes (141).

7.5.2: Cardiovascular Diffusion Tensor Imaging Histological Validation

7.5.2.1: Primary Eigenvector Angle: The Helix Angle

In 1995 Reese et al. built on the theory of myocardial anisotropy and published the first reconstruction of human in vivo cDTI depicting myocyte orientation (360). They theorised that the dominant diffusion direction, i.e. the primary eigenvector (λ_1), would coincide with the local myocardial fibre orientation. The angle between primary eigenvector and the circumferential myocardial plane was referred to as the helix angle (derivation discussed in Chapter 8: Methods) and compared with Streeter's assessment of transmural fibre orientation (figure 7.16). Although cDTI estimates did not include the relative plateau in angular change at the mid myocardium, both agreed on the progression from positive angles in the endocardium to negative angles in the epicardium (figure 7.16)(360).

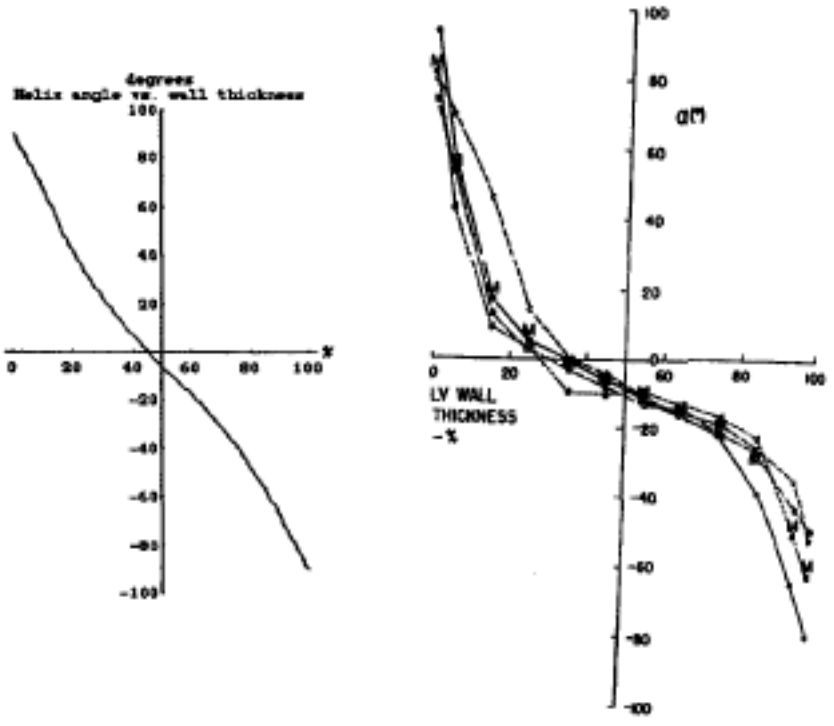

Figure 7.16: On the left is a plot of the primary eigenvector angle, or helix angle, at progressive myocardial depths from the endocardium. In comparison, on the right, is Streeter's assessment of transmural myocardial fibre angulation. Both agree on the progression from positive angles in the endocardium to negative angles in the epicardium, however the cDTI acquisition does not display the same midwall plateau in angle progression (360).

Quantitative agreement between the primary eigenvector and histological myocardial fibre orientation has been demonstrated in canine RV (142), rabbit LV (143, 144) and bovine LV (145). Numerous ex vivo and in vivo cDTI studies have now been performed and each study has provided further confirmation of the gradually progressive helical arrangement of myocytes reported by Pettigrew (5, 7, 13, 19, 59, 85, 92, 142-147, 149, 151, 152, 154, 294, 361-370). Estimates of the helix angle range vary greatly across ex vivo (85, 143, 144, 147, 153) and in vivo cDTI acquisitions (19, 149, 371). Inter-study variation is likely due to differences across species, sequence protocols, acquired resolution and post processing techniques; consequently the optimal method of helix angle quantification remains a matter of debate. Approaches to date have included reporting the transmural range (150); the average angulation per transmural layer (epicardium, endocardium and epicardium) (19); and the transmural helix angle gradient, which is the average radial gradient through the myocardial wall from a best fit linear projection (372). The limitation of the first two techniques is sensitivity to inconsistencies in ROI drawing during post processing, whereas the latter represents data smoothing.

7.5.2.2: Secondary and Tertiary Eigenvectors: Myolaminar Orientations

Cerebral DTI studies have predominantly focused on the primary eigenvector, with secondary and tertiary eigenvector data contributing to the assessment of anisotropy only. In contrast, the secondary and tertiary eigenvectors have been demonstrated to correspond independently with important structural components of the myocardium. In 1998, in rabbit hearts, Scollan et al. observed that secondary and tertiary eigenvector data followed a consistent transmural pattern much like the primary eigenvector (144). They therefore suggested that the non-random orientation of these eigenvectors implied correspondence with an additional level of microstructural organisation, such as myolaminae (144). Corroborating this hypothesis was the similarity between tertiary eigenvector orientation and Le Grice et al.'s depiction of myolaminae (4, 9). In 2003 Tseng et al. validated DTI eigenvector orientation directly against histological cleavage plane in bovine hearts, illustrating correspondence between the sheetlet plane and

sheetlet normal with the secondary and tertiary eigenvectors respectively (145). Subsequently a bimodal population of sheetlets has been demonstrated in canine hearts (in all myocardial regions except the epicardium) (85, 153), murine hearts (373) and rat hearts (13), thereby echoing the histological findings of Arts et al.(8) and Ashikaga et al. (374) (figure 7.17).

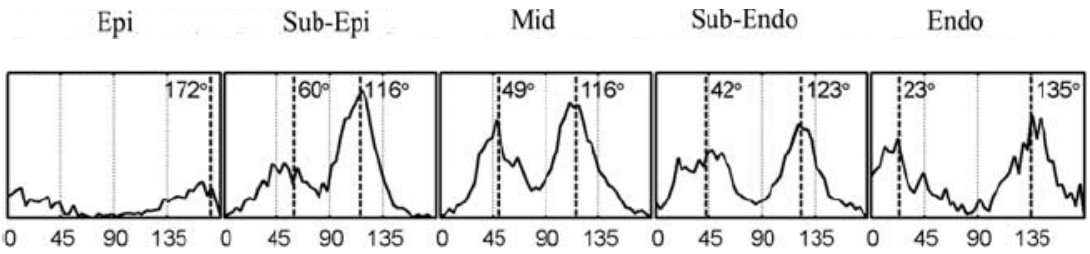

Figure 7.17: Histograms of the tertiary eigenvector intersection angle pooled from 7 canine hearts. With the exception of the immediate epicardial region, each segment of the myocardium demonstrates a bimodal population of sheetlets at approximately 90° to one another (85).

In 2011 Kung et al. performed a detailed histological analysis, combined with DTI validation, demonstrating the presence of two sheetlet populations in ovine hearts (7). The authors attributed prior observations of a single sheetlet population to tissue preparation artefact. They also theorised that both the secondary and tertiary eigenvectors corresponded with orthogonally orientated sheetlet planes. However, in reality, it is unlikely that tissue biology adheres rigidly to orthogonal axes. Sheetlet planes are likely to be more frequently orientated at angles greater and less than 90°. In this situation the resulting secondary eigenvector (ε2) will in fact reflect the midpoint of the acute angle between myolaminar planes and the tertiary eigenvector (ε3) will reflect the midpoint of the obtuse angle between planes (figure 7.18).

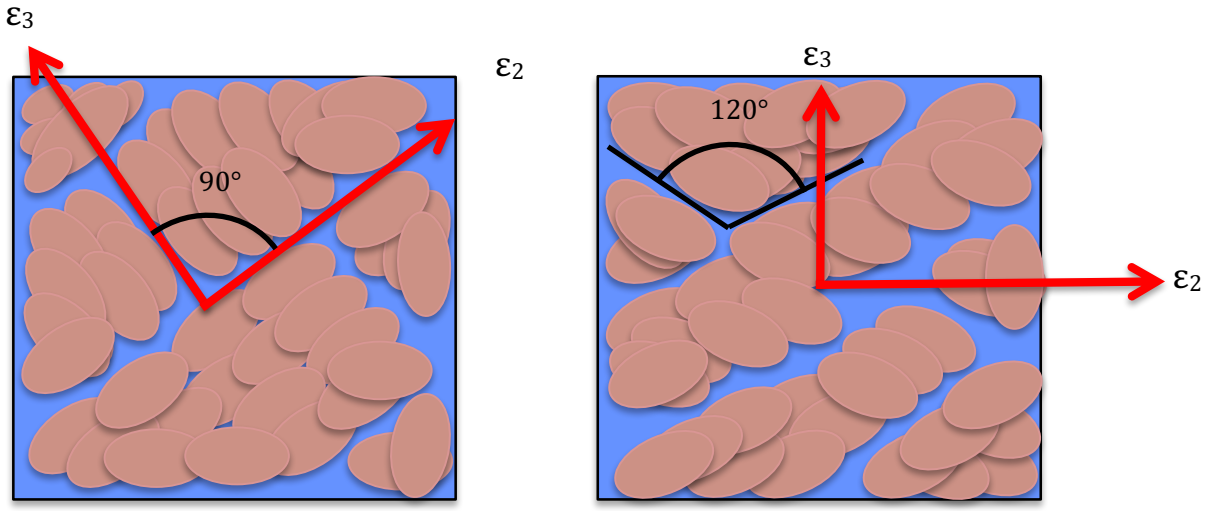

Figure 7.18: Illustration of potential intra-voxel myolaminae orientation. Voxels are represented in 2D and perpendicular to the myocyte long axis i.e. the myolaminar plane. In the first scenario myolaminae are orientated at right angles to one another, diffusion therefore occurs in orthogonal directions and both ε_2 and ε_3 represent histological myolaminar planes. In the second scenario myolaminae are orientated at 120°, diffusion is not orthogonal therefore ε_2 defines the midpoint between the acute angle (60°) and ε_3 the midpoint between obtuse angles.

7.5.3: Review of Cardiovascular Diffusion Tensor Imaging Studies

7.5.3.1: Introduction

Following histological validation of cDTI parameters, subsequent ex vivo studies have applied the technique to gain further insights into myocardial structure and mechanics in health and disease. Early pre-clinical work has focused on in vivo sequence development, which ultimately culminated in the first human clinical cDTI studies.

7.5.3.2: Ex Vivo Cardiovascular Diffusion Tensor Imaging Studies

7.5.3.2.1: Normal Myocardial Architecture and Mechanics

Transmural heterogeneity:

In 2007 Jiang et al. examined transmural anisotropy in sheep myocardium, highlighting that previous studies had assumed scalar quantities (e.g. eigenvalues and FA) were transumural

homogeneous (364). They examined formalin fixed sheep hearts and care was taken during ROI drawing to consistently exclude papillary muscle contributions to subendocardial measures. They reported a constant FA from the epicardium (0.35±0.05) to epi-midwall, (0.35±0.04) followed by a steady decline from the endo-midwall (0.32±0.05) to endocardium (0.27±0.06). This was attributed to an increase in λ_2 and λ_3 and non-significant decrease in λ_1. The decline in FA coincided with the transition to circumferentially orientated fibres, which in the sheep hearts were present in the midwall, and endocardium. They also detected regional variation, with steeper decline in FA in lateral and posterior (inferior) walls (364). The authors related their observations to the work of Le Grice et al., who previously described an increase in the extracellular volume from the epicardium to endocardium, in conjunction with an increase in sheetlets and shear-layers in canine myocardium (4); greater endocardial λ_2 and λ_3 values therefore provide further support for this theory.

Phasic Changes in Myocyte and Sheetlet Orientation:

One of the major strengths of cDTI is its ability to interrogate myocardial structures in different contractile states. This technique has provided the first opportunity to non-invasively investigate the contractile contributions of myocytes and myolaminae, and thus test the theory of myolaminar reorientation. As discussed in chapter 4, both Chen et al. (12) and Hales et al. (13) applied the technique to experiments with rat hearts, chemically arrested in both systolic and diastolic confirmations. Regarding myocyte orientation, Chen et al. reported a shift in myocyte orientation, derived from the primary eigenvector helix angle, towards a more longitudinal orientation in end systole at both the subepicardium (-50±10° to -60±7°) and subendocardium (47±9° to 65±10°) (figure 7.19).

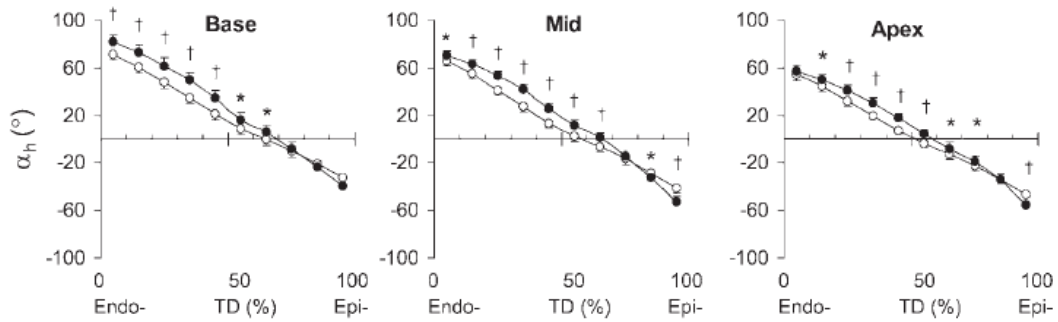

Figure 7.19: Transmural helix angle at basal, mid and apical ventricular levels in chemically arrested diastole (black circles) and systole (white circles) demonstrating a shift towards greater angles Chen at el (12).

Hales et al. (13) also observed a systolic shift, in helix angle derived myocyte orientation, towards a more longitudinal orientation in subendocardial myocytes, however the opposite was observed in subepicardial myocytes, where fewer myocytes were observed to have a longitudinal orientation (figure 7.20).

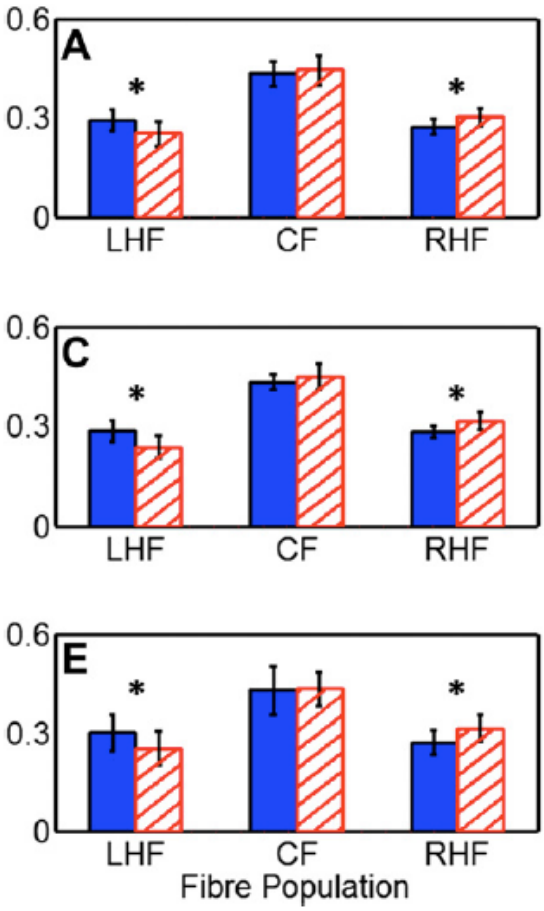

Figure 7.20: Changes in helix angle between diastole (blue bars) and systole (red striped bars) at basal, mid and apical ventricle. In systole there are a greater number of endocardial myocytes with a longitudinal, right helical orientation (RHF: >30°), however there were fewer epicardial myocytes with longitudinal, left helical orientation (LHF: <-30°) (13).

There were technical differences between these studies that may have contributed to the observed differences: Hales et al. studied live, perfused Langendorff hearts chemically arrested in systole, in contrast, Chen et al. studied fixed hearts in the systolic confirmation. In previous work Hales et al. demonstrated that fixation alters the orientation of the primary eigenvector, although this data suggests that change predominantly affects the number of circumferential, rather than epicardial, longitudinal myocytes (375). Despite the discrepancy, both studies demonstrate minimal change in myocyte orientation between phases. The authors therefore deduced, as hypothesised by Le Grice, that fibre re-orientation may contribute to circumferential ventricular shortening, however this relatively minor shift in myocyte orientation could not account for the degree of radial thickening observed in systole.

Addressing this point, both studies also interrogated phasic sheetlet orientations through secondary/ tertiary eigenvector data. Chen et al. observed sheetlets occurring as a single population with a predominantly positive angulation basally (measured against the radial axis) and negative angulation apically. Compared to diastole, end systolic sheetlet orientation, had a more radial orientation (figure 7.21). Although regional variation in sheetlet angulation was observed, the trend in re-orientation was observed throughout the ventricle. On average they observed a change in sheetlet angle from 36° to 20° and the authors calculated that sheetlet reorientation could account therefore for up to 40% of radial thickening.

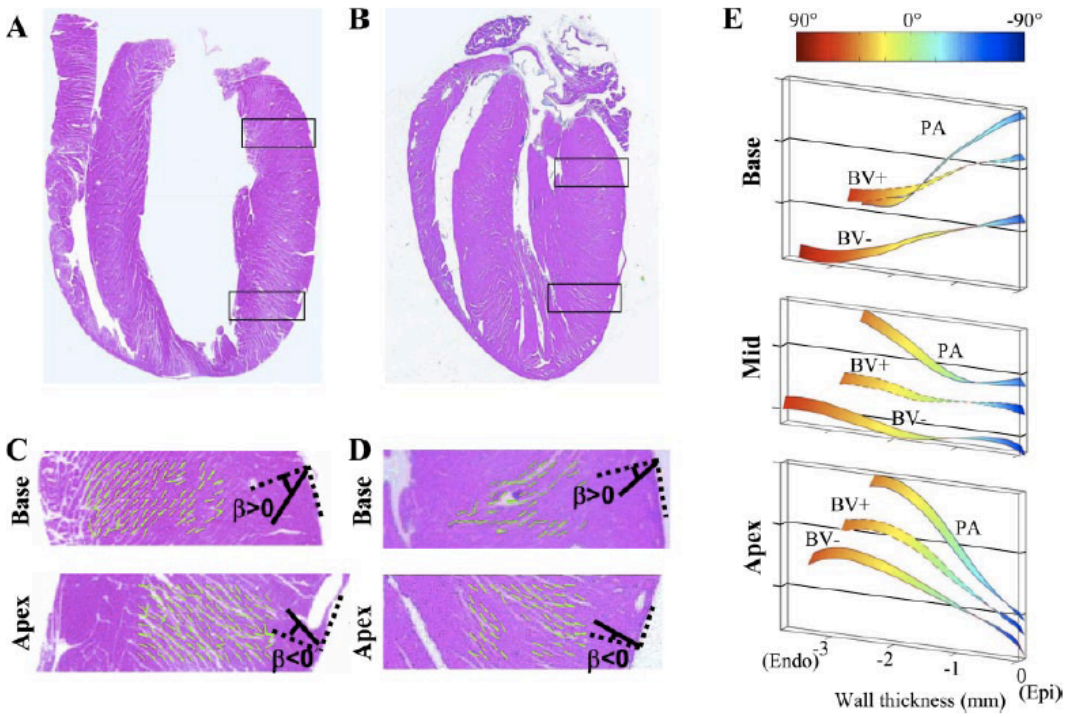

Figure 7.21: Histologically derived sheetlet angles in diastole (A & C) and systole (B & D). The angulation of sheetlets in systole can be seen to decrease (i.e. become more radial) in both basal and apical regions. In figure E, transmural DTI derived sheets are colour coded according to helix angle. As demonstrated histologically, sheetlets in the end systolic confirmation (BV-) have a more radial confirmation than end diastolic sheetlets (PA) (12).

In contrary to the above, Hales et al. detected 2 transmural sheetlet populations, of opposite polarity, both histologically and with DTI. Populations were defined as the β- group (<-30°), which were dominant subendocardially and the β+ group (>30°), which were dominant subepicardially. Nonetheless they observed the same pattern of mobility between phases, with a shift to a more radial confirmation in systole such that the angle between the sheetlet populations increased. The authors calculated from their data that the observed mobility could account for between 16-32% of radial thickening from the ventricular apex to base (figure 7.22) (13).

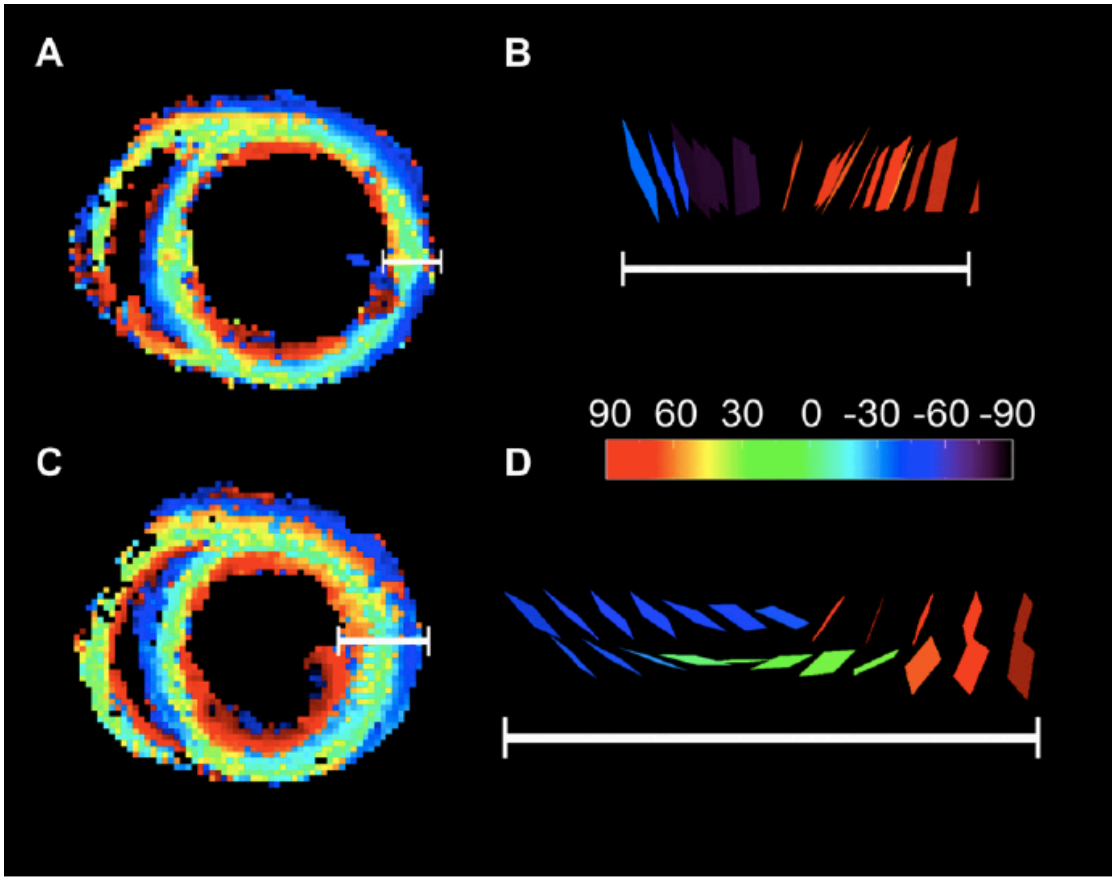

Figure 7.22: Short axis view through the mid ventricle in a rat heart demonstrating the persisting helical pattern from A diastole to C systole. In B and D the transmural sheetlet orientation from the lateral LV wall is represented via tiles in diastole and systole respectively. The colour coding and 3D orientation illustrates that the sheetlets are observed to take a more radial/ circumferential orientation from diastole (B) to systole (D) (13).

Following on from Hales et al., the same Oxford based research group have since conducted two further detailed analyses in rat (92) and rabbit (376) myocardium, arrested in different contractile states. In the rat heart experiment, Lohezic et al. acquired images with both cDTI and its sister technique, diffusion spectrum imaging (DSI), which permits identification of more than one myocyte population per voxel (92). They confirmed Hales et al.'s previous findings of increased right-handed myocytes combined with reduced left-handed myocytes in the contractile state. They also detected a reduction in FA in the contractile state with both cDTI (slack 0.32±0.02 v contracture 0.28±0.02) and DSI, which was predominantly driven by a reduction in the size of the primary eigenvector (eigenvalue, λ_1). This wasn't the case in Hales et al., however the discrepancy was attributed to superior SNR in the more recent study. A proposed hypothesis for the FA reduction was myocyte shortening and thickening during contraction.

In rabbit hearts, arrested in the relaxed state, Teh et al. (376) detected an increase in subendocardial λ_2 and λ_3, combined with reduced anisotropy and increased diffusivity, mirroring the observations of Jaing et al. (364). However, in contrast, this pattern was also observed in the subepicardium. In the contractile state, no difference was found in fractional anisotropy between the phases, therefore agreeing with Hales et al. (13), but contradicting Lohezic et al. (92). ADC was also found to be lower in the contracted state with higher 'transverse anisotropy' (λ_2 /λ_3), however the authors conceded that this could have resulted from technical factors, rather than a true representation of the microstructure. Sheetlet orientations, inferred from tertiary eigenvector tractography data, were observed in 'V' shapes, at the LV apex, as depicted by Hales et al. and histologically by Kung et al. (7). Interestingly sheetlets in 'N' shaped confirmations were also observed at the RV insertion points.

In summary, these studies have advanced our understanding of myocyte and sheetlet myobility through direct non-invasive interrogation of myocardium in different species.

Myocyte tracking – Tractography:

A diffusion imaging team based at Massachusetts General Hospital, lead by at Prof David Sosnovik, have been at the forefront of developing diffusion derived myocyte tractography (146). The group have acquired images with both diffusion tensor and diffusion spectrum imaging, reconstructing primary eigenvector data into 'tracts' (figure 7.23). Results are visually impressive, however other researchers have acknowledged the limitations of such data, i.e. that tracts are streamlines of eigenvectors rather than true anatomical features (376), nonetheless the data are an important contribution to the field.

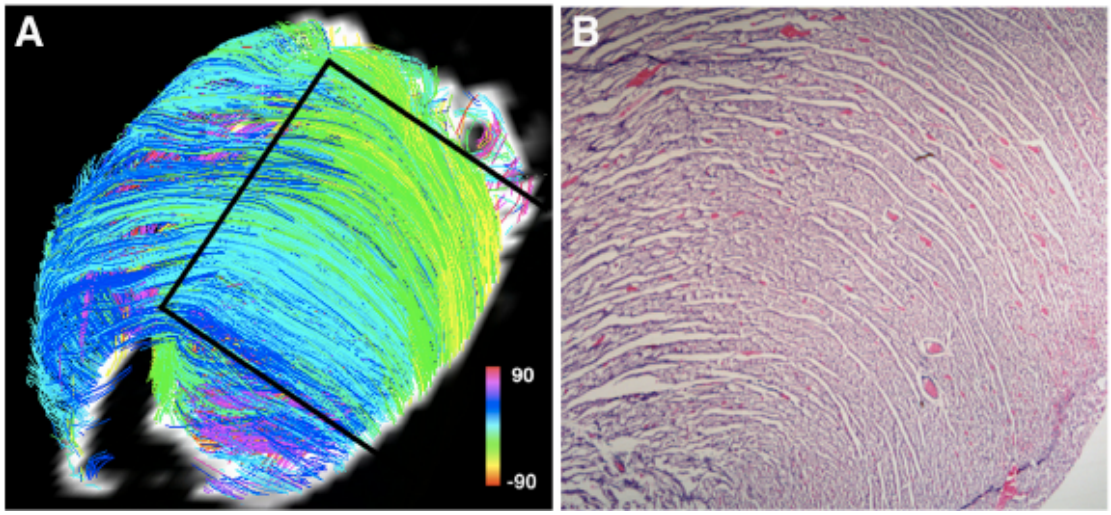

Figure 7.23: A: Example of a mouse heart imaged with diffusion spectroscopy with myocyte orientation depicted by reconstructed tractograms. B: Haematoxylin stained myocardium of the respective area demonstrating similar structure (146).

Whole Heart atlases:

Technical developments in ex vivo cDTI have facilitated the acquisition of detailed, 3D, whole heart datasets, such as the work of Lombaert et al., who computed an atlas of human heart, primary eigenvector derived, myocytes orientation from 10 ex vivo human hearts (147, 152). They are numerous potential opportunities for such data, including improved computational modelling of myocardial processes. In the case of electrical transmission, accurate modelling may improve our understanding of arrhythmia generation and guide interventions such as radio-frequency ablations and cardiac pacing (4, 88, 152, 377).

7.5.3.2.2: Structural Consequences of Cardiovascular Disease Processes

Myocardial Infarction:

In 1998 Hsu et al. theorised that diffusion weighted imaging could detect acute changes in ischaemic myocardium, similar to the changes observed in acutely ischaemic cerebrum (378). In a rabbit heart Langendorff experiment, hearts were arrested for diffusion weighted imaging before and after acute myocardial infarction. The ADC of the acutely ischaemic myocardium was observed to gradually decrease after 60mins, in contrast to remote myocardium where the ADC

was constant. As with ischaemic cerebrum, decrease in ADC was thought represent cytotoxic swelling of irreversibly injured myocytes, and the delay in onset attributable to the presence of collateral arterial supply with the myocardium. The authors thus concluded that diffusion imaging could enable the identification of non-viable myocardium in context of acute infarction.

Chen et al. were the first authors to study established myocardial infarcts with cDTI (362). In contrast to acute infarction, 4 week-old infarcted rat myocardium was found to have a higher ADC compared to control myocardium; results were later replicated in porcine hearts by Wu et al. (379) and Nguyen et al. (342). The elevation in ADC was explained by collagen fibres replacement of dead myocytes with resulting expansion of the extracellular space; water is therefore less constrained, translating to a higher ADC. Within regions of infarction the transmural pattern of helical cellular arrangement was maintained, however infarcted myocardium was less anisotropic. The persistence of helical structure was attributed to collagen deposition in line with the original myocardial scaffolding, which preserves tissue orientation and therefore the primary eigenvector. Despite preservation of the primary eigenvector, there was a greater spread in regional collagen fibre orientation compared to non-infracted tissue, which the authors referred to as 'disarray'. Upon analysis with cDTI this was one of the contributing factors in the comparative reduction in FA observed in infarcted tissue.

Winklhofer et al. were the first to report cDTI findings in human hearts post myocardial infarction (380). They studied 26 post mortem hearts, and in keeping with Chen et al. and Wu et al. (362, 379), found elevated ADC and reduced FA in infarct regions. They also studied intra-infarction helix angles, and unlike Chen at al. (362), they reported a loss of right-handed subendocardial myocytes in chronic infarcts. Most studies avoided intra-infarct helix measures due to the extent of myocardial thinning, therefore Winklhofer et al.'s results are likely to reflect a greater proportion subendocardial, as opposed to transmural infarcts.

Sosnovik et al. also interrogated intra-infarct helix angles with diffusion spectrum imaging (DSI) tractography (318). They studied rat hearts at 3 weeks post infarction. No reference to myocardial wall thickness was made. In contradiction to Chen et al. they reported highly disrupted infarct architecture, deduced from a reduction in tracts and loss of the original helical pattern. The presence of residual tracts, with orthogonal orientations, were compared to corresponding histological sections and interpreted as 'persisting myofibres', which the authors postulated may serve as a substrate for malignant arrhythmia. Although visually impressive, other authors would argue against such interpretations from highly smoothed, interpolated data. Moreover the random, disorganised pattern demonstrated within infarcts is at odds with histological reports of infarct structure and Chen et al.'s porcine model of infarction (362)(figure 7.24).

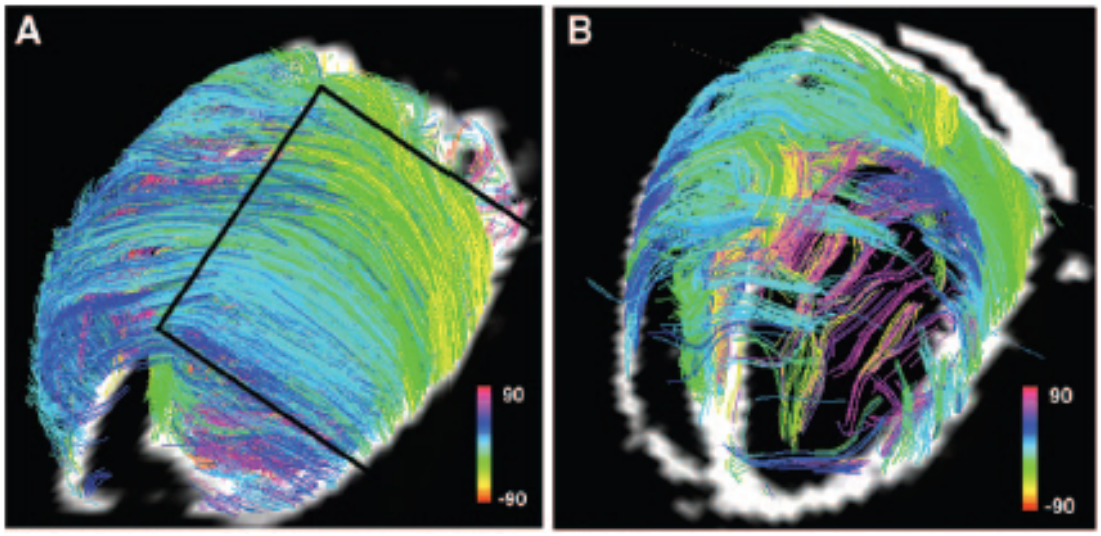

Figure 7.24: DSI tractography of the anterior epicardial surface of a mouse heart A: before and B: after infarction. In B there is a reduction in established tracts in the infarct region with few persisting orthogonally orientated tracts (318).

Over all, the majority view appears to be of elevated ADC and reduced FA in established infarcts, otherwise we are far from a consensus on ex vivo infarct data. The small study samples, heterogeneity of infarction, interspecies differences and inter-centre technical differences are just some of the potential reasons for discrepancy.

Heart Failure:

Microstructrual myocardial remodelling in heart failure has also been the subject of cDTI studies. In 2006 Helm et al. studied helix angles and sheetlet angles in a canine model of heart failure (381). Although the LV wall thickness was reduced in the dilated, failing hearts, the innate helix angle pattern was largely preserved, however the authors highlighted that the transmural helix angle gradient (angular rate of change) was greatly increased. Surprisingly only the septal region demonstrated a significant change in sheetlet angulation, with a greater longitudinal orientation, to which the authors ascribed the observed wall thinning.

Li et al. examined HA patterns in hamsters with a heart failure and aging hamsters compared to controls (382). As per Helm et al. they found no significant difference in HA patterns between cohorts, however they described greater 'angular dispersion', i.e. greater HA standard deviation in comparative endocardial and midwall myocytes in the dilated cardiomyopathy group. In contrast to these studies, Eggen et al. observed a shift towards more obliquely orientated basal and mid ventricular myocytes in post mortem human hearts with heart failure (383).

Li et al. also examined ADC and FA values between cohorts (382). The myocardium of hamsters with heart failure demonstrated greater ADC and reduced FA; interestingly aged hearts showed similar changes, to a lesser degree, in the absence of LV dilatation or wall thinning. Histological comparison demonstrated fibrosis with expanded extracellular space in aged and failing hearts, which correlated with the observed changes. The authors also identified a subgroup of voxels, predominantly in the mid wall, in failing hearts where the pattern was reversed with reduced ADC and elevated FA. On CT imaging these regions appeared to coincide with focal myocardial calcification (figure 7.25).

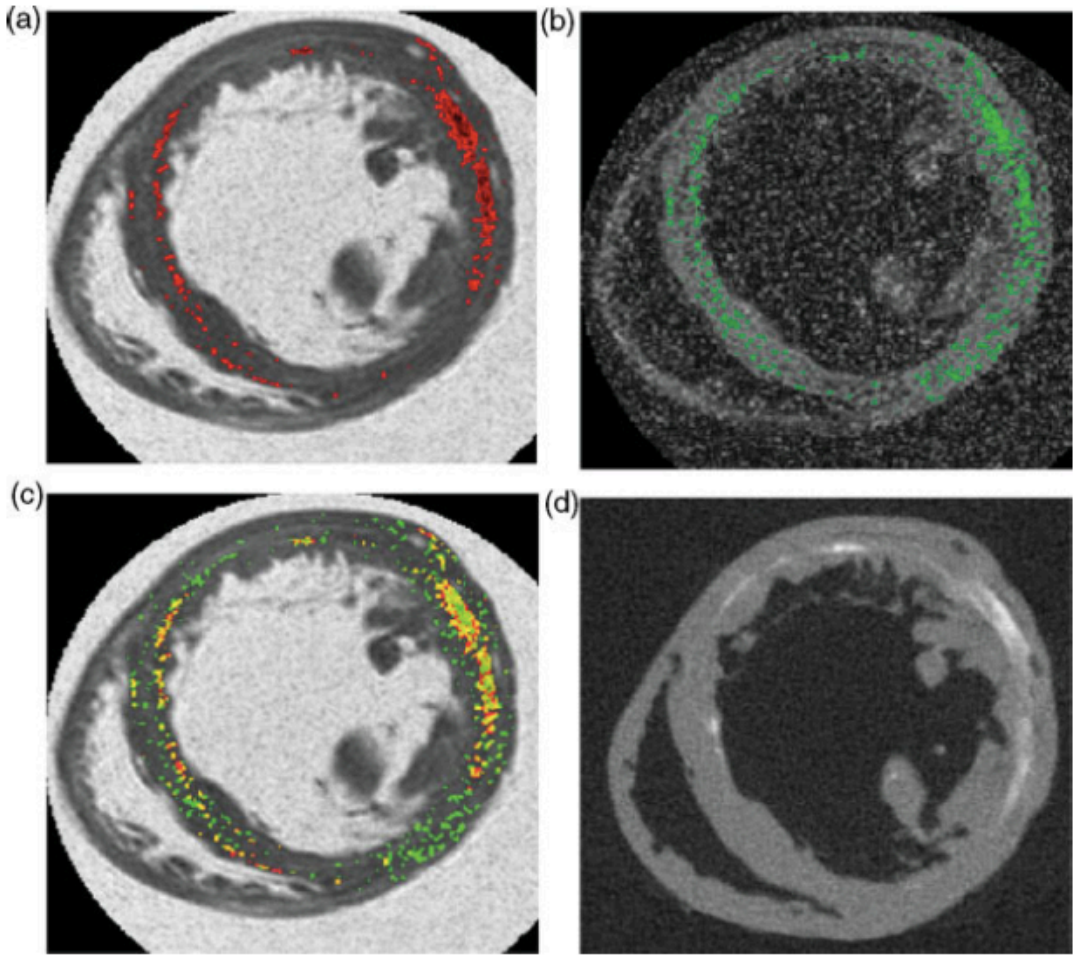

Figure 7.25: Short axis section through the mid ventricle of a hamster with heart failure. Regions of reduced diffusivity (a) and high FA (b) are well matched on co-registration (c) and appear to correlate with regional myocardial calcification on CT (382).

More recently Abdullah et al. studied diffusivity, FA and eigenvalue measures with cDTI in 14 human hearts with established heart failure, correlating results with digital miscroscopy assessment of collagen content (384). As per Li et al., they found a 12% increase in myocardial diffusivity, which corresponded with an increase in the secondary and tertiary eigenvalues; these measures were positively correlated with collagen deposition with correlation co-efficients ranging from 0.56-0.62. A 22% decrease in FA was also observed and negatively correlated with the extent of collagen deposition, r= -0.51. The authors therefore concluded that cDTI could serve as a complimentary CMR measure of fibrosis.

Left Ventricular Hypertrophy & Hypertrophic Cardiomyopathy

Researchers from The Biomedical Engineering in Zurich in combination with pathologists Professor Anderson and Prof Lunkenheimer applied cDTI to study myocyte orientation in a mouse model of left ventricular hypertrophy (385). In addition to helix angle measurement the 'intrusion angle' was calculated which represents the angle between the epicardial tangent plane and the primary eigenvector in the X-Y plane (figure 7.26)

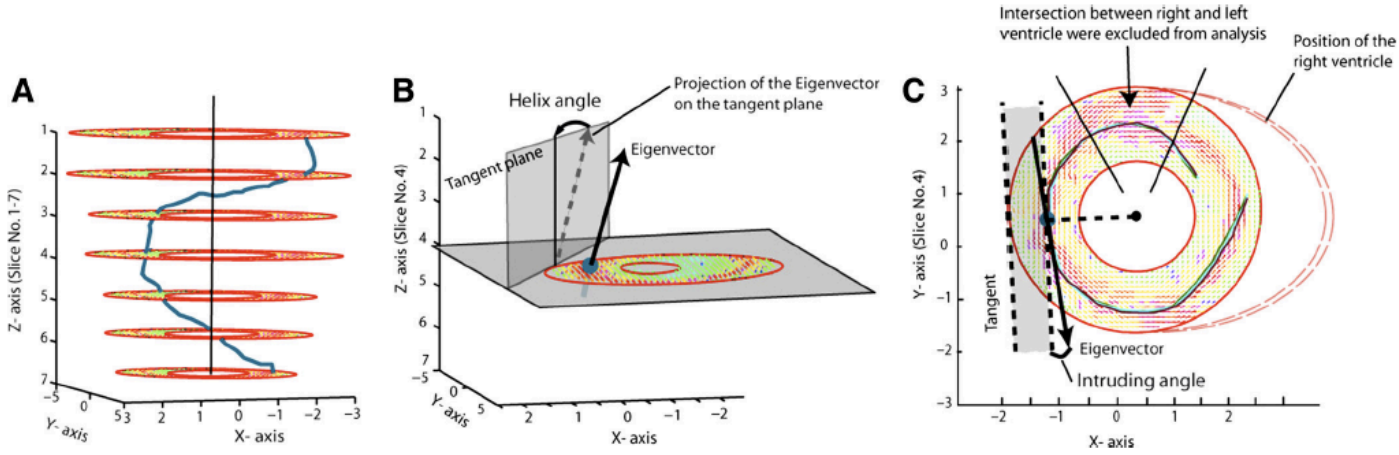

Figure 7.26: Illustration of cDTI angular calculations. A: Representation of short axis slices against the standard x-y-z coordinate system. B: The helix angle is calculated form the angle between the y-x axis, or radial axis, and the z axis component of the projection of the primary eigenvector onto the epicardial tangent plane. C: The intrusion angle is the angle X-Y axis component of the same primary eigenvector projection (385).

Despite the observed differences in myocyte size, LV wall thickness and cardiac mass, on the whole helix angles were comparable been hypertrophied and normal hearts, with marginally deeper epicardial myocyte angles in response to hypertrophy. Intrusion angles were generally greater in the hypertrophied hearts, but not consistently. The authors commented that analysis of secondary and tertiary eigenvectors would have been of interest but beyond the scope of the study.

Two groups have utilised diffusion imaging to investigate pathophysiological mechanisms in animal models of hypertrophic cardiomyopathy. Ripplinger et al. studied a, transgenic rabbit model of HCM with a β-myosin heavy chain-Q403 mutation and clinical phenotype similar to

humans (386). Transgenic mice were found to have an increased spread of helix angles, driven by greater endocardial angles, which the authors postulated could be a contributing factor in arrhythmia genesis & maintenance. Subsequently Wang et al. studied a β-myosin binding protein C knock out mouse model of HCM with diffusion spectrum imaging (DSI) (292). In knock out mice helix angles were found to transition more rapidly from a left-handed, epicardial orientation to circumferential orientation. In the mid and endocardial regions DSI derived tractograms displayed 'reduced coherence'. During post processing, alignment of the primary eigenvector, of adjacent voxels, into tracts was permitted if vectors were within ±17.5° of one another. In knockout mice these limits were exceeded more frequently, thus resulting in shorter tracts, or loss of coherence, which the authors interpreted as evidence of disarray.

7.5.3.3: Preclinical In Vivo Diffusion Tensor Imaging Studies

As previously discussed, the major potential for DTI is its ability to non-invasively interrogate myocardial structure in living hearts, however a number of technical challenges must be overcome to achieve this. Ex vivo cDTI data are acquired with diffusion weighted-spin echo sequence, where winding and unwinding gradients are separated by a 180° pulse. In vivo this sequence fails as cardiac motion from contraction is several orders great than diffusion, thereby impeding successful image generation. The focus of pre-clinical in vivo studies has therefore been the validation and development of in vivo sequences that can circumvent cardiac contraction. Full details of preclinical in vivo studies are outlined in the next section addressing in vivo cDTI sequences.

7.5.3.4: Clinical In Vivo Diffusion Tensor Imaging Studies

7.5.3.4.1: Normal Myocardial Architecture and Mechanics

Myocyte and sheetlet components of contraction

In 2000 Tseng et al., of Massachusetts General Hospital, compared myocyte orientation, derived from a novel cDTI sequence, with components of myocardial strain (367, 387). This research team were at the forefront of in vivo cDTI research and the first to illustrate the winding helical pattern of human myocytes in vivo (figure 7.27) (360, 367). Primary eigenvector data was derived from cDTI acquired in a single phase between systole and diastole with superimposed strain data. Tseng et al. reported a symmetrical progression from epicardial to endocardial angulation in all volunteers. Global LV myocardial shortening, in line with myocyte plane, was found to be of a similar magnitude to shortening in the cross-myocyte or sheetlet plane, however fibre shortening was transmurally uniform, whereas cross-fibre shortening was observed to increase from the epicardium to the endocardium. In the epicardium myocyte orientation coincided with the direction of maximum contraction epicardially and direction of least contraction endocardially.

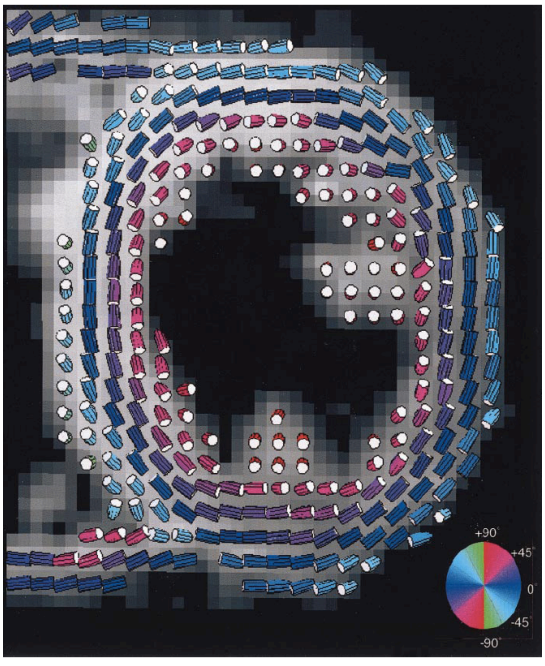

Figure 7.27: Mid ventricular short axis cDTI acquisition. The orientation of the primary eigenvector is represented, per voxel, by cylinder graphics colour coded according to the helix angle (367).

Following from this, the same group assessed laminar components, in vivo, from the secondary and tertiary eigenvectors in combination with strain analysis (368). Again cDTI eigenvector data were acquired from a single phase, between systole and diastole, with strain data superimposed. In many aspects the results agreed with Le Grice et al. (9) and Costal et al. (11), in particular with regards to the contribution from sheetlet function to radial thickening, however, in contrast, they estimated sheetlet shear, or re-orientation, to be less important than other components of sheetlet function, such as sheet extension (figure 7.28). Notably there was significant heterogeneity between subjects and regionally around the LV.

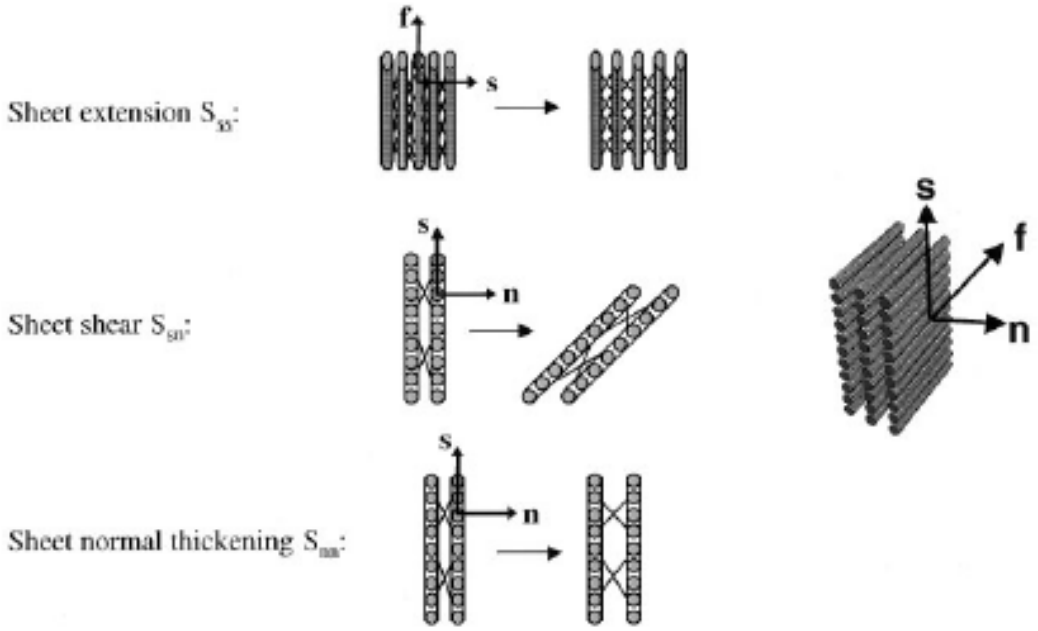

Figure 7.28: Different components of laminar function as proposed by Dou et al. Sheetlet extension Sss represents positive strain the cross fibre direction (secondary eigenvector direction). Sheet shear, Ssn, represents sheetlet reorientation/ slippage. Sheetlet normal thickening, Snn, represents positive strain in the tertiary eigenvector direction (368).

Mekkaoui et al. compared cDTI tractography derived myocyte orientation in systole and diastole as part of a Royal Brompton Hospital – Massachusetts General Hospital collaboration (155). In comparison to diastole, systolic subepicardial and subendocardial myocytes assumed a more oblique/ longitudinal orientation, therefore replicating earlier ex vivo work. The authors therefore suggested that this could explain the observed long axis ventricular shortening during systole (figure 7.29).

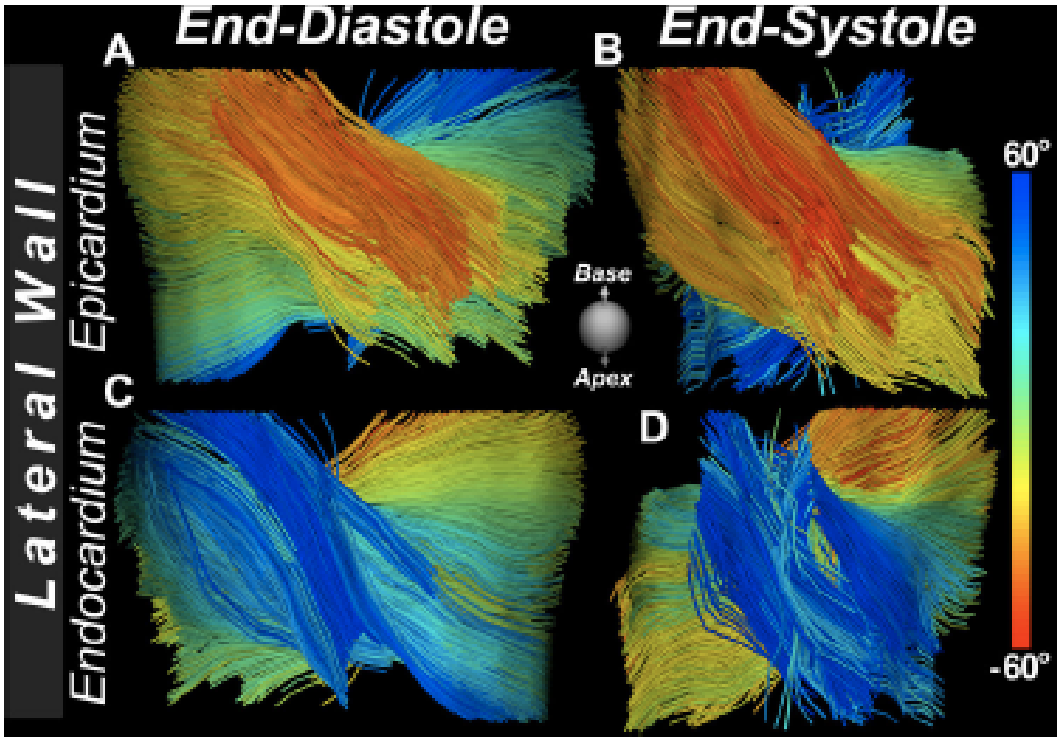

Figure 7.29: Comparison of myocyte orientation in systole and diastole derived from in vivo cDTI tractography. In systole epicardial and endocardial myocytes adopt a more longitudinal confirmation. This may account for long axis LV shortening in systole (155).

Whole heart in vivo cDTI

In its current format, cDTI acquisitions are comparatively longer than standard clinical acquisitions due to the need for multiple directions and averages; standard protocols therefore limit myocardial coverage to select slices. Toussaint et al. proposed a technique which permits full in vivo myocardial coverage without prolonging acquisition time (149, 388). In healthy volunteers, full myocardial coverage was demonstrated from a limited cDTI acquisitions using a 'dense approximation scheme'. The results were comparable with fully acquired ex vivo datasets with accurate representation of myocyte helix angles. Although results were impressive, a high degree of data approximation and smoothing was required to generate results. In the context of disordered helix angles, this may result in underestimation or misinterpretation deviated helices.

7.5.3.4.2: Architectural Consequences of Cardiovascular Disease Processes

Myocardial Infarction

Investigators from Massachusetts General and the National Taiwan University Hospital collaborated to investigate myoarchitectural consequences of myocardial infarction with in vivo cDTI (369, 370). Wu et al.'s work is arguably to most recognised in the field, investigating acute myocardial infarction in 37 patients (369), 17 of whom where re-imaged in the chronic infarct stage (370).

In the acute myocardial infarction study patients were imaged at a median of 26 days post infarct, range 10-42 days, which, by contemporary standards, would be considered beyond the acute phase (389). In keeping with this the authors reported regional wall thinning and significantly elevated infarct zone ADC, compared to remote and adjacent zones, as ex vivo infarct data has previously demonstrated. Interestingly there was a gradient in ADC values from infarct ($8.24\pm2.01x10^{-6}cm^2/s$) to adjacent ($7.69\pm1.73x10^{-6}cm^2/s$) and remote myocardium ($7.38\pm1.73x10^{-6}cm^2/s$) combined with subtle reductions in wall motion and myocardial thickness in adjacent zones. As for FA, despite the marginal difference, anisotropy was reported as significantly reduced in infarct zones (FA 0.26±0.03) compared to remote myocardium (FA 0.27±0.04). The percentage of right-handed and left-handed myocytes were reduced and increased respectively within infarcts with the latter being a significant predictor of infarct area on multivariate analysis.

In the group's second study, data 17 patients from the original study were reimaged at a median of 213±59 days post infarction (370). The first reported finding was a reduction in remote and adjacent zone ADC from the acute to chronic infarct stage. On closer inspection, this appears to be attributable to a significant increase in quoted ADC values for acute adjacent zone (9.2 ± 0.5(standard error of the mean)$x10^{-6}cm^2/s$) and remote zone ($8.1\pm0.5\ x10^{-6}cm^2/s$), in the smaller sample size, compared to their previous publication. Remote zone FA was marginally

greater in the chronic infarct stage (0.27±0.01 v 0.29±0.01, p=0.018). Neither a significant improvement in remote or adjacent zone wall thickening, nor mean helix angles were demonstrated between acute and chronic infarct. Despite this, reduced adjacent zone ADC and increased mean remote zone helix angles were reported to correlate with improved adjacent zone wall thickening. Similarly reduced remote zone ADC and increased adjacent zone helix angles correlated with remote zone wall thickening.

Hypertrophic Cardiomyopathy

As discussed in Chapter 5, Tseng et al., of the Massachusetts General Hospital, published the first in vivo cDTI study of patients with hypertrophic cardiomyopathy. They studied 5 patients with HCM and 5 controls with cDTI combined with strain analysis (294). They reported the ability to detect disarray in HCM patients through reduced FA in the hypertrophied septum (0.56), compared to the lateral wall (0.75). Greater longitudinally orientated myocytes were also detected within hypertrophied septum. On strain analysis reduced radial, myocyte direction, cross myocyte direction and shear strain were observed in the septum, with positive correlation between FA and cross myocyte and shear strain. The authors therefore concluded that myocyte disarray was detectable non-invasively and that it was responsible for impaired strain in hypertrophied segments. Drawing conclusions from such a small study sample should be avoided; it is surprising that the group did not build on this work with a larger cohort. The sample images offered in the paper also raised questions regarding their post processing technique as they demonstrated ragged regions of interest with no exclusion of edge pixels in the subepicardium or subendocardium. As a result, in the HCM images in particular, the bulky papillary muscles are incorporated into the analysis along with contributions from the right ventricle on the subepicardium of the septum. Both would have a direct effect on helix angle and FA calculations.

7.5.4: In vivo Cardiovascular Diffusion Tensor Imaging Sequences

7.5.4.1: Introduction

As previously discussed above the major strength of DTI is its ability to non-invasively interrogate myocardial structure in living hearts, however a number of technical challenges must be overcome to achieve this. The greatest limiting factor affecting cDTI is movement artefact from cardiac contraction; a number of adaptations to the original Stejskal and Tanner sequence (335) have therefore been required to facilitate in vivo imaging. As with other CMR sequences, cardiac gating is essential to ensure that diffusion measures are made at identical points in the cardiac cycle. Methods for limiting respiratory motion include instructed breath holding (149, 294, 359, 369), synchronised breathing (367, 368, 387) and navigator approaches, which time acquisitions with both the respiratory and cardiac cycles (19, 360). This section describes the feasibility, strengths and weaknesses of contemporary in vivo cDTI sequences.

7.5.4.2: Monopolar Spin Echo

Non-cardiac diffusion imaging is traditionally acquired with the Stejskal-Tanner spin echo sequence with an EPI readout (figure 7.30), however this sequence performs poorly when applied to in vivo cardiac acquisitions; diffusion gradients are placed at different points in the same cardiac cycle, with resulting susceptibility to bulk cardiac motion, creating an ‘all or none’ phenomenon in image generation (390).

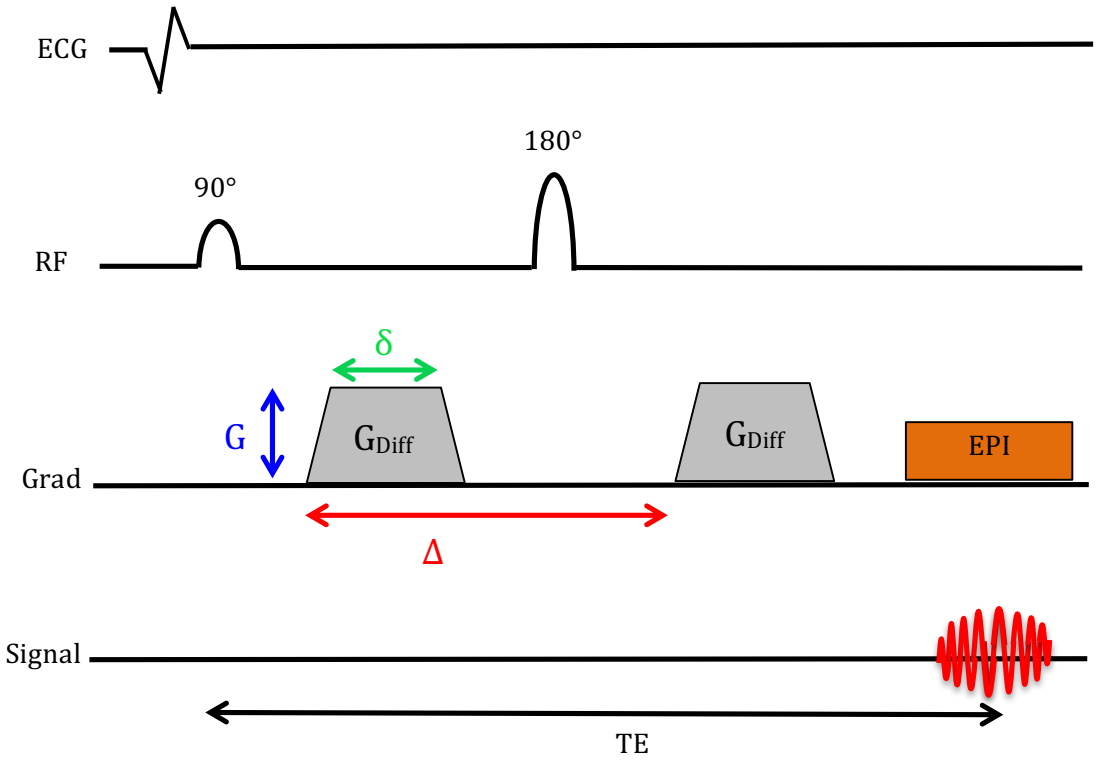

Figure 7.30: The Stejskal-Taner spin echo sequence applies winding and unwinding diffusion gradients (G_{Diff}), separated by a 180° pulse, within one cardiac cycle. Signal losses therefore occur due to bulk cardiac motion rather than diffusion.

7.5.4.3: Monopolar Diffusion Weighted Stimulated Echo Sequence

The diffusion weighted stimulated echo acquisition mode (DW-STEAM) sequence is an adaptation of spin echo, where the refocusing 180° pulse is split into two 90° pulses (306, 359). Winding and unwinding diffusion gradients, of the same polarity (monopolar), are triggered to identical points in consecutive cycles (figure 7.31). The resulting diffusion sensitizing period (Δ) is long, allowing for small diffusion gradients; consequently the sequence is far less sensitive to bulk cardiac motion than spin echo, facilitating feasible in vivo cardiac diffusion (151, 306, 360, 366, 387). DW-STEAM is typical combined with an EPI read out and was utilised by Edleman et al. for the first in vivo cardiac study (359).

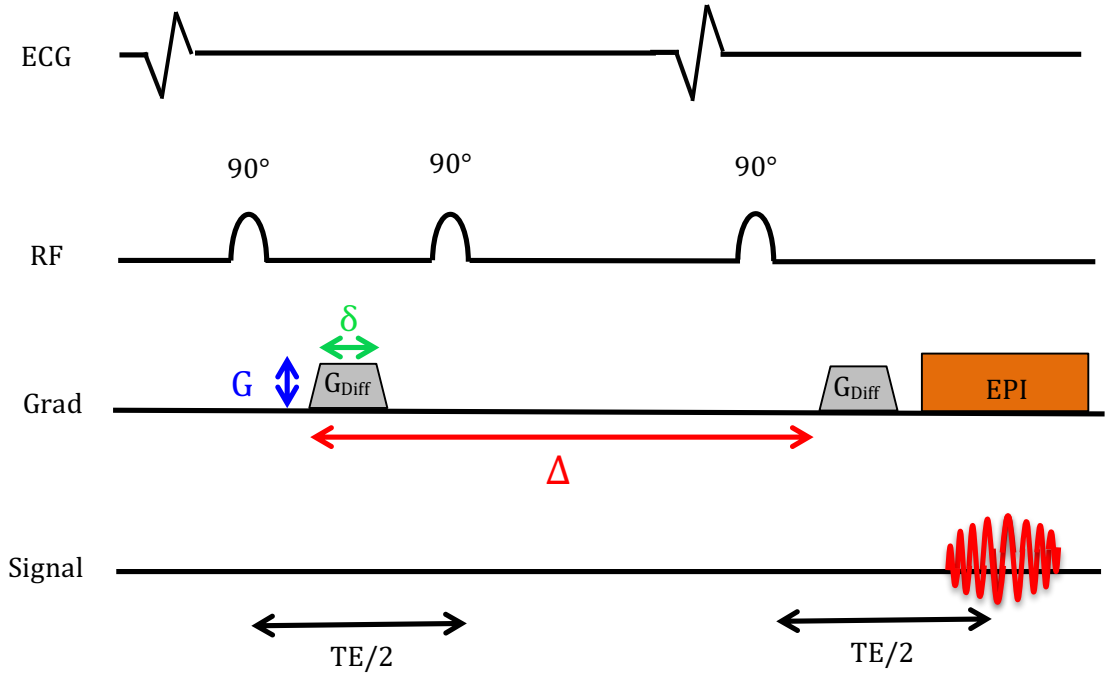

Figure 7.31: Monopolar diffusion weighted stimulated echo sequence (DW-STEAM) Winding and unwinding diffusion gradients of the same polarity, size (G) and duration (δ) are applied at identical trigger points in consecutive cycles. The diffusion sensitizing period (Δ), also known as the mixing time, is therefore equal to the patient's RR interval. The sequence is a modification of spin echo with the 180° pulse split into two 90° pulses.

7.5.4.3: Bipolar Diffusion Gradients

In 2002 Dou et al. proposed an alternative to monopolar diffusion sequences. Monopolar gradients were replaced with bipolar gradients, applied in quick succession within the same cardiac cycle (151). As the resulting diffusion sensitizing period is short, the size (G) and duration (δ) of the diffusion weighting gradients must be greater to achieve the same diffusion weighting/ b value. In this variation, although diffusion encoding is complete in the same cardiac cycle, bipolar gradients mimic velocity (flow) encoding gradients, and thus acquire a phase shift proportional to the velocity of the myocardium. In order to achieve velocity compensation, the bipolar gradient pair are repeated in the following cardiac cycle, following a STEAM sequence (figure 7.32).

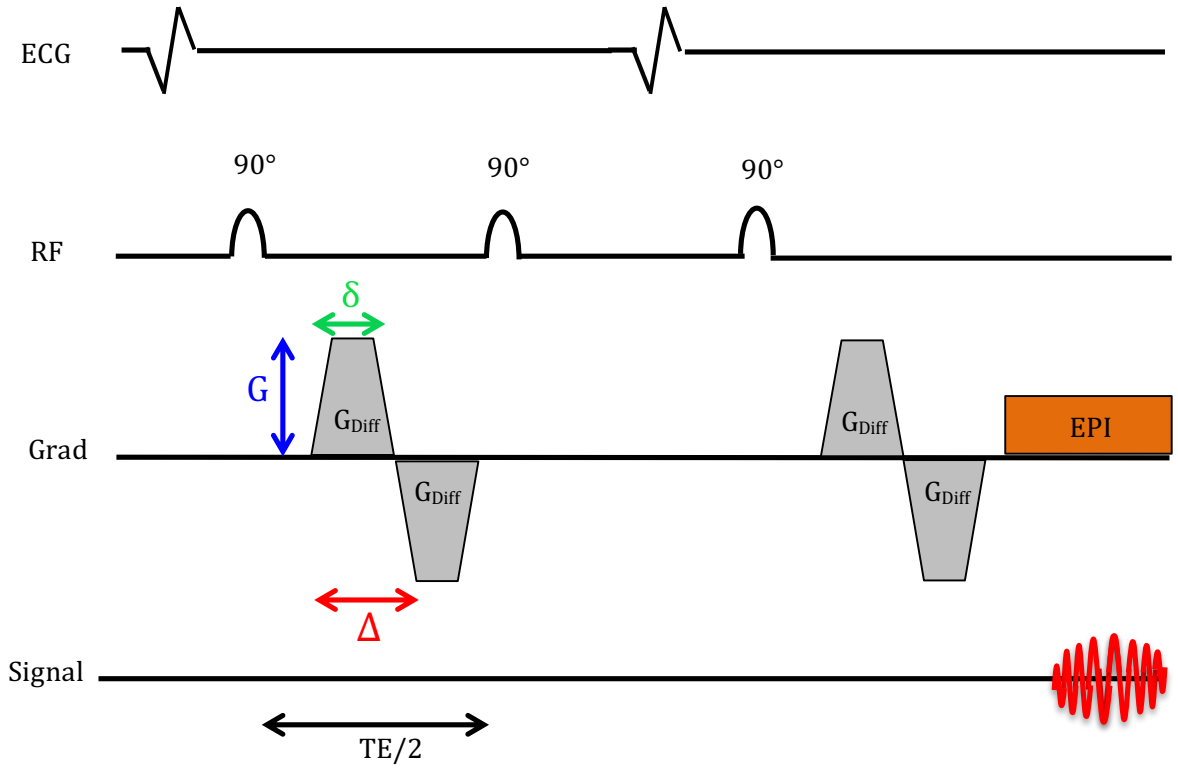

Figure 7.32: Bipolar diffusion weighted stimulated echo sequence proposed by Dou et al. (151): Winding and unwinding diffusion gradients of the same size (G) and duration (δ), but opposite polarity (bipolar) are applied in short succession (Δ). The gradients are then repeated after a stimulated echo protocol to compensate for flow encoding of the bipolar gradient pair.

7.5.4.4: Comparison of Diffusion Weighted Sequences

7.5.4.4.1: Signal to Noise Ratio

Although DW-STEAM is an improvement on spin echo, the advantages of the stimulated echo sequence are partly offset by the inherently poor SNR of the technique. During monopolar STEAM the diffusion sensitivity is maximised by a long period between gradients, however the same delay leads to a loss of SNR, compared to spin echo, through T1 decay (390). In comparison to monopolar, the bipolar STEAM sequence suffers T1 decay with none of the gains in diffusion sensitivity. Due to the limitations of STEAM, Gamper et al. proposed an alternative, spin echo (SE) method of velocity compensated bipolar gradient diffusion imaging (391) (figure 7.33).

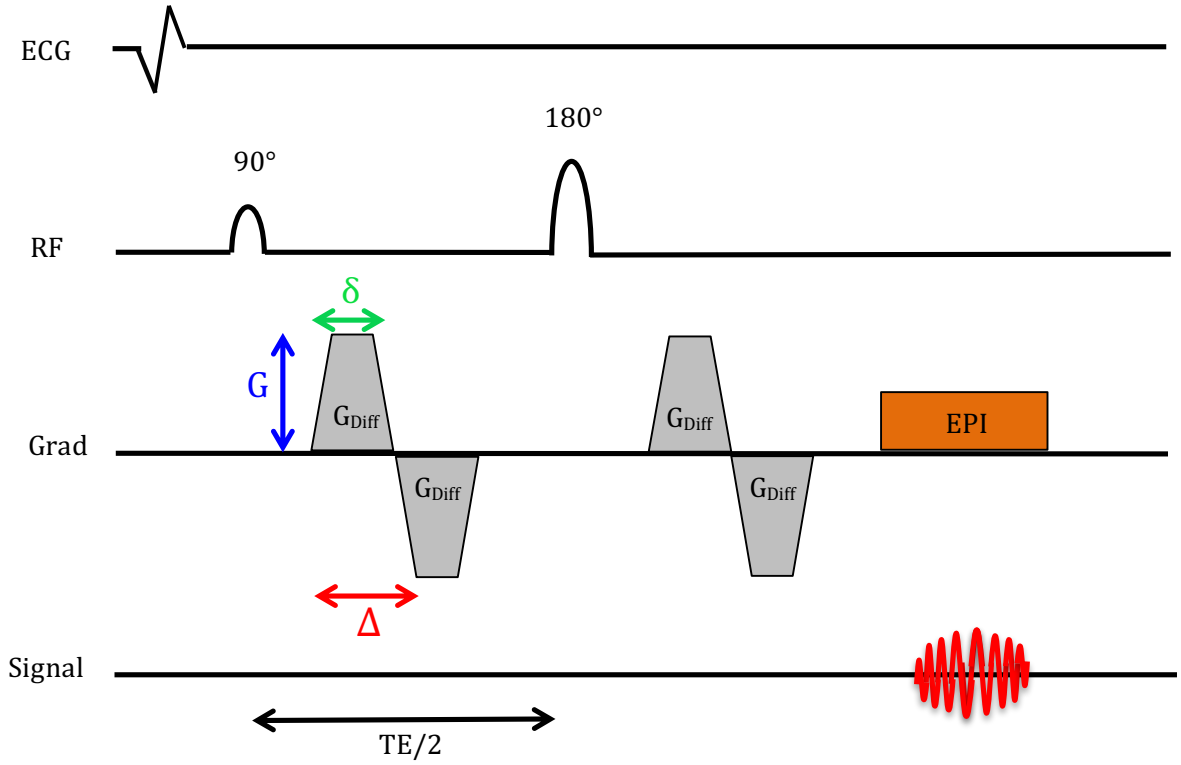

Figure 7.33: Bipolar diffusion weighted, velocity compensated, spin echo sequence proposed by Gamper et al. (391). Two bipolar diffusion gradient pairs are applied either side of a 180° pulse. The sequence runs over 1 cardiac cycle with less T1 decay and therefore greater SNR than its STEAM equivalent.

In a comparison study of in vivo monopolar DW-STEAM and bipolar SE, von Deuster et al. recently reported a 2.3-2.9 times greater SNR in the bipolar SE sequence (392).

7.5.4.4.1: Motion susceptibility

Diffusion gradients are typically triggered to relatively quiescent points in the cardiac cycle to limit movement during gradient application. However these intervals are short, especially at higher heart rates, the comparatively longer duration of the bipolar gradients are therefore potentially more motion sensitive than monopolar.

In light of the superior SNR, diffusion sequence developments since 2015 have focused on improving the phase correction component of the bipolar SE sequence. Both Stoeck et al. (371) and Nguyen et al. (393) have proposed methods of 'seconder order motion correction' for bipolar

SE sequences which address phase shifts occurring as a consequence of myocardial acceleration in addition to those resulting from constant velocities (figure 7.34).

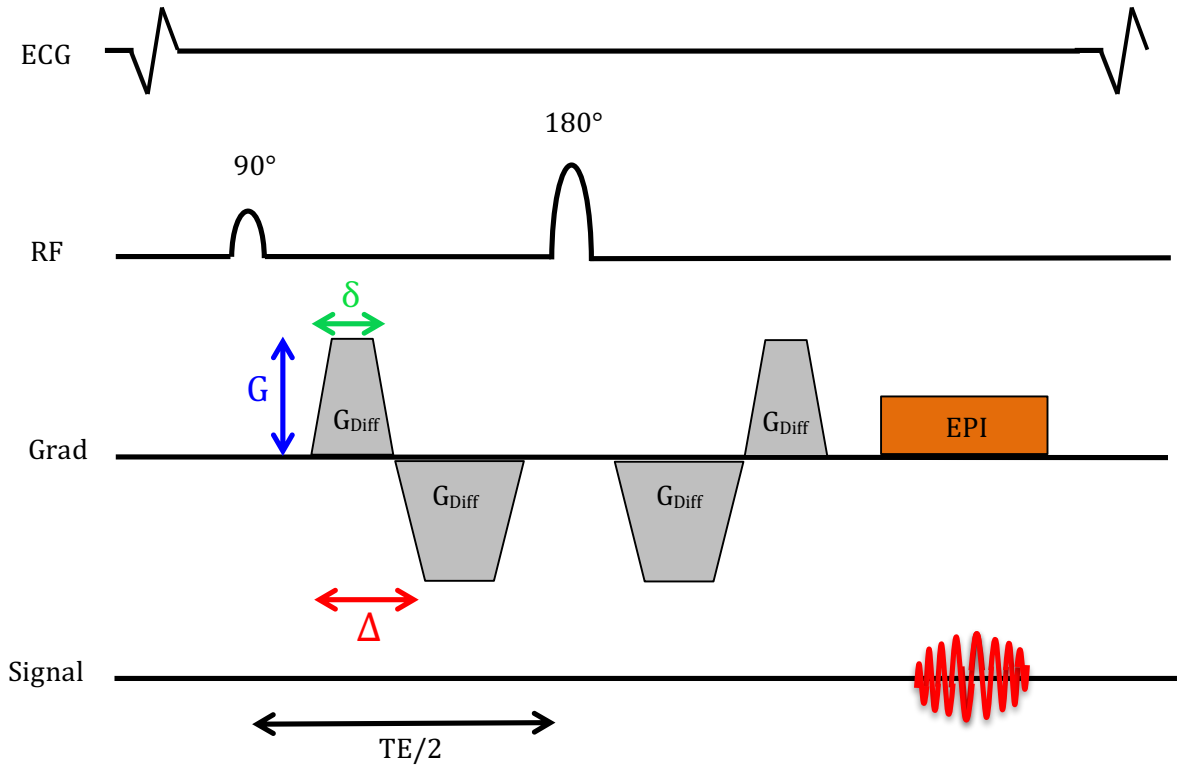

Figure 7.34: Bipolar diffusion weighted, second order motion corrected, spin echo sequence proposed by Stoeck et al. (371). Two bipolar diffusion gradient pairs are applied either side of a 180° pulse. Compared to the Gamper et al.(391) sequence, second order motion correction of acceleration induced phase shifts is achieved by modulating the negative polarity components of the bipolar gradient pair combined with revers timing of the second gradient pair.

7.5.4.3.2: Diffusion sensitivity

The diffusion sensitivity of a sequence is dictated by the diffusion weighting of a length of time between diffusion gradients (Δ). The monopolar STEAM sequence allows a greater window for diffusion of particles, thus the sensitivity of the sequence is comparatively greater. Longer diffusion times may also translate to enhanced tissue characterisation as protons have longer to diffuse through the network of cells and shear layers, thus the monopolar derived diffusion image may more accurately reflect the complexity of the underlying myocardium.

7.5.4.3.3: Strain susceptibility

The concept of strain artefacts during monopolar imaging was first introduced by Reese et al. (360, 366). They proposed that myocardial deformation, during the course of diffusion encoding, would alter the observed diffusion signal losses. Mathematical workings were supported experimentally with a gelatine phantom, which was deformed with a plunger during the diffusion time (Δ) and allowed to relax before the rewinding gradient was applied (366). In this study material deformation was assessed with a stimulated echo phase contrast sequence and related to diffusion measures via the monopolar STEAM diffusion sequence (figure 7.35). In response to transient gelatine compression (representative of negative strain), diffusion signal losses measured along the direction of compression were increased, leading to an artificially increased measured diffusivity. Conversely, diffusion signal losses measured in the perpendicular direction to compression (representative of positive strain) were decreased leading to an artificially reduced result for the diffusion coefficient.

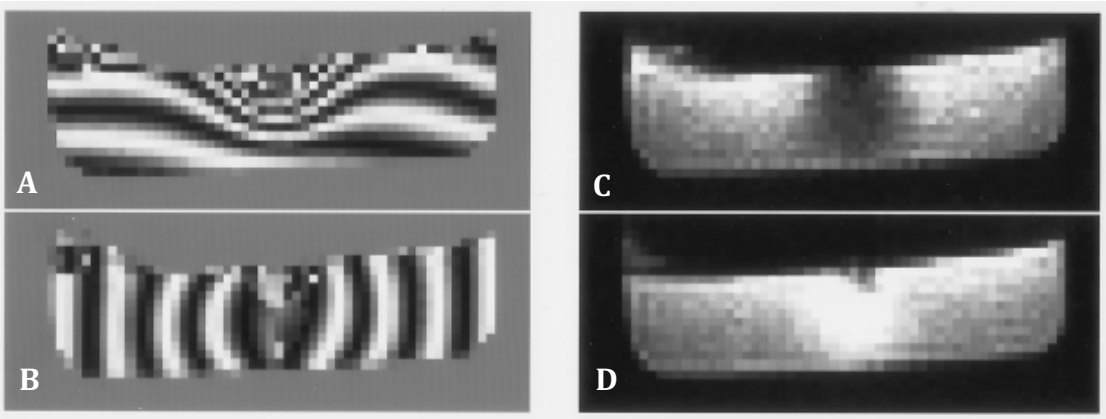

Figure 7.35: Gelatin phantom diffusion-deformation experiment. The phantom was imaged with a stimulated echo phase contrast sequence applied along the y-axis (A) and x-axis (B); and with a monopolar STEAM sequence along the y-axis (C) and x-axis (D) with plunger compression by 1cm during Δ. In response to compression with the plunger, phase contrast stripes applied along the axis of compression (A) were observed to bunch, and the measured signal losses increased (C). In contrast, phase contrast stripes applied in the perpendicular direction to compression were observed to spread (B), and the resulting diffusion losses decreased (D) (366).

Relating this work to in vivo imaging, the authors postulated that positive myocardial strain, or stretching, between gradient pulses, would produce an apparently lesser measure of diffusion in the same direction (relative to the underlying tissue). Conversely, negative myocardial strain, or

shortening, of the myocardium in one direction would produce an apparently greater measure of diffusion in the same direction, thereby introducing strain artefacts (figure 7.36) (366, 394).

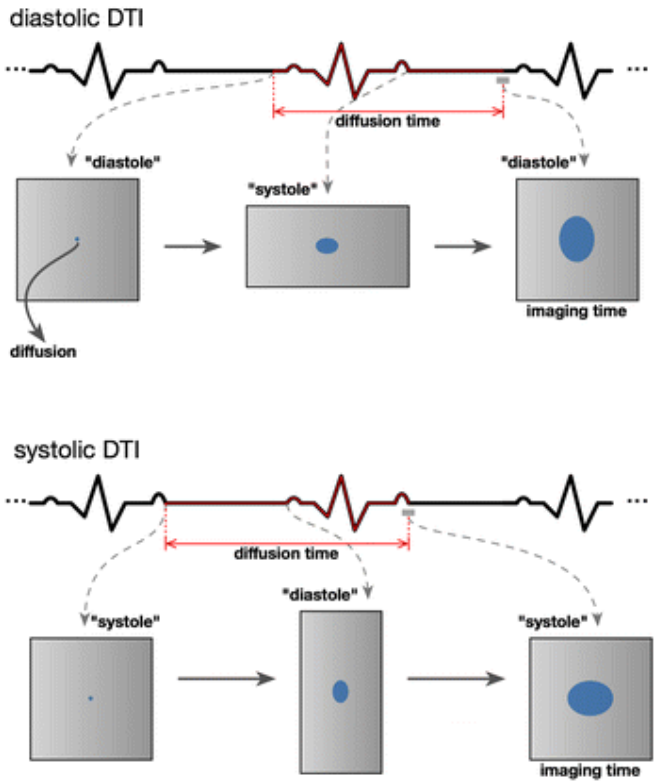

Figure 7.36: Representation of the Reese et al. theory of acquired strain artefacts in monopolar diffusion sequences: When diffusion weighted gradients are timed with diastole the excited myocardium passes through systole and is temporarily stretched (e.g. radial thickening); on return to diastole, measured diffusion is reduced in the direction of stretch. If gradients are timed with systole the excited myocardium temporarily passes through diastole and is temporarily shortened (e.g. radial relaxation); on return to systole the measured diffusion is increased in the direction of shortening (394).

To mitigate against the impact of strain, Reese et al. first devised a method of strain correcting the monopolar acquired diffusion tensor (366). However the theory of strain artefacts and correction methods are contentious. Firstly, as discussed in the first 4 Chapters, myocardial structure is anisotropic, strain is therefore highly complex and bares little similarity to compression of an isotropic gelatine material. The current understanding of myolaminar mechanics suggests that shear layers function via reorientation rather than stretching or shortening, and thus may not produce the artefact theorised by Reese et al. (figure 7.37) (394, 395).

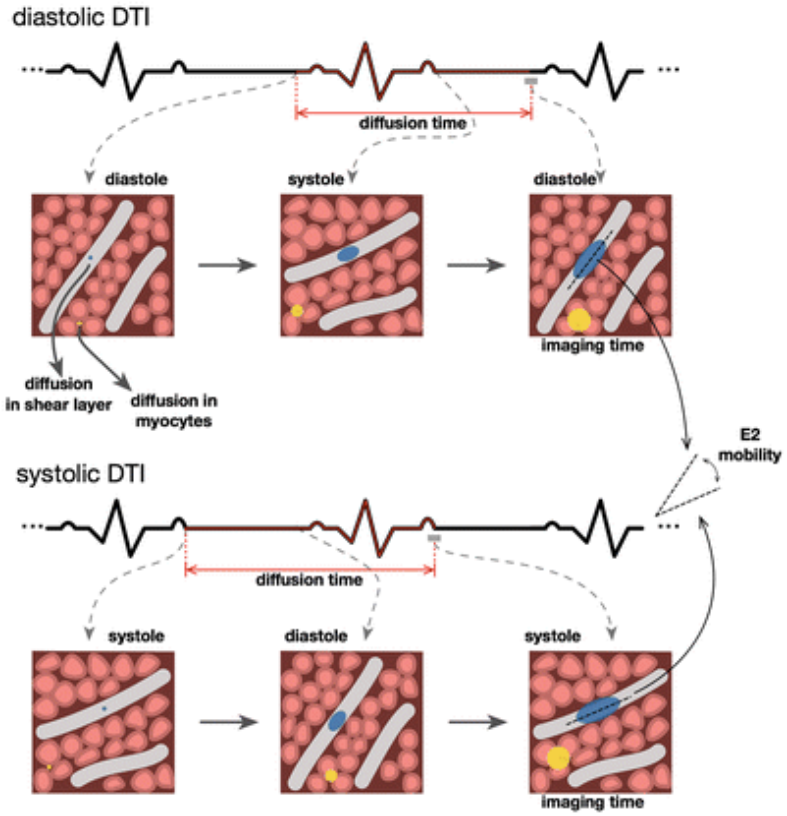

Figure 7.37: Illustration of myocardial diffusion imaging with the monopolar STEAM sequence. The emitted signal from shear layers is likely to outweigh intra-myocyte diffusion as water is freer. In contrast to the isotropic gelatin model, shear layers are theorised to rotate rather than stretch or shorten (395).

In subsequent work the same group highlighted 'sweet spots' in the cardiac cycle where positive and negative strain are balanced such that the net effect of strain on measured diffusion is zero, therefore permitting strain free monopolar STEAM acquisitions (387). However diffusion imaging during cardiac cycle 'sweet spots' creates unique problems. During the sweet spots the myocardium is actively moving, increasing the risk of motion artefacts throughout gradient application. Both ventricular contraction and relaxation strain curves (figure 7.38) are also different, with the likelihood of subtle differences in myocardial shape and positioning and further risk of artefact. Moreover, restricting DTI imaging to the mid points between systole and diastole limits the potential for this technique to improve understanding of myolaminar dynamics.

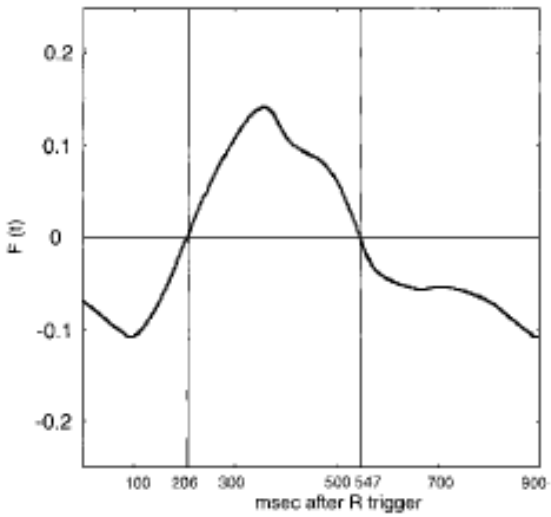

Figure 7.38: In vivo cardiac cycle 'sweet spots': The above graph shows the time course of radial myocardial strain computed from 2D CMR imaging. The subject specific sweet spots, denoted by vertical lines, are determined from mean radial strain and represent the two points were monopolar diffusion gradients can be applied such that the net effect of strain is zero (387).

Finally the group published the bipolar STEAM sequence as a strain insensitive alternative to phasic in vivo diffusion imaging (Dou et al.) (figure 7.34) (151). Although the bipolar gradients are comparatively long, provided the endcoding duration is sufficiently short (<30ms) motion artefacts can be limited (151, 390).

7.5.5: Practical Considerations & Sequence Optimisation

7.5.5.1: Introduction

A number of factors must be considered when optimising DTI for purpose, techniques which aim to improve SNR or diffusion sensitivity must be balanced against acceleration methods. This section covers contemporary methods of sequence optimisation.

7.5.5.2: SSEPI and Parallel Imaging

To ensure that DTI protocols maintain acceptable scan duration, sequence protocols require rapid imaging readouts and often incorporate acceleration methods. The most commonly utilised

imaging method is single shot echo planar imaging (SSEPI) which produces all the echoes required to fill k space after 1 RF pulse (discussed in Chapter 6) (307, 396). In the 1990s the event of SSEPI dramatically reduced imaging times, permitting clinically feasible in vivo DTI for the first time. SSEPI can be combined with additional acceleration methods, such as parallel imaging, to further reduce scanner times. However the advantage of parallel imaging techniques is partially offset by the reduction in SNR associated with under sampling k space.

7.5.5.3: Number of Orientations Acquired

When solving the diffusion tensor, a minimum of 6 unique non-parallel diffusion directions are required, unless the structure displays axial symmetry, in which case only 4 directions are required (347). Greater accuracy is achieved by increasing the acquired directions; cerebral imaging experiments have demonstrated the optimal sampling scheme comprises of 30 unique orientations (328, 397-399). However there are no such experiments in myocardium, and acquiring more directions is at the expense of imaging time. The operator must therefore set the number of orientations based on the study objective and clinical feasibility.

7.5.5.4: Optimum b-Value

The b value determines the diffusion weighting of a sequence, and affects estimates of the diffusion coefficient and other quantitative parameters. In 1995, Eis et al. demonstrated that for a set number of measurements, the most accurate assessment of ADCs were achieved by combining the reference image ($b=0 s mm^{-2}$) with one consistent, rather than multiple b values (400). As the b value increases, so too does the gradient size (G) and/ or duration (δ). During monopolar STEAM in vivo cardiac imaging, the b value is also determined by the subject's heart rate i.e. the duration between gradients (Δ). In practice the applied b value is limited by the scanner's gradient power and myocardial motion, with the bipolar protocol being most susceptible to these limits. SNR losses must also be taken into consideration when setting the b

value, as greater diffusion weighting will result in poorer SNR. A number of studies have investigated optimal diffusion weighting in cerebral imaging, with the optimal value reported to be around 900-1000smm^{-2} (328, 397, 401, 402). At the time of this study there were no available data with respect to the optimal diffusion weighting in myocardium. Previously most in vivo studies have opted for values between 300-500smm^{-2} (151, 294, 359, 360, 366, 368-370, 387).

7.5.5.5: Number of Measurements per Image

As previously discussed, the nature of diffusion imaging is the detection of signal loss, thus DTI is an inherently poor SNR technique, consequently each imaging frame must be repeatedly acquired and the signal from each repetition combined, in a process called averaging, to generate sufficient SNR for diffusion tensor calculation. Once more, there is no study data to guide the optimal number of average in myocardial imaging, however in the context of cerebral imaging, Jones et al., calculated the optimal ratio of diffusion weight images: reference image as 8.7:1 (397). Naturally the more averages acquired, the better the SNR, however once again, in vivo, the number acquired is limited by acceptable scan durations. Additionally, the more averages acquired, the greater the risk of registration artefacts between averages.

7.5.6: Limitations and Artefacts

7.5.6.1: Poor SNR

As discussed above, the main limitation of the DTI technique is poor SNR. This necessitates multiple acquisitions of the same frame to build sufficient signal. The result is significantly longer studies and limited myocardial coverage. The event of high field clinical scanners, such as 3 Tesla, has improved SNR, but the need for averages remains. Poor SNR has an additional knock-on effect on resolution, as larger voxels are required to generate adequate signal.

7.5.6.2: Bulk Motion

Regardless of the sequence protocol, bulk cardiac motion remains a significant limiting factor for cDTI. Even micro-movements, during the relatively quiescent points of the cardiac cycle, can introduce artefacts in signal measurement (391, 403). In theory respiratory artefacts are likely to affect the myocardial signal uniformly, as the whole heart is shifted preventing delivery of both winding and unwinding diffusion gradients with gross signal loss. Conversely, signal losses from myocardial contraction may be comparatively inconspicuous, due to regional or transmural heterogeneity, with greater potential to evade quality control, leading to movement artefacts in the resulting image.

7.5.6.3: Poor Resolution and Gaussian Assumptions

The myocardium is composed of a complex network of cardiomyocytes, approximately 20μm x 100μm. Voxels typically in the order of 2-4mm^2 x 6-12mm for in vivo cDTI (19, 151, 387) may therefore contain more than one myocyte population. DTI makes the assumption that intra-voxel diffusion is Gaussian, with diffusion occurring in an ellipsoid shape. While some intra-voxel myocyte populations will result in Gaussian diffusion patterns, many will not, and the resulting diffusion ellipsoids fail to reflect the complexity of the underlying myocardium. A variety of advanced imaging techniques have been developed to overcome this including multi-tensor models (404), Q ball imaging and diffusion spectrum imaging (318), however presently they are beyond the scope of in vivo cDTI. Directional information from the primary eigenvector, must therefore be interpreted within the context of tensor anisotropy, which gives some indication of intra-voxel diffusion uniformity.

7.5.6.4: Diffusion Weighting Within a Sequence

Any given diffusion sequence protocol will contain additional gradients with inherent diffusion weighting, which can be calculated by: $b= (\gamma G\Delta)^2(\Delta-\delta/3)$. When designing a protocol it is therefore beneficial to keep these contributions to a minimum. When unavoidable, such gradients must be accounted for when assigning the b value to both the diffusion weighted image and the reference image (328, 405).

7.5.6.5: Noise and Fractional Anisotropy

Noise within MRI signal intensities results in scatter, or reduced precision, in cDTI indices (402). However, in the case of anisotropy measures, noise can also introduce bias. For example, when diffusion is truly isotropic the eigenvalues should be equal. The ordering of eigenvalues from largest (primary eigenvalue) to smallest (tertiary) in this case is simply a reflection of the noise. In the presence of noise, some eigenvalues will increase and some will decrease. In each voxel the largest is selected as the primary eigenvector, decreasing in magnitude to the tertiary. Over a number of image voxels, the overall effect is to increase the primary eigenvalue from its true value and reduce the tertiary, while the secondary remains approximately constant. This manifests as a more anisotropic ellipsoid which results in an increased FA. This eigenvalue-repulsion effect persists in anisotropic tissue and is most evident at low b-values where the ratio of signal loss in each encoding direction to the noise level is smaller than at high b-values.

With increasing b-values, at some point the signal in the diffusion encoded images will approach the level of noise in the images. The measured signal loss is then actually the difference between the signal intensity in the reference image and the background noise. As the signal loss is not as large as it would be for the noise free case, the measured diffusion is reduced in this direction. The largest signal loss is the direction of greatest diffusivity and this effect, therefore is most dominant in the primary eigenvalue and a reduced primary eigenvalue results in a loss of anisotropy and a reduced FA value, described by Jones et al. as ‘squashing the peanut’ (406). Both

of these effects are greater at higher noise levels. Tissues with lower true FA are more effected by eigenvalue repulsion than tissues with higher FA and attenuation of the primary eigenvalue at high b-values has a greater effect on tissue with higher FA (figure 7.39) (399, 402, 406, 407).

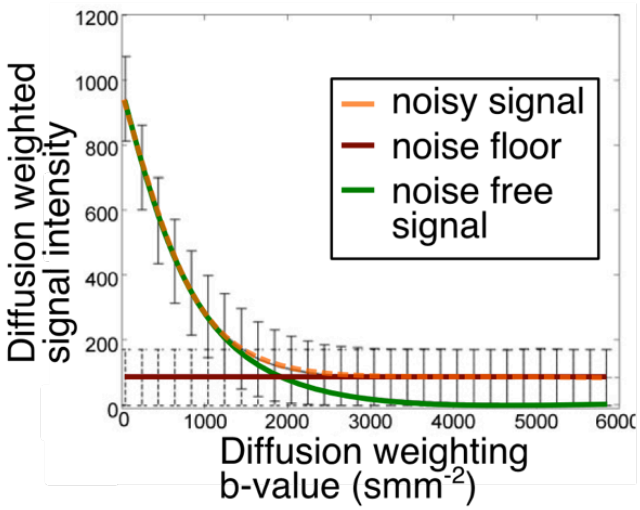

Figure 7.39: Illustration of the impact of b value and noise on diffusion weighting signal intensity. At greater b values signal losses are more pronounced and the diffusion signal intensity is reduced. At higher b values, when the resulting signal intensity is less than the 'noise floor', the measured signal is equal to the difference between the reference imaging and background noise. The resulting measured diffusion is therefore reduced. Adapted from Jones et al. (406)

7.5.6.6: Mean Diffusivity Dependency on the B Value & SNR

Although the ADC of myocardium, and therefore MD, should be independent of the b value, insufficient diffusion weighting can lead to under estimation of MD. Poor SNR, regardless of the b value will have a similar effect. The eigenvalue repulsion effect described above does not affect the MD as the increase of the primary is balanced by the reduction in the tertiary eigenvector. However, the reduction of the primary eigenvalue at high b-values does result in a reduction in the measured MD. While the reduction in FA due to this effect is only seen once the b-value exceeds a certain threshold, the effect of the attenuation of the primary eigenvalue is present even at low b-values, but the underestimation of MD increases with increasing b-value (408) (409).

7.5.6.7: Inhomogeneity of B0 field

Within the main magnetic field, differences in the magnetic susceptibility between adjacent tissues result in B_o inhomogeneities. Inhomogeneities are most evident in areas with large susceptibility differences, such as lung and myocardium. Field variations increase linearly with field strength and are thus exacerbated at 3Tesla (314, 323). Field inhomogeneities behave like a background gradient, altering the phase of the measured signal. During EPI inhomogeneity can also lead to a large distortion in the phase encoding direction. The true impact of field inhomogeneity on quantitative cDTI parameters is unknown, however localised cardiac 'shimming' has been demonstrated to improve field homogeneity (323).

CHAPTER 8: METHODS

8.1: In vivo Cardiovascular Diffusion Tensor Imaging Sequence Development at the Royal Brompton Hospital

8.1.1: Introduction

In vivo cDTI is technically challenging, with inherently poor SNR. The event of higher field clinical CMR scanners therefore brought new opportunities due to the intrinsically higher SNR and longer T1 values. In 2010 a 3 Tesla scanner was installed in the NIHR Biomedical Research Unit at the Royal Brompton Hospital, which paved the way for a implementation of a reliable in vivo cDTI sequence.

8.1.2: Monopolar STEAM Sequence Development

Initial sequence development work was undertaken by physicists Sonia Nielles-Vallespin and David Firmin, with collaborative support from David Sosnovik (146, 365) and Timothy Reese (360, 366) from the Martinos Centre for Biomedical Imaging, Massachusetts General Hospital. Early post processing was performed by Choukri Mekkaoui (155), also of Massachusetts General Hospital, and subsequently by Pedro F. Ferreira, who established a unique in-house built platform for post processing of future cDTI acquisitions.

Initial experiments with spin-echo and bipolar stimulated echo acquisition mode (STEAM) sequences (see chapter 7 for a description of the various sequence types) were disappointing, with significant artefact due to bulk cardiac motion during diffusion gradients. Future experiments therefore focused on the monopolar STEAM sequence described by Reese et al. (figure 8.1) (360).

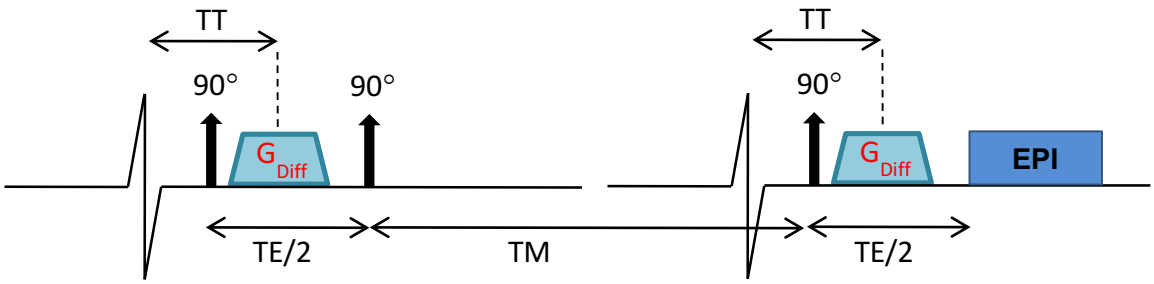

Figure 8.1: Monopolar diffusion weighted stimulated echo sequence (DW-STEAM) adopted by the Royal Brompton Hospital. After a 90° pulse the initial winding diffusion gradient is applied at a set trigger point (TT) after the R-wave. This is followed by a second 90° pulse applied at half the echo time (TE). The diffusion mixing time (TM) continues on till the third 90° pulse, following which the diffusion unwinding gradient is timed to an identical TT. The sequence has an EPI read out timed to place the acquisition of the central k-space line at TE/2 from the third 90degree pulse, and is also combined with parallel imaging to reduce the duration of the EPI readout.

8.1.3: Comparison of Breath Hold and Navigator Acquisitions

This sequence was implemented with both multiple breath holds (BH) and diaphragmatic navigators (NAV) and assessed for reproducibility of quantitative cDTI parameters (19). Ten healthy volunteers were scanned on two separate occasions with both BH and NAV on each sitting. Imaging was performed in 3 mid ventricular short axis slices during the mid-systolic pause for both b_{ref} and b_{main}. Diffusion weighting was set at b=350s/mm^2 based on previous literature as there were no available data on optimal values in myocardium.

There were no significant statistical differences in FA, MD and HA values between the three slices or regionally around the ventricle, thus cDTI data was post processed for global FA and MD values. HA data were calculated for endocardial, midendocardial, midepicardial and epicardial layers (figure 8.2).

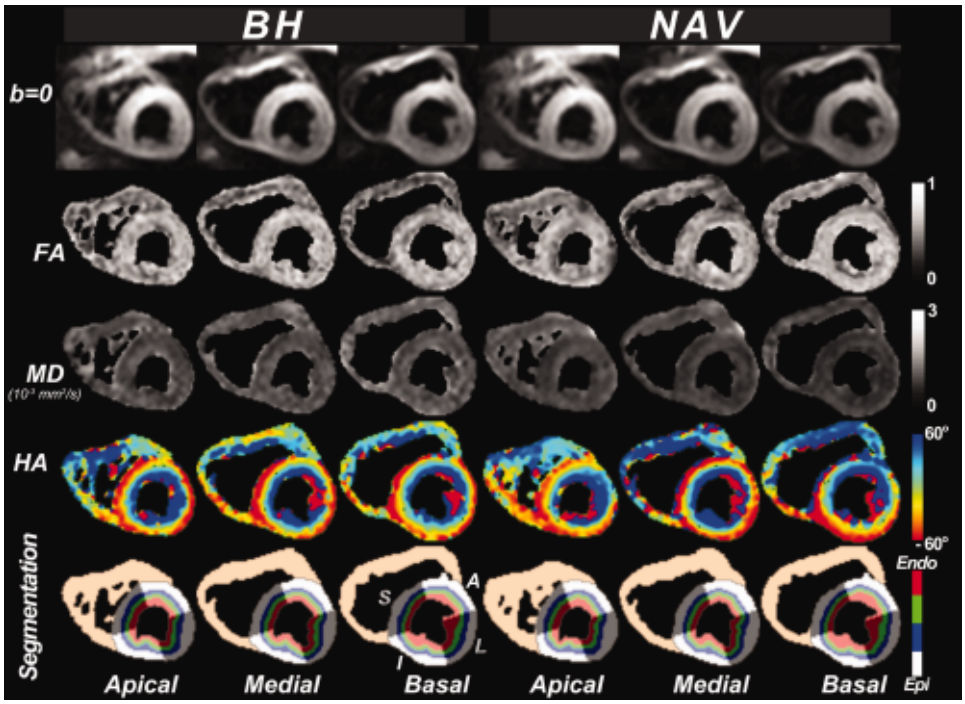

Figure 8.2: BH and NAV images from an example patient. The three slices are labelled apical, medial and basal. B_{ref} images and derived FA, MD and HA parameter maps are displayed for each slice with both techniques. HA maps are shown in a rainbow like colour scale, Excellent reproducibility is demonstrated for both techniques at all three levels. In each case the HA is seen to rotate from a left-handed (red) orientation to a right-handed orientation (blue) (19).

The technique was successful in all subjects and both techniques were highly reproducible. Comparing both techniques mean FA values were 0.6±0.04 and 0.6±0.03, and MD values were 0.8±0.02 x$10^{-3}$$mm^2$/s and 0.9±0.03x$10^{-3}$$mm^2$/s for BH and NAV respectively, with no statistically significant difference. Mean HA values for BH were: Endocardium 23±9°, midendocardium 20±6°, midepicardium -1±7°, epicardium: -17±7° and for NAV were: Endocardium 8±8°, midendocardium 14±9°, midepicardium -1±8°, epicardium: -13±6°. As a result there were statistically significant HA differences between techniques in the endocardial and midendocardial layers (figure 8.3). On further analysis this appeared to be driven by a small percentage of frames which were accepted in error by the navigator, which consequently reduced the SNR of the b=350s/mm^2 NAV acquisitions.

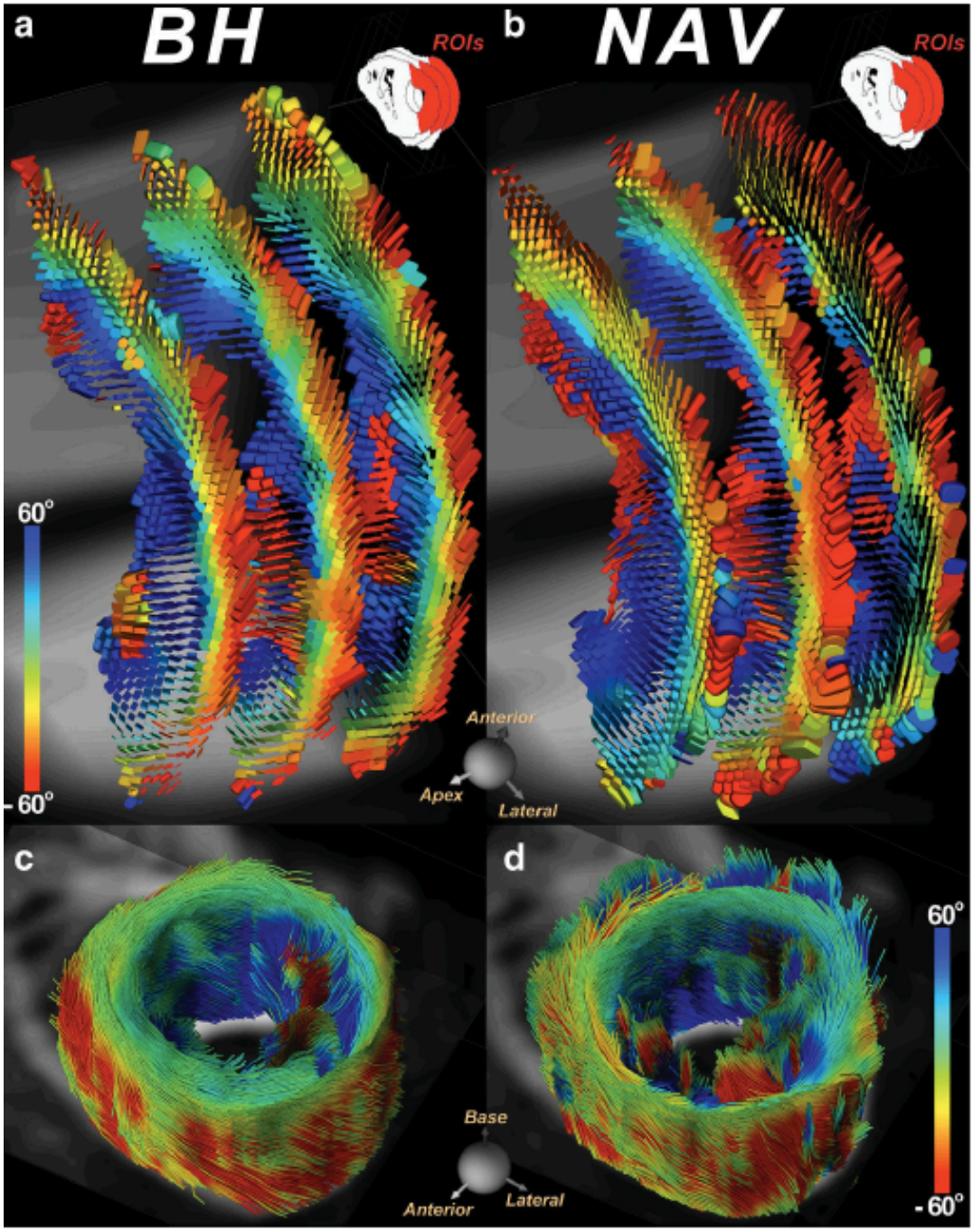

Figure 8.3: Three-dimensional visualisation of the tensor information derived from both NAV and BH sequence protocols. a & b illustrate the full tensor as superquadric glyphs for the lateral LV wall in all three slices. The glyphs are colour coded according to the helix angle and the shape of the glyphs reflects the degree of anisotropy. In both a & c the subendocardium has some contribution from papillary muscles (red), the glyphs the progress from a right-handed (blue) orientation to a left-handed orientation in the epicardium (red). Subendocardial and subepicardial glyphs are more rounded, i.e. more isotropic, in the NAV sequence due to the comparatively poorer SNR. c & d display the primary eigenvector data in all three slices in tractograms, with colour coding according to the helix angle. Stretched Tracts with a greater spread of transverse angles in the in the subendocardium and subepicardium are again indicative of reduced SNR (19).

8.1.4: Comparison with Previous Literature

8.1.4.1: Mean Diffusivity

Compared to the literature MD results concurred with Reese et al. (0.87±x10^{-3}mm/s, 1.5Tesla, voxel size 3x3x9)(360), but were greater than Dou et al. (0.60±0.11x10^{-3}mm/s, 1.5Tesla, voxel size 4x4x12)(151) and Wu et al. (0.65±0.03x10^{-3}mm/s, 1.5Tesla, voxel size 1.9x1.9x8)(370). The exact cause of the disparity is unclear but is likely, in part, attributable to differences in resolution, post processing techniques, field strength and SNR between studies. In vivo MD estimates cannot be compared to ex vivo studies due to the change in diffusivity with tissue preservation techniques.

8.1.4.2: Helix Angle

In vivo helix angle ranges quoted in the literature are highly varied, however the range derived from this sequence (40 to -32°) was notably narrower than previous ex vivo (85, 143, 144, 147, 153) and histological reports (3). The limited resolution of this sequence is one possible explanation; this results in averaging of myocyte orientations within a voxel, with potential loss of angular spread. Other possible contributors include the exclusion of edge pixels with ROI drawing and thresholding during post processing.

8.1.4.3: Fractional Anisotropy

Quantitative estimates of myocardial anisotropy via FA were again similar to Reese et al. (0.65±0.03)(360); but slightly less anisotropic than Dou et al. (0.7±0.1)(151); more anisotropic than Wu et al. (0.33±0.02)(370); and more anisotropic than ex vivo estimates by Abdullah et al. (0.27±0.02)(384) and Winklhofer et al. (0.37±0.08)(380). Again discrepancies are likely attributable to differences in resolution, SNR, post processing techniques and, in the case of the ex-vivo data, tissue fixation effects(410)

8.1.5: Summary

This study demonstrated successful implementation of the monopolar STEAM sequence for in vivo cDTI, in a small cohort of healthy volunteers. Both NAV and BH protocols demonstrated a high degree of reproducibility for all quantitative parameters. However, the BH protocol was favourable, with greater reliability, translating to improved SNR in the b=350s/mm^2 data. This work therefore set the foundations for larger 3Tesla cDTI studies in healthy volunteers and comparative analyses with patients with hypertrophic cardiomyopathy.

8.3: In vivo Diffusion Weighted Stimulated Echo Acquisition Mode (DW-STEAM) Sequence Implementation

8.3.1: Introduction

The initial focus of this project was the evaluation of the Nielles-Vallespin et al. (19) DW-STEAM sequence in a large cohort of healthy volunteers and patients with hypertrophic cardiomyopathy. Given the limited experience of in vivo cDTI at 3Tesla, the aim was to ensure consistent high quality image acquisition through refinement of the cDTI imaging protocol. This work was conducted in tandem with sequence optimisation work, led by physicist Dr. Andrew Scott, and post-processing development lead by Dr. Pedro Ferreira, with supervision from Prof David Firmin, to ensure continual progression of the cDTI technique.

8.3.2: Cardiovascular Magnetic Resonance Imaging Hardware

All CMR data were acquired on a clinical 3Tesla scanner (Magnetom Skyra, Siemens AG Healthcare Sector, Erlangen, Germany) equipped with an anterior cardiac 18-element matrix coil, a 48-element spine matrix coil, and a standard 45-mT/m gradient strength at 200T/m/s maximum slew rate.

8.3.3: DW-STEAM Acquisition Protocol

The DW-STEAM sequence is shown in figure 8.1. A single-shot EPI readout was combined with GRAPPA parallel imaging (acceleration factor of 2) to reduce to the duration of the EPI readout (305). The echo train was further shortened with zonal excitation which reduces the field of view in the phase encoding direction (411). This has the added benefit of reducing image distortion due to B_0 inhomogeneity. As per Nielles-Vallespin et al. diffusion weighting was set at b=350s/mm^2 in the absence of data indicating the optimal diffusion weighting in myocardium, and based on previously literature where b values ranging from b=300-420s/mm^2 were demonstrated as sufficiently sensitive to interrogate myocardial structures (366, 367, 369, 370, 387). However in the DW-STEAM sequence the duration between gradients (Δ), and thus the b value, is dependent on the subject's heart rate, such that a heart rate of 60bpm is consistent with b=350s/mm^2, but faster heart rates result in less diffusion weighting and slower heart rates increase the diffusion weighting. During the reference 'b=0' acquisitions, diffusion weighting gradients are replaced with spoiler gradients to avoid unwanted magnetisation pathways ensuring equal T1- and T2-weighting in all images, however these spoilers still carry a degree of diffusion encoding which must be accounted for. Consequently the true b value of the reference for this sequence was estimated at b=15s/mm^2 (19).

After initial LV localisation images a short axis retro-gated SSFP cine sequence was acquired at mid ventricular level to determine the timing of peak systole and the most quiescent period of diastole, which were used as the trigger times (TT) for cardiac DTI acquisitions. Fat saturation was applied to minimise the contributions of epicardial and chest wall fat to the images. Localized first and second-order shimming and frequency adjustment were performed over the extent of the LV within the imaging planes. The sequence has the following parameters for at a heart rate of 60bpm: TE 23ms, TR 2000ms (2 RR intervals), echo train length = 24 readouts, duration 13ms (depending on the field of view), field of view 360 x 135mm^2, in plane spatial resolution

2.8x2.8mm^2 interpolated to 1.4x1.4mm^2 with a slice thickness of 8mm. Three ventricular slices were acquired with a slice gap of 4mm.

The DW-STEAM sequence was implemented with the multiple BH technique described above (19). Each BH has a duration of 18 heart beats which is comprised of the following:

- 2 heart beats for EPI phase correction lines
- 2 heart beats for external GRAPPA reference lines
- 2 heart beats for the b reference images
- 12 heart beats for 6 non-parallel diffusion encoding directions, b=350s/mm^2

Each slice acquisition was repeated a minimum of 8 times, but typically 10 times, to ensure 8-10 averages per slice for sufficient SNR.

8.3.4: DW-STEAM Scanning Observations and Protocol Developments.

During sequence implementation a number of limitations were observed which prompted DW-STEAM protocol adjustments (figure 8.4).

8.3.4.1: Poor Breath Holding

As breath holding is required for 18 beats for each average, it is not surprising that some subjects were unable to hold their breath for the full acquisition. Breathing before the sequence is completed results in loss of data from the final direction. Initially this meant that the same direction was affected each time. To avoid these effects, the sequence was amended such that the directions were acquired in a different order for each average (each breath hold).

8.3.4.2: Delayed Breath Holding Start

Failure to commence breath holding in time with the start of the sequence was observed to result in a ghosting artefact throughout all the directions. This was attributed to the mis-registration of the phase correction and parallel imaging reference lines with the reference and diffusion

encoded data. In order to avoid this, patients were given more time to commence breath holding and chest wall movements were observed in the control room with a video link to the scanner bore camera.

8.3.4.3: Arrhythmia

Poor image quality was observed in patients with atrial fibrillation, bi or trigeminy, Wenckebach, sinus arrhythmia and frequent ectopy. This was thought to be due to subtle changes in ventricular size between the 2 diffusion gradients. As the heart tissue is not in the same position at the timing of the first and second diffusion encoding gradients, the phase slope created by the first diffusion encoding gradient is not completely reversed by the second gradient and signal loss occurs. Patients with rare ectopy were included by acquiring additional averages, however patients with all other aforementioned rhythms were excluded due to poor data quality.

8.3.4.4: Bradycardia

Poor quality data was observed in patients with heart rates under 50 beats per minute. This was attributed to T1 decay during the mixing time.

8.3.4.5: Diastolic Trigger Failure

Intermittent image loss was observed in some patients with late diastolic trigger times. This was found to be a result of the EPI data collection overlapping the R-wave of the next cardiac cycle. The scanner ignores the R-wave during the imaging gradients and the trigger is missed. To prevent this, the acquisition window and repeat time (TR) were minimised during diastolic acquisitions. Where possible the trigger time was also set to the beginning of the diastolic pause, or quiescent period.

A: Good acquisition

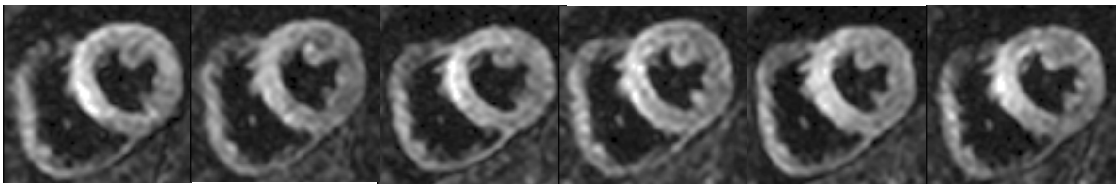

B: Poor breath holding

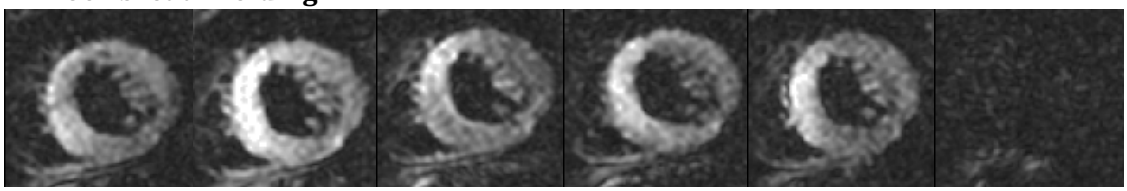

C: Delayed breath hold start

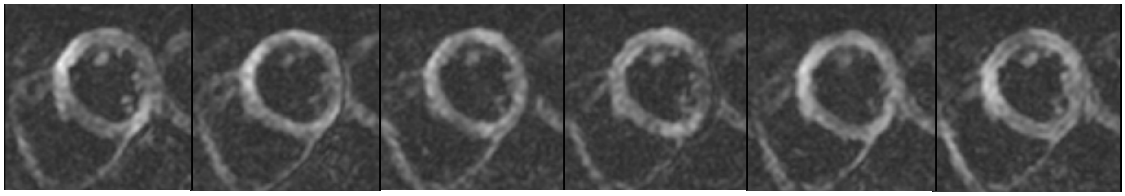

D: Sinus arrhythmia

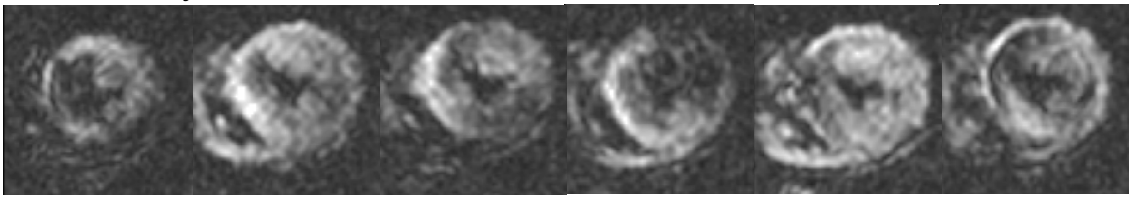

E: Bradycardic signal loss

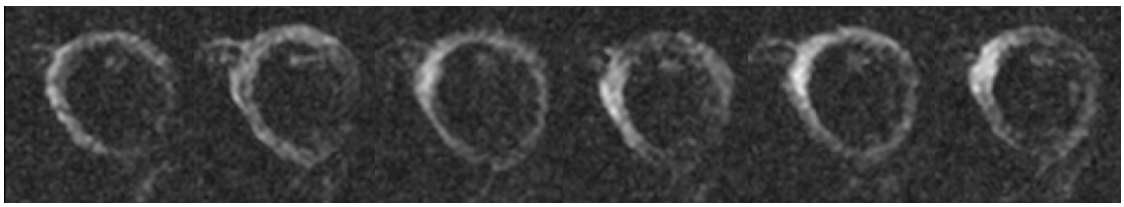

F: Diastolic trigger failure

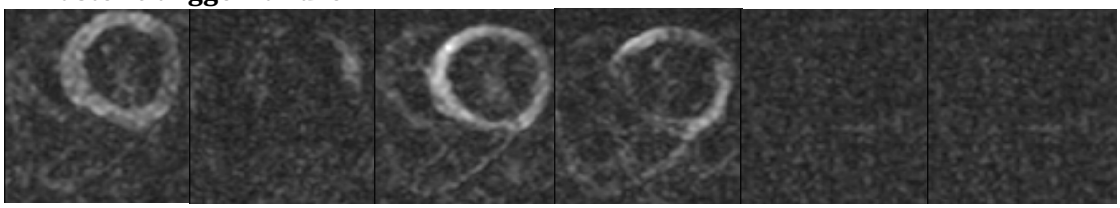

Figure 8.4: Examples of diffusion weighted images from in vivo cDTI acquisitions. Each row demonstrates the 6 diffusion directions acquired from a single breath hold. **A**: Optimal acquisitions with good quality data from all 6 directions. **B**: Poor breath holding leads to loss of data from the final direction. **C**: Late breath holding affects the phase correction lines and GRAPPA reference lines leading to ghosting artefacts through all 6 directions. **D**: Prominent sinus arrhythmia or frequent ectopy can result in poor quality data from 1 or more directions. **E**: In subjects with heart rates slower than 50 beats per min, greater signal losses can affect image quality. **F**: Late diastolic trigger times can result in image loss through 'sequence failure'.

8.3.5: Diffusion Tensor Imaging Analysis

8.3.5.1: Initial Post Processing

All diffusion tensor data were analysed using customised software written by Dr Pedro Ferreira, Royal Brompton Hospital, using MATLAB (Mathworks, Massachusetts, USA), (figure 8.5). Each of the processing steps are outlined below with examples.

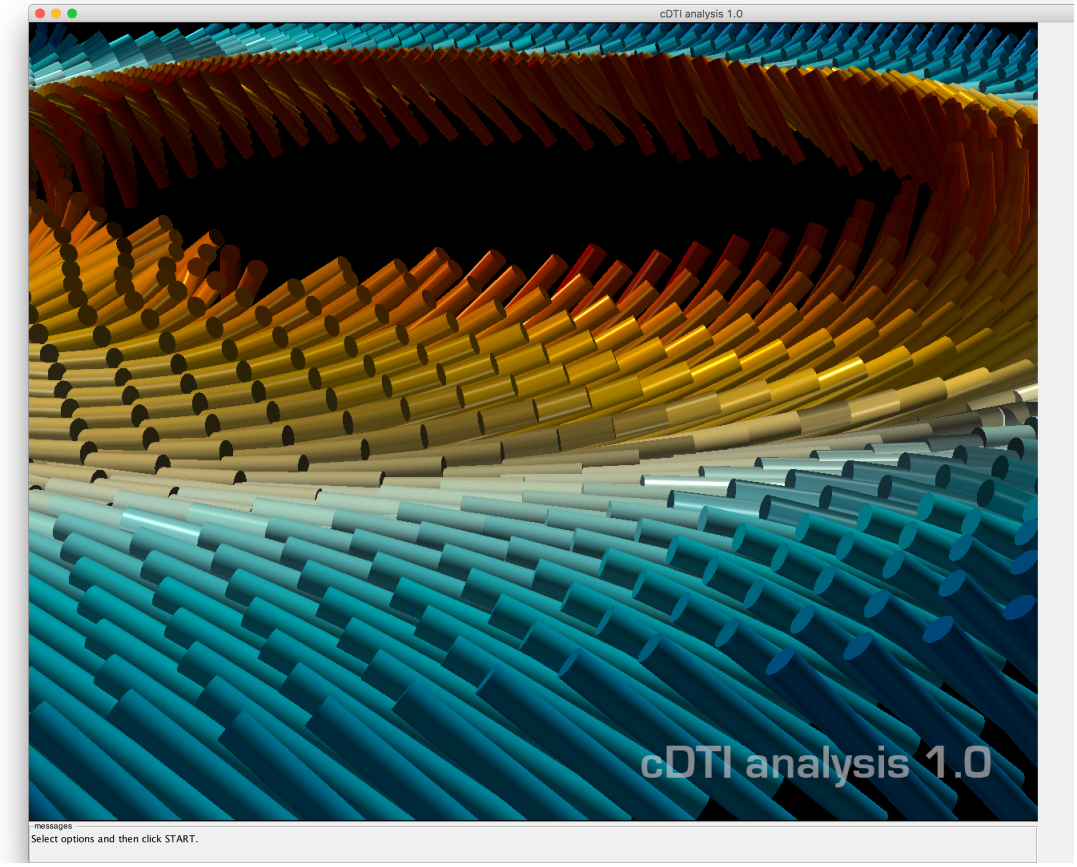

Figure 8.5: Customised cDTI analysis platform

8.3.5.1.1: Rejection of bad frames and co-registration

During the first processing step, the images for each diffusion encoding direction were screened and frames corrupted by breathing or arrhythmia artefact were rejected:

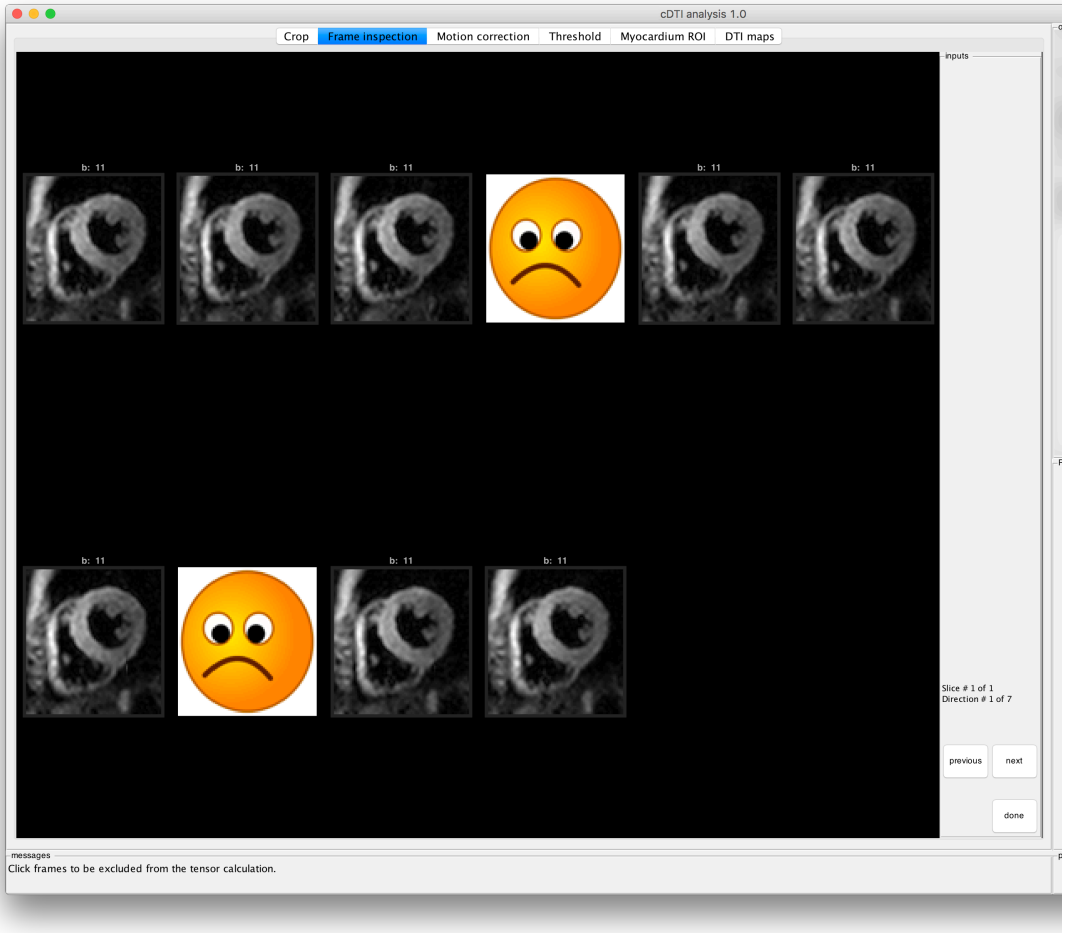

Figure 8.6: Rejection of bad frames. Each average for each phase encoding step was reviewed. Poor quality frames were manually rejected.

The accepted frames were then co-registered to correct for intra-subject variations in breath-hold position (in-plane only) with a cross-correlation based algorithm for rigid displacement (figure 8.7)(412):

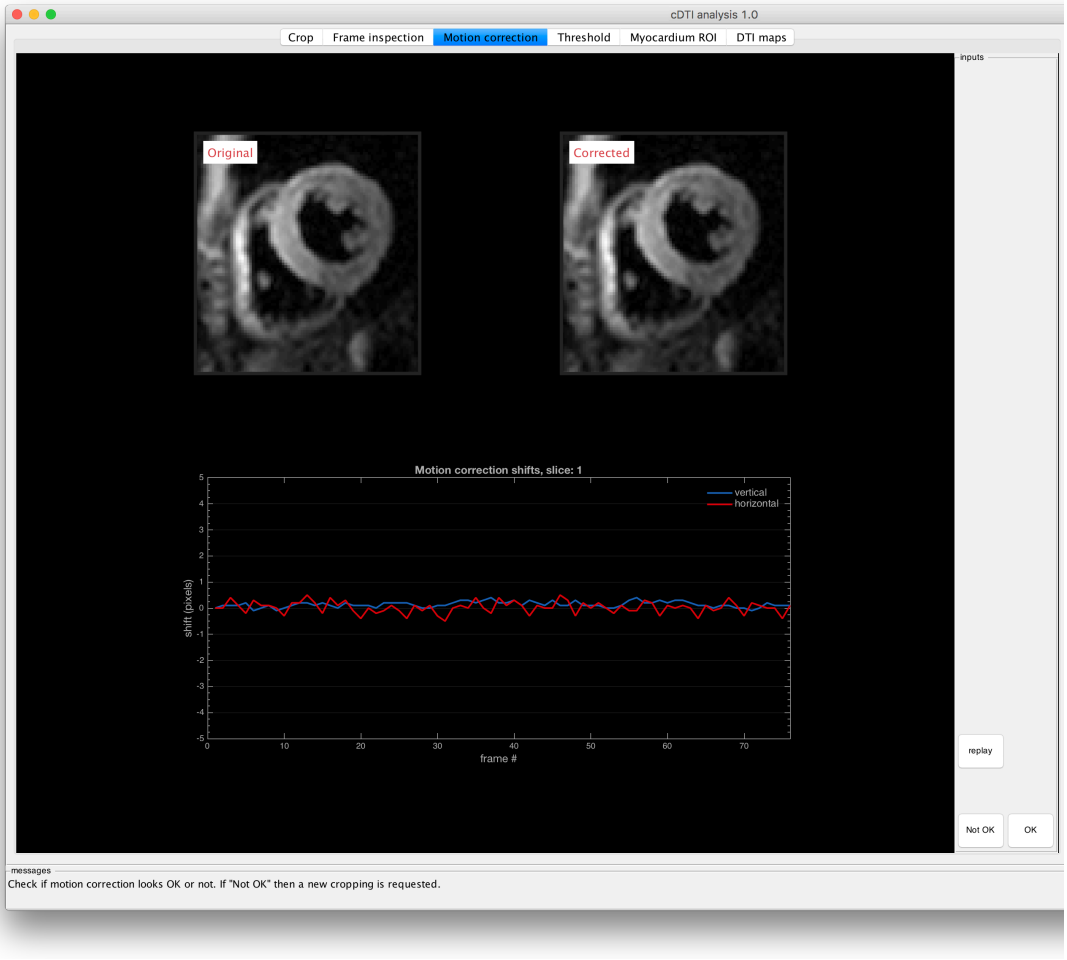

Figure 8.7: Each average for each direction are co-registered, adjusting for inplane motion.

8.3.5.1.2: Myocardial thresholding and selection

The myocardium was segmented from the blood pool using simple thresholding:

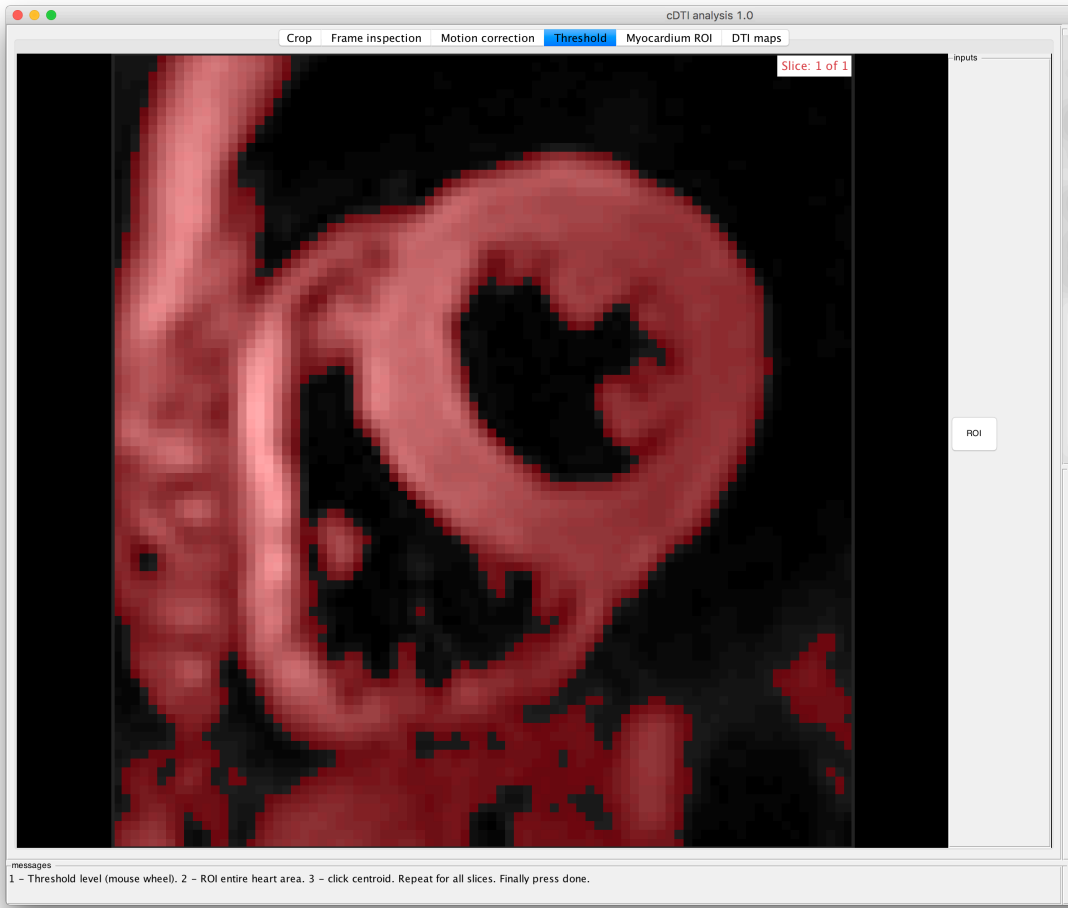

Figure 8.8: Manual thresholding the myocardium

The myocardium was then manually isolated from the surrounding structures:

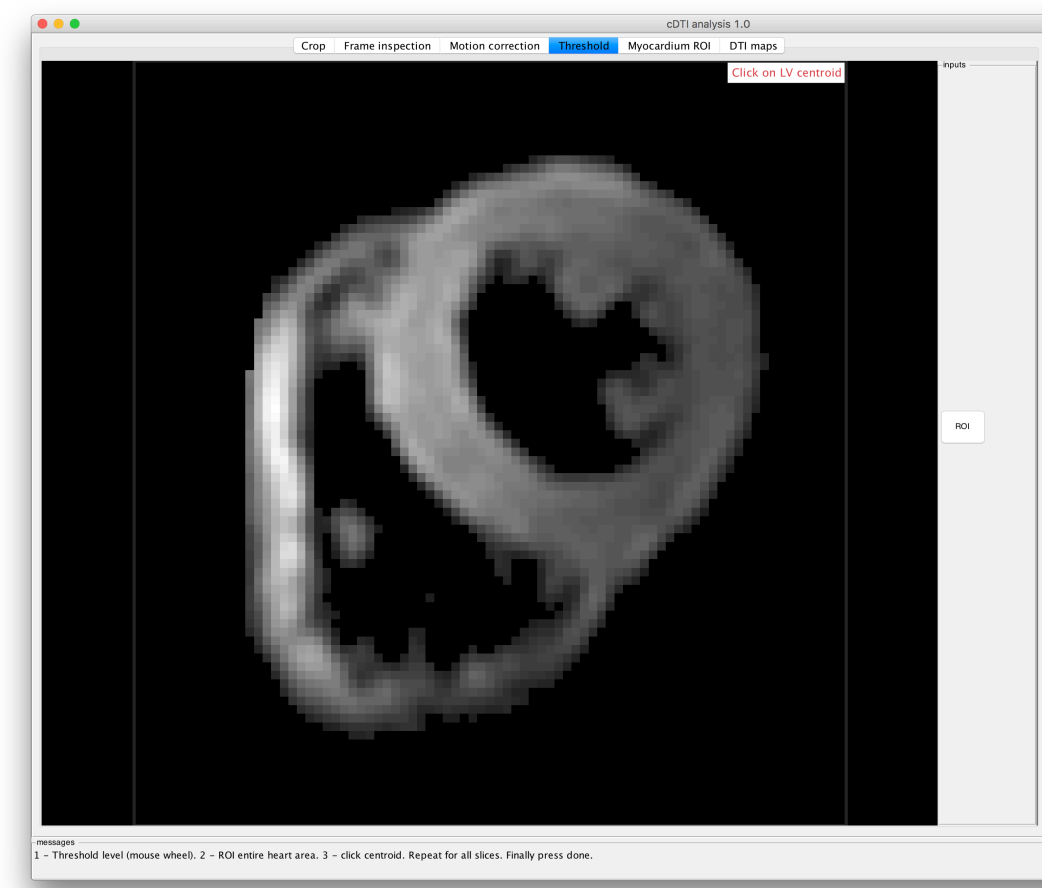

Figure 8.9: Surrounding structures such as the diaphragm and chest wall are manually excluded from the image.

8.3.5.1.3: Region of interest drawing & segmentation

Following these steps the program generates a pixel wise map of approximate myocardial helix angulation. This aids the selection of both the left ventricular endocardial and epicardial borders by highlighting the contribution from vertical papillary muscles and the right ventricle, which were manually excluded from analysis:

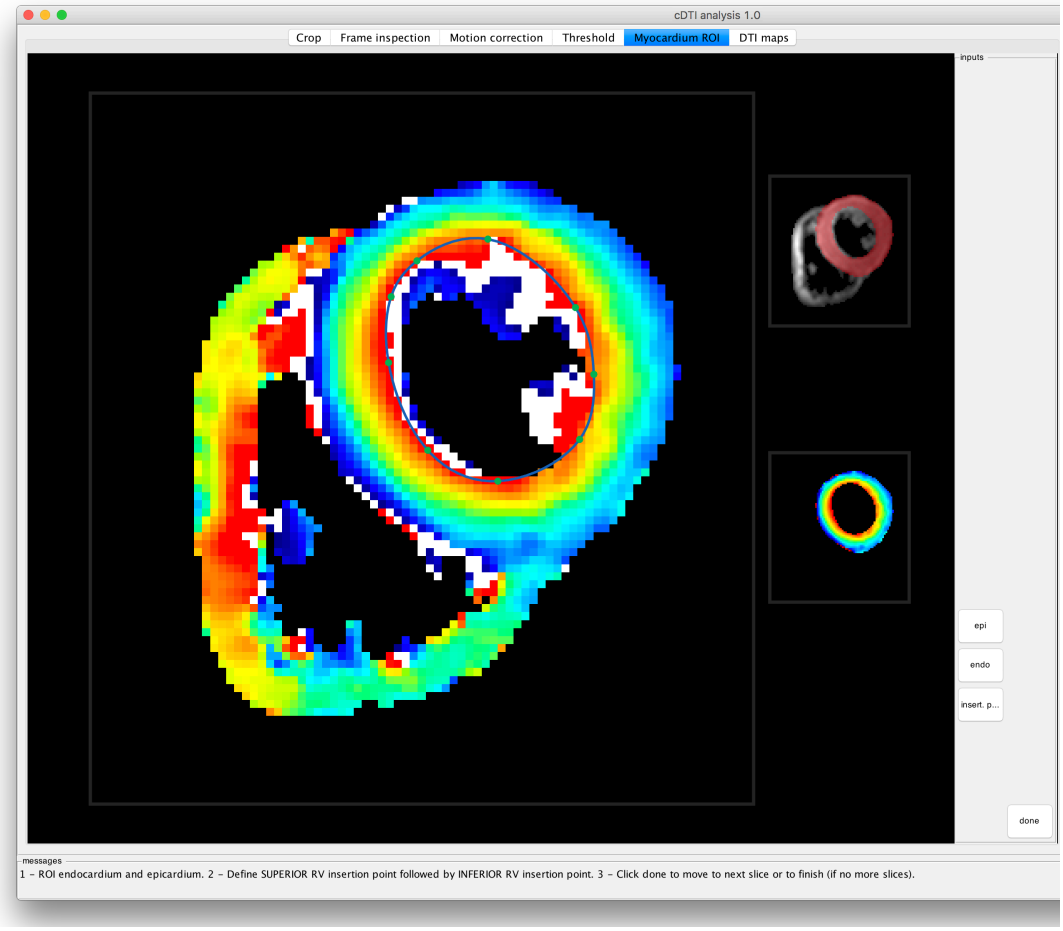

Figure 8.10: Edge pixels and papillary muscles with a vertical/non-helical axis are visualised in white are excluded from the analysis.

The right ventricular superior and inferior insertion points were then identified to guide regional segmentation of the left ventricular myocardium:

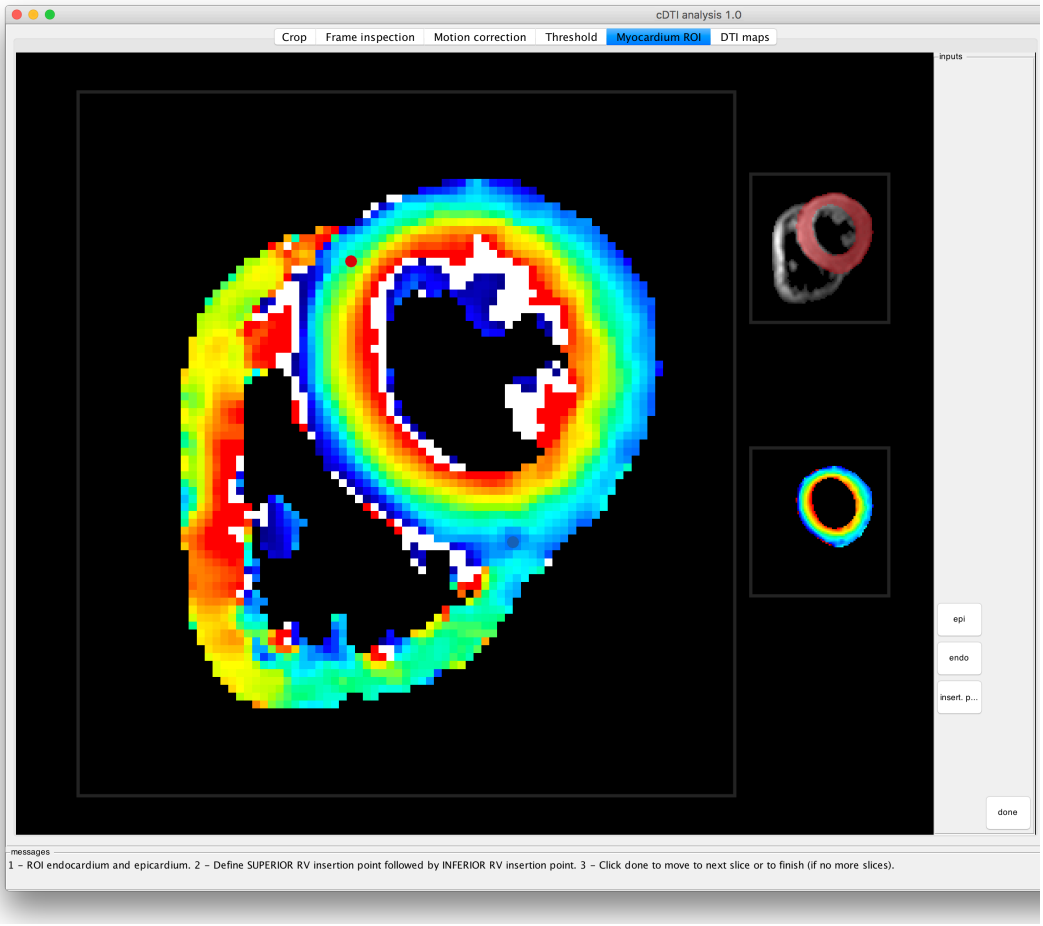

Figure 8.11: A red dot is placed in the mid myocardium (green helix angle) adjacent to the superior RV insertion point.

8.3.5.2: Diffusion Tensor and Eigensystem Calculation

All tensor and subsequent eigensystem calculations were performed within the software written by physicist Dr Pedro Ferreria. A rank 2 diffusion tensor was generated for each voxel using the signal intensity data from each of the six averaged directions and the reference image (402). The eigensystem (eigenvectors: e1, e2 and e3 and their respective eigenvalues: λ_1, λ_2 and λ_3) were then calculated for each tensor. A small number of eigenvalues (approximately 3%) were found to be negative. Diffusivity cannot be negative; negative values are therefore the likely product of local artefact, noise or mis-registration. To resolve this issue negative eigenvalues were replaced with the mean of the corresponding non-negative eigenvalues in neighbouring voxels.

8.3.5.3: Quantitative Diffusion Parameter Calculations

8.3.5.3.1: Introduction

Once the diffusion tensor and eigensystem is calculated for each voxel, cDTI data can be further analysed with quantitative parameters. Numerous quantitative parameters exist and the parameters selected for analysis can be chosen based on the research question.

8.3.5.3.2: Mean diffusivity

MD(ADC) is one of the most widely quoted measures of diffusivity and therefore serves as a useful benchmark between studies. MD reflects underling tissue composition and is higher in less structured tissues with high water content, compared to dense tissue structures (343). The potential sensitivity of in vivo MD to myocardial disease processes had been highlighted by investigators such as Wu et al., who demonstrated greater ADC (MD) measures in regions of myocardial infarction, compared to adjacent and remote myocardium (369, 370). Nguyen et al. later highlighted that MD has the potential to detect myocardial fibrosis without the need for contrast (342) and could new insights into myocardial composition in HCM (293). The MD was calculated per voxel as follows:

$$MD\ (ADC) = \frac{\lambda_1 + \lambda_2 + \lambda_3}{3}$$

8.3.5.3.3: Fractional Anisotropy

Diffusion anisotropy was assessed in each voxel via FA, using the following calculation:

$$FA = \sqrt{\frac{3}{2}} \sqrt{\frac{(\lambda_1 - (\lambda))^2 + (\lambda_2 - (\lambda))^2 + (\lambda_3 - (\lambda))^2}{\lambda_1^2 + \lambda_2^2 + \lambda_3^2}}$$

FA ranges from 0 to 1, with 0 representing a completely isotropic structure and 1 representing a completely anisotropic structure (332). Prior to cDTI there had been no means of non-invasively assessing myocyte organisation. Tseng et al. highlighted the potential diagnostic utility of FA by demonstrating reduced FA in the septum of HCM patients compared to healthy controls (294), however further analysis is required in larger cohorts and across HCM phenotypes.

As discussed above, previous in vivo estimates of both myocardial FA and MD have varied greatly, the degree to which technical factors such as sequence type and post processing techniques have contributed remains unknown. In our centre Nielles-Vallespin et al. demonstrated intra-centre reproducibility in small cohort of healthy volunteers (19), the logical next step therefore was to examine reproducibility within our patient population of hypertrophic cardiomyopathy; inter-centre reproducibility; and the natural variability of these parameters across a larger study population.

8.3.5.3.4: Helix angle

The primary eigenvector (e1) was presumed to be aligned with myocyte orientation (142-145). Primary eigenvector data can be represented in a number of ways (147, 150), however the most

common format is the helix angle (HA). HA calculation requires the definition of the local cardiac coordinate system: The longitudinal axis was aligned parallel to the left ventricular long axis, from the apex to the base; the circumferential axis was defined perpendicular to the longitudinal axis and tangential to the epicardial surface, running in a counter clockwise direction when viewed from the base to apex; and finally the radial axis was derived from the cross product of the previous two axes and runs from the centre of the left ventricular chamber towards the epicardium (figure 8.11). For each voxel, e1 was projected on the local wall tangent plane; the HA was then defined as the angle between this projection and the circumferential plane, with the range -90 to 90°. The angle was positive (right-handed helix) if rotated in a counter-clockwise direction from the circumferential plane, when viewed from the epicardium inwards, and negative (left-handed helix) if rotated clockwise. Typically, the HA progresses transmurally from negative epicardially to positive in the endocardium. HA data was therefore represented in transmural subdivisions.

8.3.5.3.5: Helix angle gradient

Primary eigenvector data can also be represented by the transmural helix angle gradient (HAG). This method produces a single transmural value, which better lends itself to statistical comparisons than an angle with interchangeable polarity. The gradient was calculated from best-fit radial projections running from the centre of the ventricle to each pixel in the epicardial border. This data was then either represented as degrees per mm wall thickness (°/mm) or degrees per percentage depth (°/% depth). The caveat to this method is that drawing a best fit line represents data smoothing and makes the assumption that HA varies proportionally to transmural depth; HAG comparisons were therefore supported by descriptive HA data.

8.3.5.3.6: Secondary eigenvector angle

The secondary eigenvector (e2) is perpendicular to e1, in the cross-myocyte plane. It is the second largest eigenvector and is presumed to align with sheetlet and shear layer microstructures (7, 8, 85, 144, 374). The secondary eigenvector angle (E2A) was calculated by first defining the cross-

myocyte direction, perpendicular to both e1 and the radial direction, for every voxel (figure 8.12). E2 was then projected on to the cross-myocyte – radial plane and E2A was calculated as the angle between this projection and the cross-myocyte direction. The angulation was measured in the range -90 to 90, with positive angles indicating clockwise rotation away from the cross-myocyte plane and negative angles indicating anti-clockwise rotation.

8.3.5.3.7: Secondary eigenvector angle mobility

The change in E2A between cardiac phases in a subject was referred to as 'E2A Mobility'. This was calculated as the difference in mean, absolute E2A values, between systole and diastole. Absolute E2A values are E2A without the polarity, and were utilised in mobility calculations to permit appreciation of the total angular change relative to the local wall tangent plane (figure 8. 11)

8.3.5.3.8: Tractography

To aid visualisation of myocyte orientation derived from the primary eigenvector, the primary eigenvector of adjacent voxels was processes into tracts using a Runge-Kutta approach with PARAVIEW (Kitware, NM, USA). Tracts are colour-coded according to the local helix-angle. Due to the extensive data smoothing associated with this technique, tracts were utilised for visualisation only, with no quantitative analysis.

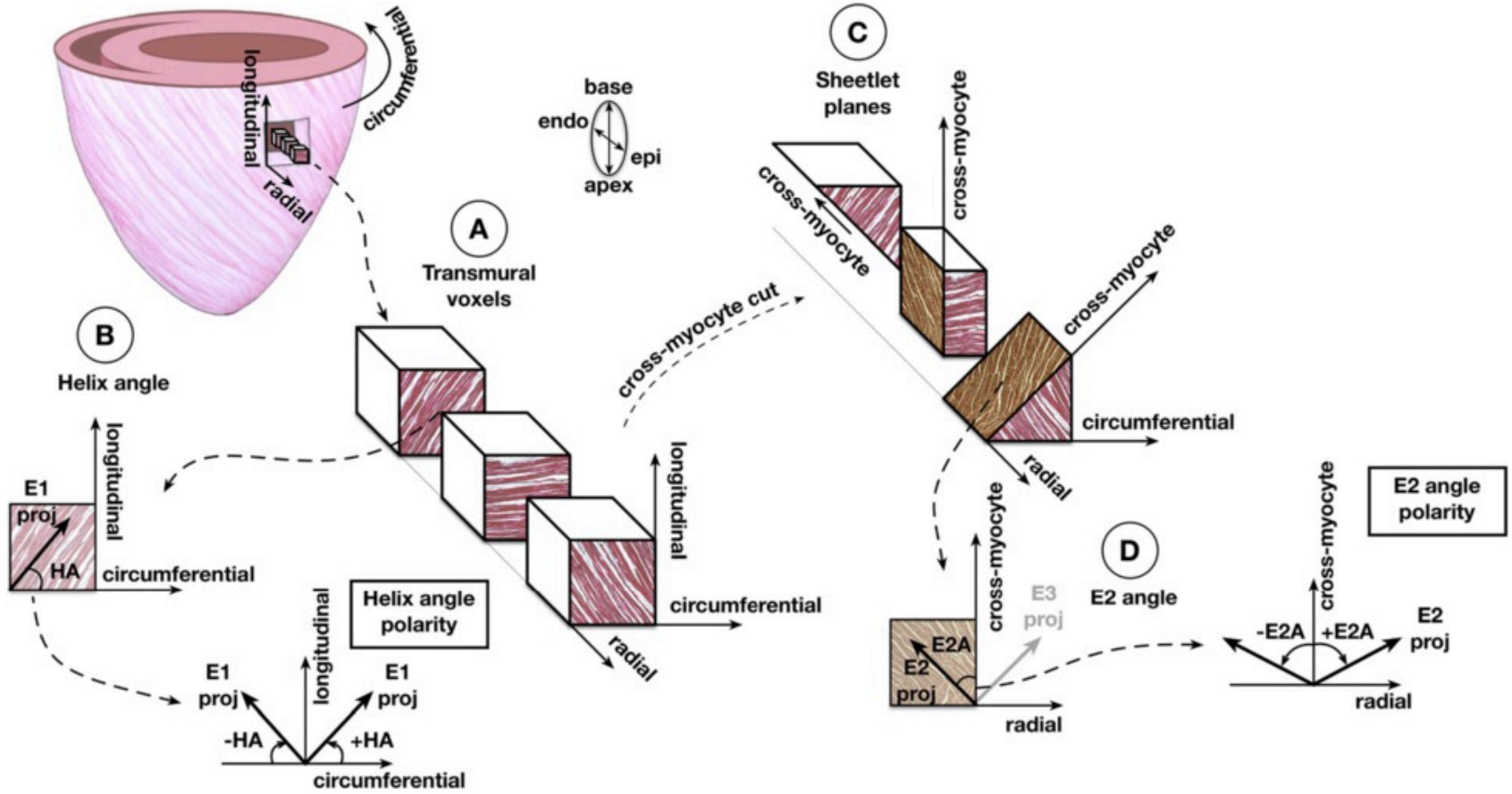

Figure 8.12: Diagram illustrating how helix angle (E1A) and E2A values were calculated for each voxel. **A)** Three non-contiguous voxels are represented at increasing transmural depth from the subepicardium to subendocardial. The derived orthogonal cardiac coordinates, (longitudinal, circumferential and radial) are marked. **B)** Helix angle is calculated between the circumferential direction and the projection of the primary eigenvector, presumably parallel to myocytes, in the tangential plane shown. Examples of positive and negative helix angles are shown below. **C)** The voxels are each sectioned perpendicular to E1proj to derive the cross-myocyte plane. Note this plane rotates transmurally as E1 rotates. E2A it presumed to align with sheetlet and shear layer microstructures, which are represented with brown shading. **D)** The E2 angle is measured between the secondary eigenvector projection and cross-myocyte direction in the wall tangent plane. Examples of positive and negative E2 angles are shown on the right reproduced from Ferreira, Kilner, McGill et al. (395)

8.4: Assessment of Left Ventricular Volumes, Function and Mass

8.4.1: Introduction

CMR provides accurate assessment of ventricular volumes, mass and EF due to its accuracy and reproducibility (41, 413, 414). Its lack of ionising radiation gives it a favourable profile for safe repeat/ surveillance imaging. Unlike echo, images are not limited by acoustic windows.

8.4.2: Acquisition

Volumetric data were acquired from breath hold, retrospectively gated bSSFP cine sequences. Ventricular volumes were determined from a series of short axis images planned perpendicularly to the two and four chamber long axis images. The short axis stack cine was acquired from the atrioventricular groove to the ventricular apex, resolution 1.7x1.7x7mm^3 with a 3mm slice gap. Typically 25 frames (cardiac phases) were acquired per slice, covering the entire cardiac cycle.

8.4.3: Analysis

All volumetric analysis was performed with CMR Tools software (Cardiovascular Imaging Solutions, London, UK). The end diastolic and systolic phases were manually assigned based on visual assessment of the maximum and minimum ventricular volumes. The central axis was then defined for each short slice in both phases, following which the epicardial and endocardial borders were traced in both cardiac phases. Semi-automated blood pool thresholding permitted separation of the blood pool from endocardial trabeculae and papillary muscles, such that they were included in the assessment of myocardial mass and excluded from the blood pool. The software also permitted exclusion of the atria from analysis by assigning the valve plane in both cardiac phases.

End diastolic (EDV) and systolic volumes (ESV) were calculated from the sum of the blood pool signal from all short axis slices for both the left and right ventricles. The volume of blood ejected from the heart with each beat i.e. stroke volume (SV) was calculated by subtracting

the ESV from EDV. EF was expressed as a percentage fraction of the EDV (EF (%) = SV / EDV x 100). Myocardial volume was calculated from the signal between the epicardium and the blood pool, including the papillary muscles in the volume. LV mass was calculated by multiplying myocardial volume by the density of myocardium (1.05g/ml) to give the mass in grams.

8.5: Assessment of Focal Myocardial Fibrosis: Late Gadolinium Enhancement Imaging

8.5.1: Introduction

A major strength of CMR is undoubtedly its excellent tissue characterisation capabilities. The most widely used tissue characterisation technique is LGE which permits the assessment of focal fibrotic burden (310, 311). Normal myocardium is tightly packed with an estimated extracellular space of approximately 25-28% (40), however, in regions of myocardial damage, the myocardium is replaced by collagen with resulting expansion of the extra cellular space. Regional extracellular expansion can be identified by exploiting the CMR contrast properties of gadolinium. Gadolinium is paramagnetic and therefore increases the local magnetic field in the vicinity of the contrast molecule, which shortens the relaxivity (T2, but predominantly T1) of the local tissue water. Gadolinium can be safely delivered to the extracellular space by chelation to an injectable soluble compound, which is then renally excreted. However, caution must be taken when injecting gadolinium in patients with a history of renal impairment. Historically, in a minority of patients with severe renal dysfunction, injection with gadolinium resulted in a condition called nephrogenic systemic fibrosis (NSF) (415, 416). This manifests as irreversible skin plaques and joint contractures secondary to systemic collagen deposition induced by the direct toxic effects of gadolinium (416, 417). To date there have been no reported cases of NSF in patients with normal renal function and the incidence of NSF in patients who have received the standard dose of 0.1mmol/kg is near zero, regardless of their renal function (415, 416). The risk of NSF is also

dependent on the chemical structure of the gadolinium compound. The risk is lowest in compounds with a cyclical structure, high kinetic stability and low risk of gadolinium dissociation, as opposed to a linear structure and low kinetic stability (table 8.1)(416).

Trade Name	Structure	Net Charge	Kinetic Stability	NSF cases
Omniscan	Linear	Non-ionic	Low	Yes
Optimark	Linear	Non-ionic	Low	Yes
Magnevist	Linear	Ionic	Medium	Yes
Multihance	Linear	Ionic	Medium	Yes
Primovist	Linear	Ionic	Medium	No
Vasovist	Linear	Ionic	Medium	No
Gadovist	Macrocyclic	Non-ionic	High	No
Prohance	Macrocyclic	Non-ionic	High	No
Dotarem	Macrocyclic	Ionic	High	No

Table 8.1: List of Gadolinium compounds based on structure, charge, kinetic stability and reported cases of NSF. There have been no reports of NSF in compounds with a macrocyclic structure. The highest risk of NSF is from compounds with a linear structure and non-ionic charge (Adapted from Reiter et al. (416)).

The term late gadolinium enhancement relates to the timing of acquisitions, due to the poor vascularity of fibrotic regions, sufficient time (~10-15 mins) must also be allowed for gadolinium to perfuse into these regions. The gadolinium then collects in the fibrotic regions with expanded extracellular space, shortening T1 in comparison to surrounding tissues. The contrast enhancement from gadolinium is further improved by combining contrast injection with a T1 weighted, inversion recovery sequence. This tips all of the magnetisation into the negative M_z axis with a non-selective 180° RF pulse such that recovery of longitudinal magnetisation, and thus signal emission, is entirely dependent on the T1 properties of the tissue. The timing of the image acquisition, or trigger delay (TD), is set to diastole to reduce to the impact of cardiac motion on the image. The timing of the image acquisition, or inversion time (TI), can then be set to coincide with the point that the normal myocardium has recovered longitudinal magnetization back to zero, with no signal produced, known as the null point. Nulling the myocardium provides maximum contrast from fibrotic regions which produce high signal intensities. The null point increases with time from the contrast injection and thus the TI must be increased for subsequent acquisitions, which may be difficult in inexperienced hands. The dependence on TI can be reduced

by using a technique called phase sensitive inversion recovery (PSIR) (418). In contrast to standard inversion recovery, where only the magnitude of the signal is measured, phase sensitive reconstruction improves contrast by preserving the sign (phase) of the magnetisation (figure 8.14)(418, 419). To improve LGE interpretation, acquisitions can be repeated with swapped phase and frequency encoding directions. This is known as 'phase swapping' and will eliminate or move artefacts present in the original image, thereby differentiating between artefacts and true LGE.

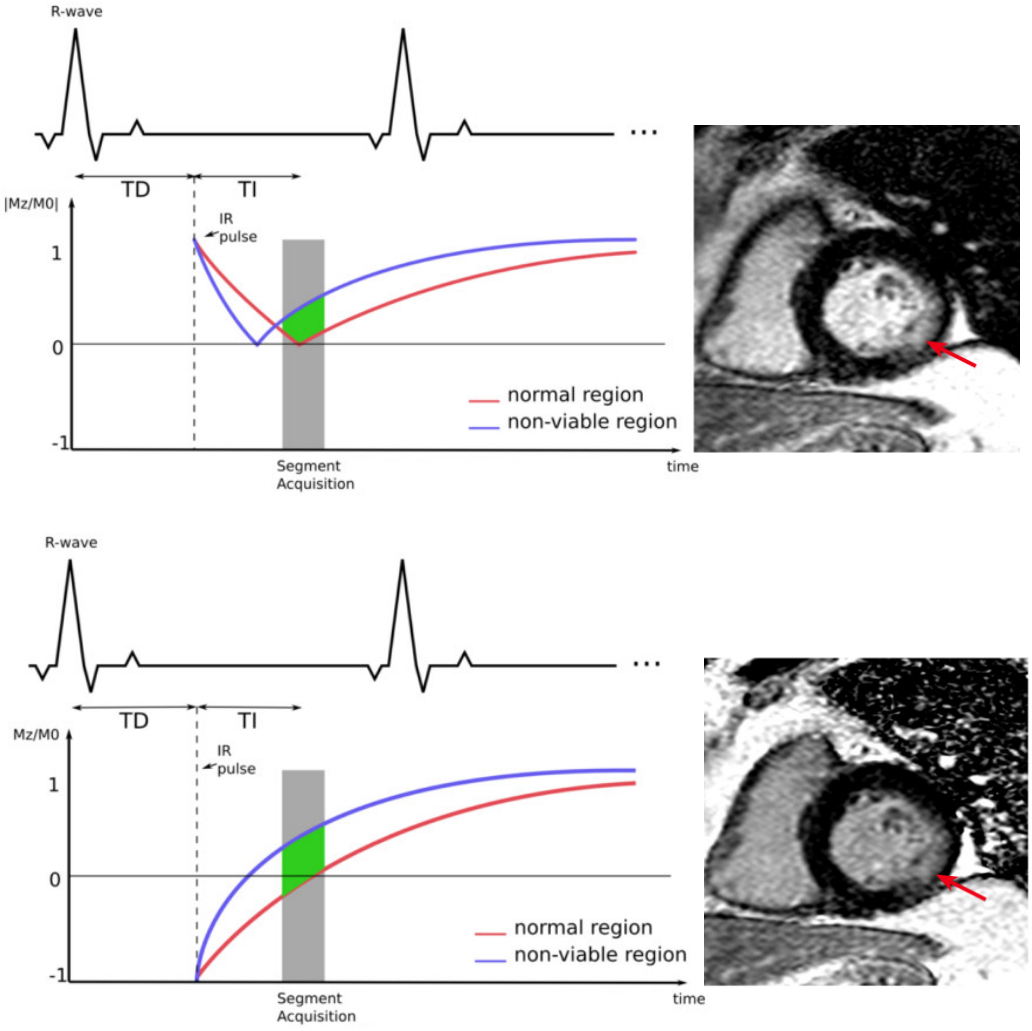

Figure 8.14: Illustration of magnitude (top panel) and phase sensitive inversion recovery (PSIR) (bottom panel) sequences for LGE with corresponding images. An area of myocardial LGE is marked with a red arrow. TD is the trigger delay and TI is the inversion time. This illustrates that in standard inversion recovery imaging, only the magnitude of the signal is measured which reduces the contrast from surrounding structures and places less significance on the TI. Adapted from Ferreira et al. (419).

8.5.2: Acquisition

LGE imaging sequences were acquired in all patients with hypertrophic cardiomyopathy. LGE acquisitions were performed at the end of study protocols to prevent gadolinium reducing the T1 in diffusion sequences. Prior to scanning, all patients were cannulated and blood was drawn to determine renal function. No patients with an eGFR <30 were included in the study. Gadovist (macrocyclic structure) was injected at 0.1mmol/kg and imaging commenced at ≥10mins after injection. All images were acquired with a PSIR sequence (spatial resolution 1.3x1.3x8mm^3), with the TD set to diastole, combined with a gradient echo read out. This protocol provided both a magnitude and a phase sensitive image for each LGE slice. Initially a single mid ventricular short axis slice was acquired at increasing inversion times to determine the optimal starting TI. Long and short axis images were then acquired in the same planes as the long axis cines and ventricular short axis stack, resulting in whole heart coverage. The LGE images were repeated with phase swap acquisitions.

8.5.3: Analysis

All LGE images where visually assessed for significant LGE. The pattern of LGE was used to confirm a diagnosis of HCM and exclude patients with alternative/ additional pathology (figure 8.15). Quantitative assessment of LGE was undertaken by two methods: Visual segmented analysis and 'Full width half maximum' (183, 420, 421) .

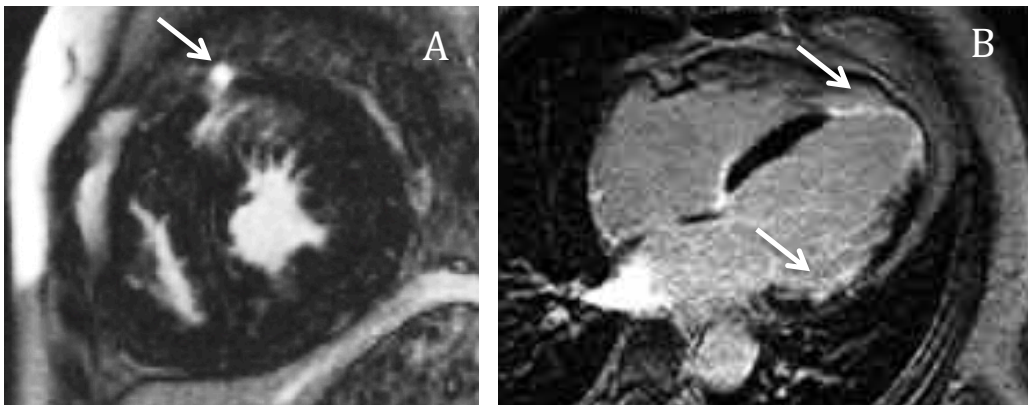

Figure 8.15: A) Example of HCM pattern of LGE extending from the superior RV insertion point to the hypertrophied anteroseptum. B) Example of myocardial infarction pattern of LGE with transmural apical-apical LGE and subendocardial basal inferolateral LGE.

8.5.3.1: Visual Segmented Analysis

Each short axis LGE image was divided into equal segments, with the number dictated by the analysis undertaken. The superior RV insertion point was marked as the starting point and segments were counted in a clockwise direction. LGE was then defined as being present or absent in each segment.

8.5.3.2: Full Width Half Maximum

In contrast the 'full width half maximum' approach quantifies the percentage of fibrotic, LGE mass within the total myocardium. This method has been demonstrated to yield a non-significant difference in the median LGE mass compared to visual assessment (420). This analysis was performed using CVI42 software (Circle Cardiovascular Imaging, Calgary, Canada). As per volumetric analyses, both the endocardium and epicardium were manually defined in each short axis slice. Using the magnitude images the region of brightest LGE signal intensity was then manually defined. The software then identified all signal intensities measuring 50% of this maximum or more in each slice, giving a total volume of myocardial LGE (figure 8.16). This was multiplied by 1.05g/ml (density of myocardium) to give the total LGE/fibrotic mass, which was expressed as a percentage of global LV mass.

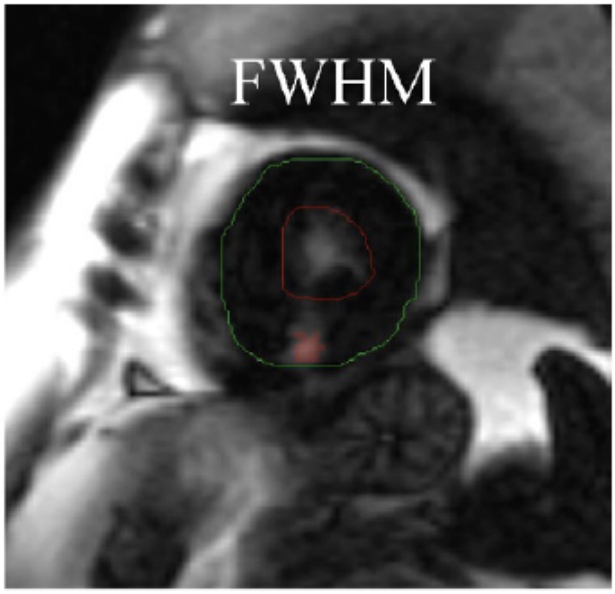

Figure 8.16: Example of full width half maximum analysis. The endocardium and epicardium are manually defined. The region of brightest signal intensity is identified and the software identifies all other pixels with signal intensity equal to 50% of this value or more (420).

8.6: Safety in the Scanner Environment

To ensure safety within the scanner environment, all volunteers and staff were screened with a questionnaire before entering (figure 8.17). The questionnaire identified contraindications to entering the scanner room including the presence of implanted/ surgical devices (e.g. pacemakers and aneurysm clips); metal foreign bodies (e.g. ocular metal fragments); and pregnancy. The questionnaire also prompts removal of loose ferromagnetic objects which may accelerate towards the magnet isocentre, risking injuring. For patients receiving gadolinium the questionnaire also screens for contractions to contrast injection including renal and liver impairment.

Royal Brompton & Harefield NHS
NHS Foundation Trust

Cardiovascular Magnetic Resonance Unit
Tel: 020 7351 8800

Royal Brompton Hospital
Sydney Street
London SW3 6NP

Checklist & Information prior to having a Magnetic Resonance Scan

Name	Date of birth	Hospital Number	Height	Weight

As explained in the Patient Information Leaflet, we need to know about any metallic objects or implants in the body, and some other conditions.	Yes	No
Do you have a pacemaker, a defibrillator, or pacing wires in your heart?		
Do you have any other implants or metal in your body? eg: Hearing aid, ear implant, spine implant, programmable hydrocephalus shunt, others		
Have you had any operation on your head or spine?		
Have you had an injury to an eye which might have left metal in it?		
Have you ever had cardiac surgery?		
Do you suffer from epilepsy, diabetes, asthma or allergies (If yes, please circle which)?		
Are you wearing a drug-releasing patch?		
Are you aware of any problems with your kidneys or are you on kidney dialysis?		
Are you awaiting a liver transplant?		
Have you had recent major surgery or major illness?		
Are you pregnant?		
Are you able to lie flat? If not, please state why.		
Have you removed your watch, bankcards, spectacles, hearing aids, keys, coins, jewellery, and hairgrips? (Gold rings are not a problem)		
	Please tick	

Please note that this is a teaching hospital, and there may be doctors/staff in training observing the scan. You may need an injection of contrast agent during the scan, called gadolinium. Pictures may be taken using techniques developed by researchers at Royal Brompton Hospital that are only available here. These points are explained in detail on the Patient Information Leaflet which we ask you to read fully.

I have explained the procedure to the patient. In particular, I have explained the intended benefits, serious or frequently occurring risks. I have discussed what the procedure is likely to involve, the benefits and risks of any available alternative treatments (including no treatment) and any particular concerns of those involved.

Consentor's Signature ..... Date: .....

By signing below you acknowledge that you have read the Patient Information Leaflet (overleaf), that the procedure has been explained to you by a qualified person, and that you have answered the above questions correctly.

Patient's Signature: ..... Date: .....

Witness' Signature: ..... Date: .....

Figure 8.17: Royal Brompton Hospital CMR safety checklist

8.7: Statistics

The applied statistics are discussed in each results chapter. All statistics were analysed using IBM SPSS 20.0 statistics software, 2012, IBM corporation, New York, USA.

RESULTS

CHAPTER 9: REPRODUCIBILIY OF IN VIVO CARDIOVASCULAR DIFFUSION TENSOR IMAGING IN PATIENTS WITH HYPERTROPHIC CARDIOMYOPATHY

9.1: Introduction

The breath-hold monopolar STEAM sequence demonstrated reproducibility in healthy volunteers (19), however this cannot be extrapolated to patient populations. The success the monopolar of STEAM sequence is dependent on a stationary region of interest between diffusion gradients. Hypertrophic cardiomyopathy (HCM) is associated with an increased risk of arrhythmia and also breathlessness as a consequence of systolic/ diastolic ventricular impairment and intra cavity obstruction (14). The first stage of this project was thus to determine in the reproducibility, and baseline parameter values, for breath-hold monopolar STEAM in a small cohort of patients with hypertrophic cardiomyopathy. Published in: **Laura-Ann McGill**, Tevfik F Ismail1, Sonia Nielles-Vallespin, Pedro Ferreira, Andrew D Scott1, Michael Roughton, Philip J Kilner, S Yen Ho, Karen P McCarthy, Peter D Gatehouse, Ranil de Silva, Peter Speier, Thorsten Feiweier, Choukkri Mekkaoui, David E Sosnovik, Sanjay K Prasad1, David N Firmin and Dudley J Pennell et al, Reproducibility of in-vivo diffusion tensor cardiovascular magnetic resonance in hypertrophic cardiomyopathy, Journal of Cardiovascular Magnetic Resonance, 2012; 14:86 (422).

9.2: Methods

9.2.1: Patient Recruitment

Ten patients with HCM were recruited for this study. Patients with HCM were identified from the specialist cardiomyopathy clinic run by Dr Sanjay Prasad and Dr John Baksi at the Royal Brompton Hospital. A diagnosis of HCM was made in line with current European Guidance (14):

- LV wall thickness of ≥15mm in one or more myocardial segments measured by any imaging modality (CMR, echocardiography, CT) in the absence of loading conditions such as hypertension/ aortic stenosis.
- LV wall thickness of 13-15mm in combination with one or more of the following: a genetic mutation consistent with HCM, positive family history, symptom profile consistent with HCM, ECG or additional imaging features consistent with HCM.

Patients were excluded if they had contraindications to CMR and gadolinium contrast or significant comorbidities including hypertension and ischaemic heart disease. Patients with sustained atrial arrhythmias incompatible with cardiac diffusion tensor imaging (cDTI) such as atrial fibrillation were also excluded. Clinical information regarding genetic testing and risk factors for sudden death were collected for each patient.

9.2.2: Ethical Approval

Ethical approval for recruitment of patients with hypertrophic cardiomyopathy was granted by the NRES Committee South East Coast Surrey (REC reference 10/H0701/112). Patients were given an information sheet, prior to giving consent, outlining the study objectives and logistics. All volunteers were made aware they were free to withdraw their consent to participation at any point in the process.

9.2.3: Image Acquisition

The 10 patients were scanned on two separate days at 3T to establish intra-centre reproducibility. cDTI was performed during the end systolic pause identified from a mid

ventricular short axis bSSFP cine acquisition in each subject. Data were acquired in 3 mid ventricular short axis slices, typically for 10 image repetitions, before signal averaging to improve SNR. Repetitions up to a maximum of 13 where performed when poor breath-holding or arrhythmia were observed to have spoiled previous acquisitions, and the order in which the diffusion directions were acquired was rotated to avoid loss of the same direction on recurrent breath holds. The slice position for both studies were matched by measuring the distance from the centre of the region of interest to the mitral annular plane.

Functional and volumetric data were determined from retrospectively bSSFP cine acquisitions in 3 long axis planes a stack of short axis slices from the ventricular base to the apex. LGE was performed at the end of the study in the same slices as the cine acquisitions using a PSIR sequence. In the event of ambiguous LGE, images were repeated with phase swapping of the frequency coding direction to aid differentiation of artefacts from true enhancement.

The typical duration of the scan was 75-90mins. Full details of all sequence parameters are discussed in Chapter 8.

9.2.4: Diffusion Tensor Analysis

Following initial post processing steps the eigensystem (eigenvalues and eigenvectors) were calculated from the diffusion tensor for each voxel. Three diffusion parameters were determined from the eigensystem: FA, MD and HA. For the helix angle, left-handed epicardial helix angles were assigned a negative value and right-handed endocardial helix angles assigned a positive valve, with myocytes with no angulation (zero) representing circumferential myocytes (64, 423). For quantitative analysis of cDTI parameters the myocardium was divided into the conventional 4 LV segments: anterior, septal, inferior, lateral. HA analysis further segmented the myocardium transmurally into endocardial, mesocardial and epicardial layers. This was performed by dividing

the local myocardium into three equal thickness layers, bound by the epicardial and endocardial borders. All cDTI analysis was performed by a single observer, on completion off all studies, blinded to clinical data. 3D visualisation of the tensor with superquadric glyphs (358) was implemented using Python and Paraview (Kitware, NM, USA) software. The post-processing and analysis time was approximately 3 hours per study.

9.2.5: Functional, Volumetric and Late Gadolinium Enhancement Image Analysis

Ventricular volumes, function, mass, and EF for all patients were measured for the LV using CMRtools software (Cardiovascular Imaging Solutions, London). All volume and mass measurements were indexed to BSA calculated using the Du Bois method (41). LGE imaging was analysed qualitatively via visual segmented analysis with LGE recorded as present/ absent for each segment (anterior, lateral, inferior, septal). In addition the extent of LGE was quantified using CVI42 software (Circle Cardiovascular Imaging Inc, Calgary, Canada) with a full-width half-maximum threshold and expressed as percent of LV mass.

9.2.6: Statistical Analysis

MD, FA and HA values were analysed globally (all segments, all slices), by slice (3 slices), and by LV wall (common wall segments averaged from all 3 slices). HA was additionally analysed in 3 layers (epicardium, mesocardium, endocardium) because of the known transmural variation in HA.

Inter-study reproducibility was assessed using the SD of the difference between the scans, and the coefficient of variation (CoV) (SD of the difference between the scans divided by the measurement mean).. HA CoVs were not calculated as the mesocardial HA passes through zero preventing rendering it unsuitable for division. Bland-Altman plot analysis was also performed (424). Differences in the CoV were assessed using a variance ratio test. Data from the initial study were compared to assess for differences between LV walls, and slices for FA and MD. For HA

values were compared between slices and layers using hierarchical (patients – slices – layers) mixed effects model. The lateral wall and mid slice were chosen as reference regions for comparison, because the lateral wall is less commonly affected by hypertrophy in HCM, and the mid-slice is furthest from potential anomalous measurement relating to the apex or left ventricular outflow tract. All values were found to be normally distributed using the Kolmogorov-Smirnov test, and are therefore shown as mean±standard deviation (SD). Statistical significance was set to $p < 0.01$ to account for the number of statistical tests performed. Statistical modelling was performed by Michael Roughton, Royal Brompton Hospital statistician.

9.3: Results

9.3.1: Study Population

The baseline characteristics and CMR data from the patients are outlined in table 9.1. Only 2 out of the 10 patients has undergone genetic testing with no pathological mutations associated with HCM found.

Figures 9.1 and 9.2 show example data for an example patient with highly reproducible data and the least reproducible data respectively. The top 4 panels show maps for b_{ref} (grey-scale), FA (green-orange), MD (blue-white) and helix angle (rainbow) for each of the three slices in initial and repeat studies. Matching LGE images are shown below with arrows marking regional enhancement. Plots outlining the measured FA and MD values are shown with the error bars representing the standard deviation for each segment, in each slice. The blue lines included in the tables represent the mean±2SD limits as reported by Nielles-Vallespin et al. in healthy volunteers (19). In figure 9.1, no major differences are observed either in the maps or plots between scans. However in figure 9.2, the least reproducible example, differences can be appreciated in the maps and plots, particularly in the mid and basal septal segments due to an apparent signal loss artefact

appreciable in the b_{ref} images. The HA maps demonstrate noisy pixels with artefacts which are not reproducible. No definite change is seen regions of LGE.

	HCM Patients (n=10)
Age years	57±9
Male n (%)	9 (90%)
Body Surface Area m^2	1.99 ±0.2
LV morphology & risk factors for sudden death	
Asymmetrical septal hypertrophy n (%)	7 (70%)
Apical hypertrophy n (%)	3 (30%)
Number of risk factors for sudden death: media (range)	1 (0-1)
CMR characteristics	
Indexed LV EDV, ml/m^2	70 ±12
Indexed LV ESV, ml/m^2	16 ±4
LV Ejection Fraction, %	77 ±5
LV Mass Index, g/m^2	102±32
Maximum End-diastolic Wall Thickness, mm	22 ±5
Presence and location of late gadolinium enhancement	9 (90%)
Septum	50%
Anterior	20%
Inferior	20%
Lateral	10%
Extent of late gadolinium enhancement (% of LV mass)	4.5%±5.6%

Table 9.1: Baseline patient characteristics (mean±SD, or number of patients (%))

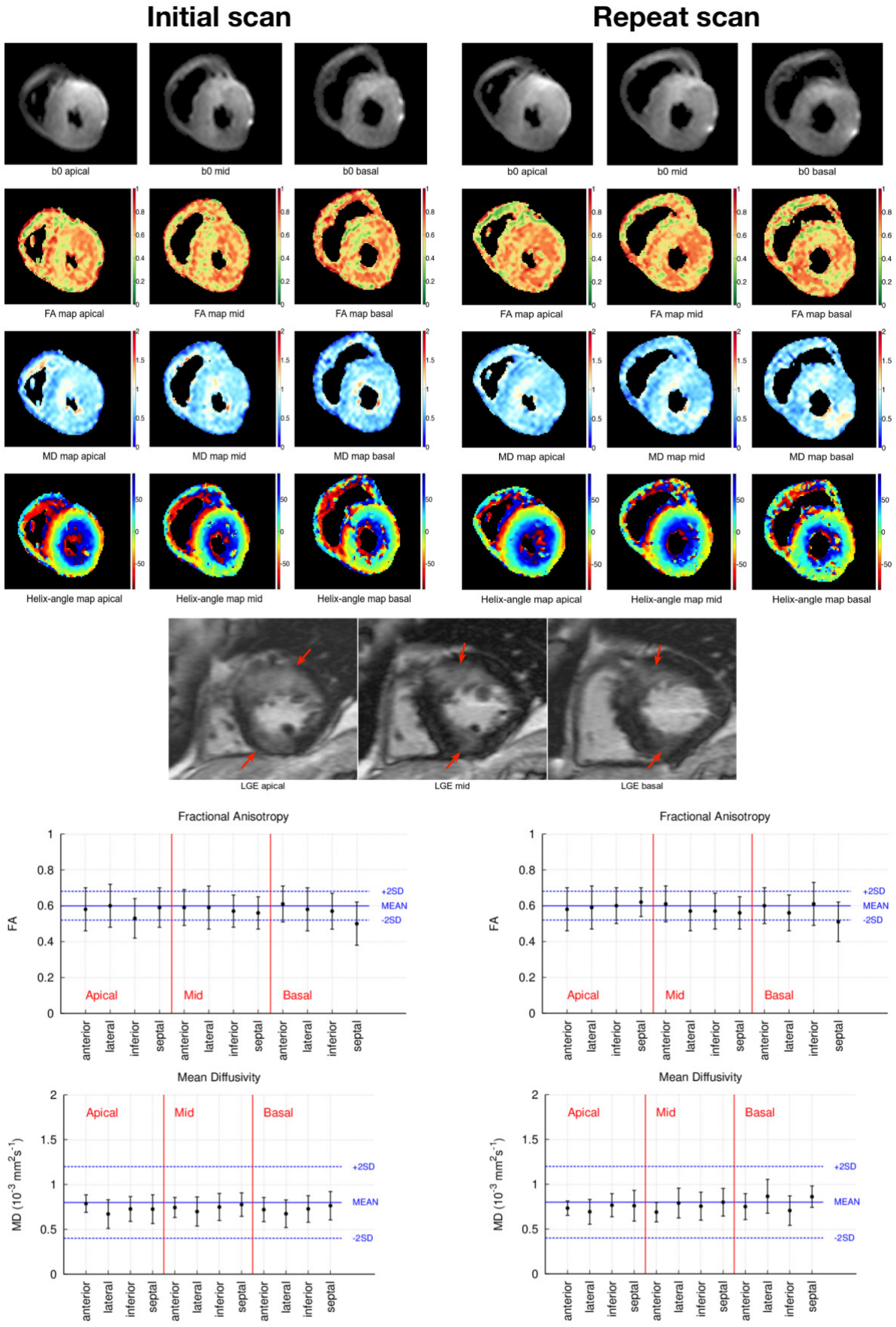

Figure 9.1: Example of patient with a highly reproducible dataset (422)

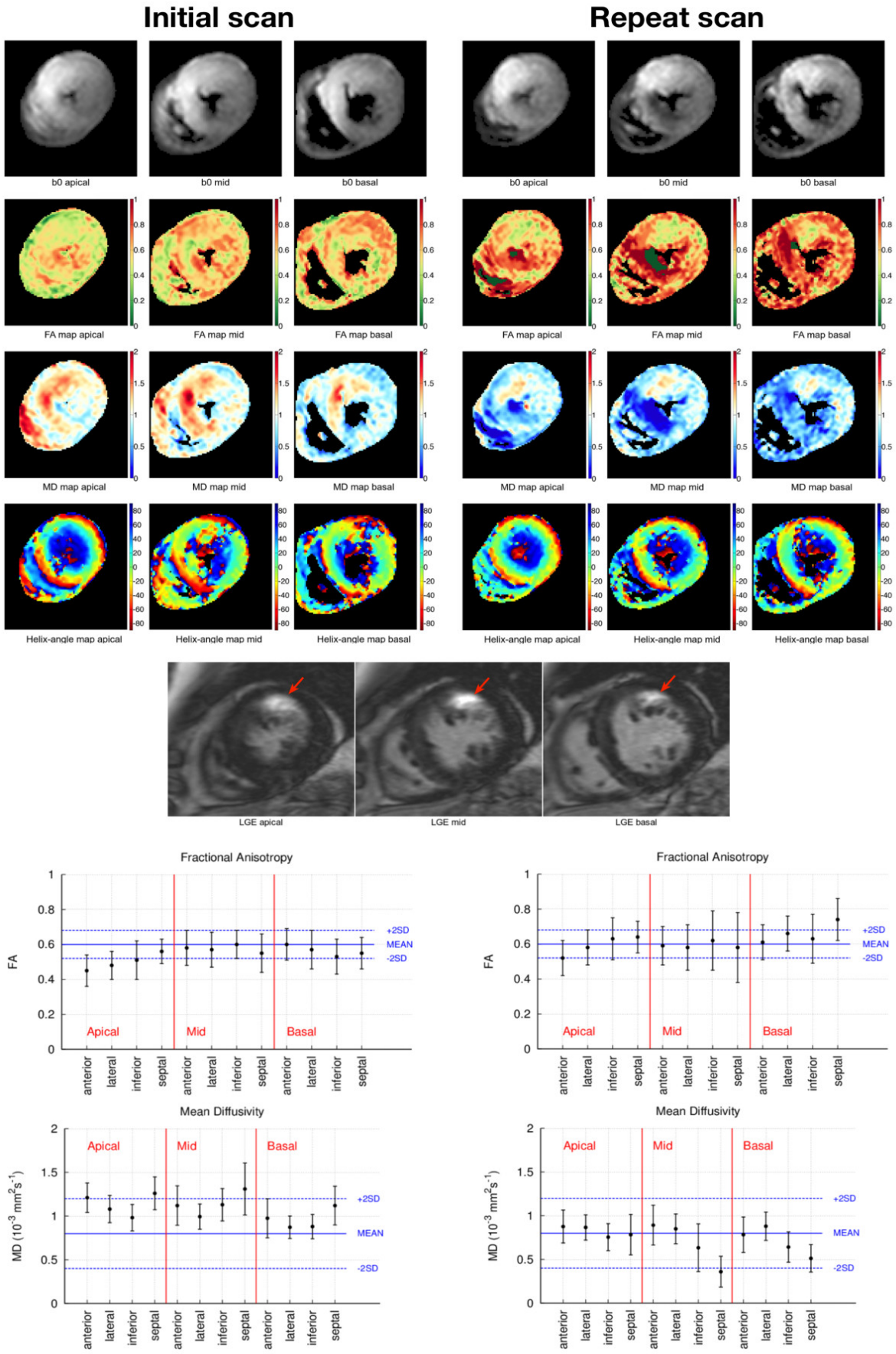

Figure 9.2: Patient with the least reproducible dataset out of 10 patients (422)

9.3.2: Quantitative Parameter Results

9.3.2.1: Fractional Anisotropy

The mean global FA in the 10 patients in the initial study was 0.61±0.04 (table 9.2). When analysed by slice and regional wall there where no significant differences in FA values around the ventricle.

Fractional Anisotropy	N	Mean	SD	Difference	95% Confidence interval		p value
Global	10	0.61	0.04				
Slice							
Mid	10	0.62	0.04	Reference			
Apical	10	0.61	0.05	-0.02	-0.04	0.01	0.25
Basal	10	0.61	0.05	-0.02	-0.04	0.01	0.25
LV wall							
Lateral	10	0.61	0.04	Reference			
Anterior	10	0.62	0.04	0.002	-0.02	0.02	0.90
Inferior	10	0.61	0.04	-0.003	-0.02	0.02	0.79
Septal	10	0.61	0.06	-0.003	-0.02	0.02	0.77

Table 9.2: Fractional anisotropy results from the initial study from each patient.

9.3.2.2: Mean Diffusivity

The mean global MD from the initial study was 0.75±0.15 x 10^{-3} mm^2/s. There were no significant differences in MD between slices. When analysed by LV wall, MD was significantly greater in the septal wall than the reference lateral wall (0.78±0.19 x $10^{-3}mm^2/s$ vs 0.71±0.16 x 10^{-3} mm^2/s; $p < 0.001$) (table 9.3).

Mean Diffusivity	N	Mean	SD	Difference	95% Confidence interval		p value
Global	10	0.75	0.15				
Slice							
Mid	10	0.75	0.18	Reference			
Apical	10	0.79	0.15	0.04	-0.02	0.10	0.16
Basal	10	0.73	0.15	-0.02	-0.08	0.04	0.60
LV wall							
Lateral	10	0.71	0.16	Reference			
Anterior	10	0.76	0.15	0.04	0.004	0.08	0.029
Inferior	10	0.74	0.14	0.03	-0.01	0.07	0.16
Septal	10	0.78	0.19	0.07	0.03	0.11	<0.001

Table 9.3: Mean diffusivity results from the initial study ($x10^{-3}mm^2/s$)

9.3.2.3: Helix Angle

Global LV helix angles showed transmural progression from left handed in the epicardium (−34±8°), near perpendicular to the imaging plane in the mesocardium (4±7°), to right handed in the endocardium (39±8°). When analysed by slice, there were no statistically significant differences between slices ($p<0.01$) (table 9.4). Three-dimensional analysis of the cDTI data is demonstrated in figure 9.3 as superquadric glyphs. The colour and orientation/shape of the glyphs are determined by the helix angle and the eigensystem respectively.

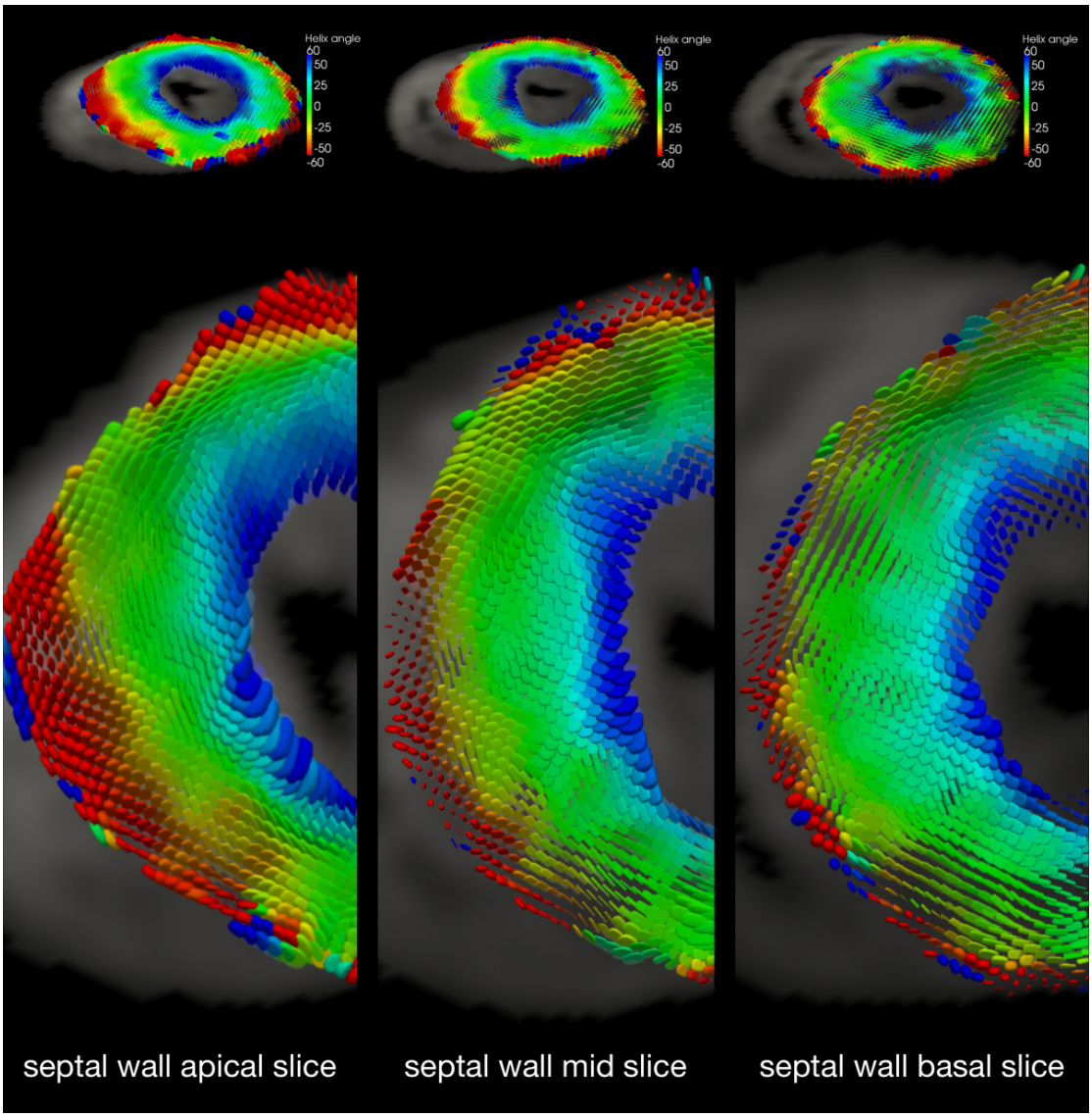

Figure 9.3: Cardiac diffusion tensor data from an example HCM patient. Data are represented in superquadric glyphs from the septal wall in each ventricular slice presented. The glyphs are colour coded according to the primary eigenvector helix angle with left-handed epicardial myocytes in red, circumferential myocytes in green and right-handed endocardial myocytes in blue. The secondary and tertiary eigenvectors are expressed in the shape of the glyphs, with rounded glyphs representing more isotropic data and linear glyphs more anisotropic data. The typical helical pattern observed in normal myocardium is maintained with a higher predominance of circumferential (green) myocytes in the basal slice (422).

Helix Angle	N	Mean	SD	Difference	95% Confidence interval		p value
Global							
Endo	10	39	8				
Meso	10	4	7				
Epi	10	−34	8				
Slice							
Endo layer							
Mid	10	40	5	Reference			
Apical	10	41	7	1	−3	5	0.58
Basal	10	36	6	−3	−7	−0.1	0.044
Meso layer							
Mid	10	3	3	Reference			
Apical	10	4	5	1	−2	4	0.37
Basal	10	4	4	1	−2	3	0.72
Epi layer							
Mid	10	−34	3	Reference			
Apical	10	−34	7	1	−3	4	0.73
Basal	10	−35	4	−1	−4	3	0.82

Table 9.4: Helix angle values for the initial study (degrees)

9.3.3: Reproducibility

Initial and repeat studies were performed 167±21 days apart. There were no clinical events or changes in treatment in the intervening period. Data were successfully collected in all patients.

9.3.3.1: Fractional Anisotropy

FA demonstrated good reproducibility of data between initial and repeat studies (table 9.5). The global SD between the initial and repeat studies was ±0.05 and the CoV was 7.2%, demonstrating low variance. Bland-Altman plots demonstrate minimal bias between studies (figure 9.3).

Fractional Anisotropy	N	Mean value	Mean difference	SD of difference	95% limits of agreement		Coefficient of variation
Global	10	0.62	−0.008	0.045	−0.10	0.08	7.2%
Slice							
Apical	10	0.61	−0.013	0.054	−0.12	0.09	8.8%
Mid	10	0.62	0.001	0.051	−0.10	0.10	8.2%
Basal	10	0.61	−0.013	0.043	−0.10	0.07	7.1%
LV wall							
Anterior	10	0.62	−0.009	0.042	−0.09	0.07	6.8%
Lateral	10	0.61	0.012	0.059	−0.10	0.13	9.7%
Inferior	10	0.62	−0.018	0.053	−0.12	0.09	8.6%
Septal	10	0.62	−0.017	0.053	−0.12	0.09	8.5%

Table 9.5: Fractional anisotropy reproducibility demonstrating minimal variance between scans

9.3.3.2: Mean Diffusivity

Table 9.6 outlines MD reproducibility data, comparing the initial and repeat studies. MD data showed acceptable reproducibility at each level of analysis although the inter-study reproducibility of MD was comparatively poorer than for FA ($p = 0.003$). The global SD between the initial and repeat studies was $\pm 0.14 \times 10^{-3}$ mm^2/s with a CoV of variation 18.6%. Bland-Altman plots (figure 9.4) demonstrate minimal bias.

9.3.3.3: Helix Angle

HA reproducibility data, comparing the initial and repeat studies are provided in table 9.7. The associated plots are shown in figures 9.4 and 9.5. The global mean SD of the difference in HA between the initial and repeat studies was ±5°, ±3° and ±3° in the endocardial, mesocardial and epicardial layers respectively. On Bland-Altman plots there was neglibible bias in for the endocardial and mesocardial layers with a non-significant bias of 3° in the epicardial layer on repeat study. Analysis of HA by slice demonstrated good reproducibility with SD of the difference ranging from ±3-11°.

Mean Diffusivity	N	Mean value	Mean difference	SD of difference	95% limits of agreement		Coefficient of variation
Global	10	0.73	0.05	0.14	-0.2	0.3	18.6%
Slice							
Apical	10	0.76	0.04	0.18	-0.3	0.4	23.0%
Mid	10	0.72	0.05	0.16	-0.3	0.4	22.2%
Basal	10	0.70	0.05	0.12	-0.2	0.3	16.4%
LV wall							
Anterior	10	0.73	0.06	0.11	-0.3	0.3	15.4%
Lateral	10	0.71	0.03	0.16	-0.3	0.3	22.9%
Inferior	10	0.72	0.05	0.14	-0.2	0.3	19.5%
Septal	10	0.75	0.07	0.23	-0.4	0.5	30.9%

Table 9.6: Reproducibility analysis of mean diffusivity demonstrating acceptable variance, but inferior reproducibility compared to FA.

Helix Angle	N	Mean value	Mean difference	SD of difference	95% limits of agreement	
Global						
Endo	10	38	1	5	−8	11
Meso	10	4	−1	3	−7	6
Epi	10	−33	−3	3	−8	3
Slice						
Apical endo	10	40	3	11	−18	24
Apical meso	10	4	0.0	6	−12	12
Apical epi	10	−32	−4	6	−16	9
Mid endo	10	39	2	6	−10	14
Mid meso	10	3	−1	5	−10	8
Mid epi	10	−33	−3	7	−16	10
Basal endo	10	37	−1	4	−9	8
Basal meso	10	4	−1	3	−7	5
Basal epi	10	−34	−2	5	−11	7

Table 9.7: Helix angle (degrees) reproducibility demonstrating minimal difference between means. The coefficient of variation was not calculated.

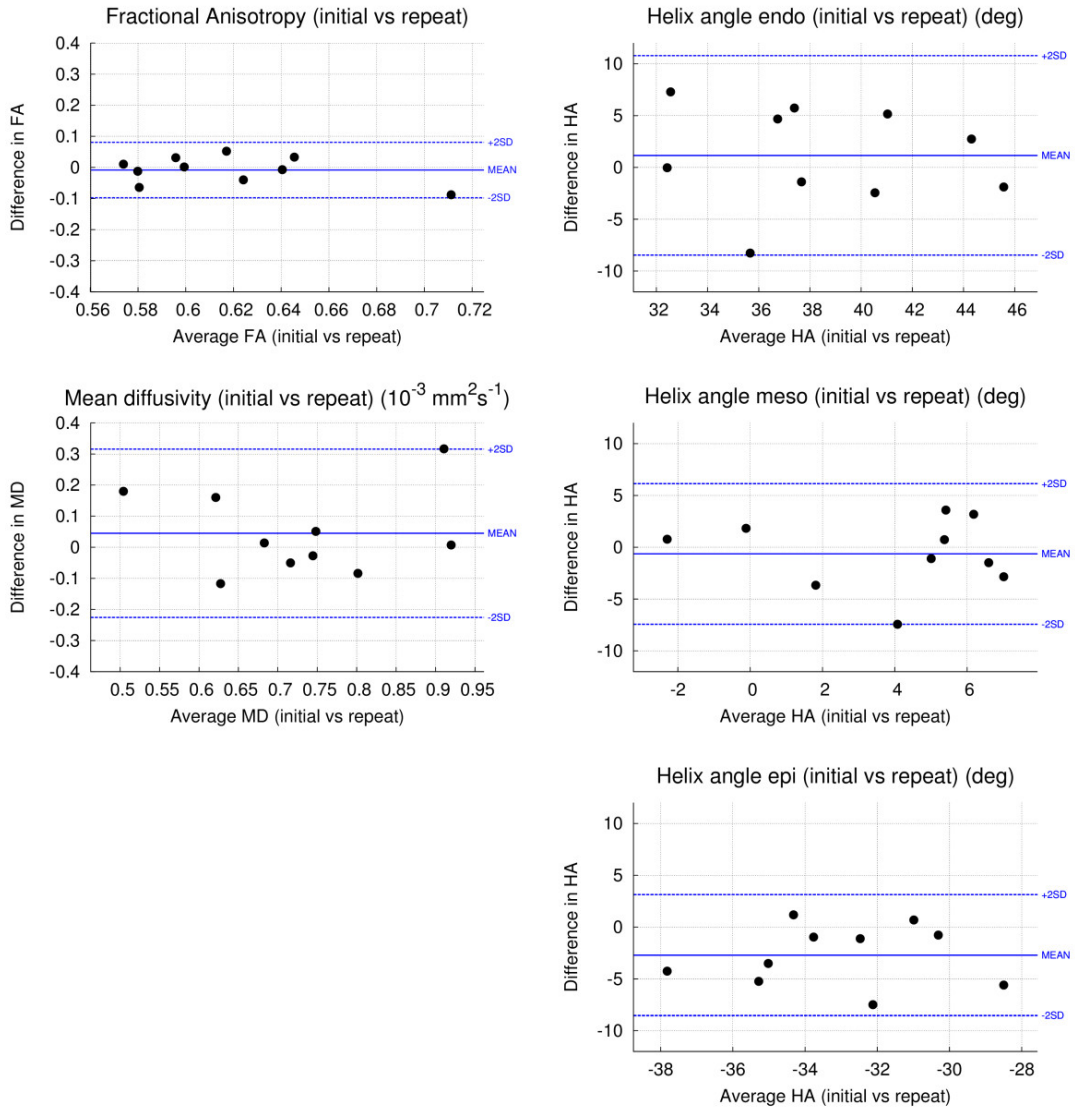

Figure 9.4: Bland-Altman plots for global FA and MD and HA plots per transmural layer (endocardial, mesocardial and epicardial) (422).

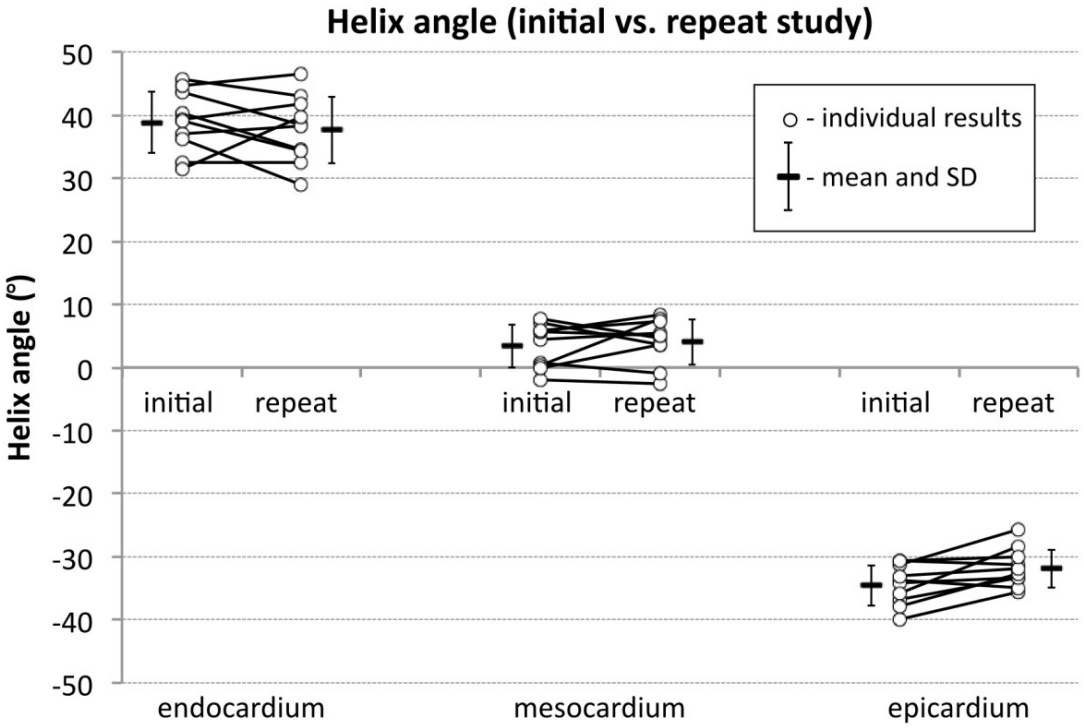

Figure 9.5: Line plots of the mean global HA values for the initial and repeat studies in for the endo, meso and epicardial layers for all 10 subjects. The mean±1 SD is shown (422).

9.4: Discussion

In vivo cDTI is especially challenging in patient cohorts due to the potential for bulk cardiac motion artefacts from respiration and arrhythmia. This work demonstrates good reproducibility of quantitative parameters with monopolar DW-STEAM sequence in patients with hypertrophic cardiomyopathy. In keeping with the assessment by Nielles-Vallespin et al. in healthy volunteers (19), FA was found to be the most reproducible parameter, with an inter-study CoV for global FA of 7.2% and values ranging from 6.8% to 9.7% for slices and walls. MD performed relatively poorer but remained reasonably reproducible with a CoV of 18.6% for global MD and values ranging from 15.4% to 30.9% for slices and walls. HA also demonstrated good reproducibility with the SD of the difference between studies ranging between ±3 to 5° for global transmural layers.

The baseline values for quantitative parameters in this work were somewhat surprising. Global FA was 0.61±0.04 with no significant difference between septum (0.61±0.06) and lateral wall

(0.61±0.04). This contradicts Tseng et al. who measured an FA of 0.56 in the septum and 0.78 in the lateral wall in HCM patients (p=0.03), which they interpreted as evidence septal disarray (294). Reasons for the marked difference are unclear but may relate to differences in scanner hardware (1.5T for Tseng and 3T in this work) and post processing techniques. As pointed out in Chapter 5, figures provided by Tseng et al. appear to indicate inclusion of data from noisy edge pixels, the RV and papillary muscles which may have skewed results (294).

In addition to the lack of regional difference, the global FA result (0.61±0.04) was within 1 SD of the global FA in healthy volunteers in Nielles-Vallespin et al. (0.60±0.04). This was unexpected as it implies that either that there is no evidence of myocardial disarray in this cohort of HCM patients, or the FA derived from these sequence parameters is too insensitive to detect it. Global MD was 0.75±0.15 x $10^{-3}mm^2/s$, which again was within 1 SD of MD in healthy volunteers with the same sequence (Nielles-Vallespin 0.80±0.1 x $10^{-3}mm^2/s$)(19). MD results have proven very inconsistent across the literature ranging from 0.61±0.11 x $10^{-3}mm^2/s$ in Dou et al. (151) to 1.04±0.14 x $10^{-3}mm^2/s$ in Stoeck et al. (360); differences in resolution, sequence parameters, in particular the b value, are likely contributors. We demonstrated significant regional differences in MD with greater MD in the septum (0.78±0.19 x $10^{-3}mm^2/s$) and anterior wall (0.76±0.15 x $10^{-3}mm^2/s$ compared to the lateral wall (0.71±0.16 x 10^{-3} mm^2/s). One explanation could be the expected fibrosis/ expansion of the interstitium in the hypertrophied septum of HCM patients (178, 183), which would be expected to permit freer diffusion. However technical factors are also likely to have contributed. Although not formally measured, SNR in the lateral wall could be less than the septum and anterior wall as it is remote from the anterior receiver coil with comparatively reduced local wall thickness. Consequently lateral wall MD may be underestimated (406). Artefactually greater septal reduced lateral MD could also result from mis-registration of averages, which may not necessarily affect the myocardium homogeneously.

HA data were also surprising. Aside from obvious artefacts within the maps in some patients, helical data demonstrated the normal helical arrangement of myocytes, with smooth progression from a left-handed epicardial helix through to a right-handed endocardial helix (figure 9.3). Given the reported disarray in HCM one might expect evidence of disordered helices. Tseng et al. (294) described a greater proportion of left-handed myocytes in the septum of HCM patients, however figure 9.5 illustrates that this could be attributed to the inclusion of RV myocardium. Helix angles were divided into 3 transmural layers, as opposed to 4 layers in Nielles-Vallespin et al. (19), therefore are not directly comparable, however the spread of angles in this work was greater (endocardium: 23±9° v 39±8°, epicardium -17±7° v -34±7°). This may reflect a greater proportion of longitudinally orientated myocytes in the hypertrophied HCM myocardium, however again it may be a consequence of post processing inconsistencies, with more stringent ROI drawing likely to translate to less acute longitudinal angles.

9.5: Limitations

A number of potential technical limitations have been addressed above. The modest acquired resolution of this sequence (2.8 x 2.8 x 8cm^3) will affect edge pixels in particular, increasing the likelihood of partial voluming effects with possible skewing of FA, MD and HA data, particularly in thinner myocardium. The impact of strain on quantitative parameters in this work is unknown. Although this would not affect reproducibility, it may impact on global and regional FA and MD results (366).

9.6: Conclusion

The monopolar DW-STEAM sequence demonstrates clinically valid reproducibility in HCM patients. The apparent lack of a disarray signal in FA is disappointing, however this work is the first step towards recruitment of larger cohorts to analyse this further. In light of inconsistencies

in FA and MD results across the literature, investigation into potentially technical contributors and the natural variation in these parameters in the wider population is warranted.

CHAPTER 10: INNATE HETEROGENEITY OF CARDIOVASCULAR DIFFUSION TENSOR IMAGING PARAMETERS IN HEALTHY VOLUNTEERS

10.1: Introduction

Thus far we have demonstrated good intra-centre reproducibility of cDTI parameters in healthy volunteers and patients with hypertrophic cardiomyopathy, however values for quantitative cDTI parameters are inconsistent across the literature, with quoted values for FA and MD ranging between 0.33 to 0.78 and 0.60 to 1.04 $x10^{-3}mm^2/s$ respectively (150, 151, 294, 360, 369, 370, 387). The extent to which differences in scanner hardware, sequence parameters and post processing techniques had contributed, as opposed to the natural population heterogeneity, was unknown. To investigate potential technical contributors we collaborated with John Radcliffe Hospital, Oxford, cDTI research team, led by Prof S. Neubauer, results published in Elizabeth M Tunnicliffe, Andrew D Scott, Pedro Ferreira, Rina Ariga, **Laura-Ann McGill,** Sonia Nielles-Vallespin, Stefan Neubauer, Dudley J Pennell, Matthew D Robson and David N Firmin, Intercentre reproducibility of cardiac apparent diffusion coefficient and fractional anisotropy in healthy volunteers, journal of cardiovascular magnetic resonance, 2014; 16:31 (372); and Elizabeth M Tunnicliffe, Pedro Ferreira, Andrew D Scott, Rina Ariga, **Laura-Ann McGill**, Sonia Nielles-Vallespin, Stefan Neubauer, Dudley J Pennell, Matthew D Robson, David Firmin, Intercentre reproducibility of second eigenvector orientation in cardiac diffusion tensor imaging, 2016, 18(Suppl 1):P35 (425).

From the offset Oxford reported significantly different in vivo values for MD and FA, despite minor differences in the DW-STEAM sequence protocol. For systolic measures they reported an

MD range of 1.10 to 1.40x10^{-3}mm^2/s and FA range of 0.3-0.5 translating to ~0.3-0.7 x10^{-3}mm^2/s increased in MD and ~0.3-0.1 decrease in FA compared to our healthy volunteer values reported in Nielles-Vallespin et al. (19). Oxford therefore sought to validate their MD measures via phantoms with MD ranges within range of previous quoted values in myocardium (372). Phantoms were imaged with both the in vivo monopolar DW-STEAM sequence a Stejskal-Tanner spin echo sequence and compared with published reference values (343). The resulting MD measures were in agreement with the Stejskal-Tanner sequence and comparable with phantom reference values, with a maximum difference between DW-STEAM the reference of 0.05 x10^{-3}mm^2/s (table 10.1) (372).

	Mean diffusivity (×10-3 mm2/s)		
	Literature value at 19.3°C (343)	Stejskal-Tanner	Monopolar DW-STEAM
Undecane	0.994	1.00 ± 0.02	1.00 ± 0.10
Dodecane	0.770	0.79 ± 0.01	0.80 ± 0.07
Tridecane	0.623	0.63 ± 0.02	0.67 ± 0.09
Pentadecane	0.395	0.40 ± 0.01	0.42 ± 0.10

Table 10.1: Results from phantom validation of the monopolar DW-STEAM sequence conducted at Oxford. Results from the monopolar DW-STEAM were within 1 SD of published mean diffusivities for each phantom (372).

These results raised questions about the results from our centre, consequently physicists Dr Nielles-Vallespin and Dr Scott undertook detailed analysis of sequence components and implementation the Royal Brompton Hospital. As discussed in chapter 7, the diffusion weighted signal is derived from the subtraction of a diffusion weight image (b_{main}) and a reference image (b_{ref}). In the b_{ref} images, diffusion gradients are replaced by spoilers to avoid unwanted magnetisation, ensuring T1 and T2 values are equal in both sets of images. However, these spoiler gradients still carry a degree of diffusion weighting. Previous publications had not addressed to the true diffusion weighting of such gradients, and our initial estimates attributed a diffusion weighting of ~b=15s/mm^2. Further investigation revealed that this was an underestimate, and the true diffusion weighting at 3T was 135s/mm^2. Underestimating the b_{ref} weighting will result

in underestimation of MD and overestimation of FA, thus explaining the discrepancy between the two centres. After reprocessing the breath hold results from Nielles-Vallespin et al. with b_{ref}=135s/mm², global results for MD and FA were as follows (426):

MD = 1.14±0.15 ×10-3 mm2/s

FA = 0.46±0.04

Having made this correction, additional technical factors were assessed via an inter-centre reproducibility study of systolic E2A (425). On initial comparison of ten healthy volunteer scans performed and analysed independently at each site, a non-significant bias was detected in systolic and diastolic MD and systolic FA, however diastolic FA was significantly greater (bias 0.04, p<0.001) in scans performed and analysed at Oxford (figure 10.1) (372).

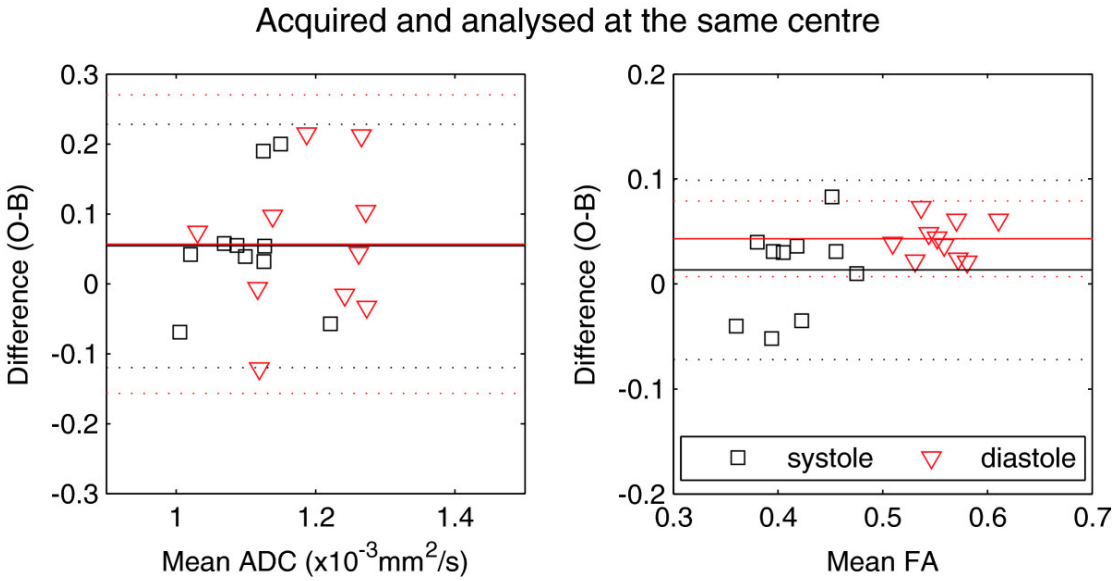

Figure 10.1: Bland-Altman plots of Oxford (O) and Brompton (B) initial inter-centre reproducibility. Systolic comparisons are represented by □ and diastolic by ∇. In the left hand plot both mean diastolic and systolic ADC (MD) had a non-significant bias towards greater MD measures at Oxford. In the right hand image, there was a negligible bias average systolic FA, and a significant bias towards greater diastolic FA measures at Oxford (372).

On further investigation it transpired that the majority of the difference was driven by differences in analysis, rather than acquisitions, with Oxford tending towards more restrictive ROIs (figure 10.2). With matched ROIs all parameters were highly reproducible in both phases for MD, FA and HAG with the CoV ranging between 3-11% (372) therefore matching the degree of intra-centre reproducibility reported in Nielles-Vallespin et al. (19). For E2A measures, with similar ROIs,

results were again comparable between centres with no significant difference on paired t-testing, with an inter-centre CoV of 7% for systolic E2A and 15% for diastolic E2A. The apparently poorer performance of diastolic measures was attributed to the smaller numeric value of diastolic E2A (21±5°) versus systolic E2A (55±4°) (CoV=SD/mean). This work therefore represents a further step towards clinical valid cDTI.

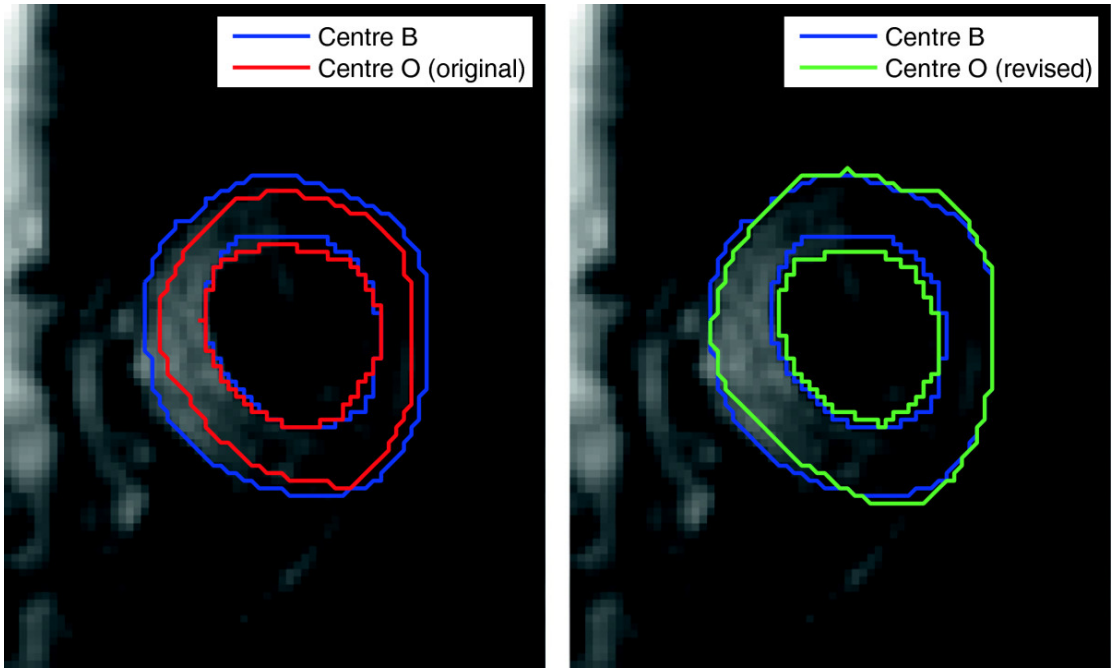

Figure 10.2: Comparison of ROIs drawn at the Brompton and Oxford. Initially epicardial ROIs were comparatively restrictive at Oxford (red) and were revised to match the Brompton (green) (372).

Before moving towards comparisons with hypertrophic cardiomyopathy patients, the logical next step was to examine the innate heterogeneity of cDTI parameters in a larger population of healthy volunteers. Previous cDTI healthy volunteer studies had comprised of small cohorts of around 5-10 subjects (19, 150, 294, 368, 369, 372), and the association between quantitative parameters and subject anthropometrics was therefore unknown. This was addressed via recruitment of a larger healthy volunteer cohort, with a broad age, for cDTI acquisitions and assessment of MD, FA, HAG and E2A values in systole and diastole, published in: **L.A. McGill**, P.F. Ferreira, A.D. Scott, S. Nielles-Vallespin, A. Giannakidis, P.J. Kilner, P.D. Gatehouse, R. de Silva, D.N. Firmin and D.J. Pennell, Relationship between cardiac diffusion tensor imaging parameters and anthropometrics in healthy volunteers, journal of cardiovascular magnetic resonance, 2016, 18:2 (427-429).

10.2: Methods

10.2.1: Study population

Healthy volunteers were identified via an email advert & poster sent out across the Royal Brompton and Harefield Trust. The following exclusion criteria were applied:

- History of pre-existing medical conditions e.g. any cardiovascular disease, chronic obstructive pulmonary disease and cerebrovascular disease.
- Any risk factor for cardiovascular disease (excluding age and gender) e.g. hypertension, diabetes, hypercholesterolaemia, smoking, significant family history of cardiovascular disease
- History of regular medication usage, PRN medication use was permitted.
- Any symptoms consistent with a history of undiagnosed cardiovascular disease
- Previous abnormalities identified on cardiovascular imaging including CMR, echo and angiography

Prior to recruitment all volunteers underwent a screening process where the above questions were addressed in combination with a routine blood pressure check, ECG and physical examination.

10.2.2: Ethical Approval

Ethical approval for healthy volunteer advertisement and recruitment was granted by the NRES Committee South East Coast Surrey (REC reference 10/H0701/112). Volunteers were given an information sheet, prior to giving consent, which covered the potential for incidental findings and their management. All volunteers were made aware they were free to withdraw their consent to participation at any point in the process.

10.2.3: Image Acquisition

cDTI was performed with DW-STEAM at 3T during the end systolic and diastolic pauses identified from a mid-ventricular short axis bSSFP cine acquisition in each subject. Data were acquired in 3

mid ventricular short axis slices, typically for 10 image repetitions, with a range of 8-13, before signal averaging to improve SNR. More repetitions were acquired when poor breath holding was noted to have spoiled previous acquisitions. The diffusion weighting was set to b_{main}=350s/mm^2 and b_{ref} was 135s/mm^2 in line with recent data (426). To ensure the same slice was imaged during both systolic and diastolic acquisitions the slice position was tracked between systole and diastole with a breath-hold spoiled gradient echo (GRE) sequence with a spatial modulation of magnetisation (SPAMM) tagging prepulse in the 2 and 4 chamber views. The linear tags were separated by 16 mm and were perpendicular to the long-axis with an acquired spatial resolution of 2.1x1.7mm in-plane and slice thickness of 6mm. The displacement of the linear tag closest to the central mid- ventricular slice was manually tracked from the systolic to the diastolic phase. Functional and volumetric data were determined from retrospective bSSFP cine acquisitions in 3 long axis planes and a stack of short axis slices from the ventricular base to the apex. The typical duration of the scan was 55-70mins. Full details of all sequence parameters are discussed in Chapter 8.

10.2.4: Image Analysis

Following initial post processing steps the eigensystem (eigenvalues and eigenvectors) were calculated from the diffusion tensor for each voxel. MD, FA and HA data were calculated as previously described (chapter 8). For the helix angle, left-handed epicardial helix angles were assigned a negative value and right-handed endocardial helix angles assigned a positive valve, with myocytes with no angulation (zero) representing circumferential myocytes (64, 423). To obtain a single, transmural value relating to helix angle, a gradient was calculated from best-fit radial projections drawn from the epicardial border to the centre of the ventricle. The gradient data are presented in two formats: HAG (degrees/mm) and HAg (degrees/%depth). Both HAG (372) and HAg (371) have previously been employed in HA analyses, both were included on this occasion to permit comparison of both results both with (HAG) and without (HAg) division by local wall thickness.

The secondary eigenvector (E2) was taken to represent the mean sheetlet orientation with E2A derived from the angle between E2 and the cross-myocyte direction. This angle was measured in the range 0–90, with zero degrees as being aligned to the local LV wall. E2A mobility uses the absolute value of the angle, ignoring the polarity, to provide a measure of change of angulation. E2A mobility was defined as the change of mean absolute E2A values from diastole to systole.

For quantitative analysis of cDTI parameters the myocardium was divided into the conventional 4 LV segments: anterior, septal, inferior, lateral. HA analysis further segmented the myocardium transmurally into endocardial, mesocardial and epicardial layers. This was performed by dividing the local myocardium into three equal thickness layers, bound by the epicardial and endocardial borders.

Global values for FA, MD, HAg and E2A were calculated in systole and diastole. Regional measures were determined by then dividing the myocardium into the 4 conventional segments (anterior, septal, inferior, lateral), grouping the same segments in each slice. The post- processing and analysis time on this occasion was approximately 1 h per subject.

10.2.5: Functional and Volumetric Analysis

Ventricular volumes, function, mass, and EF for all patients were measured for the LV using a semi-automated threshold-based technique (CMRtools, Cardiovascular Imaging Solutions, London) and indexed to body surface area.

10.2.6: Statistical Analysis

Cohort characteristics are presented as the mean±SD or median & range, and percentage for categorical data. Variations in parameters between slices were assessed, with no discernible between slice difference for FA, MD, HAG and Hag, as previously described in

McGill et al. (422). Global and regional data are thus presented from all three slices to increase the number of points per parameter. For E2A data, significant inter-slice variations were detected, therefore data are presented by slice, and regionally for the mid slice only. Global systolic and diastolic values were compared with a paired t-test. Comparison of regional data was conducted with a repeated measures ANOVA. Post hoc analysis was performed with a two-tailed paired t-tests, with Bonferroni correction (applied directly to the p value), taking the lateral wall as the reference. Significance was set at $p<0.05$.

cDTI parameters were analysed for association with the following covariates: age, gender, BSA, EF, left ventricular end diastolic volume (LVEDV), left ventricular end systolic volume (LVESV), LV mass and maximum LV wall thickness in diastole (MWTd). The association between covariates and global systolic and diastolic quantitative cDTI parameters were assessed with simple linear regression with significance set at $p<0.05$. For HA data regression was performed for both HAg and HAG in case normalising the gradient to the local wall thickness eliminates anthropometric associations.

10.3: Results

10.3.1: Study Population

The baseline characteristics and CMR data for the study population are given in table 10.2. A total of 46 volunteers where recruited, 2 were excluded due to ECG irregularities and 1 further subject was excluded based on poor quality diastolic data.

Baseline Characteristics	N = 43
Age: (years &range)	45 (24–74)
Male subjects	26 (60%)
RR interval (ms)	960 ± 160
BSA: (m2)	1.88 ± 0.20
BMI: (kg/m2)	24.5 ± 3.0
LVEDV: (mL)	146 ± 33
LVESV: (mL)	47 ± 13
LVM: (g)	128 ± 32
MWTd (mm)	9 ± 1.2
LVEF: (%)	68 ± 6

Table 10.2: Baseline subject characteristics, mean±SD or median and range. BSA body surface area, BMI body mass index, LVEDV Left ventricular end diastolic volume, LVESV Left ventricular end systolic volume, LVM, Left ventricular mass, MWTd Maximum wall thickness in diastole, LVEF left ventricular ejection fraction.

10.3.2: Global and Regional cDTI Results

10.3.2.1: Fractional Anisotropy

Comparative regional systolic and diastolic FA values are given in table 10.3. Systolic and diastolic FA maps from an example patient are given in figure 10.3. Global diastolic FA was significantly greater than systolic FA (0.56±0.04 v 0.47±0.05, $p<0.01$). Significant regional differences were detected in both phases with comparatively less anisotropy in the lateral wall.

Fractional Anisotropy	N = 43	p value
Systolic:		ANOVA: F = 5.21, p = 0.003
Lateral	0.46 ± 0.05	Reference
Anterior	0.48 ± 0.05	p = 0.017
Inferior	0.48 ± 0.06	p = 0.007
Septal	0.46 ± 0.07	p = 1.0
Diastolic:		ANOVA: F = 16.0, p <0.001
Lateral	0.52 ± 0.07	Reference
Anterior	0.59 ± 0.05	p < 0.001
Inferior	0.59 ± 0.05	p < 0.001
Septal	0.54 ± 0.09	p = 0.004

Table 10.3: Fractional anisotropy in systole and diastole, mean±SD

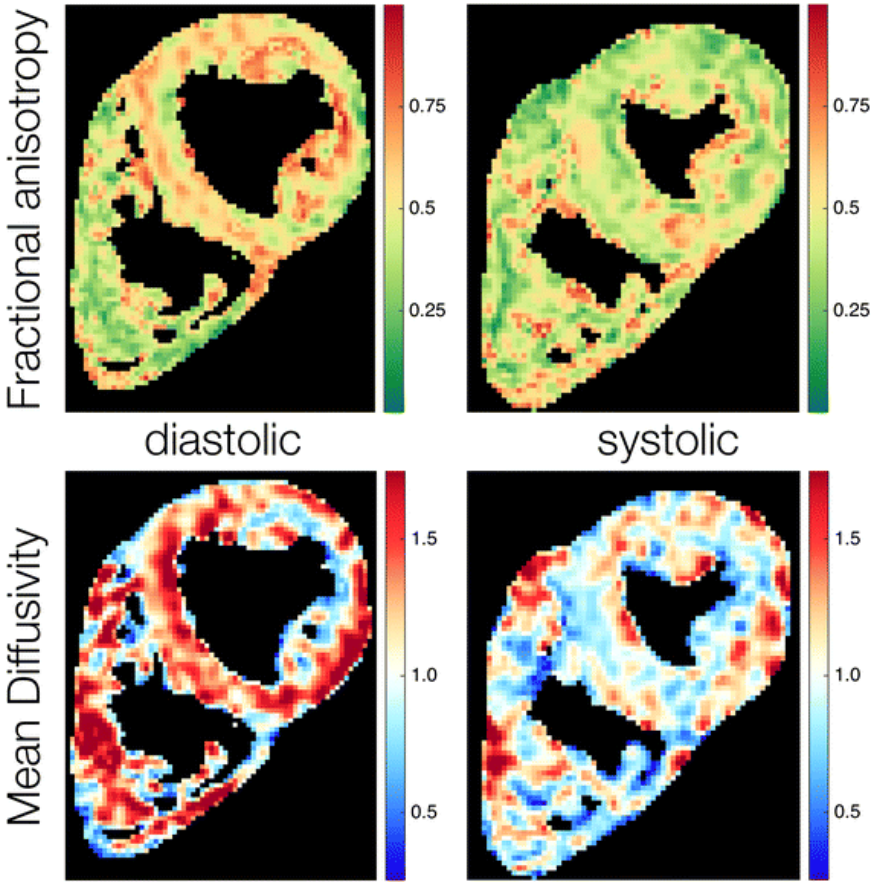

Figure 10.3: Colour scaled systolic and diastolic FA and MD maps in an example patient. In diastole both FA and MD are greater (more orange and red respectively) (427).

10.3.2.2: Mean Diffusivity

Regional systolic and diastolic MD values are given in table 10.4. Systolic and diastolic MD maps from an example patient are given in figure 10.3. Global diastolic MD was significantly greater than systolic MD (1.11±0.13 v 0.93±0.14 × 10^{-3} mm^2/s, p<0.001). There were no statistically significant regional differences in systolic MD. In diastole lateral wall MD was significantly greater than anterior and inferior wall.

Mean Diffusivity (×10^{-3} mm^2/s)	**N = 43**	**p value**
Systolic:		ANOVA: F = 1.50, *p* = 0.22
Lateral	0.95 ± 0.16	
Anterior	0.90 ± 0.18	
Inferior	0.93 ± 0.18	
Septal	0.94 ± 0.18	
Diastolic:		ANOVA: F = 14.3, *p* <0.001
Lateral	1.20 ± 0.24	Reference
Anterior	0.99 ± 0.15	*p* <0.001
Inferior	1.05 ± 0.18	*p* = 0.01
Septal	1.20 ± 0.25	*p* = 1.0

Table 10.4: Regional mean diffusivity in systole and diastole, mean ± SD

10.3.2.3: Helix Angle

Transmural and regional helix angle values are represented in a Bullseye plot in figure 10.4. The helix angle in systole and diastole are depicted in 3D in figure 10.5. Epicardial and endocardial transmural helix angles were more longitudinally orientated in systole compared to diastole (Epi: -35±5° v -30±6°, p<0.001; Endo: 34±5° v 25±5°, p<0.001). Regional, systolic and diastolic HAg (°/%) values are displayed in table 10.5. In keeping with the helix angle data, global systolic HAg was significantly greater than global diastolic HAg (0.91±0.11° v 0.68±0.1°, p<0.001). In both cardiac phases significant regional HAg differences were observed, with the greatest HAg in the septum in both cardiac phases (table 10.5).

Helix Angle Gradient (°/%)	N = 43	p value
Systolic:		ANOVA: F = 24.0, $p < 0.001$
Lateral	0.90 ± 0.16	Reference
Anterior	0.98 ± 0.21	$p = 0.13$
Inferior	0.76 ± 0.15	$p < 0.001$
Septal	1.0 ± 0.12	$P = 0.007$
Diastolic:		ANOVA: F = 51.9, $p < 0.001$
Lateral	0.58 ± 0.13	Reference
Anterior	0.72 ± 0.12	$p < 0.001$
Inferior	0.61 ± 0.13	$p = 1.0$
Septal	0.83 ± 0.14	$p < 0.001$

Table 10.5: Regional Helix angle gradient in systole and diastole, mean ± SD

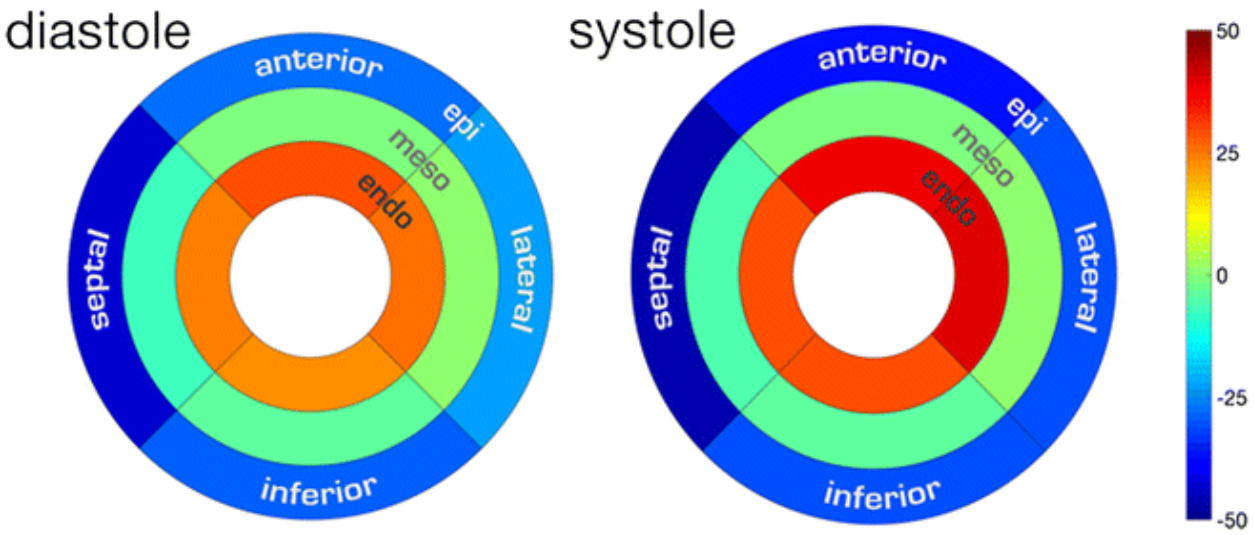

Figure 10.4: Bullseye plot of the average helix angle per LV regional wall and transmural layer in both systole and diastole. In systole epicardial and endocardial helix angles are more longitudinally orientated (deeper blue and deeper red respectively) (427).

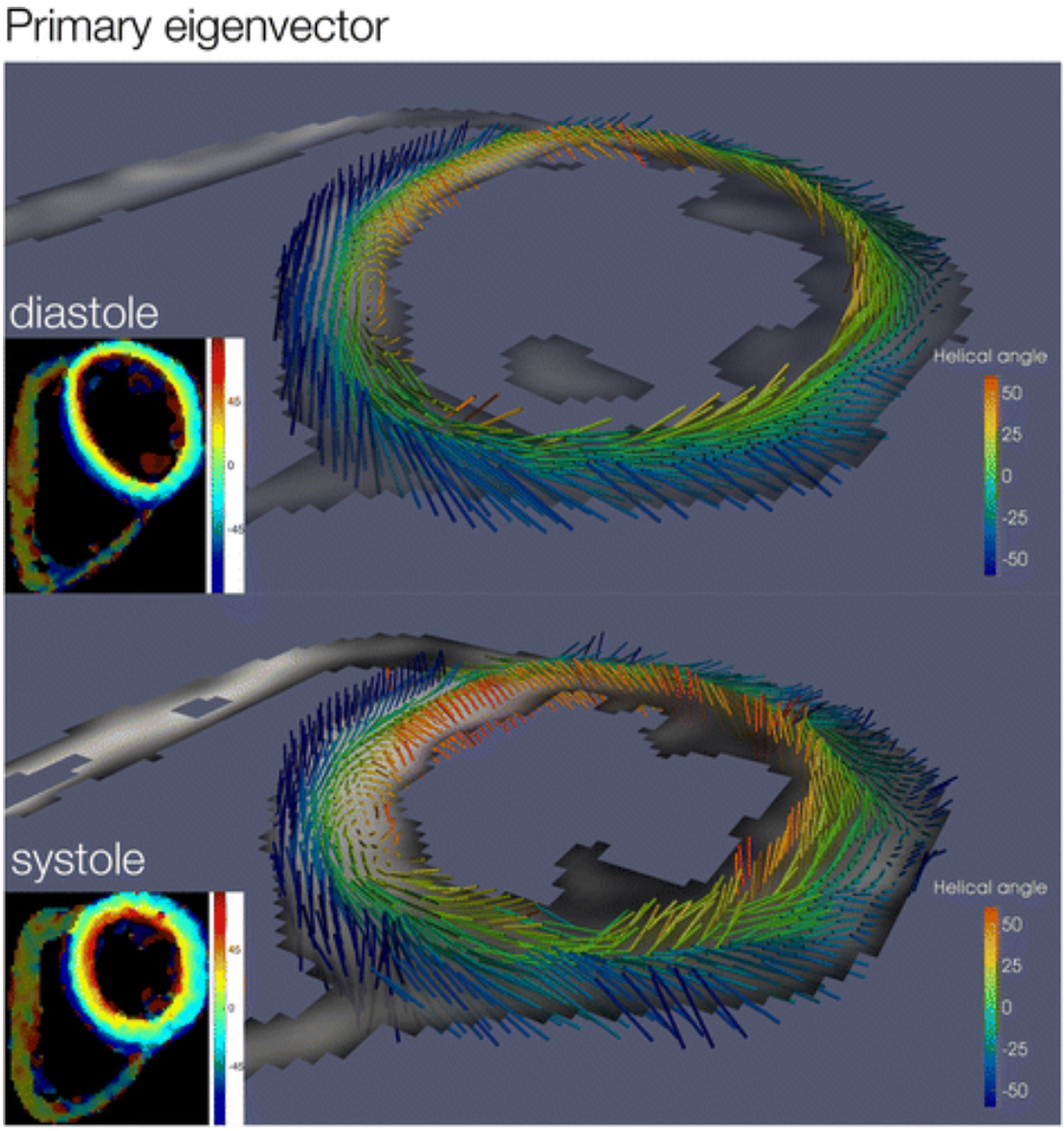

Figure 10.5: 3D representation of primary eigenvector, helix angle data in diastole and systole showing a progression of myocytes from a left-handed helix in the epicardium (blue), to circumferential in the mesocardium (green) to a right-handed helix in the endocardium (red) (427).

10.3.2.4: Secondary Eigenvector Angle

E2A angles and E2A mobility in both cardiac phases showed significant inter-slice variation with greatest angulation in the basal slice (Systole: apical 47±6°, mid 54±6°, basal 58±4° $p < 0.001$; Diastole: apical 23±5°, mid 26±6°, basal 29±6° $p < 0.001$; Mobility: apical 24±9°, mid 27±8°, basal 29±7°, p=0.006). Mid slice values for regional systolic and diastolic E2A are given in table 10.6. E2A in systole and diastole are represented in 3D in figure 10.6. Global (mid-slice) E2A was

significantly greater in systole than diastole (E2A 54±6° v 26±6°, p<0.001), with a global E2A mobility of 27±8°. Significant differences in regional E2A were detected in both phases with the smallest angles in the anterior wall (table 10.6).

Secondary Eigenvector Angle (°)	***N* = 43**	***p* value**
Systolic:		ANOVA: F = 5.07, *p* = 0.02
Lateral	55 ± 8	Reference
Anterior	51 ± 8	*p* = 0.019
Inferior	55 ± 7	*p* = 1.0
Septal	55 ± 10	*p* = 1.0
Diastolic:		ANOVA: F = 16.8, *p* < 0.001
Lateral	24 ± 8	Reference
Anterior	22 ± 8	*p* =1.0
Inferior	30 ± 7	*p* <0.001
Septal	30 ± 10	*p* =0.002
Mobility:		ANOVA: F = 4.64, *p* = 0.004
Lateral	31 ± 11	Reference
Anterior	29 ± 11	*p* = 0.43
Inferior	24 ± 10	*p* = 0.009
Septal	26 ± 14	*p* = 0.11

Table 10.6: Regional E2A in systole and diastole and regional E2A mobility, mean±SD. Data are from the mid slice only.

10.3.3: Relationship Between Subject Anthropometrics and cDTI Parameters

10.3.3.1: Fractional Anisotropy

There was a significant relationship between global systolic FA and RR interval with a decrease in FA of 0.013 for every 100 ms increase in RR interval (Standardised coefficient −0.43, p = 0.004). No subject characteristics were associated with global diastolic FA.

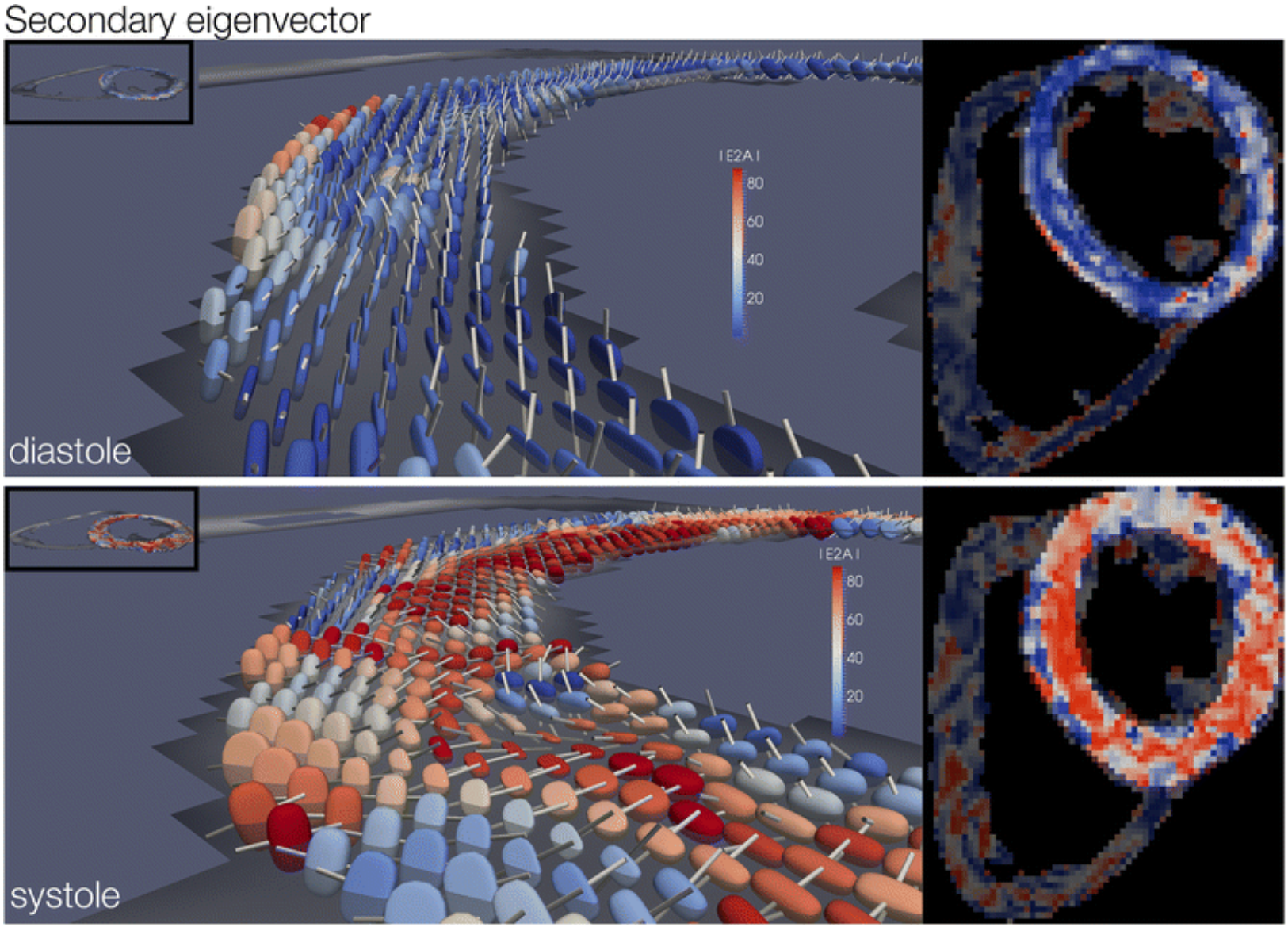

Figure 10.6: Data from the interventricular septum of an example patient represented in super quadric glyphs. The stick bars and colour indicate the orientation of the secondary eigenvector, the shape of the glyph represents the full tensor. E2A has a predominantly vertical orientation in diastole (blue) and horizontal orientation in systole (red) (427).

10.3.3.2: Mean Diffusivity

Global diastolic MD was $0.078x10^{-3}mm^2/s$ less in male patients (Standardised coefficient −0.31, p=0.046). Diastolic MD was inversely related to RR interval (Standardised coefficient −0.30, p = 0.048), with a 100ms increase in RR interval associated with $0.024x10^{-3}$ mm^2/s decrease in MD. LV wall thickness was also inversely related to diastolic MD (−0.37, p=0.015). There were no significant associations between subject anthropometrics and global systolic MD.

10.3.3.3: Helix Angle Gradient

Global systolic HAg (°/%) was inversely related to RR interval (Standardised coefficient -0.51, p<0.001), with a 100 ms increase in RR interval accounting for a decrease in HA between the endo and epicardium of 3°. There was also an inverse relationship between systolic HAg and LV end diastolic volume (EDV) (Standardised coefficient -0.51, p <0.001), LV end systolic volume (ESV) (Standardised coefficient -0.33, p = 0.033) & LV mass (Standardised coefficient -0.35, p = 0.021). Global diastolic HAg was 0.11°/% less in male patients, p < 0.001. Global diastolic HAg was also inversely related to BSA (Standardised coefficient -0.44, p = 0.003), LVESV (Standardised coefficient -0.33, p = 0.031), LV Mass (Standardised coefficient -0.37, p = 0.015), and maximum wall thickness in diastole (MWTd) (Standardised coefficient -0.33, p = 0.029).

Global systolic and diastolic HAG data (°/mm) were also regressed against subject anthropometrics and demonstrated much of the same associations as HAg (Systolic HAG: 0.41°/mm less in male patients, p = 0.005; BSA (Standardised coefficient −0.39, p = 0.01), LVEDV (Standardised coefficient −0.36, p = 0.019); LVMass (Standardised coefficient −0.54, p <0.001); MWTd (Standardised coefficient −0.57, p <0.001). Global diastolic HAG v age (Standardised coefficient −0.50, p = 0.001), EF (Standardised coefficient −0.37, p = 0.014) and MWTd (Standardised coefficient −0.45, p = 0.002)).

10.3.3.4: Secondary Eigenvector Angle

For global systolic E2A, an increase in RR interval of 100ms was associated with an increase in systolic E2A of 1° ($p = 0.011$). Systolic E2A was also related to BSA (Standardised coefficient 0.36, $p = 0.019$), LV Mass (Standardised coefficient 0. 49, $p = 0.001$), LVEDV (Standardised coefficient 0.31, $p = 0.044$) and MWTd (Standardised coefficient 0.48, $p=0.001$). There were no associations between subject anthropometrics and global diastolic E2A. E2A mobility was inversely related to both age (Standardised coefficient −0.40, $p = 0.008$) and EF (Standardised coefficient 0.45, $p = 0.002$).

10.4: Discussion

This work is the largest healthy volunteer in vivo cDTI study to date, and the first to study the relationship between subject anthropometrics and quantitative cardiac parameters. Understanding the normal variation in cDTI measurements is required before findings in pathological states can be interpreted with any confidence.

10.4.1: Global and regional analysis

Global systolic FA (0.47 ± 0.05) was in keeping with the corrected values from Nielles-Vallespin et al. (systolic: 0.46 ± 0.04) (426), but greater than Tunnicliffe et al. (systolic: 0.41 ± 0.05). Diastolic global values were similar (0.56±0.04 v Tunnicliffe et al. diastolic: 0.54 ± 0.04). Subtle but significant FA regional variation was observed in both cardiac phases (5% in systole, 12% in diastole), which contrasts with healthy data from Tseng et al. (294), and our assessment in hypertrophic cardiomyopathy (Chapter 9). Although the difference is of little clinical significance, it exceeds the difference between infarct and remote myocardium previously reported by Wu et al. (369). The pattern of regional variation observed in this work is suspicious of an off-resonant spin artefact as the FA values in the lateral and septal walls are similar but different to the inferior and anterior walls. Such artefacts are most common in the phase encoding direction and are thus

capable of producing this pattern of heterogeneity. Arguing against this is that similar patterns of heterogeneity would have been expected in previous works if this were a substantial contributor. Regarding technical contributors the most likely culprit is the regional variation in SNR, which depends on wall thickness and proximity to the receiver coil.

Global phasic MD values were in agreement with Nielles-Vallespin et al. (19) and Tunnicliffe et al. (372). SNR heterogeneity is again likely to have played a part in regional heterogeneity, especially as the number of pixels across the wall is reduced in diastole. Regional variation of ~18% in diastolic MD was detected, which is greater than the difference between infarct and remote zone reported by Wu et al. (b = 300 s/mm2) (369) but significantly less than the difference between infarct and remote zone reported by Nyguen et al. (b = 400 s/mm2) (370). Given that we had previously found MD to be the least reproducibility parameter, this is further evidence that MD results should be interpreted with caution in the context of pathology.

Helix angle data is derived from the largest i.e. primary eigenvector and thus should be the most reliable parameter. However in order to appreciate the complexity of the transmural angulation data must be processed in transmural layers. This exposes the endocardium and epicardium to variation associated with ROI drawing and poor SNR is likely to have a bigger impact on edge pixels, for this reason the range in angles was not assessed. As discussed in Chapter 9, performing statistics on HA data is also fraught with difficulty as the mesocardial layer passes through zero. In order to circumvent these issues, regional subdivision data were processed as the HAg (°/%), the advantage being reduced sensitivity to ROI variation, but this is at the expense of data smoothing when drawing best fit radial lines.

10.4.2: Phase Specific Differences in cDTI Parameters

This work demonstrates significant phasic differences in cDTI parameters, with greater FA and MD in diastole. Similar parameter differences have been observed in ex vivo work by Hales et al. (FA only) (13), Lohezic et al.(92), and Teh et al. (MD only) (376). Such differences could be attributed to changes in myocyte and/or sheetlet re-orientation between the two phases, however phasic comparisons of monopolar DW-STEAM data have been criticised due to the potential for strain corruption of cDTI data (151, 366). Whilst this work was being conducted, Stoeck et al. (150), Kings College Hospital, published phasic values for strain corrected DW-STEAM data which contradicted our data, instead proposing greater MD in systole and only an minor increase in diastolic FA in the apical slice (table 10.7).

		systole		*diastole*	
		w/o correction	*with correction*	*w/o correction*	*with correction*
MD [10^{-4} mm^2/s]	*base*	*8.6±1.2**	*9.5±1.3*	*8.5±1.0**	*8.2±1.0†*
	medial	*8.8±1.4**	*10.1±1.8*	*9.2±1.1**	*8.7±1.1†*
	apex	*9.6±0.8**	*11.2±1.2*	*10.1±1.1**	*9.4±0.9†*
FA	*base*	*0.52±0.03**	*0.61±0.02*	*0.61±0.05*	*0.61±0.04*
	medial	*0.52±0.05**	*0.60±0.03*	*0.61±0.04*	*0.61±0.04*
	apex	*0.48±0.02**	*0.55±±0.02*	*0.57±0.03*	*0.57±0.03†*

* indicates statistical significance (p-value<0.05) between uncorrected and corrected data and
†indicates statistical significance between systole and diastole.
doi:10.1371/journal.pone.0107159.t001

Table 10.7: Phasic FA and MD data from Stoeck et al. (150)

We recognise that strain corruption of cDTI data is possible, however the true extent is uncertain, and current strain correction protocols are simplistic (394). Although there is the possibility of strain artefact within these results, the similarity with static, ex vivo assessment is reassuring.

In keeping with this data, an increase in positive and negative longitudinal HAs in systole has been documented in previous in vivo cDTI studies, and has been proposed as the mechanism of circumferential shortening in systole (9, 150, 155). The primary eigenvector is thought to be the least affected by strain and other artefact, and our HAG data is largely in agreement with Stoeck at al. (150). However the HA effect is small in terms of LV dynamics, therefore arguably of more interest is the documented increase in systolic E2A and associated E2A mobility. This work is in

agreement with Le Grice et al. (9) and Hales et al. (13) and the proposed theory of sheetlet re-orientation as a mechanism of radial thickening. Hales et al. reported an increase in systolic intersection angulation of 23%, 29% and 26% in the basal, mid and apical regions respectively; in comparison we report an approximate two-fold increase in E2A across the slices. The exact cause for the difference in magnitude between our data and Hales et al. is unclear but may be attributable to interspecies differences or in vivo versus ex vivo model differences.

The secondary eigenvector has been reported to be the most strain sensitive, thus we concede that strain may have artefactually increased the magnitude of this effect, nonetheless we disagree with the strain corrected values proposed by Stoeck et al. (150) and previously by Dou et al (368). Stoeck et al. report a increase in systolic sheetlet angulation from 13%, 10% and 1% at base, mid and apex. If this were the true size of the effect, this is an apparent contradiction of the Le Grice theory of sheetlet reorientation contributions towards LV radial thickening in systole (Strain discussed further in Chapter 11).

10.4.3: Relation Between Subject Anthropometrics and cDTI Parameters

There have been no previous reports relating quantitative measures of cardiac cDTI to patient anthropometrics. In monopolar STEAM acquisitions, the exact diffusion weighting applied is dependent on the heart rate, despite applying heart rate correction to the b-value, there was residual heart rate dependent variability within global systolic FA, HAg and E2A measurements. However this effect was clinically small, with variation in parameters over a heart rate range of 60–100 bpm of 14° in epicardial to endocardial helix angle, 0.05 in FA, and 4° in systolic E2A. The reason behind this effect is unclear, but may be related to shorter mixing times (diffusion sensitivity) at faster heart rates.

Global systolic and diastolic HAg were inversely related to BSA, LVEDV, LV mass, LV wall thickness and male gender. Results were near identical when the helix angle gradient was

normalised to the local wall thickness (HAG), suggesting either parameter is suitable when analysing HA. This anthropometric association is a novel finding. It suggests that in vivo myocardial adaptations are achieved by increasing the number of myocytes between the subepicardium to subendocardium, maintaining a similar range of helix angles, rather than increasing epicardial and endocardial myocyte populations with increasing HA range.

Systolic E2A correlated with BSA, LV mass and LV wall thickness such that an increase in LV mass of 50g or BSA of 0.5 m2 accounted for an increase in E2A of 4°; and a 1 mm increment in wall thickness accounted for an increase of 2°. Somewhat surprisingly E2A mobility was inversely related to EF, with an increased in EF of 10% associated with a decrease in E2A mobility of 5°. Given that sheetlet mobility has been proposed as a mechanism of systolic function, on face value this appears counter intuitive, however, this effect is clinically small and must be interpreted within the context of the normal range of EF in this healthy population. In addition, age related increases in EF combined with decreasing cardiac volumes are well documented (41), this relationship between E2A mobility and EF may therefore be a reflection of age related increases in normal range EF.

10.5 Limitations

In addition to the limitations already discussed misregistration of slice averages may not be homogeneous across the ventricle, or across the population, and therefore has the potential to skew results. Strain is a contentious issue and the true impact remains uncertain. Strain correction of these results was not conducted as we believe that the model of isotropic jelly of strain to be simplistic (366), nonetheless we concede that strain may have skewed results to a degree.

10.6 Conclusion

This work is the largest in vivo cDTI study in healthy volunteers. Regional variations in cDTI parameter were demonstrated, however, these should be interpreted within the context of potential technical limitations. This is the first study to investigate the association between quantitative cDTI parameters and subject anthropometrics, with a novel finding of increasing helix angle gradient in line with , which increases with cardiac size and wall thickness.

CHAPTER 11: INVESTIGATION OF LAMINAR MECHANICS IN HYPERTROPHIC CARDIOMYOPATHY

11.1: Introduction

Cardiovascular diffusion tensor imaging is unique in its ability to interrogate the myocardial microarchitecture in different cardiac phases. Chapter 10 demonstrated further confirmation of the theory of systolic sheetlet reorientation in healthy volunteers, however the relation between sheetlet function and cardiovascular disease phenotypes is unknown. Patients with hypertrophic cardiomyopathy (HCM) display abnormal myocardial mechanics; despite elevated EFs, radial strains of hypertrophied segments are reduced (225, 430, 431). Hypertrophy in HCM has been proposed as a compensatory mechanism for genetic sarcomeric abnormalities, resulting in a loss of contractile function (220, 432). Conversely sarcomeric mutations have also been reported to result in a gain of function, and it has been suggested that hypertrophy is the product of hyper-contraction (222, 224). Diastolic dysfunction in HCM is well recognised and associated with symptoms in affected patients (14). The origins diastolic dysfunction are disputed, but myocardial fibrosis is a potential contributor (168). cDTI presents a novel opportunity to non-invasively assess both myocyte and laminar mechanics in vivo, combined with an assessment of fibrosis in patients with HCM in a bid to improve our understanding of disease specific structure-function relations and the origins of impaired myocardial mechanics. This work was published in: Pedro F Ferreira∗, Philip J Kilner*, **Laura-Ann McGill***, Sonia Nielles-Vallespin, Andrew D Scott, Siew Y Ho, Karen P McCarthy, Margarita M Haba, Tevfik F Ismail, Peter D Gatehouse, Ranil de Silva, Alexander R Lyon, Sanjay K Prasad, David N Firmin and Dudley J Pennell, In vivo cardiovascular magnetic resonance diffusion tensor imaging shows evidence of abnormal myocardial laminar orientations and mobility in hypertrophic cardiomyopathy, journal of cardiovascular magnetic resonance, 2014;16:87 (395) * joint first authors.

11.2: Methods

11.2.1: Study population

In this explorative study 11 patients with HCM and 11 age matched healthy volunteers were recruited for cDTI acquisitions. Healthy volunteers were recruited based on inclusion & exclusion criteria outlined in Chapter 10. Patients with contradictions to cDTI, such as significant arrhythmia, were excluded from the study.

11.2.2: Ethical Approval

Ethical approval for recruitment of patients with hypertrophic cardiomyopathy and healthy volunteers was granted by the NRES Committee South East Coast Surrey (REC reference 10/H0701/112). All volunteers were given an information sheet, prior to giving consent, outlining the study objectives and logistics. All volunteers were made aware they were free to withdraw their consent to participation at any point in the process.

11.2.3: Image Acquisition

cDTI was performed with DW-STEAM at 3T during the end systolic and diastolic pauses identified from a mid ventricular short axis bSSFP cine acquisition in each subject. Data were acquired in 3 mid ventricular short axis slices, with approximately 10 (range 8-13) repetitions, before signal averaging. The diffusion weighting was set to b_{main}=350s/mm^2 and b_{ref} was 135s/mm^2 in line with recent data (426). An additional breath-hold spoiled gradient echo (GRE) sequence with a spatial modulation of magnetisation (SPAMM) tagging prepulse, in the 2 and 4 chamber views, to permit tracking of the cDTI slices between systole and diastole. Functional and volumetric data were determined from retrospectively bSSFP cine acquisitions in 3 long axis planes and a stack of short-axis slices from the ventricular base to the apex. In HCM patients, additional LGE images were acquired with a PSIR sequence, in the same image planes as functional images, with additional phase swap imaging where enhancement was ambiguous. The typical duration of the

scan was 75-90mins with LGE acquisitions. Full details of all sequence parameters are discussed in Chapter 8.

11.2.4: Diffusion Tensor Analysis

Following initial post processing steps, the eigensystem (eigenvalues and eigenvectors) were calculated from the diffusion tensor for each voxel. From this data two cDTI parameters were determined: the HA and E2A. For HA data left-handed epicardial helix angles were assigned a negative value and right-handed endocardial helix angles assigned a positive valve, in the range -90 to 90 degrees (64, 423). For E2A, the angle is presented with a range of -90, 90, being positive if rotated clockwise from the cross-myocyte direction and negative if rotated counter-clockwise. E2 mobility was defined as the change of mean absolute E2A values from diastole to systole, using the absolute value of E2A, ignoring polarity, to provide a measure of phasic change in angulation.

For 3D visualization of primary eigenvector data distributions, tractography was performed in ParaView (Kitware, NM, USA) with color-coding according to the helix angle. No further analysis was performed on the tractograms.

Mean intra-voxel sheetlet angulations in the septal and anterior wall regions, are represented by superquadric glyphs with central white sticks representing the orientation of E2. The glyphs are color coded according to their absolute E2A value and 3D visualization of tensor information was performed using Python and ParaView. All cDTI analysis was performed by a single observer, on completion off all studies, blinded to clinical data. 3D visualisation of the tensor with superquadric glyphs (358) was implemented using Python and ParaView (Kitware, NM, USA) software. The post-processing and analysis time was approximately 3 hours per study.

11.2.5: Functional, Volumetric and Late Gadolinium Enhancement Image Analysis

LV volumes, function, mass, and EF for all patients were measured using CMRtools software (Cardiovascular Imaging Solutions, London). All volume and mass measurements were indexed to BSA calculated using the Du Bois method (41).

To investigate the relation between fibrosis and mechanics in the HCM cohort the myocardium was divided into 12 short-axis segments, with the first segment determined by the superior RV insertion and subsequent segments labelled in a clockwise direction. Hypertrophy and LGE were recorded as present/ absent for each segment by 2 observer consensus resulting in the following categories: segments with hypertrophy and LGE (H+LG+); segments with hypertrophy but no LGE (H+LG-); and segments with no hypertrophy or LGE (H-LG-). The extent of LGE was then further quantified using CVI42 software (Circle Cardiovascular Imaging Inc, Calgary, Canada) with a full-width half-maximum threshold and expressed as percent of LV mass.

11.2.6: Quantitative and Statistical Analysis

The measured HA and E2A values were plotted as histograms for all subjects in order to visualize the angle distribution. For further analysis of the effects of hypertrophy, E2A data were presented in a scatter plot against LV wall thickness. Mean absolute E2A values were compared between groups with the Mann-Whitney-Wilcoxon test. Statistical significance was considered present when $p < 0.05$ after Bonferroni correction for the number of tests performed.

11.3: Results

11.3.1: Subject Characteristics

The baseline demographics and clinical characteristics of control and patient groups are shown in (table 11.1). The time spent on diffusion acquisition was 42±7 min (mean±SD) for controls, and 46±7 min for HCM patients.

	HCM Patients (n =11)	Controls (n =11)	P value
Age (years)	62 ± 9	56 ± 10	0.16
Male	8 (73%)	6 (55%)	0.40
Body surface area (m2)	1.89 ± 0.2	1.83 ± 0.2	0.52
Body mass index (kg/m2)	26.1 ± 3.6	24.2 ± 2.3	0.15
RR interval (ms)	995 ± 150	984 ± 108	0.84
Mid systolic pause (ms)	373 ± 70	353 ± 41	0.42
Mid diastolic pause (ms)	798 ± 96	731 ± 79	0.09
Indexed LV EDV (mL/m2)	65 ± 15	78 ± 16	0.08
Indexed LV ESV (mL/m2)	14 ± 5	23 ± 5	0.001
LV ejection fraction (%)	79 ± 6	71 ± 3	<0.001
LV mass index (g/m2)	104 ± 41	67 ± 15	0.009
Maximum end-diastolic wall thickness (mm)	23 ± 4	9 ± 1	<0.001

Table 11.1: Subject characteristics (Mean±SD or number (%) patients)

The ventricular morphology, risk factors for sudden death and LGE patterns for the HCM patients are summarized in table 11.2. Ten out of 11 patients had asymmetrical septal hypertrophy and 1 patient had anterior wall hypertrophy. All patients had regional fibrosis on LGE imaging usually affecting the septum and representing 9.1% of LV mass. Only 2 patients had undergone genetic screening with no identifiable abnormalities.

LV morphology & risk factors	
Asymmetrical septal hypertrophy n (%)	10 (91%)
Anterior hypertrophy n (%)	1 (9%)
LV outflow tract obstruction at rest n (%)	6 (55%)
Number of risk factors for sudden death: median (range)	0 (0-2)
Presence of late gadolinium enhancement	11 (100%)
Extent of late gadolinium enhancement (% of LV mass)	9.1 ± 3.6%
Location of gadolinium enhancement:	
Septum	10 (91%)
Anterior	4 (36%)
Inferior	2 (18%)
Lateral	4 (36%)
> 1 region	8 (73%)

Table 11.2: Characteristics of the HCM cohort.

11.3.2: Diffusion Tensor Visualisation

Figure 11.1 is a 3D diffusion tensor data comparison for an example HCM patient and control subject in systole and diastole. Tractographic representation of HA (E1) demonstrates the expected smooth transition from a negative, left-handed helix in the epicardium to a positive, right-handed helix in the endocardium in both subjects, with no change in pattern between phases. In healthy subjects E2A had a relatively vertical, wall parallel orientation in diastole and more horizontal, wall perpendicular aligment in systole, as described in Chapter 10. However, in the hypertrophied septum of HCM patients, E2A retained a horizontal, wall perpendicular orientation in both cardiac phases with little change between phases.

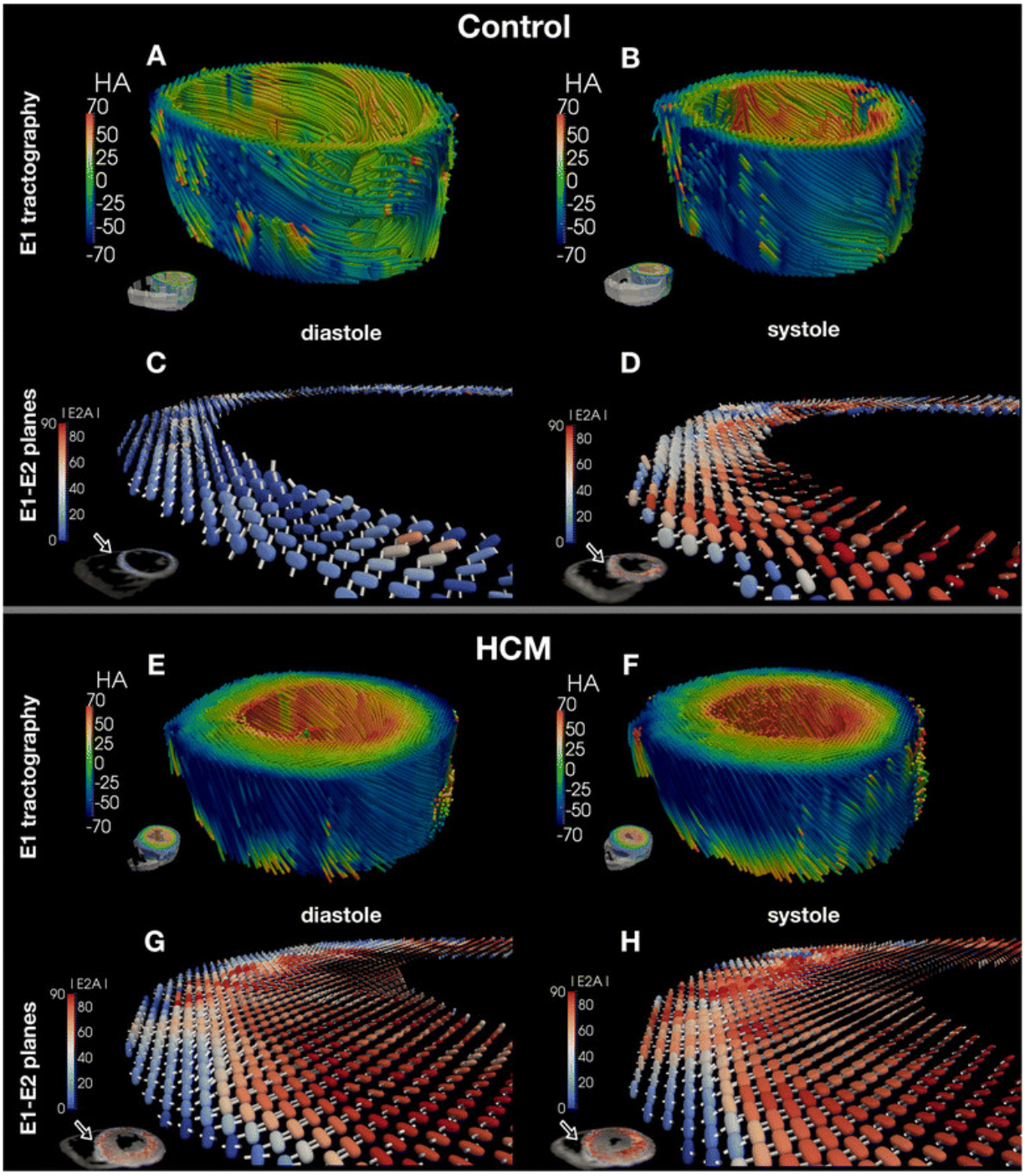

Figure 11.1: Three dimensional visualization of the primary eigenvector (E1) helix angle (HA) and secondary eigenvector angle (E2A). Panels A, B, E and F E1 tractography for a control and an HCM patient in diastole and end systole respectively. Color bars indicate the color map used for HA. Tracts are of comparatively poorer quality in diastole in control subjects due to the limited number of pixels across the myocardial wall. Panels C, D, G and H demonstrate the diffusion tensor in superquadric glyph form with white sticks indicating the direction of E2 for each tensor. The superquadric glyphs are color coded according to the absolute E2 angle as in the color bars: blue indicates more wall-parallel orietnations and red more wall-perpendicular. The glyphs typically re-orientate from blue in diastole to red in systole in the control subjects, but in the hypertrophic septal regions in HCM, E2A retains a systolic, more wall-perpendicular orientation, in both diastole as well as systole (395).

11.3.3: Diffusion Tensor Quantification

cDTI was successfully performed on all subjects. Only 3.2% of all eigenvalues were spuriously negative, for which we assigned the positive mean values of adjoining voxels.

11.3.3.1: Helix Angle

Histograms of phase specific distributions of HA for HCM and control cohorts are illustrated in figure 11.2. Both cohorts demonstrate the classical pattern of transmural myocyte orientation. Near identical myocyte HA distributions are observed in systole, however in diastole there is a subtle, relative shift from circumferential myocytes towards longitudinal myocytes in the HCM cohort.

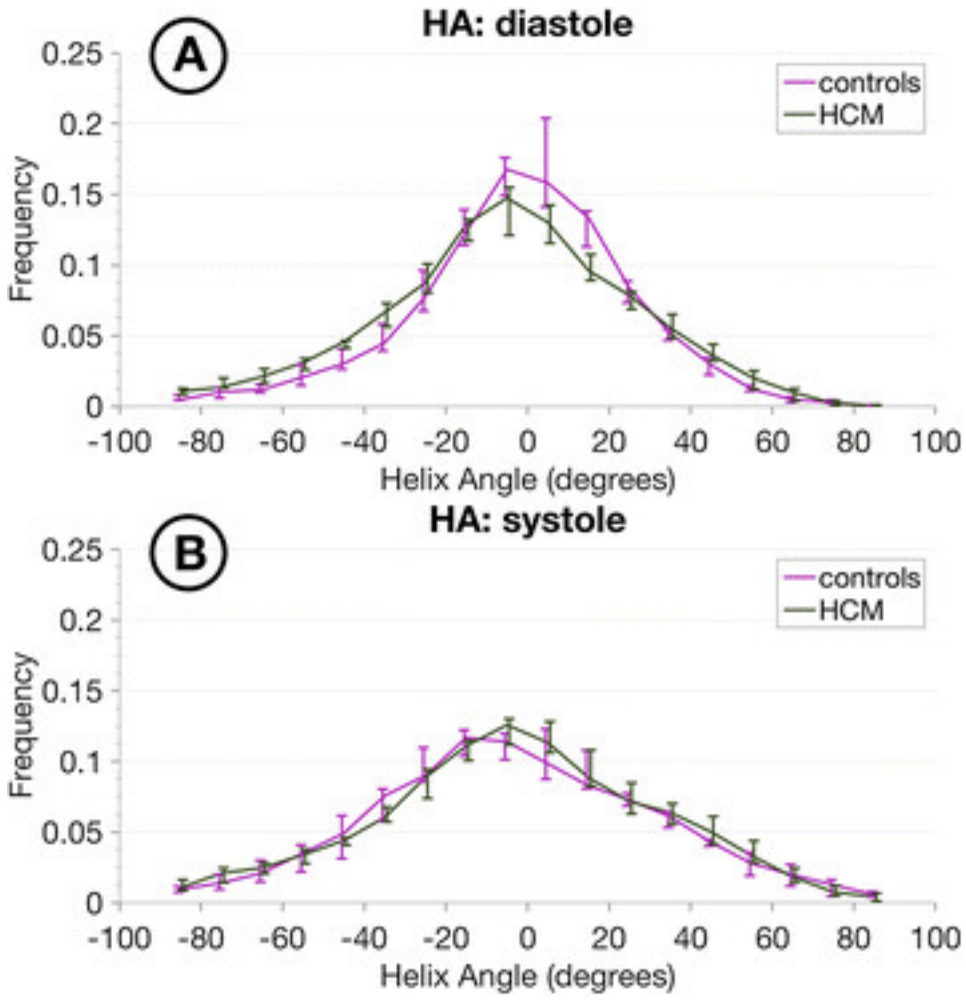

Figure 11.2: Histograms of myocardial HA values in HCM and control cohorts in both cardiac phases. Bin size is 10°. The lines represent the median for each bin and the vertical bars the corresponding interquartile range. A) Diastole, B) Systole (395).

11.3.3.2: Secondary Eigenvector Angle

Histograms of phase specific distributions of E2A data for both cohorts are demonstrated in figure 11.3. Systolic values peak at ±90 degrees for both groups, implying that average sheetlet orientations are perpendicular to local wall planes. HCM sheetlets have a comparatively exaggerated systolic response, with a greater proportion of ±90 angles. In controls the diastolic angles peak at approximately 0 degrees, implying a vertical/ wall parallel distribution of sheetlets. However, in HCM, there is little change from the systolic distribution in diastole.

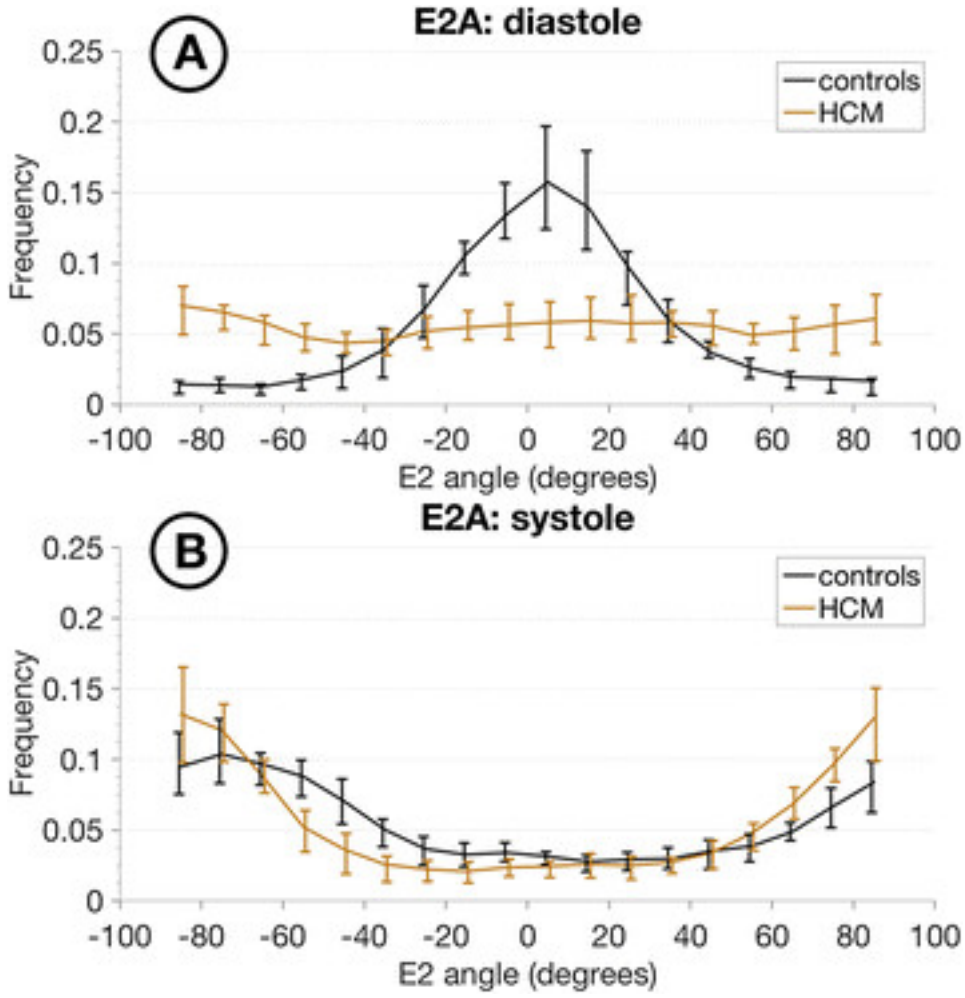

Figure 11.3: Histograms of E2A in systole and diastole for both cohorts. Bin size is 10°. Lines represent the median and interquartile range at each bin centre. In diastole (A) angles peak at zero degrees in the control cohort. In contrast the diastolic histogram is relatively flat in HCM. In systole (B) HCM patients display greater numbers of sheetlets at around ±90° (395).

On quantitative analysis of E2A (figure 11.4 and table 11.3), there was a significant difference in global mean diastolic E2A (47 v 24°, p<0.001), systolic E2A (64 v 56°, p=0.026) and E2A mobility (systolic-diastolic) (17 v 32, p<0.001) between HCM and control cohorts. Absolute E2A values were divided based on CMR measures of LVH wall thickness and LGE presence with 3 categories: hypertrophy with LGE (H+LG+); hypertrophy without LGE (H+LG-); without hypertrophy or LGE (H-LG-). There was a significant difference in diastolic E2A between non-hypertrophic segments (H-LG-) and the other two groups H+LG+ and H+LG- (p=0.0028 and p=0.0022 respectively, both after Bonferroni correction for 2 tests). There was also a significant difference in E2A in systole between hypertrophic regions and controls for H+LG+ segments and H+LG- segments (p=0.0060 and p=0.0030 respectively both after Bonferroni correction for 3 tests).

	E2A diastole median (°)	**E2A systole median (°)**	**E2A Mobility Median (°)**
Global analysis			
Controls	24	56	32
HCM	47	64	17
p-values	<0.001	0.026	<0.001
Segmental analysis			
H+LG+	58	66	8
H+LG-	55	67	13
H-LG-	38	60	28
H+LG+ vs H-LG- p-values	0.0028*	0.16*	0.012*
H+LG- vs H-LG- p-values	0.0022*	0.096*	0.020*
Controls vs H+LG+		0.0060†	<0.001†
Controls vs H+LG-		0.0030†	<0.001†
Controls vs H-LG-		0.38†	0.0186†

Table 11.3: Further analysis of E2A data based on LVH (H) and LGE (LG). *P-value multiplied by 2 for Bonferroni correction for 2 tests. †P-value multiplied by 3 for Bonferroni correction for 3 tests.

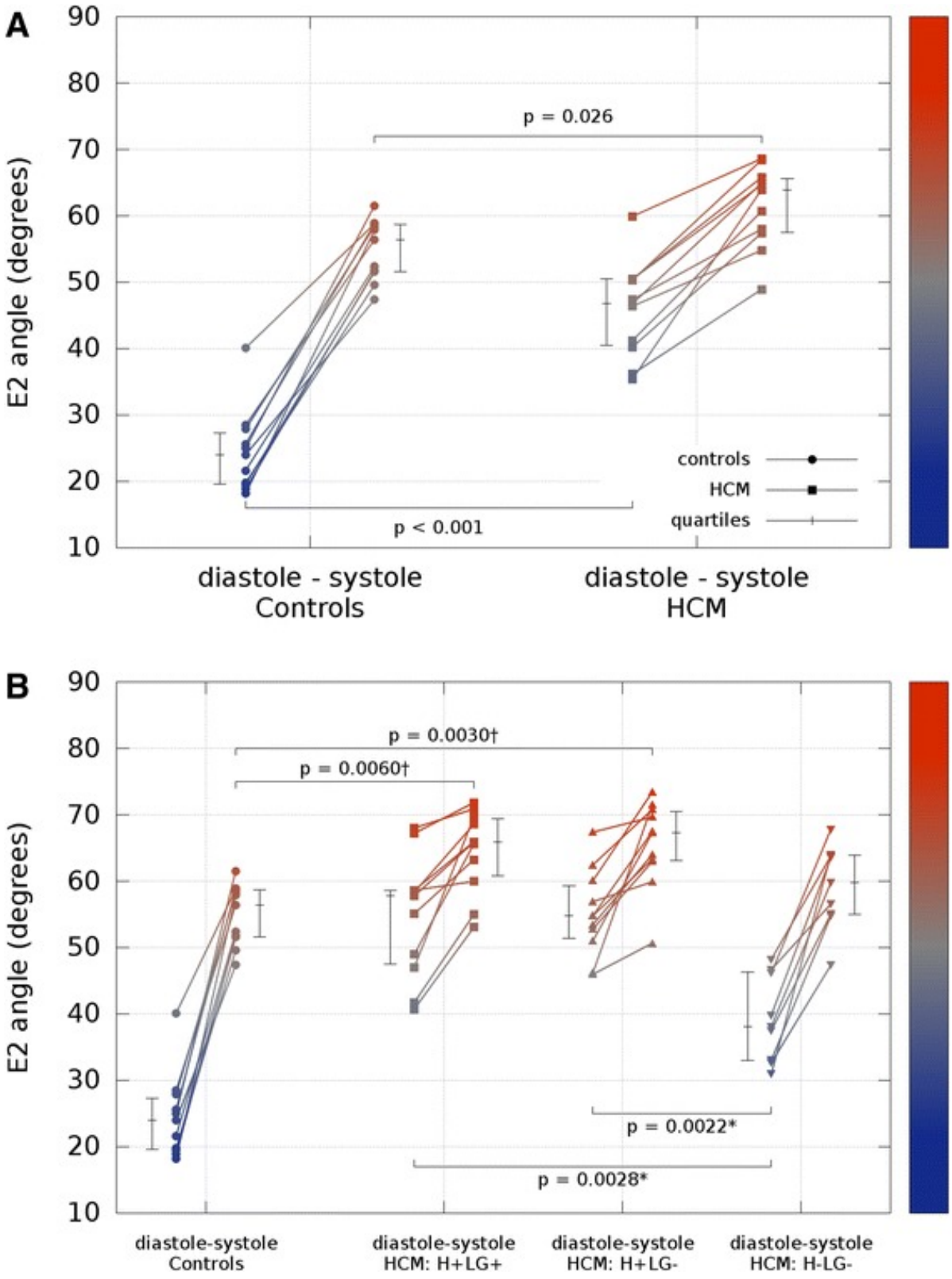

Figure 11.4: Scatter plots showing the absolute E2A in systole and diastole. A) Global mean E2A values. B) Global controls vs. the 3 HCM cohort categories: hypertrophy and LGE (H+LG+); hypertrophy but no LGE (H+LG-); and no hypertrophy or LGE (H-LG-). Black bars represent the median and interquartile range. Plots are colour coded according to the absolute E2A. *P-value multiplied by 2 for Bonferroni correction for 2 tests. †P-value multiplied by 3 for Bonferroni correction for 3 tests.

11.4: Discussion

To our knowledge this is the first study of in vivo HA and E2A data in HCM patients. As with our previous data, the observed HA pattern in both cohorts concurs with previous histological and cDTI studies (2, 147, 155, 371, 433). HA data, rather than HA gradient data (HAG) were presented for an in-depth analysis of phasic changes.

In both cohorts HA histograms demonstrate a reduced frequency circumferential myocytes in systole with a shift towards a greater proportion of longitudinal epicardial and endocardial myocytes; this is therefore in keeping with HA data from Chen et al. (12), but not Hales et al. (13), who found greater numbers of circumferential myocytes in systole. Tseng et al. described a greater proportion of left-handed oriented HA (negative) in the hypertrophied septum of HCM patients compared to controls (294). In comparison we observed a subtle relative shift towards both greater positive and negative HAs globally in diastole only.

The HCM E2A data in systole and diastole are markedly different to our observations in healthy volunteers. HCM sheetlets appear to have an inability to re-orientate to the diastolic confirmation, thereby presenting a new theory for diastolic dysfunction in HCM. Impaired sheetlet reorientation is in agreement with strain data from Tseng et al. who described reduced strain in the cross-myocyte, i.e. sheetlet plane, in HCM patients (294). Laminar diastolic dysfunction appears to be predominantly a feature of hypertrophied myocardium (H+), which could be interpreted as favouring the theory of loss of function from sarcomeric mutations and compensatory hypertrophy (219, 432). However, on the other hand, HCM sheetlets demonstrated a greater proportion of ±90° orientations in systole, compared to controls, which could be interpreted as hyper-contraction, thus favouring the theory of an increase in function due to sarcomeric mutations (222, 224). If one considers this data within the gain of function theory, potentially hyper-contractile mutant sarcomeres could result in hypertrophy via two separate

mechanisms: myocyte hypertrophy due to persistence of the contractile state and/or sheelets being 'stuck' in the systolic, radial orientation. Abnormal diastolic laminar orientation was independent of the presence of fibrosis (LG+). This is consistent with findings by Aletras et al., who found no association between the presence of fibrosis and regional contractile heterogeneity in HCM (234). Of note, only overt, regional fibrosis was assessed in this work, and it would be of interest to study the association between sheetlet reorientations and diffuse fibrosis, via ECV mapping.

11.5: Limitations

The issue of strain is particularly relevant to this works due to its focus on E2A data. E2 has previously been reported as the most strain sensitive eigenvector of the DW-STEAM sequence, as it lies in along the radial axis, where strain is greatest (150, 151, 366, 387). However, strain correction of these data was not attempted as contemporary strain correction methods over simplify myocardial strain. Current strain models assume the myocardium behaves like an isotropic jelly-like material and do not take account for the complexity of myocardial laminar architecture (394). The model generally used to predict the effects of strain implies that radial diffusivities are under estimated (366, 387), but the potential relation between the magnitude of radial diffusivities (E2) and the orientation of the secondary eigenvector (E2A) is poorly understood. When Stoeck et al. (150), conducted strain correction of DW-STEAM using this model, systolic reorientations of E2A were near abolished, thus contradicting previous reports of their role in radial myocardial thickening (9, 13). Moreover, if strain leads to an overestimation of systolic E2A, then regions with reduced strain would be expected to have reduced systolic E2 angulation. Strain is known to be reduced in hypertrophied segments of HCM myocardium (225, 430, 431), therefore based on current strain theories, there is no mechanism by which reduced strain could translate to greater systolic E2 angles.

E2A data suggested the presence of two perpendicular myocardial sheetlet populations, of opposite polarity. The absolute E2A was thus presented to quantify absolute angular change between phases. In light of the limited resolution, more than one intra-voxel sheetlet population may exist(7), such that intra-voxel E2A represents the average of these populations. The impact of SNR on E2 data has also been studied, and it is possible that poor SNR could skew data with a change in the mean intra-voxel E2A due to under-representation of one sheelet population over another. There is also the potential for lower SNR in the control data compared to the HCM data, as a greater number of voxels are available in HCM due to the thicker myocardium.

11.6: Conclusion

This work offers a novel explanation for left ventricular hypertrophy and abnormal diastolic mechanics in HCM. Although there is the potential for a confounding strain effect, the magnitude of observed E2A change between cardiac phases appears to be larger than the likely contribution from strain. Improving our understanding of the pathophysiology in HCM is a necessary step towards developing the first disease specific therapies.

CHAPTER 12: COMPARISON OF CARDIOVASCULAR PARAMETERS IN PATIENTS WITH HYPERTROPHIC CARDIOMYOPATHY, HYPERTENSION AND CONTROLS

12.1: Introduction

Contemporary clinic CMR techniques are limited assessment of macroscopic myocardial architecture. Cardiovascular diffusion tensor imaging offers novel characterisation methods which complement existing CMR capabilities. Of particular interest is its ability to determine the degree of myoarchitecutral organisation through FA, and assess myolaminar dynamics through the E2A.

HCM is a genetic disorder where the myocardial architecture is reported to demonstrate 'disarray' (15, 16); myocardial mechanics are also disordered with symptoms attributable to diastolic function and regional systolic dysfunction (14). Thus far there have been no non-invasive means of assessing disarray in vivo and the origins of mechanical abnormalities are not fully understood.

In Chapter 9 our initial assessment of FA in a small cohort of HCM patients appeared to be similar to values in healthy volunteers. In Chapter 11 markedly abnormal sheetlet reorientations were demonstrated in HCM, however the specificity of this finding is unknown. The ability to determine the presence of disarray and origin of mechanical abnormalities via cDTI could help to differentiate HCM from other aetiologies of hypertrophy and guide treatment strategies. In this chapter we compare cardiac phase specific results for FA, E2A and other cDTI parameters in a larger HCM cohort against age matched healthy volunteers and patients with hypertensive left

ventricular hypertrophy (LVH), to investigate the diagnostic utility of cDTI. These data are been published in: **Laura-Ann McGill**, Pedro Ferreira, Andrew Scott, Sonia Nielles-Vallespin, Philip Kilner, Ranil De Silva, David Firmin and Dudley Pennell, Non-invasive interrogation of myocardial disarray in hypertrophic cardiomyopathy, Heart; 2016;102: A96; and **McGill, L**, Ferreira, P, Scott, A. D., Nielles-Vallespin, S., Giannakidis, A., Kilner, P., Gatehouse, P., de Silva, R., Firmin, D and Pennell, D. J. Diffusion Tensor Imaging: Comparison of Hypertrophic Cardiomyopathy, Hypertension and Healthy Cohorts Diffusion Tensor Imaging: Comparison of Hypertrophic Cardiomyopathy, Hypertension and Healthy Cohorts, European Heart Journal Cardiovascular Imaging, 2016; 17 (Suppl 1):1615 (434, 435).

12.2: Methods

12.2.1: Study Population

Twenty-seven patients with HCM were recruited for this study from specialist cardiomyopathy clinics at the Royal Brompton Hospital. HCM was confirmed in line with current European Guidance, as previously described in Chapter 9 (14). Clinical information including risk factors for sudden death and genetic results were collected for each patient. Patients were excluded if they had a history of concomitant hypertension, were receiving anti-hypertensive medications, or had confirmed ischaemic heart disease. During recruitment around a third of screened patients had to discounted due to concomitant hypertension.

Seventeen patients with hypertension (HTN) were recruited to serve as a comparative population with LVH in the absence of morphological features/ a family history of HCM. Patients were recruited form the Anglo-Scandinavian Cardiac Outcomes Trial (ASCOT) database in collaboration with Professor Tom at Imperial College. Entry criteria to ASCOT included:

- Screening and baseline blood pressure ≥ 160/100 mm Hg untreated or ≥ 140/90 mm Hg treated with ≥ 1 drugs

- Age 40-79 years
- No previous myocardial infarction or current evidence of coronary artery disease
- ≥ 3 risk factors for a future cardiovascular event (eg, male, age ≥ 55 years, smoking, type 2 diabetes)

The patient database was screened for patients with recent echo confirmation of LVH (maximal wall thickness ≥13mm). Patients were further screened via their patient records and a questionnaire to exclude ischaemic heart disease since recruitment to ASCOT.

Data from 14 age matched healthy volunteers from Chapter 10 were included in this comparison. Patients from all cohorts were excluded if they had contraindications to CMR or sustained atrial arrhythmias which are incompatible with DW-STEAM cDTI.

12.2.2: Ethical Approval

Ethical approval for recruitment of subject from all cohorts was granted by the NRES Committee South East Coast Surrey (REC reference 10/H0701/112). All volunteers were given an information sheet, prior to giving consent, outlining the study objectives and logistics. All volunteers were made aware they were free to withdraw their consent to participation at any point in the process.

12.2.3: Image Acquisition

cDTI data were acquired with DW-STEAM at 3T during the patient specific systolic diastolic pauses, identified from a mid-ventricular short axis bSSFP cine acquisition. Three mid ventricular short axis slices were imaged, typically for 10 image repetitions (range 8-14), before signal averaging. The diffusion weighting was set to b_{main}=350s/mm^2, with b_{ref} was 135s/mm^2 as previously described (426). The slice position was tracked between phases with a spatial modulation of magnetisation (SPAMM) tagging prepulse, in the 2 and 4 chamber views. Functional and volumetric data were determined from retrospective bSSFP cine acquisitions in 3

long axis planes and a stack of short axis slices from the ventricular base to the apex. In HCM patients, additional LGE images were acquired for HCM and HTN patients with a PSIR sequence (defined in chapter 8), in the same image planes as the bSSFP cine images, with additional phase swap imaging where enhancement was ambiguous. The typical duration of the scan was 75-90mins with LGE acquisitions. Full details of all sequence parameters are discussed in Chapter 8.

12.2.4: Diffusion Tensor Analysis

Following initial post processing steps the eigensystem (eigenvalues and eigenvectors) were calculated from the diffusion tensor for each voxel. From this the following cDTI parameters were determined: FA, MD, HA, HAG, and E2A. For HA data left-handed helix angles were assigned a negative value and right-handed helix angles assigned a positive valve, with the range -90 to 90 degrees (64, 423). HAG was calculated from a best fit pas degrees/mm. For E2A, the absolute value of the angle is presented with a range of 0-90°, being 90° if rotated to a circumferential orientation. E2 mobility was defined as the change of mean absolute E2A values from diastole to systole, to provide a measure of phasic change in angulation.

For visualisation FA, MD and absolute E2A are represented in maps for example subjects with the full tensor is represented in superquadric glyphs (358) as previously described. The post-processing and analysis time was approximately 3 hours per study.

12.2.5: Functional, Volumetric and Late Gadolinium Enhancement Image Analysis

LV volumes, function, mass, and EF for all patients were measured using CMRtools software (Cardiovascular Imaging Solutions, London) as previously described. The extent of myocardial LGE was quantified with a full-width half-maximum threshold and expressed as percent of LV mass. LGE was further qualitatively assessed as present or absent in 12 short axis segments, with 'present' being equal to ≥50% in the segment, with the first marked by the superior RV insertion

point. RV insertion point fibrosis was only included if extensive in keeping with Chan et al.'s finding that RV insertion LGE is benign (187).

12.2.6: Quantitative and Statistical Analysis

Intra-cohort comparisons of septal and lateral FA were performed in line with Tseng et al. (367), to assess for significant regional differences in myocardial organization, given the predominantly septal distribution of hypertrophy in the HCM cohort. Testing was performed using a paired t-test with Bonferroni correction for multiple testing.

Global diastolic and systolic FA, MD, HAG and E2A values and E2A mobility were compared between cohorts using ANOVA, with pairwise Bonferroni corrected t-tests where appropriate. Pearson correlation was performed to examine the relation between LGE burden and MD, and between wall thickness and MD, HAG, E2A and E2A mobility. A threshold of $p<0.05$ was used in all comparisons.

12.3: Results

12.3.1: Subject Characteristics

Of the 27 patients with HCM, data was excluded due to arrhythmia in one and due to poor breath holding in another. Of the 17 hypertension patients, four were excluded due to poor quality data (3 female, 1 male) with artefacts predominately affecting the diastolic data. The baseline demographics and clinical characteristics of the 3 cohorts are displayed in table 12.1. The HTN cohort were older on average with a greater percentage of male subjects, compared to the other cohorts, however these differences did not reach statistical significance. The BSA was largest in the HTN and smallest in the controls ($p=0.01$). The LV volumes in the HCM cohort were significantly smaller than the other two cohorts ($p<0.01$) with an associated elevated EF ($p<0.01$). LV mass and LV wall thickness was largest in the HCM group and least in the control cohort

(p<0.01). The extent of LGE fibrosis and number of LGE affected segments was greater in the HCM cohort compared to the HTN cohort (p<0.01).

Baseline Characteristics	**HCM Patients (N = 25)**	**HTN Patients (N = 13)**	**Control (N = 14)**	**P value**
Age: (years &range)	60 ± 11	67 ± 11	58 ± 8	0.05
Male subjects	17(68%)	12 (92%)	7 (50%)	0.06
Body Surface Area: (m2)	1.94 ± 0.2	2.05 ± 0.2	1.80 ± 0.2	0.01
RR interval (ms)	989 ± 155	956 ± 173	964 ± 173	0.35
Blood Pressure				
Systolic	119 ± 13	143 ± 11	131 ± 12	<0.01
Diastolic	78 ± 9	81 ± 12	77 ± 9	0.47
CMR Characteristics				
LV End Diastolic Vol: (mL)	63 ± 15	79 ± 15	75 ± 14	<0.01
LV End Systolic Vol: (mL)	13 ± 5	25 ± 11	23 ± 6	<0.01
LV Ejection Fraction: (%)	80 ± 5	67 ± 11	69 ± 5	<0.01
LV Mass: (g)	109 ± 41	85 ± 15	66 ± 13	<0.01
Max Wall Thickness (mm)	22 ± 5	15 ± 1	9 ± 1	<0.01
Late Gadolinium Enhancement				
Percentage of LV mass (%)	9.86 ± 5.4	4.86 ± 3.3	N/A	<0.01
Number of Segments (Median (range))	0 (0-4)	2 (0-6)	N/A	<0.01

Table 12.1: Baseline demographics and CMR characteristics of the 3 cohort. Values are presented as mean±SD except where noted.

The clinical characteristics of the HCM cohort are outlined in table 12.2. Fourteen of the 25 HCM patients had undergone genetic testing, of these 6 had confirmed mutations (4 Myosin heavy chain, 1 Troponin T, 1 Myosin binding protein C). The median number of risk factors for sudden death was 1 with a range of 4 and 2 patients subsequent had prophylactic ICDs inserted. Asymmetrical septal hypertrophy was the most common LVH morphology (80%).

HCM Cohort Characteristics	N = 25
LVH morphology	
Asymmetrical septal hypertrophy: n, (%)	20 (80%)
Anterior hypertrophy: n, (%)	2 (8%)
Mid ventricular hypertrophy: n, (%)	1 (4%)
Apical	2 (8%)
LV outflow tract obstruction at rest: n, (%)	10 (37%)
Number of risk factors for sudden death: median (range)	1 (0-4)
Pathological mutation identified	6 (24%)

Table 12.2: HCM cohort characteristics

12.3.2: Regional Intra-Cohort Comparisons

Intra cohort comparison of systolic and diastolic cDTI parameters between septal and lateral segments are given in table 12.3. Systolic FA was more anisotropic in the septum compared to the lateral wall in the HTN cohort (p=0.024 after Bonferroni correction). There were no other intra cohort differences between septal and lateral FA.

Regional FA	Septal	Lateral	P value
HCM Systole	0.44±0.05	0.43±0.05	0.34
HCM Diastole	0.50±0.07	0.49±0.08	0.97
HTN Systole	0.50±0.07	0.45±0.07	0.024*
HTN Diastole	0.50±0.07	0.50±0.07	0.87
Control Systole	0.45±0.07	0.45±0.06	0.77
Control Diastole	0.52±0.07	0.50±0.08	0.11

Table 12.3: Septal-lateral intra-cohort comparison of FA, mean±SD.*p value multiplied by 6 for Bonferroni correction

12.3.3: Inter-cohort Comparison of cDTI Parameters

12.3.3.1: Fractional Anisotropy

FA maps from example subjects from each cohort are presented in figure 12.1. Global systolic FA was no different between cohorts. Diastolic FA was less anisotropic in HCM compared to controls (0.51±0.05 v 0.55±0.04, p=0.009), but not statistically different to HTN (0.51±0.05 vs. 0.53±0.04, p=0.51) table 12.4, figure 12.2.

Cohort	Fractional Anisotropy	p value
Systolic:		ANOVA: F = 1.67, *p* = 0.20
HCM	0.44 ± 0.05	
HTN	0.47 ± 0.06	
Control	0.46 ± 0.05	
Diastolic:		ANOVA: F = 5.0, *p*=0.011
HCM	0.51 ± 0.05	Reference
HTN	0.53 ± 0.05	*p* =0.51
Control	0.55 ± 0.04	*p* = 0.009

Table 12.4: Inter-cohort comparison of fractional anisotropy, mean±SD.

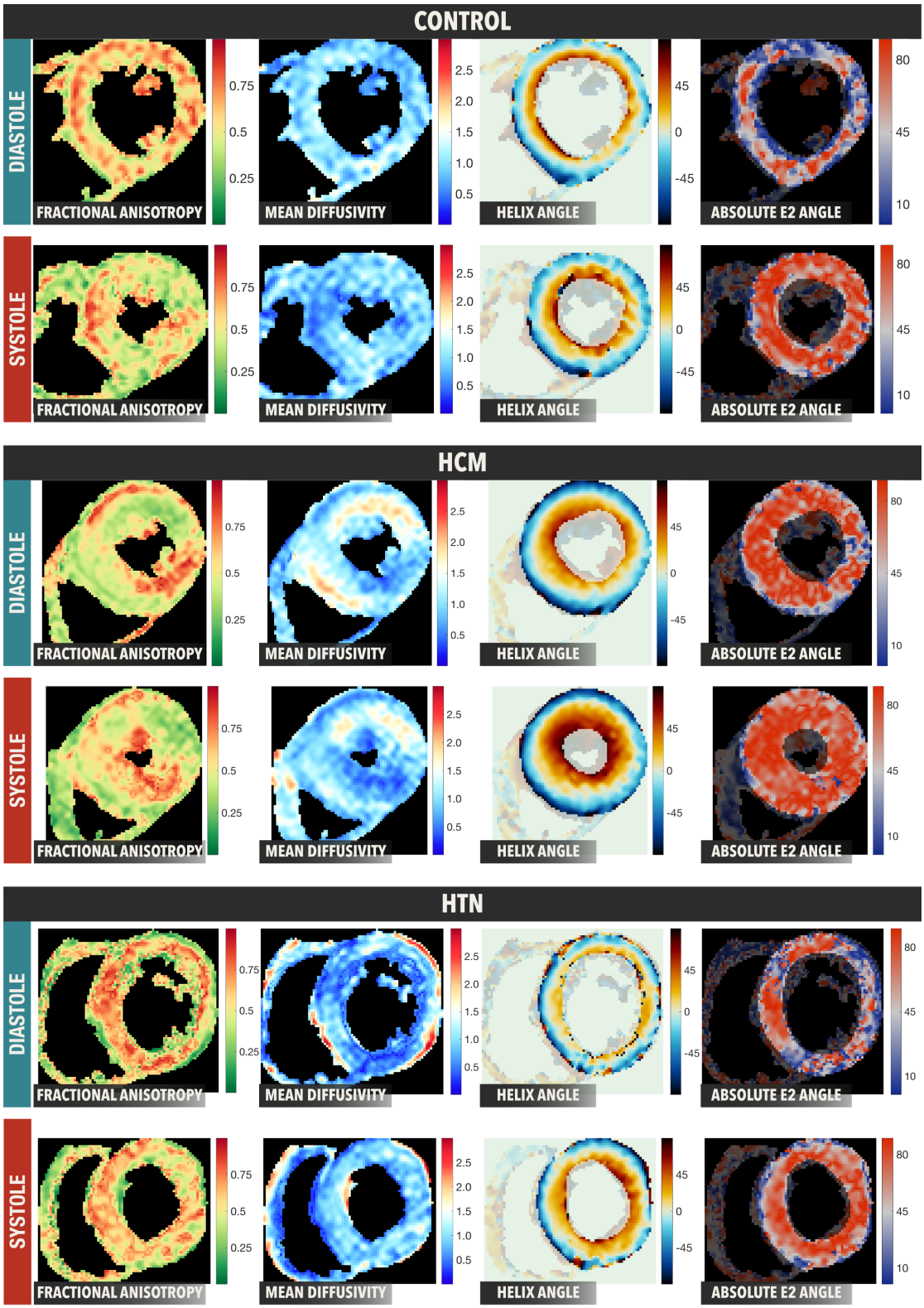

Figure 12.1: Parameter maps for FA, MD, HA and E2A from an example subject in each cohort. The control subject is at the top, HCM patient in the middle and hypertensive patients at the bottom. In the first column FA in systole (red) is visibly similar in each cohort. In diastole (green) FA is comparatively reduced in HCM, however this did not reach significance. In the second row, MD maps demonstrate regional increased diffusivity in HCM, however this only reached significance, in comparison to controls, in systole. In the third column, HA maps appear consistent across cohorts and phases. In the fourth column, absolute E2A has a more systolic orientation (red) in diastole, compared to the other cohorts.

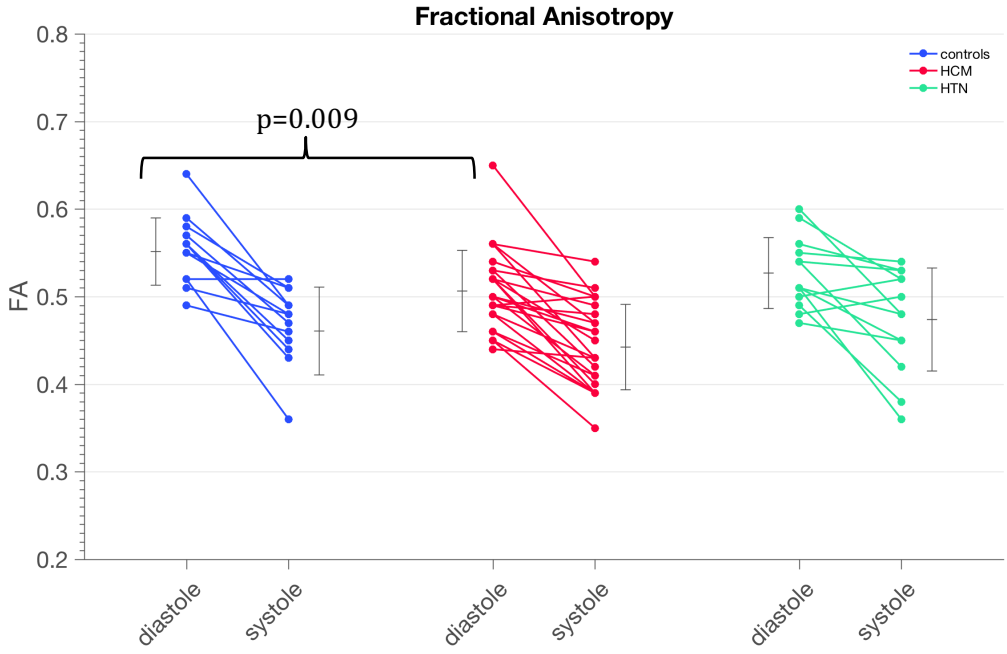

Figure 12.2: Scatter plots of fractional anisotropy in systole and diastole. Controls in blue, HCM in red, HTN in green. The bars represent the mean & 1SD. The lines join systolic and diastolic data for each subject.

12.3.3.2: Mean Diffusivity

MD maps from an example subject in each cohort are presented in figure 12.1 Global systolic diffusivity was greater in HCM compared to controls (HCM 1.07±0.13 v Control 0.91±0.13x10^{-3}mm^2/s, p=0.002) but there was no difference between HCM & HTN, table 12.5, figure 12.3. There was no difference in diastolic MD between cohorts. There was also no association between systolic MD and LGE in grams (R^2 0.04, p=0.28) or MD and LV wall thickness (R^2 0.06, p=0.09).

Cohort	Mean Diffusivity	p value
Systolic:		ANOVA: F = 7.24, *p* = 0.002
HCM	1.07 ± 0.13	Reference
HTN	0.97 ± 0.14	p=0.1
Control	0.91 ± 0.13	p=0.002
Diastolic:		ANOVA: F = 1.51, *p*=0.23
HCM	1.13 ± 0.15	
HTN	1.06 ± 0.13	
Control	1.07 ± 0.12	

Table 12.5: Inter-cohort comparison of mean diffusivity (x10^{3}mm^{2}s^{-1}), mean±SD

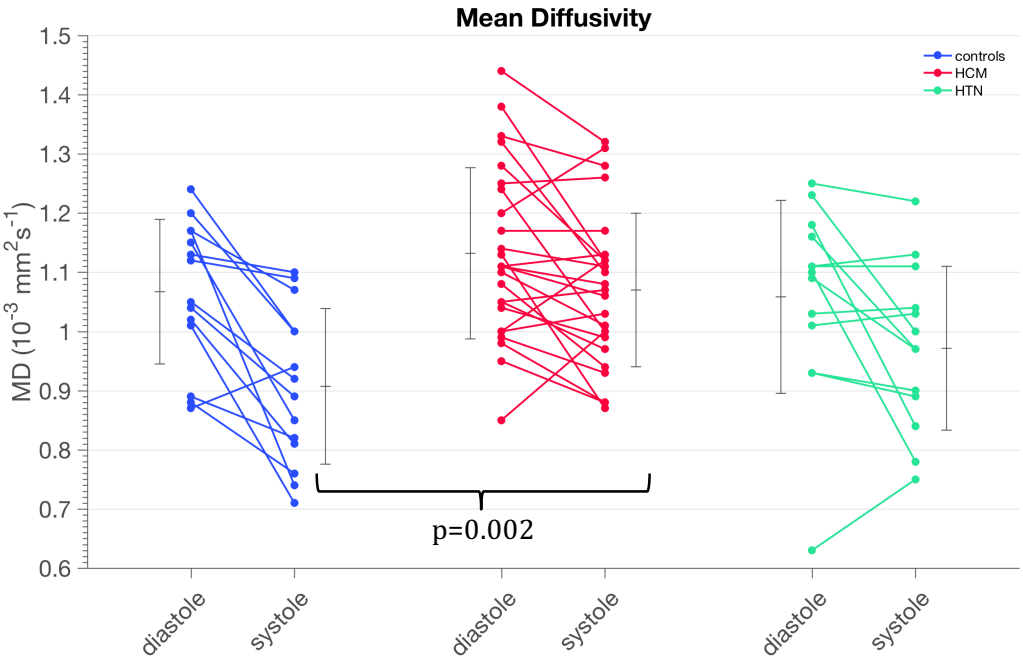

Figure 12.3: Scatter plots of mean diffusivity in systole and diastole. Controls in blue, HCM in red, HTN in green. The bars represent the mean & 1SD. The lines join systolic and diastolic data for each subject.

12.3.3.3: Helix Angle and Helix Angle Gradient

Diffusion tensor data is shown as superquadric glyphs coloured according to HA for an example subject from each cohort in figure 12.4. The HA per transmural layer in systole and diastole is illustrated in a scatter plots in figures 12.5. There is a subtle right-ward shift in helix angles (more positive), most pronounced in systole, from controls to HTN, and to HCM, $p<0.001$.

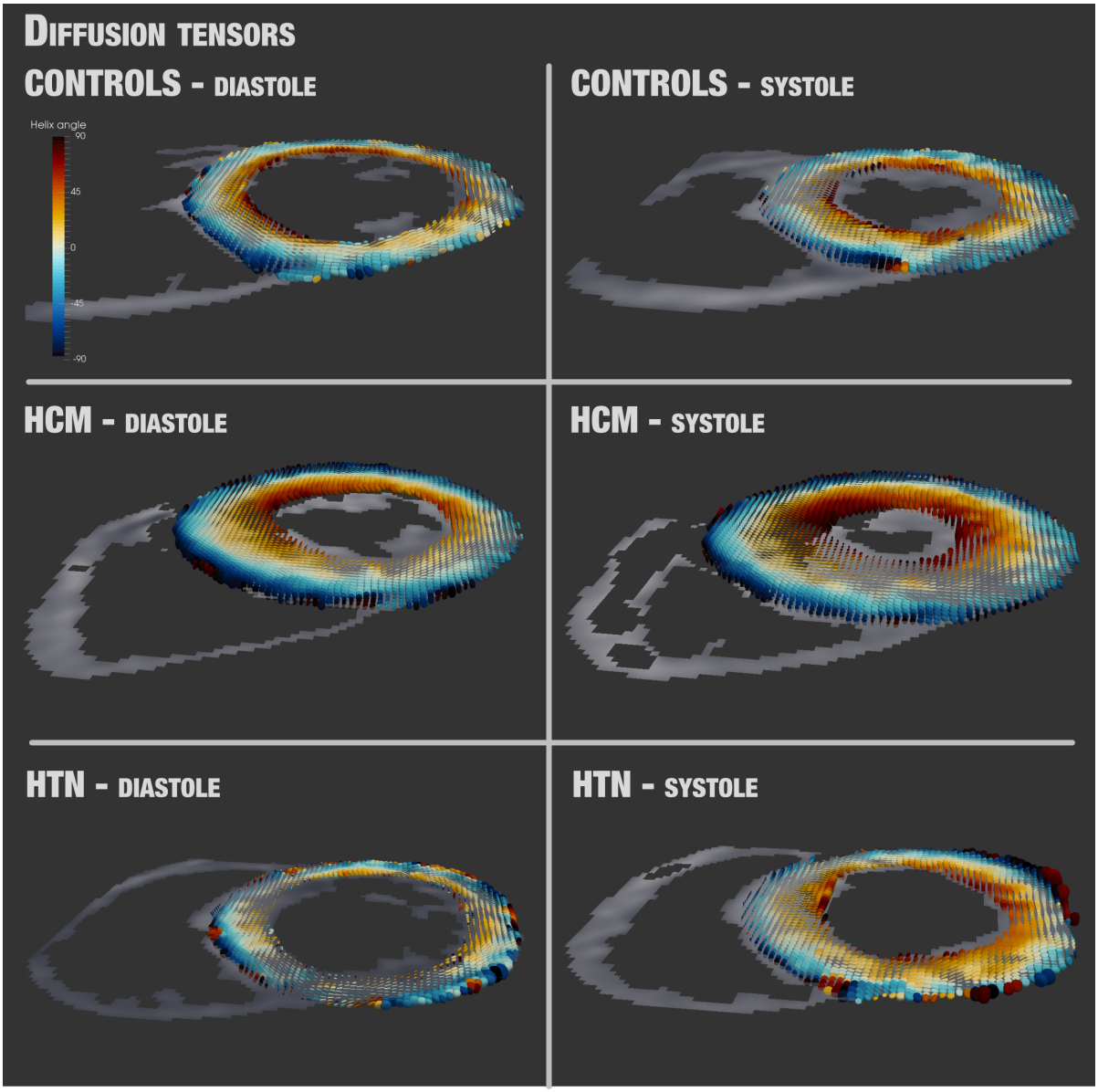

Figure 12.4: Superquadric glyphs representing the whole tensor, per pixel, in an example patient in both cardiac phases. Glyphs are colour coded according to the helix angle with blue representing left-handed epicardial myocytes, orange circumferential myocytes and red, right-handed endocardial myocytes. The same helical pattern is observed in both cohorts in both phases. In the HCM cohort a predominance of red, right-handed myocytes is observed, particularly in systole.

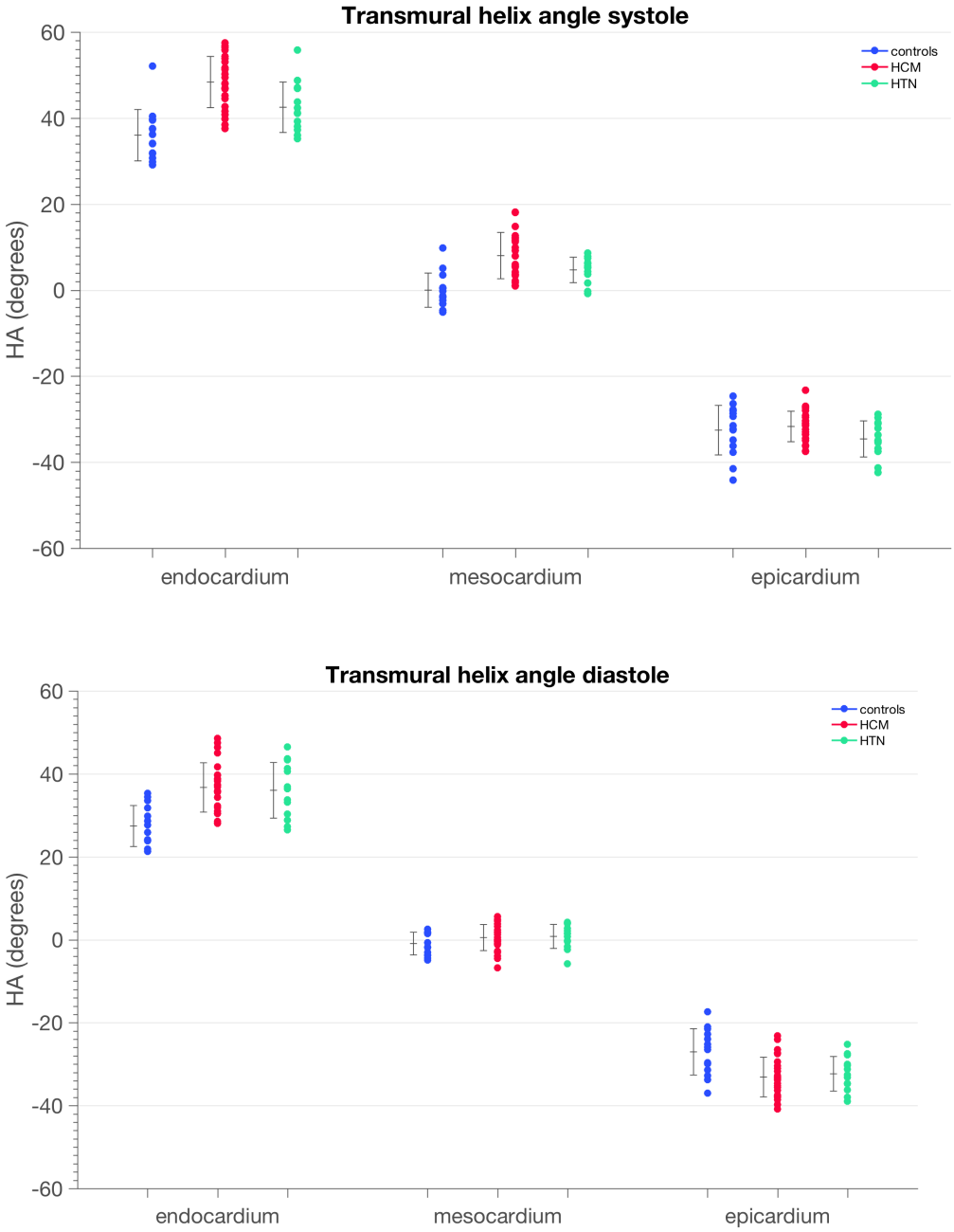

Figure 12.5: Comparative transmural helix angles for all three cohorts. Systolic data in the top graph, diastolic data in the bottom graph. Controls in blue, HCM in red, HTN in green. Bars represent the mean & 1SD. A subtle right-ward shift (most pronounced in systole) in HA is observed in HTN (green) compared to control (blue) and in HCM (red) compared to (HTN).

Both global systolic and diastolic HAG were significantly different between cohorts with a reduced rate of change in transmural HA in the HCM cohort compared to both the HTN and control cohorts, table 12.6.

Cohort	Helix Angle Gradient	p value
Systolic:		ANOVA: F = 30.0, $p < 0.001$
HCM	6.4 ± 1.0	Reference
HTN	7.4 ± 0.9	p<0.001
Control	8.6 ± 0.8	p<0.001
Diastolic:		ANOVA: F = 27.0 , p<0.001
HCM	6.5 ± 1.0	Reference
HTN	7.9 ± 0.9	p<0.001
Control	8.9 ± 1.1	p<0.001

Table 12.6: Inter-cohort comparison of helix angle gradient (°/mm), mean±SD

Combining all three cohorts there was strong correlation between both systolic and diastolic HAG and maximum LV wall thickness (Systole R^2: 0.70, p<0.001; Diastole R^2 0.61, p<0.001) (figure 12.6).

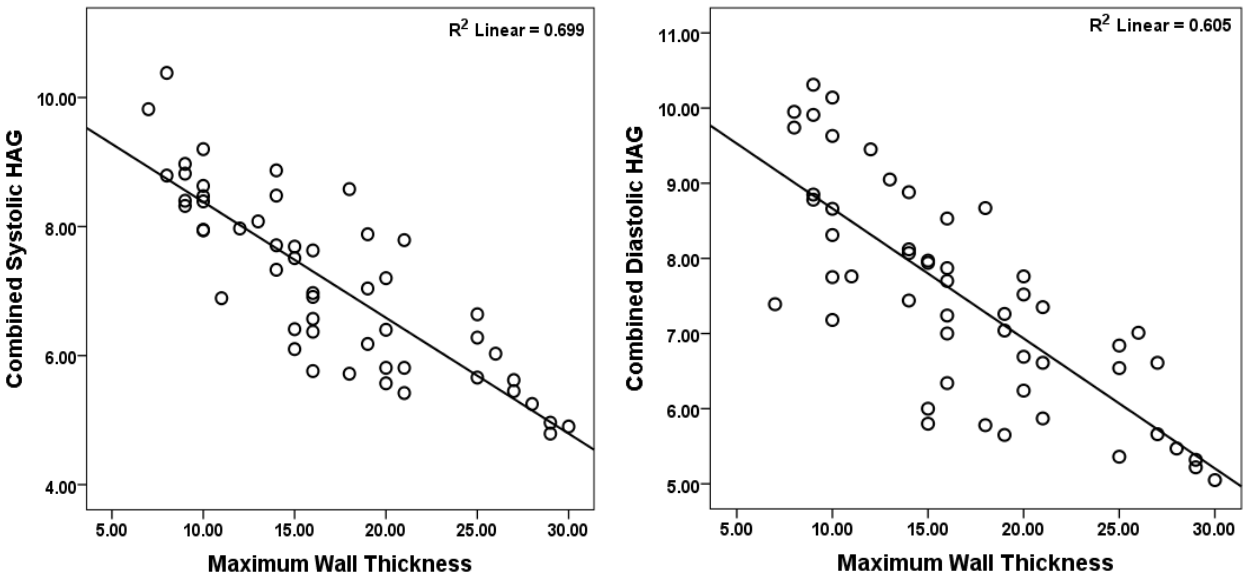

Figure 12.6: Scatter plots with regression line for systolic and diastolic HAG (°/mm) in all subjects against maximum LV wall thickness (mm). HAG demonstrates a strong inverse relationship with wall thickness in both phases.

12.3.3.4: Secondary Eigenvector Angle

Maps of absolute E2A in systole and diastole from example subjects are presented in figure 12.1 Global systolic E2A was significantly greater in HCM subjects compared to the controls. E2A orientation was more radially orientated in diastole in the HCM cohort compared to control and hypertension cohorts, table 12.7, figure 12.7.

Cohort	Secondary Eigenvector Angle	p value
Systolic:		ANOVA: F = 19.0, $p < 0.001$
HCM	62 ± 5	Reference
HTN	56 ± 6	p<0.001
Control	53 ± 4	p=0.29
Diastolic:		ANOVA: F = 52.8.0 , $p<0.001$
HCM	47 ± 7	Reference
HTN	35 ± 6	p<0.001
Control	26 ± 5	p<0.001
Mobility:		ANVOA: F = 11.6, $p<0.001$
HCM	15±6	Reference
HTN	21±9	p=0.084
Control	27±9	p<0.001

Table 12.7: Inter-cohort comparison of the secondary eigenvector angle (°), mean±SD

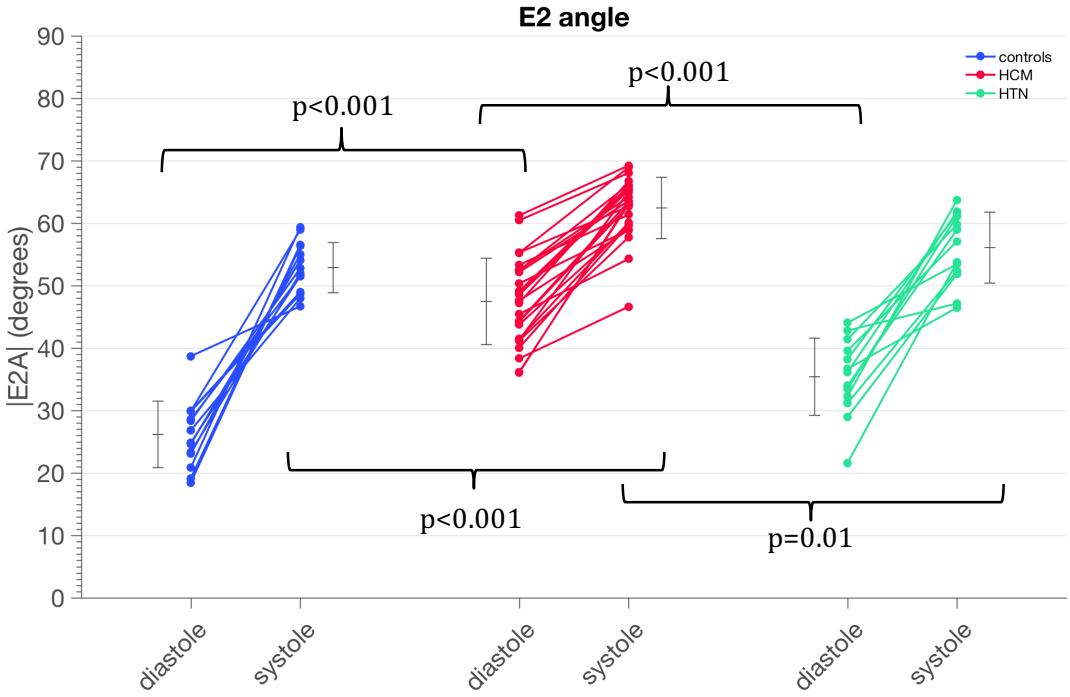

Figure 12.7: Scatter plots of the secondary eigenvector angle in systole and diastole. Controls in blue, HCM in red, HTN in green. The bars represent the mean & 1SD. The lines join systolic and diastolic data for each subject. Diastolic E2A is increased in HCM compared to compared to controls.

Combining all three cohorts there were significant correlations between both systolic and diastolic global E2A and maximum wall thickness (Systole $R^2 = 0.42$, $p<0.001$; Diastole $R^2 = 0.72$, $p<0.001$) figure 12.8.

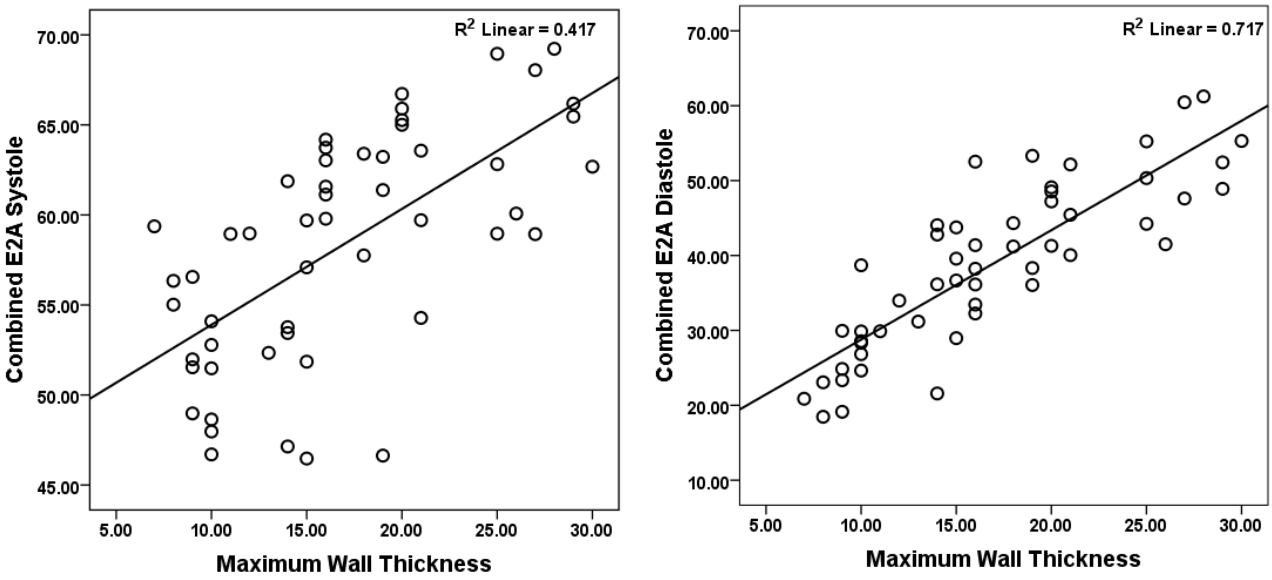

Figure 12.8: Scatter plots with regression line for systolic (left) and diastolic (right) E2A (°) in all subjects against maximum LV wall thickness (mm). In both cases there is a significant association between E2A and wall thickness, which is greatest in diastole.

E2A mobility was least in the HCM cohort (table 12.6) and the difference was significant when compared to controls ($p<0.001$), but did not reach statistical significance compared to HTN (15±6 v 21±9, $p=0.084$) (figure 12.9). Taking all three cohorts there was an inverse linear relation between E2A and wall thickness $R^2 = 0.36$, $p<0.001$, figure 12.10.

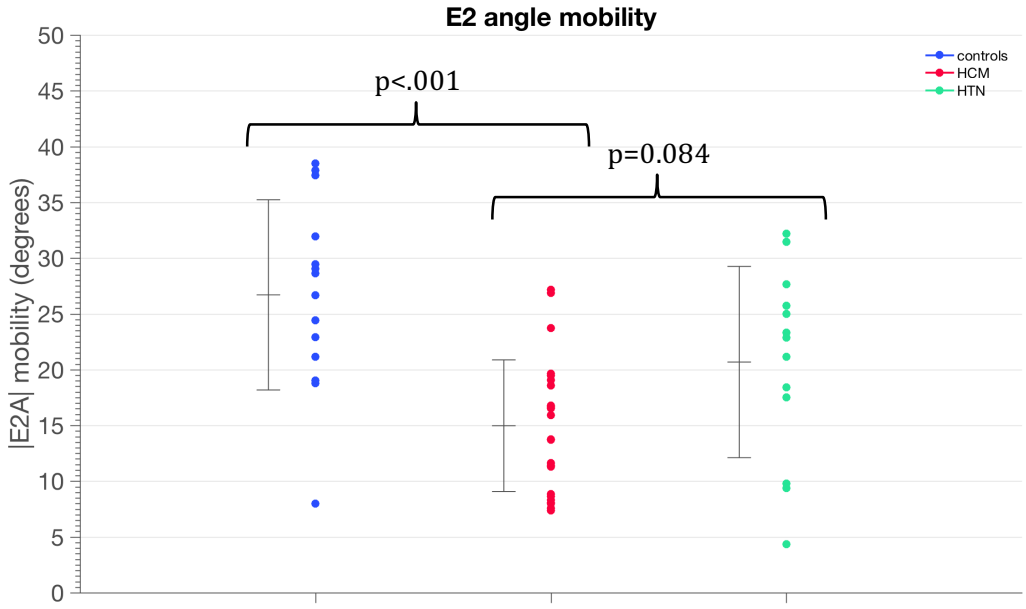

Figure 12.9: Scatter plots of secondary eigenvector angle mobility. Controls in blue, HCM in red, HTN in green. The bars represent the mean & 1SD. Mobility was significantly reduced in HCM compared to controls. Mobility was also reduced in HTN compared to controls but this did not reach significance.

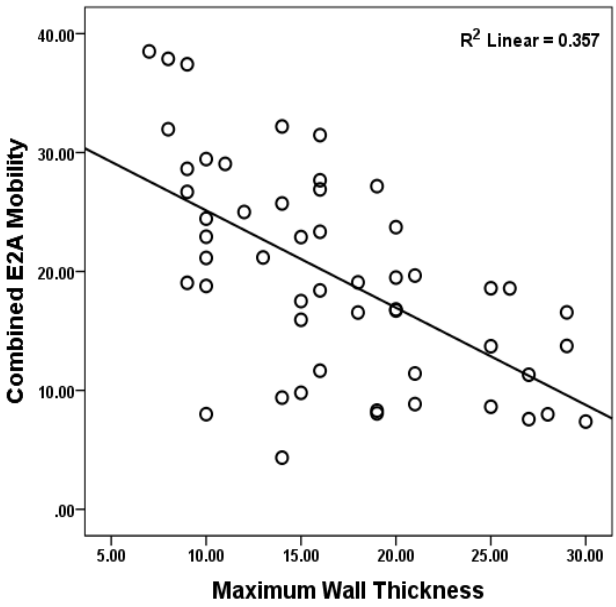

Figure 12.10: Scatter plot with regression line for E2A mobility in all subjects against maximum LV wall thickness. A significant, inverse relation between wall thickness and E2A mobility is observed.

12.4: Discussion

12.4.1: Study Cohort

To our knowledge this is the first study to compare cDTI parameters in HCM patients against both a healthy cohort and patients with hypertensive LVH. The latter cohort was included to provide a group of patients with LVH without the features of HCM (i.e. atypical pattern of LVH, family history of HCM or LGE pattern suggestive of HCM). During recruitment, it is of note that approximately a third of screened HCM patients were excluded due to concomitant hypertension. Overlap between hypertension and HCM is recognised (14), however this figure is relatively high and may be a reflection of the average age of patients in this cohort (60±11years). This also raises the possibility of a possible bimodal population in HCM, with a subgroup who acquire LVH as a result of an abnormal response to hypertension.

A relatively high number of patients in the hypertension cohort were excluded from the final analysis (4 patients) due to a combination of breath holding and arrhythmia difficulties. Possible reasons for reduced cooperation include the fact that the HTN patients were older and had a greater BSA than the HCM cohort. Patients were older as the ASCOT hypertension database has been running since 1998 with recruitment entry age of 40-79yrs and the greater body surface reflects the fact that hypertension is linked to obesity (436). Finding age matched healthy volunteers to this cohort was difficult as co-morbidities increase with advancing age, consequently the healthy cohort were younger. However our previous work has demonstrated that there is only a minor association between E2A mobility and age.

12.4.2: Regional Intra-Cohort Comparisons

There was no difference between septal and lateral FA in HCM. This contradicts Tseng et al. (294) who described reduced FA in the septum compared to the lateral wall in HCM patients. As previously, discussed the inclusion of septal RV myocytes in Tseng et al. appears to be one of the reasons for the discrepancy between our results. Reported FA values in Tseng et al. were also much higher than this work (ranging from 0.56-0.75 in HCM and 0.72-0.78 in healthy volunteers), and were largely in keeping with Dou et al. (368) and Reese et al. (366), whereas our results agreed with monopolar STEAM derived values in Nielles-Vallepsin et al.(426), Tunicliffe et al. (372) and Stoeck et al. (before strain correction) (150). Technical differences between the sequences is the most likely explanation for such discrepancies, notably the acquired resolution in Tseng et al. was greater at $3x3x3mm^2$ and may have resulted in the detection of greater anisotropy either through an improved ability to resolve FA, or artefactually through reduced SNR (406).

12.4.3: Inter-Cohort Comparison of cDTI Parameters

12.4.3.1: Fractional Anisotropy

There was no difference between cohorts in systolic FA. However there was a gradient in diastolic FA, being least anisotropic in HCM and most anisotropic in healthy cohorts, but with no significant difference between HTN and HCM cohorts. This cDTI protocol was therefore unable to detect comparatively greater myocardial disarray in the HCM patients compared to the HTN cohort. Possibilities for this result include the relatively poor resolution of this technique (acquired $2.8x2.8x8mm^3$), which may be insufficient to detect myocardial disarray occurring at more microscopic scales. An alternative possibility is that the original disarray studies suffered from selection bias, having focused on younger patients with a history of sudden cardiac death (15, 194); disarray may therefore be less prevalent in patients surviving into later decades. The final possibility is that this data represents proof that myocardial disarray is not a true entity, but rather occurs as a consequence of tissue preparation artefact (193). Obtaining a conclusive answer will require significant technical advances in cDTI and modelling studies to determine the relation between FA and underlying microstructure.

12.4.3.2: Mean Diffusivity

Systolic, but not diastolic, MD was greater in HCM compared to controls but similar to the hypertension cohort. Nguyen et al. previously demonstrated significantly greater diffusivity, in regions of LGE in HCM patients, with a diffusion-weighted imaging sequence (293). LGE represents areas of replacement fibrosis, potentially with reduced barriers to diffusion, thus the greater prevalence of LGE in HCM would be expected to translate to detectable differences in diffusivity between cohorts. The lack of clear differentiation may be related to the relative inferior reproducibility of this parameter in HCM (Chapter 9). SNR may also be important as the thicker myocardium in HCM may translate to a comparatively greater SNR in this cohort, artefactually increasing MD.

12.4.3.3: Helix Angle and Helix Angle Gradient

Patients with HCM or HTN demonstrated a subtle rightward shift in helix angle in comparison to controls. Once again this contradicts Tseng et al., who described a greater number of left-handed myocytes in HCM (294). The transmural rate of change in HA (HAG) was significantly reduced in HCM compared to the other cohorts and occurred in proportionally in relation to LV wall thickness. Together these results concur with the observation in healthy volunteers (Chapter 10), that the HA range is largely constant and the rate of change in angulation is dictated by LV size and thickness.

12.4.3.4: Secondary Eigenvector Angle and Mobility

Diastolic sheetlet orientation (E2A) was significantly greater in HCM compared to both control and HTN, however mobility was only discernibly different between HCM and controls. Diastolic E2A was strongly correlated with LV wall thickness. A weaker correlation was demonstrated between wall thickness and systolic E2A and E2A mobility. The implication therefore is that abnormal laminar mechanics are not specific to HCM. Reduced sheetlet mobility may represent a final common pathway from a number of myocyte pathophysiological processes, with resulting compensatory hypertrophy. Alternatively myocyte hypertrophy may proportionally impede sheetlet reorientation. Examining sheetlet reorientation in other aetiologies of LVH, such as amyloid, and in contrasting pathologies, such as dilated cardiomyopathies, may provide further insight.

12.5: Limitations

In addition to the potential limitations discussed, these data are derived from small cohorts and therefore may not be truly representative of their respective populations. HCM is a very heterogeneous condition with distinct patterns of LVH. The population in this work predominantly had asymmetrical septal hypertrophy, however the cDTI characteristics other

morphologies may differ. The relation between subject age or BSA and cDTI artefacts has not been examined and cannot be presumed to be consistent across populations. As discussed in Chapter 11, E2A measures the average intra-voxel sheetlet angle and cannot distinguish between co-existing intra-voxel populations.

12.6: Conclusion

DW-STEAM cDTI could not detect myocardial disarray in HCM via fractional anisotropy, however this should be revisited following sequence developments. The HA demonstrated a rightwards shift with increasing hypertrophy across all cohorts. Abnormal sheetlet mobility was observed in the presence of LVH, in proportion to the extent of hypertrophy, offering a novel insight into microstructural abnormalities in the context of LVH.

CHAPTER 13: NEW INSIGHTS INTO TRANSMURAL MYOCARDIAL HETEROGENEITY REVEALED BY DIFFUSION WEIGHTING OPTIMISATION

13.1: Introduction

Despite recent advances, in vivo cDTI is still in a developmental stage. Thus far this work has presented clinical data acquired with the monopolar diffusion weighted STEAM sequence with an effective diffusion weighting of b=215s/mm^2 (b_{main}=350s/mm^2, b_{ref}=135s/mm^2). At the outset of the research the optimal diffusion weighting for cDTI acquisitions was unknown, and the initial protocol was based on earlier work. Greater diffusion weighting leads to improved diffusion sensitivity at the expense of an increased influence of the effects of noise in the diffusion weighted images, therefore optimal diffusion weighting achieves a balance between the two. The effective diffusion weighting of a sequence is derived from the main diffusion weighting (b_{main}) minus the reference (b_{ref}). From the literature cardiac diffusion weighted studies had adopted b_{main} b=300-500s/mm^2(150, 294, 342, 368-370, 388, 389), with Nguyen et al. also utilising b=350s/mm^2 in HCM patients (342), and Stoeck et al. opting for greater diffusion sensitivity in their phase comparison work (b=500s/mm^2) (371). Few studies have published the diffusion weighting of the reference images, however our recent work demonstrated the importance of accounting for the diffusion weighting carried by reference spoiler gradients (Chapter 10) (426); the final diffusion weighting from acquisitions with b_{main}=350s/mm^2 and b_{ref}=135s/mm^2 was thus b=215s/mm^2.

Intravoxel diffusion signals are derived from any non-linear motions, described by Le Bihan as intravoxel incoherent motions (IVIM)(329). In vivo, in addition to intracellular water diffusion, diffusion-like signals, or pseudo diffusion, are also derived from capillary blood flow (329). IVIM

have been extensively studied in the brain, and Le Bihan's work separating the two components formed the basis for the development of diffusion-perfusion mismatch quantification in acute stroke imaging (437). However such studies are limited in the heart (438), and the impact of capillary diffusion components on in vivo cDTI parameters was unknown. Sequence optimisation work within our department was target to address both of these issues, with results published in Scott et al. (439).

The effect of increasing b value on MD, FA and HA is demonstrated in the parameters maps below (figure 13.1). With each increment in b_{main} (b_{ref}=15s/mm^2) from b_{main}=50s/mm^2 to b_{main}=350s/mm^2 all three parameter maps demonstrate progressively smoother data. From b_{main}=550s/mm^2 to b_{main}=950s/mm^2 FA and MD maps continue to demonstrate decreasing myocardial values. With regards to data presented earlier in this work (b_{main}=350s/mm^2, b_{ref}=135s/mm^2, diffusion weighting b=215s/mm^2), reported heterogeneity in cDTI parameters could therefore resulted from relative diffusion insensitivity.

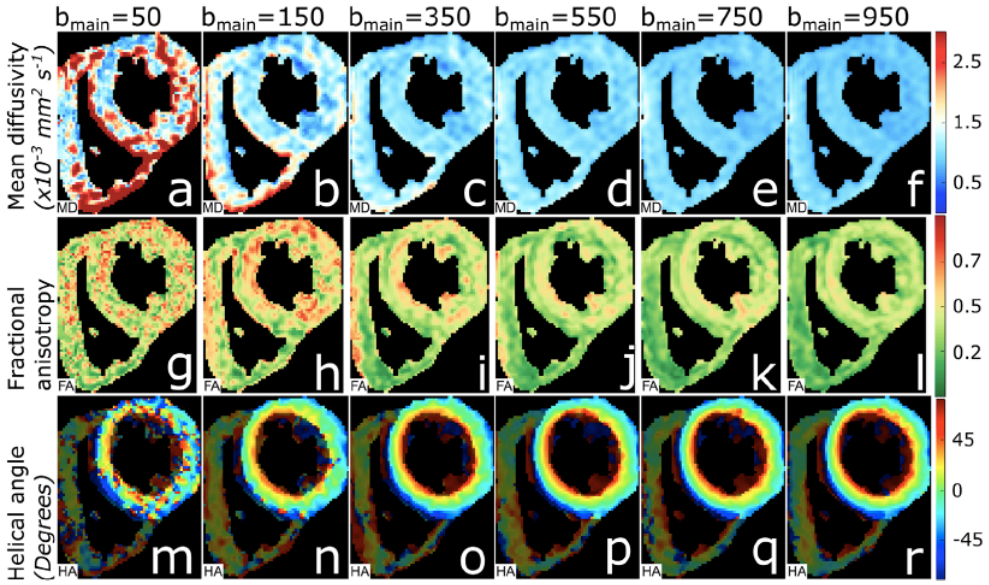

Figure 13.1: Short axis transmural maps in an example subject, at increasing b values for mean diffusivity (top row), fractional anisotropy (middle row) and helix angle (bottom row) (440).

DTI of free water results in mono-exponential decay of diffusion signal (S) defined by the following equation:

$$S = S_o \exp^{(-b.D)}$$

Where S_0 is the signal without diffusion weighting, D is the diffusivity of the tissues (i.e. MD) and b is the effective diffusion weighting of the sequence. At the b-values typically used in vivo, the signal is a weighted combination of two separate mono-exponential signal decay models. The first model dominates at lower b values, with rapid signal decay which has been demonstrated to coincide with capillary flow, i.e. perfusion. The second model is dominant at higher b values, with more gradual signal decay and is representative of passively diffusing water (438) (figure 13.2):

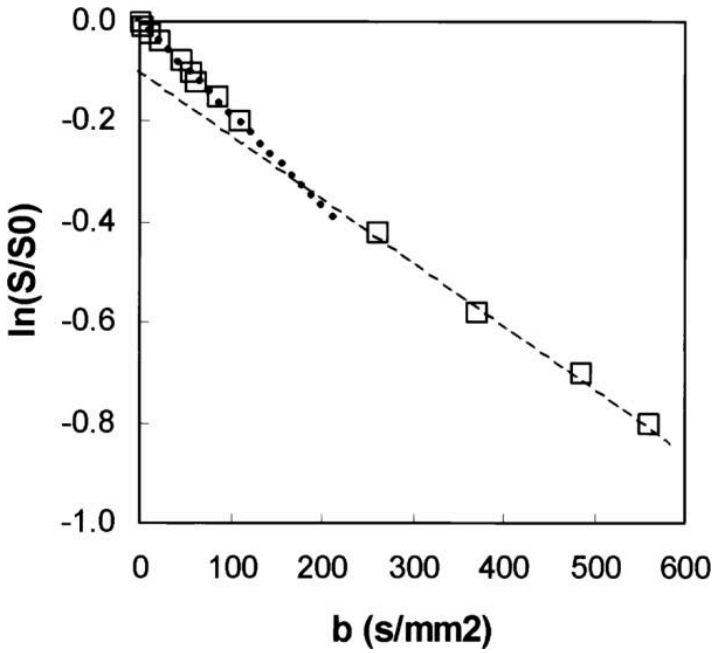

Figure 13.2: Plot of the log of the relative DTI signal loss against the diffusion weighting, or b value. For a mono-exponential model, the signal is a straight line. At b values <200s/mm^2 a rapid decline in signal is observed, coinciding with fast flow within capillaries. At higher b values the signal decay is more gradual, coinciding with diffusing water (438).

The relatively fast movement of blood within the capillaries (in comparison to the passive diffusion of water) results in a rapid signal loss with increasing diffusion weighting at low b-values. At higher b values, the signal from the fast moving capillary blood is almost completely eliminated and the difference in signal between two b-values is dominated by diffusion, with minimal contribution from perfusion. The impact of these contributions on cDTI parameters is demonstrated in figure 13.3. Combined with b_{ref}=15s/mm^2, at lower b values, MD and the helix angle gradient fell rapidly, with increasing diffusion weighting, then more gradually at >b=200s/mm^2. Conversely FA remained dependent on the b value throughout, with consistent linear trend of greater isotropy (lower FA) at increasing b values. When b_{main} was fixed at 750s/mm^2, increasing b_{ref} to 150s/mm^2 was sufficient to reduce the contributions from rapid decaying perfusion in to 0.5% of the remaining signal, but had little impact on FA.

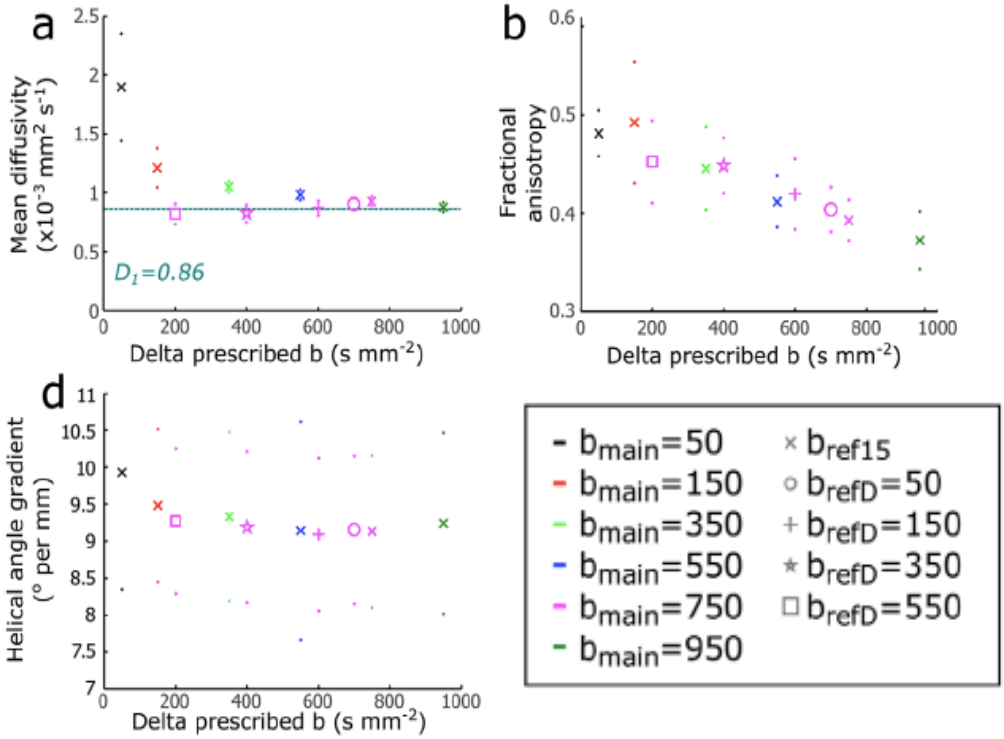

Figure 13.3: Comparison of mean diffusivity (MD), fractional anisotropy (FA) and helix angle gradient (HAG) values at increasing b values. B values are colour coded according to the b value (black through to green). With b_{main} set to 750s/mm² (pink) the impact of increasing b_{ref} (shapes) is demonstrated (440). D_1 is the slow diffusing component calculated from a bi-exponential model of diffusion fitted to all of the data.

Based on this work the optimal diffusion regimen was thus determined to be b_{ref}=150s/mm² combined with b_{main}=750s/mm², resulting in a diffusion weighting of b=600s/mm². At b_{main} values greater than 750s/mm² the benefits of improved diffusion sensitivity were offset by reductions in SNR.

This work highlights some of the technical constraints of cDTI and the limitations of drawing comparisons between studies with different diffusion weighting. The persistent dependence of FA on the diffusion weighting also raises questions as to the true anisotropy of myocardium. Optimising the diffusion sensitivity of cDTI may limit artefacts, improve myocardial characterisation and permit the detection of clinically important structural differences in cardiovascular disease groups.

On further examination of FA maps, at larger b values, a degree of transmural heterogeneity in anisotropy is observed. Greater anisotropy (greater FA) is apparent in the mesocardium, which was not appreciable at lower b values (figure 13.4).

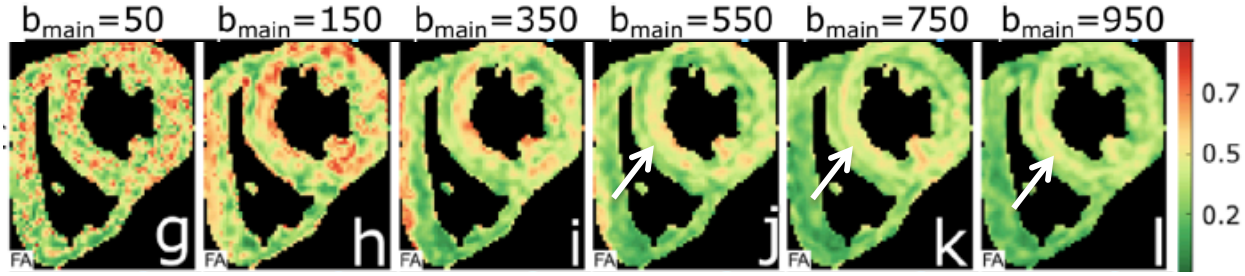

Figure 13.4: FA maps in an example subject at increasing b values. From b_{main}=550s/mm^2 to b_{main}=950s/mm^2 FA maps demonstrate a near circumferential rim of increased mesocardial FA, which is most pronounced in the septum (white arrows) (440).

Both Jiang et al. (364) and Angeli et al. (373) have demonstrated heterogeneity in transmural anisotropy in ex vivo ovine and murine hearts respectively, however this has not been assessed in vivo in human hearts. Whilst transmural heterogeneity in HA is well established, in vivo diffusivity and anisotropy have typically been assumed to be homogeneous.

This chapter re-examines myocardial heterogeneity of anisotropy and diffusivity at the improved diffusion sensitivity afforded by the b_{ref}=150s/mm^2, b_{main}=750s/mm^2 regimen, and explores the relation with additional technical factors during in vivo cDTI. Results published in: Laura-Ann McGill , Andrew D. Scott, Pedro F. Ferreira, Sonia Nielles-Vallespin, Tevfik Ismail, Philip J. Kilner, Peter D. Gatehouse, Ranil de Silva, Sanjay K. Prasad, Archontis Giannakidis, David N. Firmin and Dudley J. Pennell, Heterogeneity of fractional anisotropy and mean diffusivity measurements by in vivo diffusion tensor imaging in normal human hearts, 2015; 10(7): e0132360 (441).

13.2: Methods

13.2.1: Study Population

Twenty healthy volunteers (mean age 32 [range 22–57], 15 male) were recruited for cDTI acquisitions. Ethical approval was granted by the NRES Committee South East Coast Surrey (REC reference 10/H0701/112). All subjects gave written consent.

13.2.2: Image Acquisition

cDTI was acquired at 3T during the subject-specific end-systolic pause, identified from a bSSFP short axis cine sequence. In contrast to previous work, breath hold cDTI was performed in a single mid ventricular slice to focus data acquisition on the detection of short axis transmural and regional heterogeneity rather than LV coverage. As stated above, diffusion weighting was set at b_{main}=750s/mm^2 with b_{ref}=150s/mm^2 with a minimum of eight averages per subject. In contrast to previous protocols, b_{ref}=150s/mm^2 was acquired separately, in a different breath hold, in the same 6 directions as b_{main}. As before in earlier chapers, a standard single direction b_{ref}=15s/mm^2 image was also acquired during the breath hold used to acquire b_{main}.

To examine the impact of resolution and cDTI parameters, two protocols were applied. All 20 volunteers were scanned with protocol 1: Acquired resolution 2.8x2.8mm^2, slice thickness 8mm, field of view 360x135mm^2, echo time (TE) 24ms, with GRAPPA (Generalised auto-calibrating partially parallel acquisitions) parallel imaging at factor 2. Total scan duration was approximately 20mins. Two subjects were then re-scanned at a higher resolution, protocol 2: Acquired resolution 1.9x1.9mm^2, slice thickness 6mm, field of view of 349x125mm^2, with a TE of 37ms. A SENSE (sensitivity encoding) parallel imaging reconstruction was also used, which reconstructs in the image space, rather than k space, and the implementation available on the scanner provides increased SNR compared to the equivalent GRAPPA reconstruction. In order to compensate for the reduced SNR at the higher spatial resolution, TR was increased to 4 cardiac cycles to allow

additional T1 recovery between images. The resulting breath holds were therefore very long, at 40secs, with an average scan time of 30mins. The diffusion weighting of b_{main} and b_{ref} were unchanged between protocols.

13.2.3: Diffusion Tensor Analysis

Following initial post processing steps, the eigensystem (eigenvalues: e1, e2 and e2 (also known as λ_1, λ_2 and λ_3) and eigenvectors: ε_1 ε_2 and ε_3) was calculated from the diffusion tensor for each voxel. The exact diffusion weighting applied with a monopolar STEAM sequence is dependent on the subject's heart rate; heart rate correction was therefore applied a on a beat to beat basis in the tensor calculation.

Quantitative maps of FA and MD were calculated from the eigensystem. Myocyte orientation was determined from the primary eigenvector (ε1) and represented in an HA map. The mean, global HAG was calculated by drawing radial lines from epicardium to the central axis using a linear regression of HA with transmural depth (°/mm).

The acquisition SNR before averaging was measured using the multiple acquisition method described in Reeder et al. (442), applied to the b_{ref}=15s/mm^2 data. For quantitative analysis, the myocardium was divided into 3 transmural layers (endocardium, mesocardium and epicardium) using regions of interest placed at one-third and two-thirds through the myocardial wall. The myocardium was also analysed in 4 regional full thickness segments (septal, anterior, lateral and inferior). All cDTI analysis was performed by a single observer.

13.2.4: Statistical Analysis

The eigenvalues, MD, FA and SNR were analysed globally, transmurally, and by segment. All values were found to be normally distributed via a visual assessment of the distributions plotted as a histogram, and are therefore shown as mean±standard deviation (SD). Regional and

transmural analysis was performed with repeated measures ANOVA followed by paired t-testing between variables using the Bonferroni correction for multiple tests. The significance level was set at $p<0.05$. As only 2 individuals were scanned with protocol 2, only a visual analysis was performed.

13.3: Results

cDTI was successfully performed in all subjects. The average subject RR interval and trigger times were 917 ±187ms and 342 ±91ms respectively.

13.3.1: Helical Angle

An HA map from an example subject is shown in figure 13.5 using both the protocol described above and a similar acquisition with $b_{main}=350s/mm^2$ protocol. The increased diffusion sensitivity has resulted in a smooth HA map, free from the artefacts previous detected.

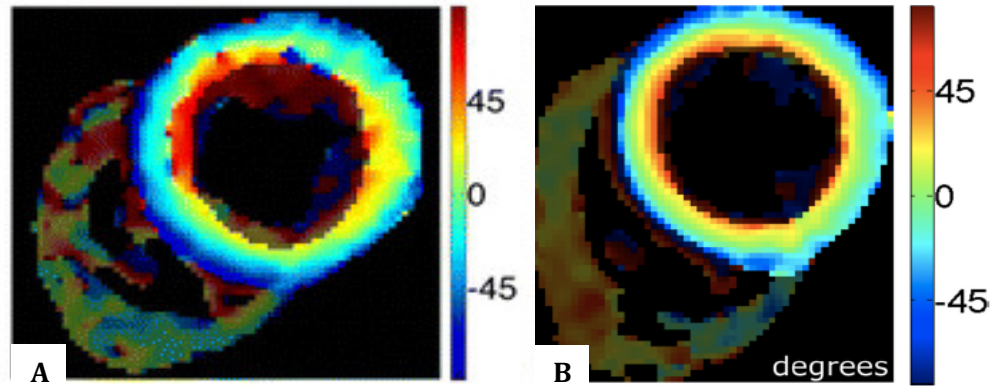

Figure 13.5: HA maps from an example subject with A: $b_{main}=350s/mm^2$, $b_{ref}=135s/mm^2$ and B: $b_{main}=750s/mm^2$, $b_{ref}=150s/mm^2$. In example B the transmural helix angle change is smoother with little evidence of artefact.

The average myocardial HAG was 9.1±1.1°/mm. Figure 13.6 illustrates the helix angle change with transmural depth from radial lines drawn from the endocardial to epicardial surface of the LV and equivalent histological observations in Streeter et al. for comparison (2). Within the region of the mesocardium there is a subtle reduction in the rate of change of HA compared to the adjacent epi- and endocardial zones.

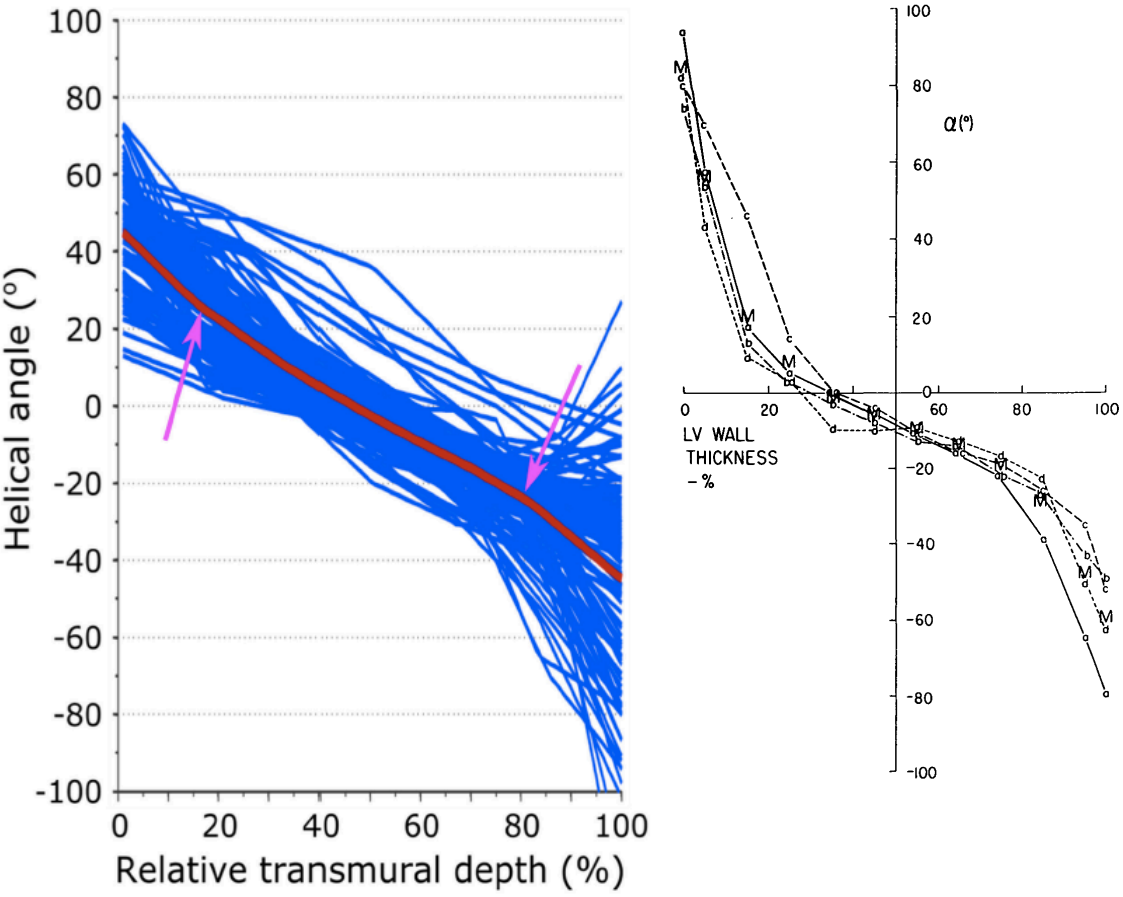

Figure 13.6: On the left radial, transmural helix angle line profiles from an example subject are shown. The x axis represents % depth from the endocardial surface. Each radial line is represented in blue, with the average shown in red. Subtle inflections are observed at the transition borders from the mesocardial zone to the epi and endocardial zones (441). In comparison, Streeter et al. demonstrated similar finding from histology, with a greater slowing of mesocardial helix angle gradient (2). Comparatively lower gradients in the epicardium and endocardium in this work were likely due to the exclusion of edge pixels during post processing and the limited spatial resolution.

13.3.2: Fractional Anisotropy

The average global FA per subject was 0.42±0.03. Example quantitative FA maps from 6 subjects are shown in figure 13.7. Nineteen out of 20 subjects demonstrated circumferentially increased mesocardial FA (yellow/orange), which in each case was most marked in the septum.

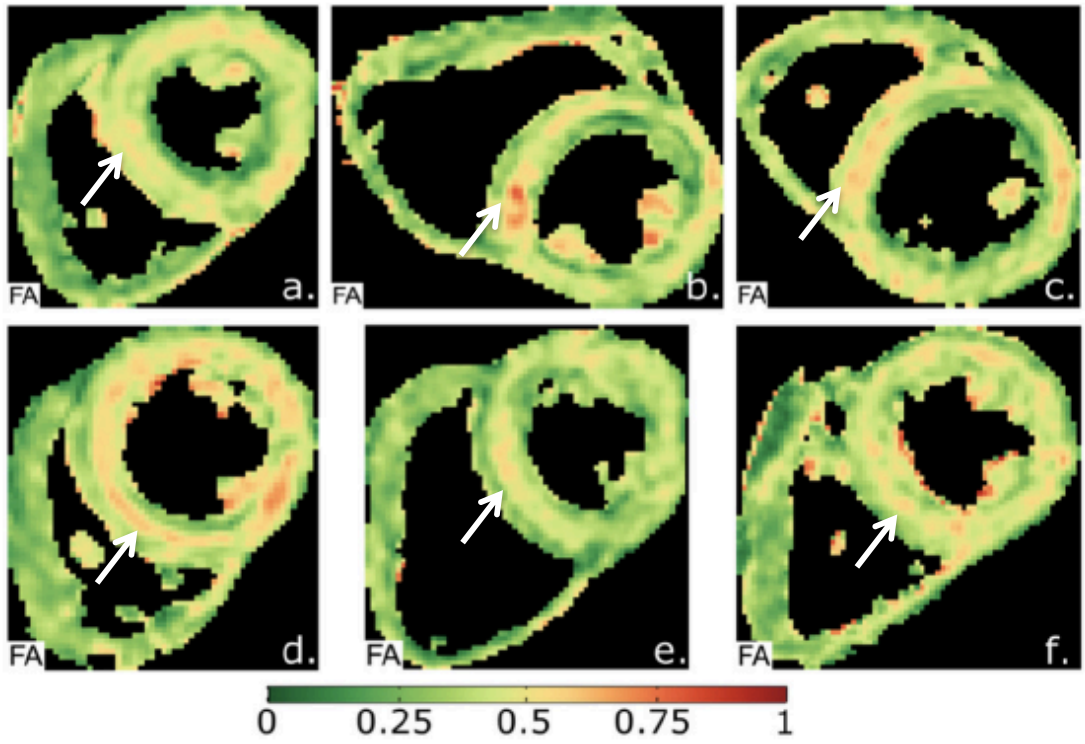

Figure 13.7: Typical examples of fractional anisotropy maps. The maps demonstrate a near circumferential increase in mesocardial anisotropy (greater FA) in comparison to the eipcardium and endocardium (441).

On transmural analysis, the FA in the mesocardium (0.46±0.04) was greater (more anisotropic) than the endocardium (0.40 ±0.04, $p<0.001$) and the epicardium (0.39 ±0.04, $p<0.001$). There was no difference between endocardial and epicardial FA ($p = 1.0$). Results for analysis of FA by regional LV wall are shown in table 13.1. With the lateral wall as the reference (0.40±0.05), inferior (0.42±0.05, $p=0.04$) and septal FA was significantly greater (0.44 ±0.03, $p = 0.011$), but no different to anterior wall FA.

Fractional Anisotropy	N = 20	p value
LV wall		ANOVA: F = 8.30, p<0.001
Lateral	0.40 ± 0.05	Reference
Anterior	0.40 ± 0.04	$p = 1.0$
Inferior	0.42 ± 0.05	$p = 0.04$
Septal	0.44 ± 0.03	$p = 0.011$

Table 13.1: Regional fractional anisotropy, mean±SD.(Bonferroni correction)

13.3.3: Mean Diffusivity

The global myocardial MD (all results $x10^{-3}mm^2/s$) per subject was 0.89±0.06. An example quantitative MD map is demonstrated in figure 13.8, with a narrowed scale to highlight transmural differences. A transmural gradient in MD was observed increasing from the epicardium to endocardium (epicardium 0.87±0.07; mesocardium 0.89±0.07; endocardium 0.91±0.08) with significantly greater MD in the endocardium compared to the epicardium (p=0.04). Results for regional analysis of MD are in table 13.2. With the lateral wall as the reference (0.87±0.08), MD was greater in the anterior wall (0.92±0.08, p=0.016) and septum (0.92±0.07, p=0.028).

Mean diffusivity	N = 20	p value
LV wall		ANOVA: F =12.8 , p<0.001
Lateral	0.87 ± 0.08	Reference
Anterior	0.92 ± 0.08	$p = 0.016$
Inferior	0.84 ± 0.08	$p = 0.89$
Septal	0.92 ± 0.07	$p = 0.028$

Table 13.2: Regional mean diffusivity ($x10^{-3}mm^2/s$), mean±SD, (Bonferroni correction)

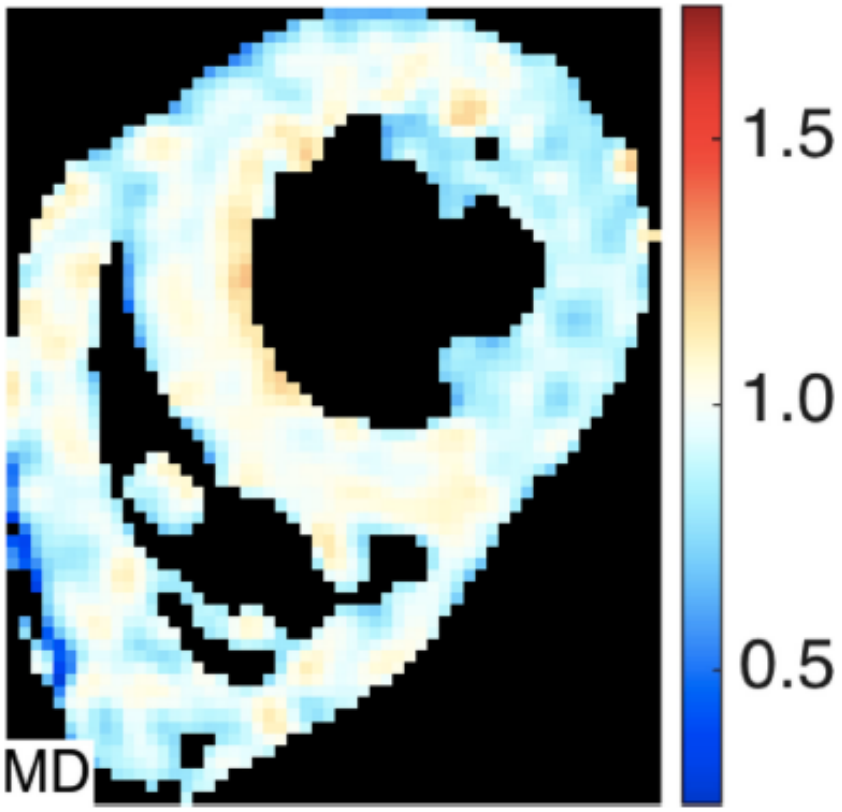

Figure 13.8: Mean diffusivity map from an example subject with a narrowed scale to emphasis differences. There is a subtle increase in septal MD compared to the other walls (441).

13.3.4: Eigenvalues

The global myocardial eigenvalues (all values in $x10^{-3}$ mm^2/s) were: e1 = 1.3±0.07, e2 = 0.85±0.08 and e3 = 0.53±0.05. The e1 in the mesocardium (1.33±0.08) was greater than in the endocardium (1.28±0.09, p = 0.001) and epicardium (1.24±0.07, p<0.001), and the e1 in the endocardium was greater than in the epicardium (p = 0.026). There was a transmural gradient in e2 increasing from the epicardium (0.80±0.07) to mesocardium (0.85±0.10; p = 0.001) and endocardium (0.90±0.08 p <0.001). e3 was smaller in the mesocardium (0.48±0.06) compared to the endocardium (0.54±0.07, p<0.001) and the epicardium (0.55±0.07, p<0.001), with no difference between endocardium and epicardium (p = 1.0).

Results for regional analysis of the eigenvalues e1, e2 and e3 are included in table 13.3. With the lateral wall (1.24±0.09) as the reference, e1 was greater in the anterior wall (1.32±0.10, p = 0.02)

and septum (1.37±0.08, p<0.001). Taking the lateral wall (0.83±0.09) as the reference, e2 was greater in the anterior wall (0.90±0.09, p = 0.005) and there were no regional significant differences in e3.

Eigenvalues	**N = 20**	**p value**
e1		ANOVA: F = 20.1, *p*<0.001
Lateral	1.24 ± 0.09	Reference
Anterior	1.32 ± 0.10	*p* = 0.019
Inferior	1.23 ± 0.10	*p* = 0.10
Septal	1.37 ± 0.08	*p* < 0.01
e2		ANOVA: F = 12.1, *p* = 0.003
Lateral	0.83 ± 0.09	Reference
Anterior	0.90 ± 0.09	*p* = 0.005
Inferior	0.81 ± 0.10	*p* = 0.91
Septal	0.85 ± 0.09	*p* = 1.0
e3		ANOVA: F = 4.24, *p* = 0.54
Lateral	0.53 ± 0.08	
Anterior	0.55 ± 0.08	
Inferior	0.49 ± 0.08	
Septal	0.53 ± 0.05	

Table 13.3: Regional eigenvalues, mean±S, Bonferroni correction

13.3.5: Signal to Noise Ratio

The average global myocardial SNR measured in the reference images was 13.2±2.2. The SNR was greater in the mesocardium (14.5±2.5) than the endocardium (13.0±2.2, p<0.001), and epicardium (12.0±2.4, p<0.001). The results for regional wall analysis are in table 13.4. With the lateral wall (11.5 ± 1.5) as the reference, the SNR was greater in the septum (16.1 ± 3.4, p<0.001) and anterior wall (14.0 ± 3.1, p<0.001).

Signal to Noise Ratio	**N = 20**	**p value**
LV wall		ANOVA: F = 34.4, p<0.001
Lateral	11.5 ± 1.5	Reference
Anterior	14.0 ± 3.1	p < 0.001
Inferior	11.7 ± 2.3	p = 1.0
Septal	16.1 ± 3.4	p < 0.001

Table 13.4: Regional signal to noise ratio, mean±SD

Figure 13.9 provides a visual comparison of transmural and regional heterogeneity for FA, MD, SNR, and the eigenvalues collectively.

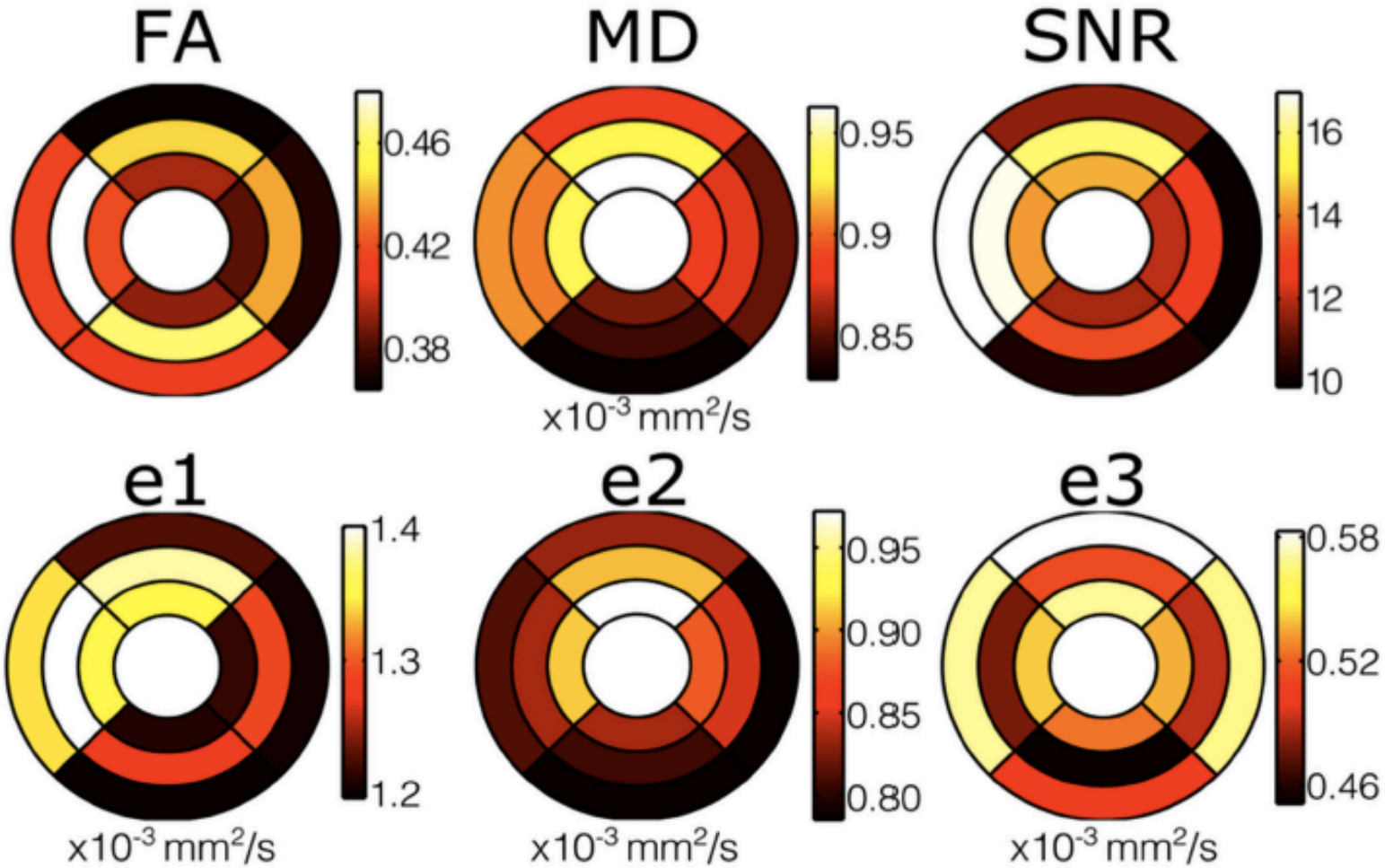

Figure 13.9: Colour Bullseye maps showing the significant heterogeneity in the distribution of FA, MD, SNR and e1-e3. The outer ring shows results from the epicardium, the middle ring represents the mesocardium, and the inner ring represents the endocardium of the single left ventricular slice. The four walls are also demonstrated in their usual positions: Upper- anterior wall; left- septum; lower- inferior wall; right- lateral wall (441).

13.3.6: Higher Resolution Imaging

Comparative HA, MD, FA & SNR maps for both standard resolution and high resolution scans for 2 volunteers are shown in figure 13.10. In both cases, SNR is lowever in the higher resolution images (global SNR 11.5 vs 15.4 in subject 1 and 8.5 vs 14.8 in subject 2), especially in the inferior and lateral walls, with worsening of the inferior wall susceptibility artefact due to the longer EPI readout. There was also a relative decrease in myocardial MD with the higher resolution sequence (higher: 0.82 vs lower: 0.88 and higher: 0.88 vs lower: 0.93 in the two subjects) and an increase in FA (higher: 0.55 vs lower: 0.48 and higher: 0.51 vs lower 0.46). In both cases the relative increase in mesocardial FA is present at both resolutions. In regions of poor SNR, the FA appears to be elevated.

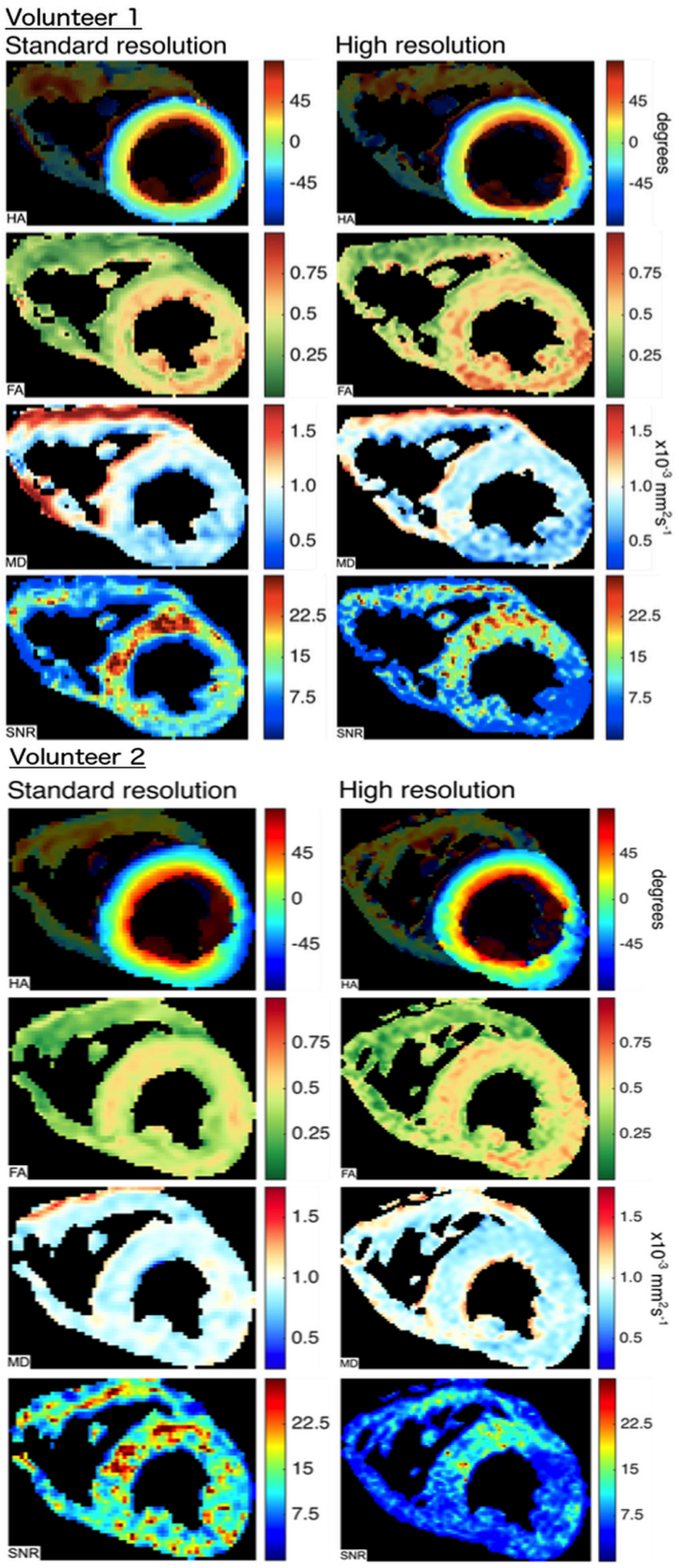

Figure 13.10: HA, FA, MD and SNR maps for 2 subjects at standard resolution (2.8x2.8x8mm^2) and higher resolution (1.9x1.9x6mm^2). In both cases the SNR is visibly reduced in the higher resolution scan in the lateral and inferior walls. At higher resolution, in regions of poor SNR, the FA is increased and MD is decreased. The transmural FA heterogeneity is maintained between standard and higher resolution acquisitions (441).

13.4: Discussion

13.4.1: Comparison with Previous Work

Global FA (0.42±0.03) and MD (0.89±0.06 $x10^{-3}$ mm^2/s) were reduced using the increased diffusion weighting in this study compared to the previous results (FA: 0.47±0.05, MD: 0.93±0.14 $x10^{-3}$ mm^2/s), owing to the greater diffusion weighting. Regional variations in FA and MD were observed which were different to, or absent, at lower diffusion sensitivities. The optimised diffusion sensitivity also permitted the detection of transmural heterogeneity in FA, with significantly greater mesocardial anisotropy, which persisted at higher resolution. As measured in vivo by cDTI, multiple factors are likely to contribute to FA and MD values, including microstructural anisotropies, microstructural dynamics and possible artefacts associated with acquisition in the beating heart.

13.4.2: Influence of Microstructure on FA and MD Measurements

When the cDTI parameters are broken down to their respective eigenvalues, the detected increase in mesocardial FA is observed to occur as a consequence of the combination of the relative elevation in mesocardial e1 and reduction in e3. Jiang et al. also demonstrated transmural FA heterogeneity in sheep, with greatest FA similarly coinciding with circumferentially orientated myocytes (364). This was attributed to a relative decrease in e2 and e3 in the region, although e1 was also increased but did not reach significance. One possible reason for the larger changes we observed in e1 is the longer mixing time (RR interval) of the DW-STEAM sequence used in our study when compared to the ex vivo spin-echo sequence used by Jiang et al. (364). Angeli et al. also demonstrated an identical transmural pattern of anisotropy to this work, however the FA differences did not reach significance (373). With regards to potential structural explanations for mesocardial anisotropy, this could be attributed to the transmural variation in the myocyte orientation. We observed a subtle reduction in the mesocardial HA gradient, which

accords with the earlier histological findings of Streeter et al. in canine hearts (2) and Greenbaum et al. in human hearts (3). Mesocardial e1 may therefore be elevated through a relative increase in intravoxel e1 alignment. More recently, myocardial anisotropy, as assessed by ex vivo cDTI, has been attributed to the magnetic properties of striated myocardial cells (443). Myocytes aligned more parallel to the main magnetic field (circumferential lateral and septal wall mesocardial myocytes) were illustrated to possess greater magnetic susceptibility, which translated to greater anisotropy. Conversely myocytes perpendicular to the magnetic field (epicardial and endocardial) possessed comparatively reduced magnetic susceptibility, translating to reduced anisotropy.

Histological studies, such as Sands et al. have demonstrated a transmural gradient in myocardial myolaminar structures, increasing from the epicardium to endocardium, with a relative absence of shear layer structures epicardially (6). The secondary eigenvector (e2) has been demonstrated to coincide with the cross-myocyte, sheetlet plane (145), therefore the increase in e2 and MD from epicardium to endocardium may be partially explained by the increase in extracellular shear layers. Both the epi to endocardial gradient in e2 and MD were also reported by Jiang et al. (364). The reduction in mesocardial e3 is more difficult to explain, but may also be attributed to the increased myocyte coherence in this layer which proportionally increased e1 at the expense of e3.

13.4.3: Influence of SNR on FA and MD Measurements

The influence of SNR on FA and MD is complex and is dependent on the b value. At low b-values, noise results in an overestimation of FA, whereas at high b-values, noise results in an underestimation of both FA and MD (406). The cut off between high and low b values are tissue specific and acquisition specific and there is limited literature in the heart (444). From this data comparatively reduced SNR in the epicardium and endocardium translated to reduced FA,

therefore a diffusion weighting of b=600s/mm^2 could be interpreted as high diffusion weighting for myocardium. In contrast, at higher resolution, a marked reduction in SNR in the lateral an inferior walls translated to visibly greater FA, therefore suggesting this constitutes a low diffusion weighting regimen. Regional reductions in MD were also observed to track regionally low SNR, which is also in keeping with a high b value regimen, however the MD pattern did not track SNR transmurally, suggesting other factors are impacting on this measure.

13.4.4: Influence of Resolution, Partial Voluming and ROIs on FA and MD Measurements

Partial voluming, where edge pixels include data from adjacent structures, such as the blood pool, could potentially contribute to the measured transmural heterogeneity of FA and MD. This would affect endocardial and epicardial measures whilst sparing the mesocardium. As partial voluming effects are greater at lower resolution, imaging was repeated at higher resolution for comparison. The transmural heterogeneity in FA maps showed little difference, suggesting that partial voluming artefact was not a significant contributor to the greater mesocardial anisotropy observed.

During collaborative inter-centre reproducibility work with Oxford (Chapter 10), restrictive ROIs demonstrated an over estimation of global FA by +0.04 in comparison to less restrictive ROIs. These data provide the explanation for this. Like partial voluming, variations in ROIs affect endocardial and epicardial layers whilst sparing the mesocardium, restrictive ROIs therefore elevate global FA by reducing contributions from these layers.

13.4.5: Influence of Strain on FA and MD Measurements

Although this work focused on a single cardiac phase, the impact of strain, on cDTI measures must still be considered. Strain is maximal in the radial, cross-myocyte direction, increasing

transmurally from the epicardium to endocardium (66). As e2 lies in the cross-myocyte plane, strain may have contributed to the observed epi to endocardial gradient in e2, however it cannot explain the heterogeneity observed in e1, e3 or FA.

In Chapter 10 we demonstrated greater MD in diastole than in systole, in both intra-centre (372, 427) and inter-centre comparisons (372). Reese et al. described an underestimation estimation of radial diffusivity in the context of strain (366). This data suggests an increase in MD towards the endocardium, if the strain theory were true the gradient should be reversed, with increasing MD towards the epicardium. To add to this confusion, Stoeck et al. contradicted Reese et al. stating that strain actually leads to an overestimation of radial diffusivities (150), however, following strain correction in the same work, MD values were increased in systole and reduced in diastole thereby implying the opposite.

13.5: Conclusions

This chapter presents evidence of transmural variations in myocardial microstructure with a detailed assessment of technical factors that might also influence FA and MD measures. While we believe that regional heterogeneity in measures may be predominantly artefactual, the detected increase in transmural anisotropy appears to accord with ex vivo cDTI and histological studies. Since publication of this work, Froeling et al. presented data at ISMRM 2016 (445) entitled 'transmural heterogeneity of in vivo whole heart diffusion parameters: architecture, physiology or artefact', where they replicated our findings of greater mesocardial anisotropy in vivo and ex vivo, with strain insensitive sequences, concluding that the effect was a consequence of the circumferential orientation of mesocardial myocytes. The question therefore remains whether the myocardium is genuinely more structured in the mesocardial layer, or if this is merely a reflection of the greater magnetic susceptibility of these myocytes, in relation to their alignment with the main magnetic field. Arguing against this theory is the fact that, in a supine subject in vivo, while anterior and inferior wall mesocardial myocytes are parallel to the main magnetic

field, septal and lateral myocytes are not, and our findings were most marked in the septum. This work suggests that quantification of FA and MD requires careful selection of the region of interest and an understanding of normal transmural variation. Further work is required to understand the true relation between cDTI assessments of diffusivity and anisotropy to the underlying architecture.

CHAPTER 14: CONCLUSIONS AND FUTURE DIRECTIONS

14.1: Summary

The aim of this thesis was to evaluate the in vivo diffusion weighted monopolar stimulated echo acquisition mode (DW-STEAM) sequence, at 3Tesla, in the acquisition of cDTI data in healthy volunteers and patients with HCM. The relation between quantitative cDTI parameters and underlying myocardial microstructure was interpreted within the context of identified technical limitations. This work included the assessment of inter-centre reproducibility in healthy volunteers and intra-centre reproducibility in patients with HCM. The theory of sheetlet re-orientation during contraction was evaluated in both cohorts, with the novel finding of aberrant sheetlet mobility in HCM.

14.2: Technical Developments

This sequence evaluation work was conducted in tandem with sequence development facilitating combined technical improvements. During initial sequence evaluation, cycling the order diffusion directions were acquired ensured the impact of poor breath holding was spread across all directions equally. Collaborative work with Oxford then brought new insights: Firstly, it allowed an error in the diffusion reference images to be identified and addressed; secondly, an inter-centre reproducibility study underlined the importance of standardising ROIs when evaluating quantitative parameters. Subsequent departmental, sequence development work established the optimal diffusion weighting for cDTI, permitting a detailed assessment of the relation between technical factors and quantification of cDTI parameters.

14.3: Inferring Myocardial Structure From Quantitative In Vivo Cardiovascular Diffusion Tensor Imaging

14.3.1: Myocardial Fibrosis Via Mean Diffusivity

MD values acquired with DW-STEAM differed between phases and in comparison to data derived from other in vivo protocols (150, 293, 294, 342, 369, 370). With the b_{main}=350s/mm^2 regimen MD was the least reproducible parameter in HCM patients, with no association between fibrosis (LGE) and MD identified, contradicting other authors (293, 342, 369, 370). This was not assessed with the optimised diffusion weightings, however limitations remain when inferring myocardial diffusivity or fibrosis from MD. Although less pronounced at higher b values, the dependency of MD on the diffusion weighting is such that the true diffusivity of in vivo myocardium is uncertain. Moreover, interpretation of regional variations is impeded by SNR heterogeneity. This measure has been proposed as a contrast free method of determining fibrosis (293, 342), with additional potential for differentiating infarcted myocardium from the area at risk (378), however contradictions to contrast injection are rare, and alternative techniques such as T1 and T2 mapping provide similar information with fewer technical challenges. Despite these limitations, inclusion of MD data in future clinical cDTI research studies remains justifiable. MD is widely used in neurological and body diffusion MRI as a sensitive biomarker of microstructural changes (446) and it may demonstrate changes in the presence of, as yet un-studied cardiac diseases, or with future developments in sequence performance. This work has also demonstrated that MD also serves as a barometer of sequence performance, providing context to other parameter measures.

14.3.2: Myocardial Organisation Via Fractional Anisotropy

FA is the most widely recognised measure of anisotropy, however this thesis highlights its limitations in application to the heart. Measured FA is dependent on the b value, such that the true anisotropy of myocardium remains uncertain (440). Like MD, FA differences between phases observed with this sequence are disputed by other authors, who cite strain as the cause (371).

The assessment of regional variation is further limited by SNR heterogeneity, and the behaviour in relation to noise is hard to predict (406, 441). The interpretation of greater mesocardial anisotropy is also difficult, although this observation was reproduced by other authors (445), greater magnetic susceptibility through the alignment of circumferential myocytes with the main magnetic field may be a contributing factor (443). In the event of in vivo sequence developments in SNR and resolution, re-evaluation of FA may be warranted, otherwise alternative measures of anisotropy should be pursued.

14.3.3: Myocyte Orientation Via Helix Angle

The HA is the most robust cDTI parameter. The known winding helical pattern of myocyte organisation was consistently identified, with particularly smooth variations in transmural HA following the optimisation of diffusion weightings. However the parameter is not immune to artefact, as Nielles-Vallespin et al. demonstrated the association between SNR and HA range (19). There are also difficulties in quantifying HA data, as mesocardial HA passes through zero and comparison of HA subdivided transmurally and regionally increases exposure to variations in ROI drawing. Assessing the HAG circumvents these issues, but by approximating transmural HA as a linear gradient, at the expense of data smoothing.

The relation between HAG and ventricular size/ thickness is interesting. There is a gradual transition through a similar range of angles, with increasing size, in all subjects, as opposed to deeper angulation. A relatively minor shift towards more positive HA was observed in systole, with a steeper transmural gradient, thereby adding further weight to the theory that myocardial deformation during contraction is reliant on sheetlet reorientation. Whether HA assessment has future clinical utility may be determined from further evaluation in other cardiovascular disease groups.

14.2.4: Sheetlet Orientation Via The Secondary Eigenvector

The ability to assess myolaminar dynamics is most exciting aspect of in vivo cDTI. A greater understanding of their contribution to LV mechanics in health and disease may pave the way to future therapeutic innovations. Sheetlets were observed to re-orientate more radially in systole, than in diastole, where they were more parallel to the local myocardial walls, in keeping with the theory of their role in radial thickening (9, 10, 13). While contemporary researchers agree with this theory (13, 150, 368), the magnitude of the effect, and the impact of strain on measurement of the secondary eigenvector angle remains contentious (150, 366, 368, 387). Resolving this issue is key to advancing the technique and knowledge within the field.

14.4: Interpretation of Hypertrophic Cardiomyopathy Myo-architecture From In Vivo Cardiovascular Diffusion Tensor Imaging

It was theorised that FA may be able to detect myocardial disarray in HCM through reduced anisotropy, however no difference was found in comparison to hypertensive patients and healthy controls. The limitations of FA in the assessment of anisotropy are in part to blame, however review of histological data reveals that disarray is not specific to HCM, and the true in vivo prevalence is unknown.

Despite the marked abnormality in LV morphology in HCM, a normal pattern of myocyte HA was observed. While surprising, Tseng et al. also reported a normal transmural HA pattern reported similar findings, although our results disagreed as to the predominance of right-handed versus left-handed myocytes (294).

Aberrant sheetlet mobility in HCM was a novel finding. When sheetlet reorientations were also assessed in hypertension, the degree sheetlet dysfunction strongly correlated with LV wall thickness in both cohorts. The question remains as to whether this represents the chicken or egg,

i.e. is LV wall thickness a function of severity of sheetlet dysfunction; or is sheetlet dysfunction a final common pathophysiological pathway in response to hypertrophy? Either way, this is a new insight into the link between microstructural abnormality and macroscopic disease expression; evaluation of sheetlet orientations in other cardiovascular diseases, such as LV impairment, may offer further insights.

14.5: Conclusion

This is one of the largest in vivo cDTI studies to date and the first to consider the microstructure of both HCM and hypertensive LVH with cDTI. Although, in its current format, assessment of mean diffusivity and fractional anisotropy is technically limited, we did find evidence of a normal transmural variation in anisotropy, which may hint at some underlying microstructural changes. Uniquely cDTI has the ability to characterise myocyte and sheetlet orientations and dynamics non-invasively and histological descriptions of the transmural helical winding of myocytes were confirmed, with an increase in myocyte gradient in diastole compared to systole. While cDTI was unable to demonstrate the expected microstructural disarray using mean diffusivity or fractional anisotropy, we were able to distinguish HCM from LVH and normal subjects using diastolic E2A. In healthy volunteers, sheetlets assessed via E2A, were observed to re-orientate from a wall parallel, to a radial orientation in systole, providing further evidence for their role in systolic radial thickening. In contrast, sheetlets in patients with hypertension and hypertrophic cardiomyopathy displayed an inability to re-orientate from the systolic to diastolic confirmation, offering a novel explanation for hypertrophy related diastolic dysfunction. This is a novel observation which may have important consequences for the future understanding of the pathophysiology of hypertrophy.

14.6: Future Directions

14.6.1: Development of 3D Strain Sequence and Assessment of Strain Artefacts

The current focus of this research group is the assessment of strain and strain artefacts. A 3D displacement encoding using stimulated echoes (DENSE) strain sequence, has been developed to facilitate prospective comparisons of in vivo cDTI data and local strain at 3T. In collaboration with NIH, Washington, an ex vivo study has been designed to definitively address strain artefacts. In NIH, data have been acquired from Langendorff prepared pig hearts, during active contraction, for comparison with stationary data in systole and diastole. This will permit direct quantification of any strain artefacts in quantification of cDTI parameters.

14.6.2: Evaluation of The Second Order Motion Correction Bipolar Spin Echo Sequence

Recent developments in cDTI sequences have focused on improving velocity and acceleration compensation of bipolar, spin echo acquisitions (371, 392, 393). Bipolar acquisitions have the advantage of freedom from strain susceptibility, however motion artefacts have proven problematic. The motion compensated diffusion encoding gradients introduced are designed to correction, targeted to address both myocardial velocity and acceleration phase offsets and may pave the way towards cardiac phase specific acquisitions, with minimal contributions from myocardial strain.

14.6.3: Evaluation of Alternative Measures of Anisotropy

The limitations of fraction anisotropy in monopolar DW-STEAM acquisitions were highlighted by this thesis. However, alternative methods of quantifying anisotropy warrant evaluation in vivo. This includes the tensor mode (447), transverse anisotropy (λ_2/λ_3)(376), and methods of assessing inter-voxel anisotropy (448). With regards to the mode of anisotropy, this is capable of resolving whether a region of anisotropy is linearly anisotropic (a stick like tensor), orthotropic,

or planar anisotropic and thus, with FA, provides a more complete description of the underlying tensor figure 14.1.

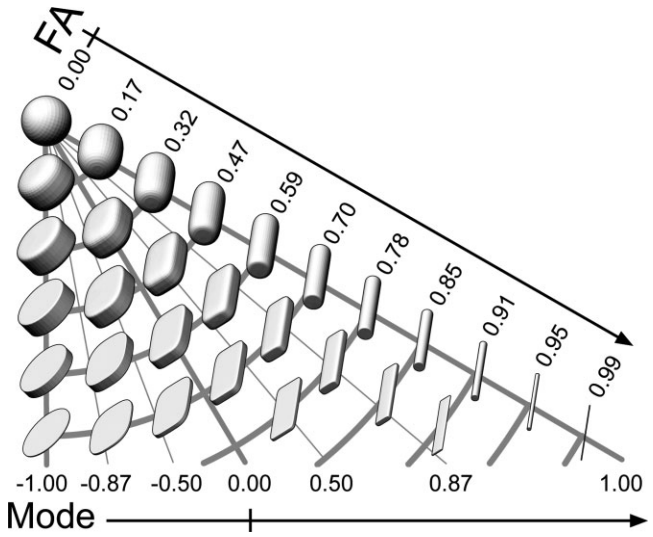

Figure 14.1: Comparison of fractional anisotropy and the mode of anisotropy. FA values from zero (top left) to 1 (bottom right). The radii represent the range of shapes that may arise with the same FA value. The mode gives additional information on the tensor shape describing planar isotropic (-1), orthotropic (0) and linear isotropic (1)(447).

14.6.4: Evaluation of Myocyte and Sheetlet Orientations in Dilated Cardiomyopathy

In hypertrophied myocardium, sheetlets demonstrated diastolic dysfunction with persistence of the systolic orientation throughout the cardiac cycle, however sheetlet orientations in other disease aetiologies have not been studied. Analysis of sheetlet mobility in ventricles with opposing shape and functional capabilities, such as the in the dilated, failing heart, may lead to a better understanding of the role of myolaminae in cardiovascular disease expression.

References

1. Pettigrew JB. On the Arrangement of the Muscular Fibres in the Ventricles of the Vertebrate Heart, with Physiological Remarks. Philosophical Transactions of the Royal Society of London. 1864;154:445-500.
2. Streeter DD, Spotnitz HM, Patel DP, Ross J, Sonnenblick EH. Fiber Orientation in the Canine Left Ventricle during Diastole and Systole. Circulation Research. 1969;24(3):339-47.
3. Greenbaum RA, Ho, S. Y., GIbson, D. G., Becker A. E., Anderson, R.H. Left Ventricular fibre architecture in man. Br Heart J. 1981;45:248-63.
4. Le Grice I, Smaill BH, Chai LZ, Edgar SG, Gavin JB, Hunter PJ. Laminar structure of the heart: ventricular myocyte arrangement and connective tissue architecture in the dog. The American journal of physiology. 1995;269:H571-82.
5. Harrington KB, Rodriguez F, Cheng A, Langer F, Ashikaga H, Daughters GT, et al. Direct measurement of transmural laminar architecture in the anterolateral wall of the ovine left ventricle: new implications for wall thickening mechanics. American journal of physiology Heart and circulatory physiology. 2005;288(3):H1324-30.
6. Sands GB, Gerneke DA, Hooks DA, Green CR, Smaill BH, Legrice IJ. Automated imaging of extended tissue volumes using confocal microscopy. Microscopy research and technique. 2005;67(5):227-39.
7. Kung GL, Nguyen TC, Itoh A, Skare S, Ingels NB, Jr., Miller DC, et al. The presence of two local myocardial sheet populations confirmed by diffusion tensor MRI and histological validation. Journal of magnetic resonance imaging : JMRI. 2011;34(5):1080-91.
8. Arts T, Costa KD, Covell JW, McCulloch AD. Relating myocardial laminar architecture to shear strain and muscle fibre orientation. American journal of physiology Heart and circulatory physiology. 2001;280:H2222-H9.
9. LeGrice IJ, Takayama Y, Covell JW. Transverse shear along myocardial cleavage planes provides a mechanism for normal systolic wall thickening. Circ Res. 1995;77(1):182-93.
10. Spotnitz HM, Spotnitz WD, Cottrell TS, Spiro D, Sonnenblick EH. Cellular basis for volume related wall thickness changes in the rat left ventricle. Journal of molecular and cellular cardiology. 1974;6(4):317-31.
11. Costa KD, Takayama Y, McCulloch AD, Covell JW. Laminar fibre architecture and three-dimensional systolic mechanics in canine ventricular myocardium. American journal of physiology Heart and circulatory physiology. 1999;276:H595-H607.
12. Chen J, Liu W, Zhang H, Lacy L, Yang X, Song SK, et al. Regional ventricular wall thickening reflects changes in cardiac fibre and sheet structure during contraction: quantification with diffusion tensor MRI. American journal of physiology Heart and circulatory physiology. 2005;289:H1898-H907.
13. Hales PW, Schneider JE, Burton RA, Wright BJ, Bollensdorff C, Kohl P. Histo-anatomical structure of the living isolated rat heart in two contraction states assessed by

diffusion tensor MRI. Progress in biophysics and molecular biology. 2012;110(2-3):319-30.
14. Elliott PM, Anastasakis A, Borger MA, Borggrefe M, Cecchi F, Charron P, et al. 2014 ESC Guidelines on diagnosis and management of hypertrophic cardiomyopathy: the Task Force for the Diagnosis and Management of Hypertrophic Cardiomyopathy of the European Society of Cardiology (ESC). European heart journal. 2014;35(39):2733-79.
15. Maron BJ, Anan TJ, Roberts WC. Quantitative analysis of the distribution of cardiac muscle cell disorganization in the left ventricular wall of patients with hypertrophic cardiomyopathy. Circulation. 1981;63(4):882-94.
16. Maron BJ, Roberts WC. Hypertrophic cardiomyopathy and cardiac muscle cell disorganization revisited: relation between the two and significance. American heart journal. 1981;102:95-110.
17. Maron BJ. Myocardial disorganisation in hypertrophic cardiomyopathy. Another point of view. Br Heart J. 1983;50(1):1-3.
18. Maron BJ, Wolfson JK, Roberts WC. Relation between extent of cardiac muscle cell disorganization and left ventricular wall thickness in hypertrophic cardiomyopathy. The American journal of cardiology. 1992;70(7):785-90.
19. Nielles-Vallespin S, Mekkaoui C, Gatehouse P, Reese TG, Keegan J, Ferreira PF, et al. In vivo diffusion tensor MRI of the human heart: reproducibility of breath-hold and navigator-based approaches. Magnetic resonance in medicine : official journal of the Society of Magnetic Resonance in Medicine / Society of Magnetic Resonance in Medicine. 2013;70(2):454-65.
20. Gray H, Leonard CH. The concise Gray's anatomy. New York: Cosimo Classics; 2005. 296 p. p.
21. Braunwald E, Bonow RO. Braunwald's heart disease : a textbook of cardiovascular medicine. 9th ed. Philadelphia: Saunders; 2012. xxiv, 1961 p. p.
22. Ho SY. Anatomy and myoarchitecture of the left ventricular wall in normal and in disease. European journal of echocardiography : the journal of the Working Group on Echocardiography of the European Society of Cardiology. 2009;10(8):iii3-7.
23. Chan KL, Veinot JP. General Anatomy of the Heart in the Chest. 2011. In: Anatomic Basis of Echocardiographic Diagnosis [Internet]. Springer London; [1-26].
24. Ritter M, Oechslin E, Sutsch G, Attenhofer C, Schneider J, Jenni R. Isolated noncompaction of the myocardium in adults. Mayo Clinic proceedings. 1997;72(1):26-31.
25. Petersen SE, Selvanayagam JB, Wiesmann F, Robson MD, Francis JM, Anderson RH, et al. Left ventricular non-compaction: insights from cardiovascular magnetic resonance imaging. Journal of the American College of Cardiology. 2005;46(1):101-5.
26. Oechslin EN, Attenhofer Jost CH, Rojas JR, Kaufmann PA, Jenni R. Long-term follow-up of 34 adults with isolated left ventricular noncompaction: a distinct cardiomyopathy with poor prognosis. Journal of the American College of Cardiology. 2000;36(2):493-500.
27. Jenni R, Oechslin E, Schneider J, Attenhofer Jost C, Kaufmann PA. Echocardiographic and pathoanatomical characteristics of isolated left ventricular non-compaction: a step towards classification as a distinct cardiomyopathy. Heart. 2001;86(6):666-71.
28. Captur G, Nihoyannopoulos P. Left ventricular non-compaction: genetic heterogeneity, diagnosis and clinical course. International journal of cardiology. 2010;140(2):145-53.

29. Stahli BE, Gebhard C, Biaggi P, Klaassen S, Valsangiacomo Buechel E, Attenhofer Jost CH, et al. Left ventricular non-compaction: prevalence in congenital heart disease. International journal of cardiology. 2013;167(6):2477-81.
30. Zemrak F, Ahlman MA, Captur G, Mohiddin SA, Kawel-Boehm N, Prince MR, et al. The relationship of left ventricular trabeculation to ventricular function and structure over a 9.5-year follow-up: the MESA study. Journal of the American College of Cardiology. 2014;64(19):1971-80.
31. Captur G, Zemrak F, Muthurangu V, Petersen SE, Li C, Bassett P, et al. Fractal Analysis of Myocardial Trabeculations in 2547 Study Participants: Multi-Ethnic Study of Atherosclerosis. Radiology. 2015:142948.
32. Tota B, Cimini V, Salvatore G, Zummo G. Comparative study of the arterial and lacunary systems of the ventricular myocardium of elasmobranch and teleost fishes. Am J Anat. 1983;167(1):15-32.
33. Sedmera D, Pexieder T, Vuillemin M, Thompson RP, Anderson RH. Developmental Pattern of the Myocardium. The Anatomical Record. 2000;258:319-37.
34. Anderson RH. Ventricular non-compaction--a frequently ignored finding? European heart journal. 2008;29(1):10-1.
35. Goenezen S, Rennie MY, Rugonyi S. Biomechanics of early cardiac development. Biomechanics and modeling in mechanobiology. 2012;11(8):1187-204.
36. Sanchez-Quintana D, Hurle JM. Ventricular myocardial architecture in marine fishes. Anat Rec. 1987;217(3):263-73.
37. Seymour RS, Blaylock AJ. The principle of laplace and scaling of ventricular wall stress and blood pressure in mammals and birds. Physiological and biochemical zoology : PBZ. 2000;73(4):389-405.
38. Ostergaard KH, Baandrup UT, Wang T, Bertelsen MF, Andersen JB, Smerup M, et al. Left ventricular morphology of the giraffe heart examined by stereological methods. Anat Rec (Hoboken). 2013;296(4):611-21.
39. Mitchell G, Skinner JD. An allometric analysis of the giraffe cardiovascular system. Comparative biochemistry and physiology Part A, Molecular & integrative physiology. 2009;154(4):523-9.
40. Kawel-Boehm N, Maceira A, Valsangiacomo-Buechel ER, Vogel-Claussen J, Turkbey EB, Williams R, et al. Normal values for cardiovascular magnetic resonance in adults and children. Journal of cardiovascular magnetic resonance : official journal of the Society for Cardiovascular Magnetic Resonance. 2015;17:29.
41. Maceira AM, Prasad SK, Khan M, Pennell DJ. Normalized left ventricular systolic and diastolic function by steady state free precession cardiovascular magnetic resonance. Journal of cardiovascular magnetic resonance : official journal of the Society for Cardiovascular Magnetic Resonance. 2006;8(3):417-26.
42. Kawel N, Turkbey EB, Carr JJ, Eng J, Gomes AS, Hundley WG, et al. Normal left ventricular myocardial thickness for middle-aged and older subjects with steady-state free precession cardiac magnetic resonance: the multi-ethnic study of atherosclerosis. Circulation Cardiovascular imaging. 2012;5(4):500-8.
43. Lee PT, Dweck MR, Prasher S, Shah A, Humphries SE, Pennell DJ, et al. Left ventricular wall thickness and the presence of asymmetric hypertrophy in healthy young army recruits: data from the LARGE heart study. Circulation Cardiovascular imaging. 2013;6(2):262-7.
44. Kovacs R, Baggish AL. Cardiovascular adaptation in athletes. Trends in cardiovascular medicine. 2015;26(1):46-52.

45. Utomi V, Oxborough D, Whyte GP, Somauroo J, Sharma S, Shave R, et al. Systematic review and meta-analysis of training mode, imaging modality and body size influences on the morphology and function of the male athlete's heart. Heart. 2013;99(23):1727-33.
46. Anderson RH, Ho SY, Redmann K, Sanchez-Quintana D, Lunkenheimer PP. The anatomical arrangement of the myocardial cells making up the ventricular mass. European journal of cardio-thoracic surgery : official journal of the European Association for Cardio-thoracic Surgery. 2005;28(4):517-25.
47. MacCallum JB. On the muscular architecture and growth of the ventricles of the heart. Johns Hopkins Hosp Rep. 1900;9:307-35.
48. Mall FP. On the muscular architecture of the ventricles of the human heart. Am J Anat. 1911;11:211-78.
49. Lev M, Simkins CS. Architecture of the human ventricular myocardium; technic for study using a modification of the Mall-MacCallum method. Laboratory investigation; a journal of technical methods and pathology. 1956;5(5):396-409.
50. Grant RP. Notes on the muscular architecture of the left ventricle. Circulation. 1965;32:301-8.
51. Torrent-Guasp F, Ballester M, Buckberg GD, Carreras F, Flotats A, Carrio I, et al. Spatial orientation of the ventricular muscle band: physiologic contribution and surgical implications. The Journal of thoracic and cardiovascular surgery. 2001;122(2):389-92.
52. Torrent-Guasp F, Buckberg GD, Clemente C, Cox JL, Coghlan HC, Gharib M. The structure and function of the helical heart and its buttress wrapping. I. The normal macroscopic structure of the heart. Seminars in thoracic and cardiovascular surgery. 2001;13(4):301-19.
53. Torrent-Guasp F, Kocica MJ, Corno AF, Komeda M, Carreras-Costa F, Flotats A, et al. Towards new understanding of the heart structure and function. European journal of cardio-thoracic surgery : official journal of the European Association for Cardio-thoracic Surgery. 2005;27(2):191-201.
54. Buckberg GD, Hoffman JI, Coghlan HC, Nanda NC. Ventricular structure-function relations in health and disease: Part I. The normal heart. European journal of cardio-thoracic surgery : official journal of the European Association for Cardio-thoracic Surgery. 2015;47(4):587-601.
55. Buckberg G, Hoffman JI, Nanda NC, Coghlan C, Saleh S, Athanasuleas C. Ventricular torsion and untwisting: further insights into mechanics and timing interdependence: a viewpoint. Echocardiography. 2011;28(7):782-804.
56. Buckberg GD. Architecture must document functional evidence to explain the living rhythm. European journal of cardio-thoracic surgery : official journal of the European Association for Cardio-thoracic Surgery. 2005;27(2):202-9.
57. Buckberg GD. Imaging, models, and reality: a basis for anatomic-physiologic planning. The Journal of thoracic and cardiovascular surgery. 2005;129(2):243-5.
58. Lunkenheimer PP, Redmann K, Anderson RH. The architecture of the ventricular mass and its functional implications for organ-preserving surgery. European journal of cardio-thoracic surgery : official journal of the European Association for Cardio-thoracic Surgery. 2005;27(2):183-90.
59. Schmid P, Jaermann T, Boesiger P, Niederer PF, Lunkenheimer PP, Cryer CW, et al. Ventricular myocardial architecture as visualised in postmortem swine hearts using magnetic resonance diffusion tensor imaging. European journal of cardio-thoracic surgery : official journal of the European Association for Cardio-thoracic Surgery. 2005;27(3):468-72.

60. Anderson RH, Ho SY, Sanchez-Quintana D, Redmann K, Lunkenheimer PP. Heuristic problems in defining the three-dimensional arrangement of the ventricular myocytes. The anatomical record Part A, Discoveries in molecular, cellular, and evolutionary biology. 2006;288(6):579-86.
61. Streeter DD, Bassett DL. An engineering analysis of myocardial fibre orientation in pig's left ventricle in systole. Anat Rec (Hoboken). 1966;155(4):503-11.
62. Sonnenblick EH, Ross J, Jr., Covell JW, Spotnitz HM, Spiro D. The ultrastructure of the heart in systole and diastole. Changes in sarcomere length. Circ Res. 1967;21(4):423-31.
63. Streeter DD, Jr., Vaishnav RN, Patel DJ, Spotnitz HM, Ross J, Jr., Sonnenblick EH. Stress distribution in the canine left ventricle during diastole and systole. Biophysical journal. 1970;10(4):345-63.
64. Streeter DD, Jr., Hanna WT. Engineering mechanics for successive states in canine left ventricular myocardium. I. Cavity and wall geometry. Circ Res. 1973;33(6):639-55.
65. Hunter PJ, Smaill BH. The analysis of cardiac function: a continuum approach. Progress in biophysics and molecular biology. 1988;52(2):101-64.
66. Waldman LK, Nosan D, Villarreal F, Covell JW. Relation between transmural deformation and local myofiber direction in canine left ventricle. Circ Res. 1988;63(3):550-62.
67. Harris SP, Lyons RG, Bezold KL. In the thick of it: HCM-causing mutations in myosin binding proteins of the thick filament. Circ Res. 2011;108(6):751-64.
68. Lopes LR, Elliott PM. A straightforward guide to the sarcomeric basis of cardiomyopathies. Heart. 2014;100(24):1916-23.
69. Sonnenblick EH, Skelton CL. Reconsideration of the Ultrastuctural basis of Cardiac Length-Tension Relations. Circulation Research. 1974;35:517-26.
70. Huxley HE. Muscle Cells. In: Brachet J, E. MA, editors. The Cell IV. New York: Academic Press; 1960. p. 365-500.
71. Sanger JW, Wang J, Fan Y, White J, Sanger JM. Assembly and dynamics of myofibrils. Journal of biomedicine & biotechnology. 2010;2010:858606.
72. Voorhees AP, Han HC. Biomechanics of Cardiac Function. Compr Physiol. 2015;5(4):1623-44.
73. Huxley HE, Hanson J. Changes in the cross-striations of the muscle during contraction and stretch and their structural interpretation. Nature. 1954;173:973-6.
74. Huxley HE. The Croonian Lecture 1970: The structural basis of muscular contraction. Proc R Soc London B. 1971;178:131-49.
75. Gerdes AM, Kriseman J, Bishop SP. Morphometric study of cardiac muscle: the problem of tissue shrinkage. Laboratory investigation; a journal of technical methods and pathology. 1982;46(3):271-4.
76. Gerdes AM, Kellerman SE, Moore JA, Muffly KE, Clark LC, Reaves PY, et al. Structural remodeling of cardiac myocytes in patients with ischaemic cardiomyopathy. Circulation. 1992;86:426-30.
77. Ibrahim M, Gorelik J, Yacoub MH, Terracciano CM. The structure and function of cardiac t-tubules in health and disease. Proceedings Biological sciences / The Royal Society. 2011;278(1719):2714-23.
78. Orchard C, Brette F. t-Tubules and sarcoplasmic reticulum function in cardiac ventricular myocytes. Cardiovascular research. 2008;77(2):237-44.
79. Lemler MS, Bies RD, Frid MG, Sastravaha AM, Zisman LS, Bohlmeyer T, et al. Myocyte cytoskeletal disorganization and right heart failure in hypoxia-induced neonatal

pulmonary hypertension. American journal of physiology Heart and circulatory physiology. 2000;279:H1365-H76.
80. Caulfield JB, Borg TK. The collagen network of the heart. Laboratory investigation; a journal of technical methods and pathology. 1979;40(3):364-72.
81. Robinson TF, Cohen-Gould L, Factor SM. Skeletal framework of mammalian heart muscle. Arrangement of inter- and pericellular connective tissue structures. Laboratory investigation; a journal of technical methods and pathology. 1983;49(4):482-98.
82. Robinson TF, Factor SM, Capasso JM, Wittenberg BA, Blumenfeld OO, Seifter S. Morphology, composition, and function of struts between cardiac myocytes of rats and hamster. Cell and tissue research. 1987;249:247-55.
83. Robinson TF, Geraci MA, Sonnenblick EH, Factor SM. Coiled perimysial fibers of papillary muscle in rat heart: morphology, distribution, and changes in configuration. Circ Res. 1988;63(3):577-92.
84. Young AA, LeGrice IJ, Young MA, Smaill B. Extended confocal microscopy of myocardial laminae and collagen network. Journal of Microscopy. 1998;192:139-50.
85. Helm P, Beg MF, Miller MI, Winslow RL. Measuring and mapping cardiac fiber and laminar architecture using diffusion tensor MR imaging. Annals of the New York Academy of Sciences. 2005;1047:296-307.
86. Pope AJ, Sands G, Smaill B, Le Grice I. Three-dimensional transmural organisation of perimysial collagen in the heart. American journal of physiology Heart and circulatory physiology. 2008;295:H1243-H52.
87. Kilner PJ, McCarthy K, Murillo M, Ferreira P, Scott AD, McGill L-A, et al. Histology of human myocardial laminar microstructure and consideration of its cyclic deformations with respect to interpretation of in vivo cardiac diffusion tensor imaging. Journal of Cardiovascular Magnetic Resonance. 2015;17(Suppl 1):Q10.
88. Hooks DA, Trew ML, Caldwell BJ, Sands GB, LeGrice IJ, Smaill BH. Laminar arrangement of ventricular myocytes influences electrical behavior of the heart. Circ Res. 2007;101(10):e103-12.
89. Caldwell BJ, Trew ML, Sands GB, Hooks DA, LeGrice IJ, Smaill BH. Three distinct directions of intramural activation reveal nonuniform side-to-side electrical coupling of ventricular myocytes. Circulation Arrhythmia and electrophysiology. 2009;2(4):433-40.
90. Criscione JC, Rodriguez F, Miller DC. The myocardial band: simplicity can be a weakness. European journal of cardio-thoracic surgery : official journal of the European Association for Cardio-thoracic Surgery. 2005;28(2):363-4; author reply 4-7.
91. Ashikaga H, Criscione JC, Omens JH, Covell JW, Ingels NB. Transmural left ventricular mechanics underlying torsional recoil during relaxation. American journal of physiology Heart and circulatory physiology. 2004;286:H640-H7.
92. Lohezic M, Teh I, Bollensdorff C, Peyronnet R, Hales PW, Grau V, et al. Interrogation of living myocardium in multiple static deformation states with diffusion tensor and diffusion spectrum imaging. Progress in biophysics and molecular biology. 2014;115(2-3):213-25.
93. Andre F, Steen H, Matheis P, Westkott M, Breuninger K, Sander Y, et al. Age- and gender-related normal left ventricular deformation assessed by cardiovascular magnetic resonance feature tracking. Journal of cardiovascular magnetic resonance : official journal of the Society for Cardiovascular Magnetic Resonance. 2015;17:25.
94. Lang RM, Bierig M, Devereux RB, Flachskampf FA, Foster E, Pellikka PA, et al. Recommendations for chamber quantification: a report from the American Society of Echocardiography's Guidelines and Standards Committee and the Chamber

Quantification Writing Group, developed in conjunction with the European Association of Echocardiography, a branch of the European Society of Cardiology. Journal of the American Society of Echocardiography : official publication of the American Society of Echocardiography. 2005;18(12):1440-63.
95. Spotnitz HM. Macro design, structure, and mechanics of the left ventricle. Journal of Thoracic and Cardiothoracic Surgery. 2000;119:1053-77.
96. Sengupta PP, Korinek J, Belohlavek M, Narula J, Vannan MA, Jahangir A, et al. Left ventricular structure and function: basic science for cardiac imaging. Journal of the American College of Cardiology. 2006;48(10):1988-2001.
97. Yip G, Abraham T, Belohlavek M, Khandheria BK. Clinical applications of strain rate imaging. Journal of the American Society of Echocardiography : official publication of the American Society of Echocardiography. 2003;16(12):1334-42.
98. Yu W, Li SN, Chan GC, Ha SY, Wong SJ, Cheung YF. Transmural strain and rotation gradient in survivors of childhood cancers. European heart journal cardiovascular Imaging. 2013;14(2):175-82.
99. Kocabay G, Muraru D, Peluso D, Cucchini U, Mihaila S, Padayattil-Jose S, et al. Normal left ventricular mechanics by two-dimensional speckle-tracking echocardiography. Reference values in healthy adults. Rev Esp Cardiol (Engl Ed). 2014;67(8):651-8.
100. Onishi T, Saha SK, Delgado-Montero A, Ludwig DR, Onishi T, Schelbert EB, et al. Global longitudinal strain and global circumferential strain by speckle-tracking echocardiography and feature-tracking cardiac magnetic resonance imaging: comparison with left ventricular ejection fraction. Journal of the American Society of Echocardiography : official publication of the American Society of Echocardiography. 2015;28(5):587-96.
101. Venkatesh BA, Donekal S, Yoneyama K, Wu C, Fernandes VR, Rosen BD, et al. Regional myocardial functional patterns: Quantitative tagged magnetic resonance imaging in an adult population free of cardiovascular risk factors: The multi-ethnic study of atherosclerosis (MESA). Journal of magnetic resonance imaging : JMRI. 2015;42(1):153-9.
102. Farsalinos KE, Daraban AM, Unlu S, Thomas JD, Badano LP, Voigt JU. Head-to-Head Comparison of Global Longitudinal Strain Measurements among Nine Different Vendors: The EACVI/ASE Inter-Vendor Comparison Study. Journal of the American Society of Echocardiography : official publication of the American Society of Echocardiography. 2015;28(10):1171-81.
103. Kempny A, Diller GP, Kaleschke G, Orwat S, Funke A, Radke R, et al. Longitudinal left ventricular 2D strain is superior to ejection fraction in predicting myocardial recovery and symptomatic improvement after aortic valve implantation. International journal of cardiology. 2013;167(5):2239-43.
104. Hartlage GR, Kim JH, Strickland PT, Cheng AC, Ghasemzadeh N, Pernetz MA, et al. The prognostic value of standardized reference values for speckle-tracking global longitudinal strain in hypertrophic cardiomyopathy. The international journal of cardiovascular imaging. 2015;31(3):557-65.
105. Doesch C, Sperb A, Sudarski S, Lossnitzer D, Rudic B, Tulumen E, et al. Mitral annular plane systolic excursion is an easy tool for fibrosis detection by late gadolinium enhancement cardiovascular magnetic resonance imaging in patients with hypertrophic cardiomyopathy. Archives of cardiovascular diseases. 2015;108(6-7):356-66.

106. Caselli S, Montesanti D, Autore C, Di Paolo FM, Pisicchio C, Squeo MR, et al. Patterns of left ventricular longitudinal strain and strain rate in Olympic athletes. Journal of the American Society of Echocardiography : official publication of the American Society of Echocardiography. 2015;28(2):245-53.
107. Simonson JS, Schiller NB. Descent of the base of the left ventricle: an echocardiographic index of left ventricular function. Journal of the American Society of Echocardiography : official publication of the American Society of Echocardiography. 1989;2(1):25-35.
108. Palmieri V, Russo C, Arezzi E, Pezzullo S, Sabatella M, Minichiello S, et al. Relations of longitudinal left ventricular systolic function to left ventricular mass, load, and Doppler stroke volume. European journal of echocardiography : the journal of the Working Group on Echocardiography of the European Society of Cardiology. 2006;7(5):348-55.
109. Lossnitzer D, Steen H, Lehrke S, Korosoglou G, Merten C, Giannitsis E, et al. 1113 MAPSE and TAPSE measured by MRI correlate with left and right ventricular ejection fraction and NTproBNP in patients with in dilated cardiomyopathy. Journal of Cardiovascular Magnetic Resonance. 2008;10(Suppl 1):A238.
110. Matos J, Kronzon I, Panagopoulos G, Perk G. Mitral annular plane systolic excursion as a surrogate for left ventricular ejection fraction. Journal of the American Society of Echocardiography : official publication of the American Society of Echocardiography. 2012;25(9):969-74.
111. Adel W, Roushdy AM, Nabil M. Mitral Annular Plane Systolic Excursion-Derived Ejection Fraction: A Simple and Valid Tool in Adult Males With Left Ventricular Systolic Dysfunction. Echocardiography. 2015;33(2):179-84.
112. Tee M, Noble JA, Bluemke DA. Imaging techniques for cardiac strain and deformation: comparison of echocardiography, cardiac magnetic resonance and cardiac computed tomography. Expert review of cardiovascular therapy. 2013;11:221-31.
113. Andre F, Lossnitzer D, Buss S, Steen H. Reference values of mitral and tricuspid annular plane systolic excursion for the evaluation of left and right ventricular performance. Journal of Cardiovascular Magnetic Resonance. 2012;14(Suppl 1):M3.
114. Mizuguchi Y, Oishi Y, Miyoshi H, Iuchi A, Nagase N, Oki T. The functional role of longitudinal, circumferential, and radial myocardial deformation for regulating the early impairment of left ventricular contraction and relaxation in patients with cardiovascular risk factors: a study with two-dimensional strain imaging. Journal of the American Society of Echocardiography : official publication of the American Society of Echocardiography. 2008;21(10):1138-44.
115. Sun YJ, Wang F, Zhang RS, Wang HY, Yang CG, Cai J, et al. Incremental value of resting three-dimensional speckle-tracking echocardiography in detecting coronary artery disease. Experimental and therapeutic medicine. 2015;9(6):2043-6.
116. Fei HW, Ali MT, Tan TC, Cheng KH, Salama L, Hua L, et al. Left Ventricular Global Longitudinal Strain in HER-2 + Breast Cancer Patients Treated with Anthracyclines and Trastuzumab Who Develop Cardiotoxicity Is Associated with Subsequent Recovery of Left Ventricular Ejection Fraction. Echocardiography. 2016;33(4):519-26.
117. Muraru D, Cucchini U, Mihaila S, Miglioranza MH, Aruta P, Cavalli G, et al. Left ventricular myocardial strain by three-dimensional speckle-tracking echocardiography in healthy subjects: reference values and analysis of their physiologic and technical determinants. Journal of the American Society of Echocardiography : official publication of the American Society of Echocardiography. 2014;27(8):858-71 e1.

118. Kaku K, Takeuchi M, Tsang W, Takigiku K, Yasukochi S, Patel AR, et al. Age-related normal range of left ventricular strain and torsion using three-dimensional speckle-tracking echocardiography. Journal of the American Society of Echocardiography : official publication of the American Society of Echocardiography. 2014;27(1):55-64.
119. Cheng A, Nguyen TC, Malinowski M, Daughters GT, Miller DC, Ingels NB, Jr. Heterogeneity of left ventricular wall thickening mechanisms. Circulation. 2008;118(7):713-21.
120. Rademakers FE, Rogers WJ, Guier WH, Hutchins GM, Siu CO, Weisfeldt ML, et al. Relation of regional cross-fiber shortening to wall thickening in the intact heart. Three-dimensional strain analysis by NMR tagging. Circulation. 1994;89(3):1174-82.
121. Kaseno H, Toyama T, Okaniwa H, Toide H, Yamashita E, Kawaguchi R, et al. Diastolic Stunning as a Marker of Severe Coronary Artery Stenosis: Analysis by Speckle Tracking Radial Strain in the Resting Echocardiogram. Echocardiography. 2015;33(1):30-7.
122. Enomoto M, Ishizu T, Seo Y, Yamamoto M, Suzuki H, Shimano H, et al. Subendocardial Systolic Dysfunction in Asymptomatic Normotensive Diabetic Patients. Circulation journal : official journal of the Japanese Circulation Society. 2015;79(8):1749-55.
123. Cong J, Fan T, Yang X, Shen J, Cheng G, Zhang Z. Maternal cardiac remodeling and dysfunction in preeclampsia: a three-dimensional speckle-tracking echocardiography study. The international journal of cardiovascular imaging. 2015;31(7):1361-8.
124. Notomi Y, Setser RM, Shiota T, Martin-Miklovic MG, Weaver JA, Popovic ZB, et al. Assessment of left ventricular torsional deformation by Doppler tissue imaging: validation study with tagged magnetic resonance imaging. Circulation. 2005;111(9):1141-7.
125. Ingels NB, Daughters GT, Stinson EB, Alderman EL. Measurement of midwall myocardial dynamics in intact man by radiography of surgically implanted markers. Circulation. 1975;52:859-67.
126. Notomi Y, Lysyansky P, Setser RM, Shiota T, Popovic ZB, Martin-Miklovic MG, et al. Measurement of ventricular torsion by two-dimensional ultrasound speckle tracking imaging. Journal of the American College of Cardiology. 2005;45(12):2034-41.
127. Young AA. Ventricular torsion: an aid to ejection? JACC Cardiovascular imaging. 2012;5(3):282-4.
128. Young AA, Cowan BR. Evaluation of left ventricular torsion by cardiovascular magnetic resonance. Journal of cardiovascular magnetic resonance : official journal of the Society for Cardiovascular Magnetic Resonance. 2012;14:49.
129. Lumens J, Delhaas T, Arts T, Cowan BR, Young AA. Impaired subendocardial contractile myofiber function in asymptomatic aged humans, as detected using MRI. American journal of physiology Heart and circulatory physiology. 2006;291(4):H1573-9.
130. Kanzaki H, Nakatani S, Yamada N, Urayama S, Miyatake K, Kitakaze M. Impaired systolic torsion in dilated cardiomyopathy: reversal of apical rotation at mid-systole characterized with magnetic resonance tagging method. Basic research in cardiology. 2006;101(6):465-70.
131. Bertini M, Delgado V, Nucifora G, Ajmone Marsan N, Ng AC, Shanks M, et al. Left ventricular rotational mechanics in patients with coronary artery disease: differences in subendocardial and subepicardial layers. Heart. 2010;96(21):1737-43.

132. Young AA, Kramer CM, Ferrari VA, Axel L, Reichek N. Three-dimensional left ventricular deformation in hypertrophic cardiomyopathy. Circulation. 1994;90(2):854-67.
133. Arts T, Veenstra PC, Reneman RS. Epicardial deformation and left ventricular wall mechanisms during ejection in the dog. The American journal of physiology. 1982;243(3):H379-90.
134. Arts T, Bovendeerd PHM, Prinzen FW, Reneman RS. Relation between left ventricular cavity pressure and volume and systolic fibre stress and strain in the wall. Biophysical journal. 1991;59:93-102.
135. Gleason WL, Braunwald E. Studies on Starling's law of the heart. VI. Relationships between left ventricular enddiatolic volume and stroke volume in man with observations on the mechanism of pulsus alternans. Circulation. 1962;25:841-8.
136. Schwinger RHG, Böhm M, Koch A, Schmidt U, Morano I, Eissner HJ, et al. The failing human heart is unable to use the Frank-Starling mechanism. . Circulation Research. 1994;74:959-69.
137. Parra DA, Vera K. New imaging modalities to assess cardiac function: not just pretty pictures. Current opinion in pediatrics. 2012;24(5):557-64.
138. He T. Cardiovascular magnetic resonance T2* for tissue iron assessment in the heart. Quantitative imaging in medicine and surgery. 2014;4(5):407-12.
139. Treibel TA, White SK, Moon JC. Myocardial Tissue Characterization: Histological and Pathophysiological Correlation. Current cardiovascular imaging reports. 2014;7(3):9254.
140. Kramer CM, Barkhausen J, Flamm SD, Kim RJ, Nagel E. Standardized cardiovascular magnetic resonance (CMR) protocols 2013 update. Journal of cardiovascular magnetic resonance : official journal of the Society for Cardiovascular Magnetic Resonance. 2013;15:91.
141. Garrido L, Wedeen VJ, Kwong KK, Spencer UM, Kantor HL. Anisotropy of water diffusion in the myocardium of the rat. Circ Res. 1994;74(5):789-93.
142. Hsu EW, Muzikant AL, Matulevicius SA, Penland RC, Henriquez CS. Magnetic resonance myocardial fiber-orientation mapping with direct histological correlation. The American journal of physiology. 1998;274(5 Pt 2):H1627-34.
143. Holmes AA, Scollan DF, Winslow RL. Direct histological validation of diffusion tensor MRI in formaldehyde-fixed myocardium. Magnetic resonance in medicine : official journal of the Society of Magnetic Resonance in Medicine / Society of Magnetic Resonance in Medicine. 2000;44(1):157-61.
144. Scollan DF, Holmes A, Winslow R, Forder J. Histological validation of myocardial microstructure obtained from diffusion tensor magnetic resonance imaging. The American journal of physiology. 1998;275(6 Pt 2):H2308-18.
145. Tseng WY, Wedeen VJ, Reese TG, Smith RN, Halpern EF. Diffusion tensor MRI of myocardial fibers and sheets: correspondence with visible cut-face texture. Journal of magnetic resonance imaging : JMRI. 2003;17(1):31-42.
146. Sosnovik DE, Wang R, Dai G, Reese TG, Wedeen VJ. Diffusion MR tractography of the heart. Journal of cardiovascular magnetic resonance : official journal of the Society for Cardiovascular Magnetic Resonance. 2009;11:47.
147. Lombaert H, Peyrat JM, Croisille P, Rapacchi S, Fanton L, Cheriet F, et al. Human atlas of the cardiac fiber architecture: study on a healthy population. IEEE transactions on medical imaging. 2012;31(7):1436-47.

148. Poveda F, Gil D, Marti E, Andaluz A, Ballester M, Carreras F. Helical structure of the cardiac ventricular anatomy assessed by diffusion tensor magnetic resonance imaging with multiresolution tractography. Rev Esp Cardiol (Engl Ed). 2013;66(10):782-90.
149. Toussaint N, Stoeck CT, Schaeffter T, Kozerke S, Sermesant M, Batchelor PG. In vivo human cardiac fibre architecture estimation using shape-based diffusion tensor processing. Medical image analysis. 2013;17(8):1243-55.
150. Stoeck CT, Kalinowska A, von Deuster C, Harmer J, Chan RW, Niemann M, et al. Dual-phase cardiac diffusion tensor imaging with strain correction. PloS one. 2014;9(9):e107159.
151. Dou J, Reese TG, Tseng WY, Wedeen VJ. Cardiac diffusion MRI without motion effects. Magnetic resonance in medicine : official journal of the Society of Magnetic Resonance in Medicine / Society of Magnetic Resonance in Medicine. 2002;48(1):105-14.
152. Benson AP, Bernus O, Dierckx H, Gilbert SH, Greenwood JP, Holden AV, et al. Construction and validation of anisotropic and orthotropic ventricular geometries for quantitative predictive cardiac electrophysiology. Interface focus. 2011;1(1):101-16.
153. Helm PA, Tseng HJ, Younes L, McVeigh ER, Winslow RL. Ex vivo 3D diffusion tensor imaging and quantification of cardiac laminar structure. Magnetic resonance in medicine : official journal of the Society of Magnetic Resonance in Medicine / Society of Magnetic Resonance in Medicine. 2005;54(4):850-9.
154. Gilbert SH, Benoist D, Benson AP, White E, Tanner SF, Holden AV, et al. Visualization and quantification of whole rat heart laminar structure using high-spatial resolution contrast-enhanced MRI. American journal of physiology Heart and circulatory physiology. 2012;302(1):H287-98.
155. Mekkaoui C, Nielles-Vallespin S, Gatehouse PD, Jackowski MP, Firmin DN, Sosnovik DE. Diffusion MRI tractography of the human heart In Vivo at end-diastole and end-systole. Journal of Cardiovascular Magnetic Resonance. 2012;14(Suppl 1):O49.
156. Nielsen PM, Le Grice IJ, Smaill BH, Hunter PJ. Mathematical model of geometry and fibrous structure of the heart. The American journal of physiology. 1991;260(4 Pt 2):H1365-78.
157. Maron BJ, Gardin JM, Flack JM, Gidding SS, Kurosaki TT, Bild DE. Prevalence of hypertrophic cardiomyopathy in a general population of young adults. Echocardiographic analysis of 4111 subjects in the CARDIA Study. Coronary Artery Risk Development in (Young) Adults. Circulation. 1995;92(4):785-9.
158. Lopes LR, Rahman MS, Elliott PM. A systematic review and meta-analysis of genotype-phenotype associations in patients with hypertrophic cardiomyopathy caused by sarcomeric protein mutations. Heart. 2013;99(24):1800-11.
159. Maron BJ, Maron MS. Hypertrophic cardiomyopathy. The Lancet. 2013;381(9862):242-55.
160. Lopes LR, Zekavati A, Syrris P, Hubank M, Giambartolomei C, Dalageorgou C, et al. Genetic complexity in hypertrophic cardiomyopathy revealed by high-throughput sequencing. Journal of medical genetics. 2013;50(4):228-39.
161. Ho CY. Genetics and clinical destiny: improving care in hypertrophic cardiomyopathy. Circulation. 2010;122(23):2430-40; discussion 40.
162. Burch M, Mann JM, Sharland M, Shinebourne EA, Patton MA, McKenna WJ. Myocardial disarray in Noonan syndrome. Br Heart J. 1992;68(6):586-8.
163. Morita H, Larson MG, Barr SC, Vasan RS, O'Donnell CJ, Hirschhorn JN, et al. Single-gene mutations and increased left ventricular wall thickness in the community: the Framingham Heart Study. Circulation. 2006;113(23):2697-705.

164. Page SP, Kounas S, Syrris P, Christiansen M, Frank-Hansen R, Andersen PS, et al. Cardiac myosin binding protein-C mutations in families with hypertrophic cardiomyopathy: disease expression in relation to age, gender, and long term outcome. Circulation Cardiovascular genetics. 2012;5(2):156-66.
165. Maron BJ, Yeates L, Semsarian C. Clinical challenges of genotype positive (+)-phenotype negative (-) family members in hypertrophic cardiomyopathy. The American journal of cardiology. 2011;107(4):604-8.
166. Landstrom AP, Ackerman MJ. Mutation type is not clinically useful in predicting prognosis in hypertrophic cardiomyopathy. Circulation. 2010;122(23):2441-9; discussion 50.
167. Klues HG, Schiffers A, Maron BJ. Phenotypic spectrum and patterns of left ventricular hypertrophy in hypertrophic cardiomyopathy: morphologic observations and significance as assessed by two-dimensional echocardiography in 600 patients. Journal of the American College of Cardiology. 1995;26(7):1699-708.
168. Hughes SE. The pathology of hypertrophic cardiomyopathy. Histopathology. 2004;44:412-27.
169. Captur G, Lopes LR, Patel V, Li C, Bassett P, Syrris P, et al. Abnormal cardiac formation in hypertrophic cardiomyopathy: fractal analysis of trabeculae and preclinical gene expression. Circulation Cardiovascular genetics. 2014;7(3):241-8.
170. Maron MS, Olivotto I, Harrigan C, Appelbaum E, Gibson CM, Lesser JR, et al. Mitral valve abnormalities identified by cardiovascular magnetic resonance represent a primary phenotypic expression of hypertrophic cardiomyopathy. Circulation. 2011;124(1):40-7.
171. Maron MS, Olivotto I, Zenovich AG, Link MS, Pandian NG, Kuvin JT, et al. Hypertrophic cardiomyopathy is predominantly a disease of left ventricular outflow tract obstruction. Circulation. 2006;114(21):2232-9.
172. Shah JS, Esteban MT, Thaman R, Sharma R, Mist B, Pantazis A, et al. Prevalence of exercise-induced left ventricular outflow tract obstruction in symptomatic patients with non-obstructive hypertrophic cardiomyopathy. Heart. 2008;94(10):1288-94.
173. Rowin EJ, Maron MS. Evidence for Left Ventricular Outflow Tract Obstruction With Minimal Septal Hypertrophy: The Case Grows Stronger for a Multimodality Imaging Strategy for Hypertrophic Cardiomyopathy. Circulation Cardiovascular imaging. 2015;8(7):e003588.
174. Patel P, Dhillon A, Popovic ZB, Smedira NG, Rizzo J, Thamilarasan M, et al. Left Ventricular Outflow Tract Obstruction in Hypertrophic Cardiomyopathy Patients Without Severe Septal Hypertrophy: Implications of Mitral Valve and Papillary Muscle Abnormalities Assessed Using Cardiac Magnetic Resonance and Echocardiography. Circulation Cardiovascular imaging. 2015;8(7):e003132.
175. Critoph CH, Pantazis A, Tome Esteban MT, Salazar-Mendiguchia J, Pagourelias ED, Moon JC, et al. The influence of aortoseptal angulation on provocable left ventricular outflow tract obstruction in hypertrophic cardiomyopathy. Open heart. 2014;1(1):e000176.
176. Elliott P, McKenna WJ. Hypertrophic cardiomyopathy. Lancet. 2004;363(9424):1881-91.
177. Moon JC, McKenna WJ, McCrohon JA, Elliott PM, Smith GC, Pennell DJ. Toward clinical risk assessment in hypertrophic cardiomyopathy with gadolinium cardiovascular magnetic resonance. Journal of the American College of Cardiology. 2003;41(9):1561-7.

178. Moon JC, Reed E, Sheppard MN, Elkington AG, Ho SY, Burke M, et al. The histologic basis of late gadolinium enhancement cardiovascular magnetic resonance in hypertrophic cardiomyopathy. Journal of the American College of Cardiology. 2004;43(12):2260-4.
179. Iles LM, Ellims AH, Llewellyn H, Hare JL, Kaye DM, McLean CA, et al. Histological validation of cardiac magnetic resonance analysis of regional and diffuse interstitial myocardial fibrosis. European heart journal cardiovascular Imaging. 2015;16(1):14-22.
180. Rudolph A, Abdel-Aty H, Bohl S, Boye P, Zagrosek A, Dietz R, et al. Noninvasive detection of fibrosis applying contrast-enhanced cardiac magnetic resonance in different forms of left ventricular hypertrophy relation to remodeling. Journal of the American College of Cardiology. 2009;53(3):284-91.
181. Mahrholdt H, Wagner A, Judd RM, Sechtem U, Kim RJ. Delayed enhancement cardiovascular magnetic resonance assessment of non-ischaemic cardiomyopathies. European heart journal. 2005;26(15):1461-74.
182. Gulati A, Jabbour A, Ismail TF, Guha K, Khwaja J, Raza S, et al. Association of fibrosis with mortality and sudden cardiac death in patients with nonischemic dilated cardiomyopathy. Jama. 2013;309(9):896-908.
183. O'Hanlon R, Grasso A, Roughton M, Moon JC, Clark S, Wage R, et al. Prognostic significance of myocardial fibrosis in hypertrophic cardiomyopathy. Journal of the American College of Cardiology. 2010;56(11):867-74.
184. Ismail TF, Jabbour A, Gulati A, Mallorie A, Raza S, Cowling TE, et al. Role of late gadolinium enhancement cardiovascular magnetic resonance in the risk stratification of hypertrophic cardiomyopathy. Heart. 2014;100(23):1851-8.
185. Green JJ, Berger JS, Kramer CM, Salerno M. Prognostic value of late gadolinium enhancement in clinical outcomes for hypertrophic cardiomyopathy. JACC Cardiovascular imaging. 2012;5(4):370-7.
186. Chan RH, Maron BJ, Olivotto I, Pencina MJ, Assenza GE, Haas T, et al. Prognostic value of quantitative contrast-enhanced cardiovascular magnetic resonance for the evaluation of sudden death risk in patients with hypertrophic cardiomyopathy. Circulation. 2014;130(6):484-95.
187. Chan RH, Maron BJ, Olivotto I, Assenza GE, Haas TS, Lesser JR, et al. Significance of Late Gadolinium Enhancement at Right Ventricular Attachment to Ventricular Septum in Patients With Hypertrophic Cardiomyopathy. The American journal of cardiology. 2015;116(3):436-41.
188. Teare D. Asymmetrical hypertrophy of the heart in young adults. Br Heart J. 1958;20:1-8.
189. St John Sutton MG, Anderson KR, O'Brien PC, Frye RL. Histopahtological specificity of hypertrophic obstructive cardiomyopathy. Br Heart J. 1980;44:433-43.
190. Maron BJ, Sato N, Roberts WC, Edwards JE, Chandra RS. Quantitative analysis of cardiac muscle cell disorganization in the ventricular septum. Comparison of fetuses and infants with and without congenital heart disease and patients with hypertrophic cardiomyopathy. Circulation. 1979;60(3):685-96.
191. Wigle ED, Silver MD. Myocardial fiber disarray and ventricular septal hypertrophy in asymmetrical hypertrophy of the heart. Circulation. 1978;58(3 Pt 1):398-402.
192. Bulkley BH, Weisfeldt ML, Hutchins GM. Asymmetric septal hypertrophy and myocardial fiber disarray. Circulation. 1977;56:292-8.
193. Becker AE, Caruso G. Myocardial disarray. A critical review. Br Heart J. 1982;47:527-38.

194. Maron BJ, Roberts WC. Quantitative analysis of cardiac muscle cell disorganization in the ventricular septum of patients with hypertrophic cardiomyopathy. Circulation. 1979;59(4):689-706.
195. Maron BJ, Epstein SE. Recent observations regarding the specificity of three hallmarks of the disease: asymmetric septal hypertrophy, septal disorganisation and systolic anterior motion of the anterior mitral leaflet. The American journal of cardiology. 1980;45:141-54.
196. Varnava AM, Elliott PM, Sharma S, McKenna WJ, Davies MJ. Hypertrophic cardiomyopathy: the interrelation of disarray, fibrosis, and small vessel disease. Heart. 2000;84(5):476-82.
197. van der Bel-Kahn J. Muscle fiber disarray in common heart diseases. The American journal of cardiology. 1977;40(3):355-64.
198. Anderson KR, Sutton MGS, Lie JT. Histopathological types of cardiac fibrosis in myocardial diseases. The Journal of pathology. 1979;128:79-85.
199. Tanaka M, Fujiwara H, Onodera T, Wu DJ, Matsuda M, Hamashima Y, et al. Pathogenetic role of myocardial fiber disarray in the progression of cardiac fibrosis in normal hearts, hypertensive hearts and hearts with hypertrophic cardiomyopathy. Japanese circulation journal. 1987;51(6):624-30.
200. Fujiwara H, Kawai C, Hamashima Y. Myocardial fascicle and fiber disarray in 25 mu-thick sections. Circulation. 1979;59(6):1293-8.
201. Jones M, Ferrans VJ, Morrow AG, Roberts WC. Ultrastructure of crista supraventricularis muscle in patients with congenital heart diseases associated with right ventricular outflow tract obstruction. Circulation. 1975;51(1):39-67.
202. Ross AA, Streeter DD, Jr. Myocardial fiber disarray. Circulation. 1979;60(6):1425-6.
203. Hoshino T, Fujiwara H, Kawai C, Hamashima Y. Myocardial fiber diameter and regional distribution in the ventricular wall of normal adult hearts, hypertensive hearts and hearts with hypertrophic cardiomyopathy. Circulation. 1983;67(5):1109-16.
204. Tanaka M, Fujiwara H, Onodera T, Wu DJ, Hamashima Y, Kawai C. Quantitative analysis of myocardial fibrosis in normals, hypertensive hearts, and hypertrophic cardiomyopathy. Br Heart J. 1986;55:575-81.
205. Varnava AM, Elliott PM, Mahon N, Davies MJ, McKenna WJ. Relation between myocyte disarray and outcome in hypertrophic cardiomyopathy. The American journal of cardiology. 2001;88(3):275-9.
206. Varnava AM, Elliott PM, Baboonian C, Davison F, Davies MJ, McKenna WJ. Hypertrophic cardiomyopathy: histopathological features of sudden death in cardiac troponin T disease. Circulation. 2001;104(12):1380-4.
207. McKenna WJ, Stewart JT, Nihoyannopoulos P, McGinty F, Davies MJ. Hypertrophic cardiomyopathy without hypertrophy: two families with myocardial disarray in the absence of increased myocardial mass. Br Heart J. 1990;63(5):287-90.
208. Unverferth DV, Baker PB, Pearce LI, Lautman J, Roberts WC. Regional myocyte hypertrophy and increased interstitial myocardial fibrosis in hypertrophic cardiomyopathy. The American journal of cardiology. 1987;59(9):932-6.
209. Maron BJ, Ferrans VJ, Henry WL, Clark CE, Redwood DR, Roberts WC, et al. Differences in distribution of myocardial abnormalities in patients with obstructive and nonobstructive asymmetric septal hypertrophy (ASH). Light and electron microscopic findings. Circulation. 1974;50(3):436-46.

210. Maron BJ, Wolfson JK, Epstein SE, Roberts WC. Intramural ("small vessel") coronary artery disease in hypertrophic cardiomyopathy. Journal of the American College of Cardiology. 1986;8(3):545-57.
211. Takemura G, Takatsu Y, Fujiwara H. Luminal narrowing of coronary capillaries in human hypertrophic hearts: an ultrastructural morphometrical study using endomyocardial biopsy specimens. Heart. 1998;79(1):78-85.
212. Chiribiri A, Leuzzi S, Conte MR, Bongioanni S, Bratis K, Olivotti L, et al. Rest perfusion abnormalities in hypertrophic cardiomyopathy: correlation with myocardial fibrosis and risk factors for sudden cardiac death. Clinical radiology. 2015;70(5):495-501.
213. Shirani J, Pick R, Roberts WC, Maron BJ. Morphology and significance of the left ventricular collagen network in young patients with hypertrophic cardiomyopathy and sudden cardiac death. Journal of the American College of Cardiology. 2000;35(1):36-44.
214. Dass S, Suttie JJ, Piechnik SK, Ferreira VM, Holloway CJ, Banerjee R, et al. Myocardial tissue characterization using magnetic resonance noncontrast t1 mapping in hypertrophic and dilated cardiomyopathy. Circulation Cardiovascular imaging. 2012;5(6):726-33.
215. Flett AS, Hayward MP, Ashworth MT, Hansen MS, Taylor AM, Elliott PM, et al. Equilibrium contrast cardiovascular magnetic resonance for the measurement of diffuse myocardial fibrosis: preliminary validation in humans. Circulation. 2010;122(2):138-44.
216. Ho CY, Abbasi SA, Neilan TG, Shah RV, Chen Y, Heydari B, et al. T1 measurements identify extracellular volume expansion in hypertrophic cardiomyopathy sarcomere mutation carriers with and without left ventricular hypertrophy. Circulation Cardiovascular imaging. 2013;6(3):415-22.
217. Watkins H, Seidman CE, Seidman JG, Feng HS, Sweeney HL. Expression and functional assessment of a truncated cardiac troponin T that causes hypertrophic cardiomyopathy. Evidence for a dominant negative action. The Journal of clinical investigation. 1996;98(11):2456-61.
218. Lankford EB, Epstein ND, Fananapazir L, Sweeney HL. Abnormal contractile properties of muscle fibers expressing beta-myosin heavy chain gene mutations in patients with hypertrophic cardiomyopathy. The Journal of clinical investigation. 1995;95(3):1409-14.
219. Marian AJ, Zhao G, Seta Y, Roberts R, Yu QT. Expression of a mutant (Arg92Gln) human cardiac troponin T, known to cause hypertrophic cardiomyopathy, impairs adult cardiac myocyte contractility. Circ Res. 1997;81(1):76-85.
220. Marian AJ. Pathogenesis of diverse clinical and pathological phenotypes in hypertrophic cardiomyopathy. The Lancet. 2000;355(9197):58-60.
221. Sorajja P, Elliott PM, McKenna WJ. The molecular genetics of hypertrophic cardiomyopathy: prognostic implications. Europace : European pacing, arrhythmias, and cardiac electrophysiology : journal of the working groups on cardiac pacing, arrhythmias, and cardiac cellular electrophysiology of the European Society of Cardiology. 2000;2(1):4-14.
222. Gomes AV, Harada K, Potter JD. A mutation in the N-terminus of troponin I that is associated with hypertrophic cardiomyopathy affects the Ca(2+)-sensitivity, phosphorylation kinetics and proteolytic susceptibility of troponin. Journal of molecular and cellular cardiology. 2005;39(5):754-65.

223. Pinto JR, Parvatiyar MS, Jones MA, Liang J, Ackerman MJ, Potter JD. A functional and structural study of troponin C mutations related to hypertrophic cardiomyopathy. The Journal of biological chemistry. 2009;284(28):19090-100.
224. Belus A, Piroddi N, Scellini B, Tesi C, D'Amati G, Girolami F, et al. The familial hypertrophic cardiomyopathy-associated myosin mutation R403Q accelerates tension generation and relaxation of human cardiac myofibrils. The Journal of physiology. 2008;586(Pt 15):3639-44.
225. Young AA, Kramer CM, Ferrari VA, Axel L, Reichek N. Three-Dimensional Left Ventricular Deformation in Hypertrophic Cardiomyopathy. Circulation. 1994;90:854-67.
226. Afonso L, Kondur A, Simegn M, Niraj A, Hari P, Kaur R, et al. Two-dimensional strain profiles in patients with physiological and pathological hypertrophy and preserved left ventricular systolic function: a comparative analyses. BMJ open. 2012;2(4).
227. Urbano-Moral JA, Rowin EJ, Maron MS, Crean A, Pandian NG. Investigation of global and regional myocardial mechanics with 3-dimensional speckle tracking echocardiography and relations to hypertrophy and fibrosis in hypertrophic cardiomyopathy. Circulation Cardiovascular imaging. 2014;7(1):11-9.
228. Pacileo G, Baldini L, Limongelli G, Di Salvo G, Iacomino M, Capogrosso C, et al. Prolonged left ventricular twist in cardiomyopathies: a potential link between systolic and diastolic dysfunction. European journal of echocardiography : the journal of the Working Group on Echocardiography of the European Society of Cardiology. 2011;12(11):841-9.
229. Smith BM, Dorfman AL, Yu S, Russell MW, Agarwal PP, Ghadimi Mahani M, et al. Relation of strain by feature tracking and clinical outcome in children, adolescents, and young adults with hypertrophic cardiomyopathy. The American journal of cardiology. 2014;114(8):1275-80.
230. Yang H, Carasso S, Woo A, Jamorski M, Nikonova A, Wigle ED, et al. Hypertrophy pattern and regional myocardial mechanics are related in septal and apical hypertrophic cardiomyopathy. Journal of the American Society of Echocardiography : official publication of the American Society of Echocardiography. 2010;23(10):1081-9.
231. Kramer CM, Reichek N, Ferrari VA, Theobald T, Dawson J, Axel L. Regional heterogeneity of function in hypertrophic cardiomyopathy. Circulation. 1994;90(1):186-94.
232. Dong SJ, MacGregor JH, Crawley AP, McVeigh E, Belenkie I, Smith ER, et al. Left ventricular wall thickness and regional systolic function in patients with hypertrophic cardiomyopathy. A three-dimensional tagged magnetic resonance imaging study. Circulation. 1994;90(3):1200-9.
233. Beache GM, Wedeen VJ, Weisskoff RM, O'Gara PT, Poncelet BP, Chesler DA, et al. Intramural mechanics in hypertrophic cardiomyopathy: functional mapping with strain-rate MR imaging. Radiology. 1995;197(1):117-24.
234. Aletras AH, Tilak GS, Hsu LY, Arai AE. Heterogeneity of intramural function in hypertrophic cardiomyopathy: mechanistic insights from MRI late gadolinium enhancement and high-resolution displacement encoding with stimulated echoes strain maps. Circulation Cardiovascular imaging. 2011;4(4):425-34.
235. Brouwer WP, Baars EN, Germans T, de Boer K, Beek AM, van der Velden J, et al. In-vivo T1 cardiovascular magnetic resonance study of diffuse myocardial fibrosis in hypertrophic cardiomyopathy. Journal of cardiovascular magnetic resonance : official journal of the Society for Cardiovascular Magnetic Resonance. 2014;26:28.

236. Geske JB, Bos JM, Gersh BJ, Ommen SR, Eidem BW, Ackerman MJ. Deformation patterns in genotyped patients with hypertrophic cardiomyopathy. European heart journal cardiovascular Imaging. 2014;15(4):456-65.
237. Germans T, Russel IK, Gotte MJ, Spreeuwenberg MD, Doevendans PA, Pinto YM, et al. How do hypertrophic cardiomyopathy mutations affect myocardial function in carriers with normal wall thickness? Assessment with cardiovascular magnetic resonance. Journal of cardiovascular magnetic resonance : official journal of the Society for Cardiovascular Magnetic Resonance. 2010;12:13.
238. Matsumura Y, Elliott PM, Virdee MS, Sorajja P, Doi Y, McKenna WJ. Left ventricular diastolic function assessed using Doppler tissue imaging in patients with hypertrophic cardiomyopathy: relation to symptoms and exercise capacity. Heart. 2002;87(3):247-51.
239. Wigle ED, Rakowski H, Kimball BP, Williams WG. Hypertrophic cardiomyopathy. Clinical spectrum and treatment. Circulation. 1995;92(7):1680-92.
240. Brutsaert DL, Sys SU, Gillebert TC. Diastolic failure: Pathophysiology and Therpeutic Implications. Journal of the American College of Cardiology. 1993;22:318-25.
241. Nagueh SF, Bachinshki LL, Meyer D, Hill R, Zoghni WA, Tam JW, et al. Tissue doppler imaging consistently detects myocardial abnormalities in patients with hypertrophic cardiomyopathy and provides a novel means for an early diagnosis before independently of hypertrophy. Circulation. 2001;104:128-30.
242. Ho CY, Sweitzer NK, McDonough B, Maron BJ, Casey SA, Seidman JG, et al. Assessment of diastolic function with Doppler tissue imaging to predict genotype in preclinical hypertrophic cardiomyopathy. Circulation. 2002;105(25):2992-7.
243. Kobayashi T, Dhillon A, Popovic Z, Bhonsale A, Smedira NG, Thamilarasan M, et al. Differences in global and regional left ventricular myocardial mechanics in various morphologic subtypes of patients with obstructive hypertrophic cardiomyopathy referred for ventricular septal myotomy/myectomy. The American journal of cardiology. 2014;113(11):1879-85.
244. Kim EK, Lee SC, Hwang JW, Chang SA, Park SJ, On YK, et al. Differences in apical and non-apical types of hypertrophic cardiomyopathy: a prospective analysis of clinical, echocardiographic, and cardiac magnetic resonance findings and outcome from 350 patients. European heart journal cardiovascular Imaging. 2015;17(6):678-86.
245. Finocchiaro G, Haddad F, Pavlovic A, Magavern E, Sinagra G, Knowles JW, et al. How does morphology impact on diastolic function in hypertrophic cardiomyopathy? A single centre experience. BMJ open. 2014;4(6):e004814.
246. Biagini E, Spirito P, Rocchi G, Ferlito M, Rosmini S, Lai F, et al. Prognostic implications of the Doppler restrictive filling pattern in hypertrophic cardiomyopathy. The American journal of cardiology. 2009;104(12):1727-31.
247. Kitaoka H, Kubo T, Okawa M, Takenaka N, Sakamoto C, Baba Y, et al. Tissue doppler imaging and plasma BNP levels to assess the prognosis in patients with hypertrophic cardiomyopathy. Journal of the American Society of Echocardiography : official publication of the American Society of Echocardiography. 2011;24(9):1020-5.
248. Xin B, Puffenberger E, Tumbush J, Bockoven JR, Wang H. Homozygosity for a novel splice site mutation in the cardiac myosin-binding protein C gene causes severe neonatal hypertrophic cardiomyopathy. American journal of medical genetics Part A. 2007;143A(22):2662-7.
249. Zahka K, Kalidas K, Simpson MA, Cross H, Keller BB, Galambos C, et al. Homozygous mutation of MYBPC3 associated with severe infantile hypertrophic cardiomyopathy at high frequency among the Amish. Heart. 2008;94(10):1326-30.

250. Maron BJ, Spirito P, Wesley Y, Arce J. Development and progression of left ventricular hypertrophy in children with hypertrophic cardiomyopathy. The New England journal of medicine. 1986;315(10):610-4.
251. Spirito P, Maron BJ. Relation between extent of left ventricular hypertrophy and age in hypertrophic cardiomyopathy. Journal of the American College of Cardiology. 1989;4:820-3.
252. Elliott PM, Gimeno JR, Thaman R, Shah J, Ward D, Dickie S, et al. Historical trends in reported survival rates in patients with hypertrophic cardiomyopathy. Heart. 2006;92(6):785-91.
253. Semsarian C, Sweeting J, Ackerman MJ. Sudden cardiac death in athletes. BMJ. 2015;350:h1218.
254. Maron MS, Rowin EJ, Casey S, Haas TS, Appelbaum E, Garberich R, et al. Risk Stratification and Outcome of Patients with Hypertrophic Cardiomyopathy Over 60 Years of Age: Does Age Count? Circulation. 2011;124((21 suppl)):14156 (abstr).
255. Maron BJ, Shen WK, Link MS, Epstein AE, Almquist AK, Daubert JP, et al. Efficiacy of implantable cardioverter-defibrillators for the prevention of sudden death in patients with hypertrophic cardiomyopathy. The New England journal of medicine. 2000;342:365-73.
256. Elliott PM, Poloniecki J, Dickie S, Sharma S, Monserrat L, Varnava A, et al. Sudden death in hypertrophic cardiomyopathy: identification of high risk patients. Journal of the American College of Cardiology. 2000;36(7):2212-8.
257. O'Mahony C, Elliott P, McKenna W. Sudden cardiac death in hypertrophic cardiomyopathy. Circulation Arrhythmia and electrophysiology. 2013;6(2):443-51.
258. O'Mahony C, Elliott PM. Prevention of sudden cardiac death in hypertrophic cardiomyopathy. Heart. 2014;100(3):254-60.
259. Anan R, Greve G, Thierfelder L, Watkins H, McKenna WJ, Solomon S, et al. Prognostic implications of novel beta cardiac myosin heavy chain gene mutations that cause familial hypertrophic cardiomyopathy. The Journal of clinical investigation. 1994;93(1):280-5.
260. Watkins H, Rosenzweig A, Hwang DS, Levi T, McKenna W, Seidman CE, et al. Characteristics and prognostic implications of myosin missense mutations in familial hypertrophic cardiomyopathy. The New England journal of medicine. 1992;326(17):1108-14.
261. Pasquale F, Syrris P, Kaski JP, Mogensen J, McKenna WJ, Elliott P. Long-term outcomes in hypertrophic cardiomyopathy caused by mutations in the cardiac troponin T gene. Circulation Cardiovascular genetics. 2012;5(1):10-7.
262. Van Driest SL, Ackerman MJ, Ommen SR, Shakur R, Will ML, Nishimura RA, et al. Prevalence and severity of "benign" mutations in the beta-myosin heavy chain, cardiac troponin T, and alpha-tropomyosin genes in hypertrophic cardiomyopathy. Circulation. 2002;106(24):3085-90.
263. Watkins H, McKenna WJ, Thierfelder L, Suk HJ, Anan R, O'Donoghue A, et al. Mutations in the genes for cardiac troponin T and alpha-tropomyosin in hypertrophic cardiomyopathy. The New England journal of medicine. 1995;332(16):1058-64.
264. Melacini P, Basso C, Angelini A, Calore C, Bobbo F, Tokajuk B, et al. Clinicopathological profiles of progressive heart failure in hypertrophic cardiomyopathy. European heart journal. 2010;31(17):2111-23.

265. Olivotto I, Cecchi F, Casey SA, Dolara A, Traverse JH, Maron BJ. Impact of atrial fibrillation on the clinical course of hypertrophic cardiomyopathy. Circulation. 2001;104(21):2517-24.
266. Guttmann OP, Rahman MS, O'Mahony C, Anastasakis A, Elliott PM. Atrial fibrillation and thromboembolism in patients with hypertrophic cardiomyopathy: systematic review. Heart. 2014;100(6):465-72.
267. Guttmann OP, Pavlou M, O'Mahony C, Monserrat L, Anastasakis A, Rapezzi C, et al. Prediction of thrombo-embolic risk in patients with hypertrophic cardiomyopathy (HCM Risk-CVA). European journal of heart failure. 2015;17(8):837-45.
268. Shapiro LM, Kleinebenne A, McKenna WJ. The distribution of left ventricular hypertrophy in hypertrophic cardiomyopathy: comparison to athletes and hypertensives. European heart journal. 1985;6(11):967-74.
269. McMurray JJ, Adamopoulos S, Anker SD, Auricchio A, Bohm M, Dickstein K, et al. ESC Guidelines for the diagnosis and treatment of acute and chronic heart failure 2012: The Task Force for the Diagnosis and Treatment of Acute and Chronic Heart Failure 2012 of the European Society of Cardiology. Developed in collaboration with the Heart Failure Association (HFA) of the ESC. European heart journal. 2012;33(14):1787-847.
270. Szelenyi Z, Fazakas A, Szenasi G, Tegze N, Fekete B, Molvarec A, et al. The mechanism of reduced longitudinal left ventricular systolic function in hypertensive patients with normal ejection fraction. Journal of hypertension. 2015;33(9):1962-9.
271. Ambale Venkatesh B, Volpe GJ, Donekal S, Mewton N, Liu CY, Shea S, et al. Association of longitudinal changes in left ventricular structure and function with myocardial fibrosis: the Multi-Ethnic Study of Atherosclerosis study. Hypertension. 2014;64(3):508-15.
272. Treibel TA, Zemrak F, Sado DM, Banypersad SM, White SK, Maestrini V, et al. Extracellular volume quantification in isolated hypertension - changes at the detectable limits? Journal of cardiovascular magnetic resonance : official journal of the Society for Cardiovascular Magnetic Resonance. 2015;17(1):74.
273. Chandra N, Papadakis M, Sharma S. Cardiac adaptation in athletes of black ethnicity: differentiating pathology from physiology. Heart. 2012;98(16):1194-200.
274. Baggish AL, Wang F, Weiner RB, Elinoff JM, Tournoux F, Boland A, et al. Training-specific changes in cardiac structure and function: a prospective and longitudinal assessment of competitive athletes. J Appl Physiol (1985). 2008;104(4):1121-8.
275. Rawlins J, Bhan A, Sharma S. Left ventricular hypertrophy in athletes. European journal of echocardiography : the journal of the Working Group on Echocardiography of the European Society of Cardiology. 2009;10(3):350-6.
276. Haykowsky MJ, Tomczak CR. LV hypertrophy in resistance or endurance trained athletes: the Morganroth hypothesis is obselete, most of the time. Heart. 2014;100:1225-6.
277. Pluim BM, Zwinderman AH, van der Laarse A, van der Wall EE. The athlete's heart. A meta-analysis of cardiac structure and function. Circulation. 2000;101(3):336-44.
278. Sharma S, Maron BJ, Whyte G, Firoozi S, Elliott PM, McKenna WJ. Physiologic limits of left ventricular hypertrophy in elite junior athletes: relevance to differential diagnosis of athlete's heart and hypertrophic cardiomyopathy. Journal of the American College of Cardiology. 2002;40(8):1431-6.
279. Scharf M, Brem MH, Wilhelm M, Schoepf UJ, Uder M, Lell MM. Atrial and ventricular functional and structural adaptations of the heart in elite triathletes assessed with cardiac MR imaging. Radiology. 2010;257(1):71-9.

280. George KP, Warburton DE, Oxborough D, Scott JM, Esch BT, Williams K, et al. Upper limits of physiological cardiac adaptation in ultramarathon runners. Journal of the American College of Cardiology. 2011;57(6):754-5.
281. Morganroth J, Maron BJ, Henry WL, Epstein SE. Comparative left ventricular dimensions in trained athletes. Annals of internal medicine. 1975;82(4):521-4.
282. Utomi V, Oxborough D, Ashley E, Lord R, Fletcher S, Stembridge M, et al. Predominance of normal left ventricular geometry in the male 'athlete's heart'. Heart. 2014;100(16):1264-71.
283. Spirito P, Pelliccia A, Proschan A, Granata M, Spataro A, Bellone P, et al. Morphology of the "athlete's heart" assessed by echocardiography in 947 elite athletes representing 27 sports. The American journal of cardiology. 1994;74:802-6.
284. Lalande S, Baldi JC. Left ventricular mass in elite olympic weight lifters. The American journal of cardiology. 2007;100(7):1177-80.
285. Basavarajaiah S, Wilson M, Whyte G, Shah A, McKenna W, Sharma S. Prevalence of hypertrophic cardiomyopathy in highly trained athletes: relevance to pre-participation screening. Journal of the American College of Cardiology. 2008;51(10):1033-9.
286. Galderisi M, Cardim N, D'Andrea A, Bruder O, Cosyns B, Davin L, et al. The multi-modality cardiac imaging approach to the Athlete's heart: an expert consensus of the European Association of Cardiovascular Imaging. European heart journal cardiovascular Imaging. 2015;16(4):353.
287. Wilson M, O'Hanlon R, Prasad S, Deighan A, Macmillan P, Oxborough D, et al. Diverse patterns of myocardial fibrosis in lifelong, veteran endurance athletes. J Appl Physiol (1985). 2011;110(6):1622-6.
288. Vinereanu D, Florescu N, Sculthorpe N, Tweddel AC, Stephens MR, Fraser AG. Differentiation between pathologic and physiologic left ventricular hypertrophy by tissue Doppler assessment of long-axis function in patients with hypertrophic cardiomyopathy or systemic hypertension and in athletes. The American journal of cardiology. 2001;88(1):53-8.
289. Sheikh N, Papadakis M, Schnell F, Panoulas V, Malhotra A, Wilson M, et al. Clinical Profile of Athletes With Hypertrophic Cardiomyopathy. Circulation Cardiovascular imaging. 2015;8(7):e003454.
290. Maron BJ, Shen WK, Link MS, Epstein AE, Almquist AK, Daubert JP, et al. Efficacy of implantable cardioverter-defibrillators for the prevention of sudden death in patients with hypertrophic cardiomyopathy. The New England journal of medicine. 2000;342(6):365-73.
291. Olivotto I, Tomberli B, Spoladore R, Mugelli A, Cecchi F, Camici PG. Hypertrophic cardiomyopathy: The need for randomized trials. Global cardiology science & practice. 2013;2013(3):243-8.
292. Wang TT, Kwon HS, Dai G, Wang R, Mijailovich SM, Moss RL, et al. Resolving myoarchitectural disarray in the mouse ventricular wall with diffusion spectrum magnetic resonance imaging. Annals of biomedical engineering. 2010;38(9):2841-50.
293. Nguyen C, Lu M, Fan Z, Bi X, Kellman P, Zhao S, et al. Contrast-free detection of myocardial fibrosis in hypertrophic cardiomyopathy patients with diffusion-weighted cardiovascular magnetic resonance. Journal of cardiovascular magnetic resonance : official journal of the Society for Cardiovascular Magnetic Resonance. 2015;17(1):107.
294. Tseng WY, Dou J, Reese TG, Wedeen VJ. Imaging myocardial fiber disarray and intramural strain hypokinesis in hypertrophic cardiomyopathy with MRI. Journal of magnetic resonance imaging : JMRI. 2006;23(1):1-8.

295. Antony R, Daghem M, McCann GP, Daghem S, Moon J, Pennell DJ, et al. Cardiovascular magnetic resonance activity in the United Kingdom: a survey on behalf of the British Society of Cardiovascular Magnetic Resonance. Journal of cardiovascular magnetic resonance : official journal of the Society for Cardiovascular Magnetic Resonance. 2011;13:57.
296. Balaban RS, Peters DC. Basic Principles of Cardiovascular Magnetic Resonance. In: Manning WJ, Pennell DJ, editors. Cardiovascular Magnetic Resonance. Second Edition ed. Philadelphia: Saunders; 2010. p. 3-18.
297. Ridgway JP. Cardiovascular magnetic resonance physics for clinicians: part I. Journal of cardiovascular magnetic resonance : official journal of the Society for Cardiovascular Magnetic Resonance. 2010;12:71.
298. Biglands JD, Radjenovic A, Ridgway JP. Cardiovascular magnetic resonance physics for clinicians: Part II. Journal of cardiovascular magnetic resonance : official journal of the Society for Cardiovascular Magnetic Resonance. 2012;14:66.
299. Brown RW, Cheng YCN, Thompson MR, Venkatesan R. Magnetic Resonance Imaging: A Preview. Magnetic resonance imaging. Second Edition ed. Hoboken, New Jersey: John Wiley & Sons, Inc.; 2014. p. 1-12.
300. Gharib AM, Elagha A, Pettigrew RI. Cardiac magnetic resonance at high field: promises and problems. Current problems in diagnostic radiology. 2008;37(2):49-56.
301. Bull S, White SK, Piechnik SK, Flett AS, Ferreira VM, Loudon M, et al. Human non-contrast T1 values and correlation with histology in diffuse fibrosis. Heart. 2013;99(13):932-7.
302. Hamlin SA, Henry TS, Little BP, Lerakis S, Stillman AE. Mapping the future of cardiac MR imaging: case-based review of T1 and T2 mapping techniques. Radiographics : a review publication of the Radiological Society of North America, Inc. 2014;34(6):1594-611.
303. Anderson LJ, Holden S, Davis B, Prescott E, Charrier CC, Bunce NH, et al. Cardiovascular T2-star (T2*) magnetic resonance for the early diagnosis of myocardial iron overload. European heart journal. 2001;22(23):2171-9.
304. Pruessmann KP, Weiger M, Scheidegger MB, Boesiger P. SENSE: sensitivity encoding for fast MRI. Magnetic resonance in medicine : official journal of the Society of Magnetic Resonance in Medicine / Society of Magnetic Resonance in Medicine. 1999;42(5):952-62.
305. Griswold MA, Jakob PM, Heidemann RM, Nittka M, Jellus V, Wang J, et al. Generalized autocalibrating partially parallel acquisitions (GRAPPA). Magnetic resonance in medicine : official journal of the Society of Magnetic Resonance in Medicine / Society of Magnetic Resonance in Medicine. 2002;47(6):1202-10.
306. Merboldt JFKD, Hänicke w, Haase A. Stimulated Echo Imaging. J Magn Reson. 1985;64:81-93.
307. Bammer R, Keeling SL, Augustin M, Pruessmann KP, Wolf R, Stollberger R, et al. Improved diffusion-weighted single-shot echo-planar imaging (EPI) in stroke using sensitivity encoding (SENSE). Magnetic resonance in medicine : official journal of the Society of Magnetic Resonance in Medicine / Society of Magnetic Resonance in Medicine. 2001;46(3):548-54.
308. Axel L, Dougherty L. Heart wall motion: improved method of spatial modulation of magnetization for MR imaging. Radiology. 1989;172(2):349-50.
309. Axel L, Dougherty L. MR imaging of motion with spatial modulation of magnetization. Radiology. 1989;171(3):841-5.

310. Kim JR, Choi KM, Judd RM. Assessment of myocardial viability in contrast enhancement. In: Higgins CB, Roos A, editors. Cardiovascular MRI and MRA. Philadelphia, PA: Lippincott Williams and Wilkins; ; 2003. p. 209-37.
311. Kim RJ, Fieno DS, Parrish TB, Harris K, Chen EL, Simonetti O, et al. Relationship of MRI delayed contrast ehancement to irreversible injury, infarct age, and contractile function. Circulation. 1999;100:1992-2002.
312. Stirrat J, White JA. The prognostic role of late gadolinium enhancement magnetic resonance imaging in patients with cardiomyopathy. The Canadian journal of cardiology. 2013;29(3):329-36.
313. Sado DM, Flett AS, Banypersad SM, White SK, Maestrini V, Quarta G, et al. Cardiovascular magnetic resonance measurement of myocardial extracellular volume in health and disease. Heart. 2012;98(19):1436-41.
314. Oshinski JN, Delfino JG, Sharma P, Gharib AM, Pettigrew RI. Cardiovascular magnetic resonance at 3.0 T: current state of the art. Journal of cardiovascular magnetic resonance : official journal of the Society for Cardiovascular Magnetic Resonance. 2010;12:55.
315. Hays AG, Schär M, Kelle S. Clinical applications for Cardiovascular Magentic Resonance Imaging at 3 Tesla. Curr Cardiol Rev. 2009;5:237-42.
316. Frayne R, Goodyear BG, Dickhoff P, Lauzon ML, Sevick RJ. Magnetic resonance imaging at 3.0 Tesla: challenges and advantages in clinical neurological imaging. Investigative radiology. 2003;38(7):385-402.
317. Kim D, Axel L. Multislice, dual-imaging sequence for increasing the dynamic range of the contrast-enhanced blood signal and CNR of myocardial enhancement at 3T. Journal of magnetic resonance imaging : JMRI. 2006;23(1):81-6.
318. Sosnovik DE, Wang R, Dai G, Wang T, Aikawa E, Novikov M, et al. Diffusion Spectrum MRI Tractography Reveals the Presence of a Complex Network of Residual Myofibers in Infarcted Myocardium. Circulation: Cardiovascular Imaging. 2009;2(3):206-12.
319. Mekkaoui C, Porayette P, Jackowski MP, Kostis WJ, Dai G, Sanders S, et al. Diffusion MRI Tractography of the Developing Human Fetal Heart. PloS one. 2013;8 :e72795.
320. Tyler DJ, Emmanuel Y, Cochlin LE, Hudsmith LE, Holloway CJ, Neubauer S, et al. Reproducibility of 31P cardiac magnetic resonance spectroscopy at 3 T. NMR in biomedicine. 2009;22(4):405-13.
321. Valeti VU, Chun W, Potter DD, Araoz PA, McGee KP, Glockner JF, et al. Myocardial tagging and strain analysis at 3 Tesla: comparison with 1.5 Tesla imaging. Journal of magnetic resonance imaging : JMRI. 2006;23(4):477-80.
322. Nael K, Fenchel MC, Kramer U, Finn JP, Ruehm SG. Whole-body contrast-enhanced magnetic resonance angiography: new advances at 3.0 T. Topics in magnetic resonance imaging : TMRI. 2007;18(2):127-34.
323. Jaffer FA, Wen H, Balaban RS, Wolff SD. A method to improve the B0 homogeneity of the heart in vivo. Magnetic resonance in medicine : official journal of the Society of Magnetic Resonance in Medicine / Society of Magnetic Resonance in Medicine. 1996;36(3):375-83.
324. Scheffler K, Lehnhardt S. Principles and applications of balanced SSFP techniques. European radiology. 2003;13(11):2409-18.

325. Wormleighton J, Parke K, Carlton J, Thraves O, McCann GP. CMR at 3.0T in routine clinical practice - tips and tricks to optimise image quality and enhance patient flow. Journal of Cardiovascular Magnetic Resonance. 2015;17(Suppl 1):T10.
326. Hoult DI, Phil D. Sensitivity and power deposition in a high-field imaging experiment. Journal of magnetic resonance imaging : JMRI. 2000;12(1):46-67.
327. Brown R, Bennett JJ. The miscellaneous botanical works of Robert Brown. London: Pulished for the Ray society by R. Hardwicke; 1866. 630 p.
328. Jonahsen-Berg H, Behrens TEJ. Diffusion MRI From Quantitive Measurement to In vivo Neuroanatomy. Second ed. Waltham, Massachusetts: Academic Press; 2014. 632 p.
329. Le Bihan D, Breton E, Lallemand D, Grenier P, Cabanis E, Laval-Jeantet M. MR Imaging of Intravoxel Incoherent Motions: Application of Diffusion and Perfusion in Neurologic Disorders. Radiology. 1986;161:401-7.
330. James T, McDonald GG. Measurement of the self-diffusion coefficient of each component in a complex system using pulsed-gradient fourier transform NMR. J Magn Reson. 1973;11:58-61.
331. Le Bihan D. Diffusion MRI: what water tells us about the brain. EMBO molecular medicine. 2014;6(5):569-73.
332. Basser PJ. Inferring microstructural features and the physiological state of tissues from diffusion-weighted images. NMR in biomedicine. 1995;8(7-8):333-44.
333. Hahn EL. Spin echoes. Phys Rev. 1950;80:580-94.
334. Carr HY, Purcell EM. Effects of diffusion on free precession in nuclear magentic resonance experiments. Phys Rev. 1954;94:630-8.
335. Stejskal EO, Tanner JE. Spin Diffusion Measurements: Spin Echoes in the Presence of a Time-Dependent Field Gradient. The Journal of Chemical Physics. 1965;42(1):288.
336. Moseley ME, Cohen Y, Mintorovitch J, Chileuitt L, Shimizu H, Kucharczyk J, et al. Early detection of regional cerebral ischemia in cats: comparison of diffusion- and T2-weighted MRI and spectroscopy. Magnetic resonance in medicine : official journal of the Society of Magnetic Resonance in Medicine / Society of Magnetic Resonance in Medicine. 1990;14(2):330-46.
337. Turner R, Le Bihan D, Maier J, Vavrek R, Hedges LK, Pekar J. Echo-planar imaging of intravoxel incoherent motion. Radiology. 1990;177(2):407-14.
338. Moseley ME, Cohen Y, Kucharczyk J, Mintorovitch J, Asgari HS, Wendland MF, et al. Diffusion-weighted MR imaging of anisotropic water diffusion in cat central nervous system. Radiology. 1990;176(2):439-45.
339. Douek P, Turner R, Pekar J, Patronas N, Le Bihan D. MR color mapping of myelin fiber orientation. Journal of computer assisted tomography. 1991;15(6):923-9.
340. Basser PJ, Mattiello J, LeBihan D. MR diffusion tensor spectroscopy and imaging. Biophysical journal. 1994;66(1):259-67.
341. Kingsley PB. Introduction to diffusion tensor imaging mathematics: Part I. Tensors, rotations, and eigenvectors. Concepts in Magnetic Resonance Part A. 2006;28A(2):101-22.
342. Nguyen C, Fan Z, Xie Y, Dawkins J, Tseliou E, Bi X, et al. In vivo contrast free chronic myocardial infarction characterization using diffusion-weighted cardiovascular magnetic resonance. Journal of cardiovascular magnetic resonance : official journal of the Society for Cardiovascular Magnetic Resonance. 2014;16:68.
343. Tofts P, lloyd D, Clark CA, Barker GJ, Parker GJM, McConville P, et al. Test liquids for quantitative MRI measurements of Self-Diffusion Coefficient In Vivio. Magnetic

resonance in medicine : official journal of the Society of Magnetic Resonance in Medicine / Society of Magnetic Resonance in Medicine. 2000;43:368-74.
344. Neil JJ. Diffusion imaging concepts for clinicians. Journal of magnetic resonance imaging : JMRI. 2008;27(1):1-7.
345. Mukherjee P, Bahn MM, McKinstry RC, Shimony JS, Cull TS, Akbudak E, et al. Differences between gray matter and white matter water diffusion in stroke: diffusion-tensor MR imaging in 12 patients. Radiology. 2000;215(1):211-20.
346. Basser PJ, Pierpaoli C. Microstructural and physiological features of tissues elucidated by quantitative-diffusion-tensor MRI. Journal of magnetic resonance Series B. 1996;111(3):209-19.
347. Le Bihan D, Mangin JF, Poupon C, Clark CA, Pappata S, Molko N, et al. Diffusion tensor imaging: concepts and applications. Journal of magnetic resonance imaging : JMRI. 2001;13(4):534-46.
348. Neil JJ, Shiran SI, McKinstry RC, Schefft GL, Snyder AZ, Almli CR, et al. Normal brain in human newborns: apparent diffusion coefficient and diffusion anisotropy measured by using diffusion tensor MR imaging. Radiology. 1998;209(1):57-66.
349. Tievsky AL, Ptak T, Farkas J. Investigation of apparent diffusion coefficient and diffusion tensor anisotrophy in acute and chronic multiple sclerosis lesions. AJNR American journal of neuroradiology. 1999;20(8):1491-9.
350. Ouyang X, Chen K, Yao L, Hu B, Wu X, Ye Q, et al. Simultaneous changes in gray matter volume and white matter fractional anisotropy in Alzheimer's disease revealed by multimodal CCA and joint ICA. Neuroscience. 2015;301:553-62.
351. Chabriat H, Pappata S, Poupon C, Clark CA, Vahedi K, Poupon F, et al. Clinical severity in CADASIL related to ultrastructural damage in white matter: in vivo study with diffusion tensor MRI. Stroke; a journal of cerebral circulation. 1999;30(12):2637-43.
352. Basser PJ, Pajevic S, Pierpaoli C, Duda J, Aldroubi A. In vivo fiber tractography using DT-MRI data. Magnetic resonance in medicine : official journal of the Society of Magnetic Resonance in Medicine / Society of Magnetic Resonance in Medicine. 2000;44(4):625-32.
353. Mukherjee P, Berman JI, Chung SW, Hess CP, Henry RG. Diffusion tensor MR imaging and fiber tractography: theoretic underpinnings. AJNR American journal of neuroradiology. 2008;29(4):632-41.
354. Mori S, Crain BJ, Chacko VP, van Zijl PC. Three-dimensional tracking of axonal projections in the brain by magnetic resonance imaging. Annals of neurology. 1999;45(2):265-9.
355. Jones DK, Simmons A, Williams SC, Horsfield MA. Non-invasive assessment of axonal fiber connectivity in the human brain via diffusion tensor MRI. Magnetic resonance in medicine : official journal of the Society of Magnetic Resonance in Medicine / Society of Magnetic Resonance in Medicine. 1999;42(1):37-41.
356. Pajevic S, Pierpaoli C. Color schemes to represent the orientation of anisotropic tissues from diffusion tensor data: application to white matter fiber tract mapping in the human brain. Magnetic resonance in medicine : official journal of the Society of Magnetic Resonance in Medicine / Society of Magnetic Resonance in Medicine. 1999;42(3):526-40.
357. The Human Connectome Project [Available from: http://www.humanconnectomeproject.org/.
358. Ennis DB, Kindlman G, Rodriguez I, Helm PA, McVeigh ER. Visualization of tensor fields using superquadric glyphs. Magnetic Resonance in Medicine. 2005;53(1):169-76.

359. Eldeman RR, Gaa J, Wedeen VJ, Loh E, Hare JM, Prasad P, et al. In Vivo Measurement of Water Diffusion in the Human Heart. Magnetic Resonance in Medicine. 1994;32:423-8.
360. Reese TG, Weisskoff RM, Smith N, Rosen BR, Dinsmore RE, VJ W. Imaging mypcardial fibre architecture in vivo with magnetic resonance. Magnetic resonance imaging. 1995;34:766-91.
361. Geerts L, Bovendeerd PHM, Nicolay K, Arts T. Characterization of the normal cardiac myofibre field in goat measure with MR-diffusion tensor imaging. American journal of physiology Heart and circulatory physiology. 2002;283:H139-H45.
362. Chen J, Song SK, Liu W, McLean M, Allen JS, Tan J, et al. Remodeling of cardiac fiber structure after infarction in rats quantified with diffusion tensor MRI. American journal of physiology Heart and circulatory physiology. 2003;285(3):H946-54.
363. Jiang Y, Pandya K, Smithies O, Hsu EW. Three-dimensional diffusion tensor microscopy of fixed mouse hearts. Magnetic resonance in medicine : official journal of the Society of Magnetic Resonance in Medicine / Society of Magnetic Resonance in Medicine. 2004;52(3):453-60.
364. Jiang Y, Guccione JM, Ratcliffe MB, Hsu EW. Transmural heterogeneity of diffuison anisotropy in the sheep myocardium charcterized by MR diffusion tensor imaging. American journal of physiology Heart and circulatory physiology. 2007;293:H2377-84.
365. Sosnovik DE, Mekkaoui C, Huang S, Chen HH, Dai G, Stoeck CT, et al. Microstructural impact of ischemia and bone marrow-derived cell therapy revealed with diffusion tensor magnetic resonance imaging tractography of the heart in vivo. Circulation. 2014;129(17):1731-41.
366. Reese TG, Wedeen VJ, Weisskoff RM. Measuring Diffusion in the Presence of Material Strain. Journal of magnetic resonance Series B. 1996;112(3):253-8.
367. Tseng WYI, Reese TG, Weisskoff RM, Brady TJ, VJ W. Myocardial fibre shortening in humans: initial results of MR imaging. Radiology. 2000;216:128-39.
368. Dou J, Tseng WY, Reese TG, Wedeen VJ. Combined diffusion and strain MRI reveals structure and function of human myocardial laminar sheets in vivo. Magnetic resonance in medicine : official journal of the Society of Magnetic Resonance in Medicine / Society of Magnetic Resonance in Medicine. 2003;50(1):107-13.
369. Wu MT, Tseng WY, Su MY, Liu CP, Chiou KR, Wedeen VJ, et al. Diffusion tensor magnetic resonance imaging mapping the fiber architecture remodeling in human myocardium after infarction: correlation with viability and wall motion. Circulation. 2006;114(10):1036-45.
370. Wu MT, Su MY, Huang YL, Chiou KR, Yang P, Pan HB, et al. Sequential changes of myocardial microstructure in patients postmyocardial infarction by diffusion-tensor cardiac MR: correlation with left ventricular structure and function. Circulation Cardiovascular imaging. 2009;2(1):32-40.
371. Stoeck CT, von Deuster C, Genet M, Atkinson D, Kozerke S. Second-order motion-compensated spin echo diffusion tensor imaging of the human heart. Magnetic resonance in medicine : official journal of the Society of Magnetic Resonance in Medicine / Society of Magnetic Resonance in Medicine. 2016;75(4):1669-76.
372. Tunnicliffe EM, Scott AD, Ferreira P, Ariga R, McGill LA, Nielles-Vallespin S, et al. Intercentre reproducibility of cardiac apparent diffusion coefficient and fractional anisotropy in healthy volunteers. Journal of cardiovascular magnetic resonance : official journal of the Society for Cardiovascular Magnetic Resonance. 2014;16:31.
373. Angeli S, Befera N, Peyrat JM, Calabrese E, Johnson GA, Constantinides C. A high-resolution cardiovascular magnetic resonance diffusion tensor map from ex-vivo

C57BL/6 murine hearts. Journal of cardiovascular magnetic resonance : official journal of the Society for Cardiovascular Magnetic Resonance. 2014;16:77.
374. Ashikaga H, Covell JW, Omens JH. Diastolic dysfunction in volume-overload hypertrophy is associated with abnormal shearing of myolaminar sheets. American journal of physiology Heart and circulatory physiology. 2005;288:H2603-H10.
375. Hales PW, Burton RA, Bollensdorff C, Mason F, Bishop M, Gavaghan D, et al. Progressive changes in T(1), T(2) and left-ventricular histo-architecture in the fixed and embedded rat heart. NMR in biomedicine. 2011;24(7):836-43.
376. Teh I, Burton RA, McClymont D, Capel RA, Aston D, Kohl P, et al. Mapping cardiac microstructure of rabbit heart in different mechanical states by high resolution diffusion tensor imaging: A proof-of-principle study. Progress in biophysics and molecular biology. 2016;121(2):85-96.
377. Benson AP, Aslanidi OV, Zhang H, Holden AV. The canine virtual ventricular wall: a platform for dissecting pharmacological effects on propagation and arrhythmogenesis. Progress in biophysics and molecular biology. 2008;96(1-3):187-208.
378. Hsu EW, Xue R, Holmes A, Forder JR. Delayed reduction of tissue water diffusion after myocardial ischemia. The American journal of physiology. 1998;275(2 Pt 2):H697-702.
379. Wu EX, Wu Y, Nicholls JM, Wang J, Liao S, Zhu S, et al. MR diffusion tensor imaging study of postinfarct myocardium structural remodeling in a porcine model. Magnetic resonance in medicine : official journal of the Society of Magnetic Resonance in Medicine / Society of Magnetic Resonance in Medicine. 2007;58(4):687-95.
380. Winklhofer S, Stoeck CT, Berger N, Thali M, Manka R, Kozerke S, et al. Post-mortem cardiac diffusion tensor imaging: detection of myocardial infarction and remodeling of myofiber architecture. European radiology. 2014;24(11):2810-8.
381. Helm PA, Younes L, Beg MF, Ennis DB, Leclercq C, Faris OP, et al. Evidence of structural remodeling in the dyssynchronous failing heart. Circ Res. 2006;98(1):125-32.
382. Li W, Lu M, Banerjee S, Zhong J, Ye A, Molter J, et al. Ex vivo diffusion tensor MRI reflects microscopic structural remodeling associated with aging and disease progression in normal and cardiomyopathic Syrian hamsters. NMR in biomedicine. 2009;22(8):819-25.
383. Eggen MD, Swingen CM, Iaizzo PA. Analysis of fiber orientation in normal and failing human hearts using diffusion tensor MRI. IEEE International Symposium on Biomedical Imaging: From Nano to Macro. IEEE Eng Med Biol Mag. 2009;13(3):642-5.
384. Abdullah OM, Drakos SG, Diakos NA, Wever-Pinzon O, Kfoury AG, Stehlik J, et al. Characterization of diffuse fibrosis in the failing human heart via diffusion tensor imaging and quantitative histological validation. NMR in biomedicine. 2014;27(11):1378-86.
385. Schmitt B, Fedarava K, Falkenberg J, Rothaus K, Bodhey NK, Reischauer C, et al. Three-dimensional alignment of the aggregated myocytes in the normal and hypertrophic heart. J Appl Physiol (1985). 2009;107:921-7.
386. Ripplinger CM, Li W, Hadley J, Chen J, Rothenberg F, Lombardi R, et al. Enhanced transmural fiber rotation and connexin 43 heterogeneity are associated with an increased upper limit of vulnerability in a transgenic rabbit model of human hypertrophic cardiomyopathy. Circ Res. 2007;101(10):1049-57.
387. Tseng WY, Reese TG, Weisskoff RM, Wedeen VJ. Cardiac diffusion tensor MRI in vivo without strain correction. Magnetic resonance in medicine : official journal of the Society of Magnetic Resonance in Medicine / Society of Magnetic Resonance in Medicine. 1999;42(2):393-403.

388. Toussaint N, Sermesant M, Stoeck CT, Kozerke S, Batchelor PG. In vivo human 3D cardiac fibre architecture: reconstruction using curvilinear interpolation of diffusion tensor images. Medical image computing and computer-assisted intervention : MICCAI International Conference on Medical Image Computing and Computer-Assisted Intervention. 2010;13(Pt 1):418-25.
389. Laissy JP, Gaxotte V, Ironde-Laissy E, Klein I, Ribet A, Bendriss A, et al. Cardiac diffusion-weighted MR imaging in recent, subacute, and chronic myocardial infarction: a pilot study. Journal of magnetic resonance imaging : JMRI. 2013;38(6):1377-87.
390. Froeling M, Strijkers GJ, Nederveen AJ, Chamuleau SA, Luijten PR. Diffusion Tensor MRI of the Heart – In Vivo Imaging of Myocardial Fiber Architecture. Current cardiovascular imaging reports. 2014;7:9276.
391. Gamper U, Boesiger P, Kozerke S. Diffusion imaging of the in vivo heart using spin echoes--considerations on bulk motion sensitivity. Magnetic resonance in medicine : official journal of the Society of Magnetic Resonance in Medicine / Society of Magnetic Resonance in Medicine. 2007;57(2):331-7.
392. von Deuster C, Stoeck CT, Genet M, Atkinson D, Kozerke S. Spin echo versus stimulated echo diffusion tensor imaging of the in vivo human heart. Magnetic resonance in medicine : official journal of the Society of Magnetic Resonance in Medicine / Society of Magnetic Resonance in Medicine. 2015;76(3):862-72.
393. Nguyen C, Fan Z, Xie Y, Pang J, Speier P, Bi X, et al. In vivo diffusion-tensor MRI of the human heart on a 3 tesla clinical scanner: An optimized second order (M2) motion compensated diffusion-preparation approach. Magnetic resonance in medicine : official journal of the Society of Magnetic Resonance in Medicine / Society of Magnetic Resonance in Medicine. 2016;76(5):1354-63.
394. Axel L, Wedeen VJ, Ennis DB. Probing dynamic myocardial microstructure with cardiac magnetic resonance diffusion tensor imaging. Journal of cardiovascular magnetic resonance : official journal of the Society for Cardiovascular Magnetic Resonance. 2014;16:89.
395. Ferreira PF, Kilner PJ, McGill LA, Nielles-Vallespin S, Scott AD, Ho SY, et al. In vivo cardiovascular magnetic resonance diffusion tensor imaging shows evidence of abnormal myocardial laminar orientations and mobility in hypertrophic cardiomyopathy. Journal of cardiovascular magnetic resonance : official journal of the Society for Cardiovascular Magnetic Resonance. 2014;16:87.
396. Turner R, von Kienlin M, Moonen CT, van Zijl PC. Single-shot localized echo-planar imaging (STEAM-EPI) at 4.7 tesla. Magnetic resonance in medicine : official journal of the Society of Magnetic Resonance in Medicine / Society of Magnetic Resonance in Medicine. 1990;14(2):401-8.
397. Jones DK, Horsfield MA, Simmons A. Optimal strategies for measuring diffusion in anisotropic systems by magnetic resonance imaging. Magnetic resonance in medicine : official journal of the Society of Magnetic Resonance in Medicine / Society of Magnetic Resonance in Medicine. 1999;42(3):515-25.
398. Jones DK. The effect of gradient sampling schemes on measures derived from diffusion tensor MRI: a Monte Carlo study. Magnetic resonance in medicine : official journal of the Society of Magnetic Resonance in Medicine / Society of Magnetic Resonance in Medicine. 2004;51(4):807-15.
399. Skare S, Hedehus M, Moseley ME, Li TQ. Condition number as a measure of noise performance of diffusion tensor data acquisition schemes with MRI. J Magn Reson. 2000;147(2):340-52.

400. Eis M, Hoehn-Berlage M. Correction of gradient crosstalk and optimization of measurement parameters in diffusion MR imaging. J magn Reson Ser B. 1995;107:222-34.
401. Armitage PA, Bastin ME. Selecting an appropriate anisotropy index for displaying diffusion tensor imaging data with improved contrast and sensitivity. Magnetic resonance in medicine : official journal of the Society of Magnetic Resonance in Medicine / Society of Magnetic Resonance in Medicine. 2000;44(1):117-21.
402. Kingsley PB. Introduction to diffusion tensor imaging mathematics: part III. Tensor calculation, noise, simulations, and optimization. Concepts Magn Reson Part A Bridg Educ Res. 2006;28A:155-79.
403. Soares JM, Marques P, Alves V, Sousa N. A hitchhiker's guide to diffusion tensor imaging. Frontiers in neuroscience. 2013;7:31.
404. Malcolm JG, Shenton ME, Rathi Y. Filtered multitensor tractography. IEEE transactions on medical imaging. 2010;29(9):1664-75.
405. Kingsley PB. Introduction to diffusion tensor imaging mathematics: Part II. Anisotropy, diffusion-weighting factors, and gradient encoding schemes. Concepts in Magnetic Resonance Part A. 2006;28A(2):123-54.
406. Jones DK, Basser PJ. "Squashing peanuts and smashing pumpkins": how noise distorts diffusion-weighted MR data. Magnetic resonance in medicine : official journal of the Society of Magnetic Resonance in Medicine / Society of Magnetic Resonance in Medicine. 2004;52(5):979-93.
407. Basser PJ, Pajevic S. Statistical artifacts in diffusion tensor MRI (DT-MRI) caused by background noise. Magnetic resonance in medicine : official journal of the Society of Magnetic Resonance in Medicine / Society of Magnetic Resonance in Medicine. 2000;44(1):41-50.
408. Skare S, Li T, Nordell B, Ingvar M. Noise considerations in the determination of diffusion tensor anisotropy. Magnetic resonance imaging. 2000;18(6):659-69.
409. Jones DK, Cercignani M. Twenty-five pitfalls in the analysis of diffusion MRI data. NMR in biomedicine. 2010;23(7):803-20.
410. Giannakidis A, Gullberg GT, Pennell DJ, Firmin DN. Value of formalin fixation for the prolonged preservation of rodent myocardial microanatomical organization: Evidence by MR diffusion tensor imaging. Anat Rec (Hoboken). 2016;299(7):878-87.
411. Feinberg DA, Hoenninger JC, Crooks LE, Kaufman L, Watts JC, Arakawa M. Inner volume MR imaging: technical concepts and their application. Radiology. 1985;156(3):743-7.
412. Guizar-Sicairos M, Thurman ST, Fienup JR. Efficient subpixel image registration algorithms. Optics letters. 2008;33(2):156-8.
413. Maceira AM, Prasad SK, Khan M, Pennell DJ. Reference right ventricular systolic and diastolic function normalized to age, gender and body surface area from steady-state free precession cardiovascular magnetic resonance. European heart journal. 2006;27(23):2879-88.
414. Bellenger NG, Davies LC, Francis JM, Coats AJ, Pennell DJ. Reduction in sample size for studies of remodeling in heart failure by the use of cardiovascular magnetic resonance. Journal of cardiovascular magnetic resonance : official journal of the Society for Cardiovascular Magnetic Resonance. 2000;2(4):271-8.
415. Rose TA, Choi JW. Intravenous Imaging Contrast Media Complications: The Basics That Every Clinician Needs to Know. The American journal of medicine. 2015;128(9):943-9.

416. Reiter T, Ritter O, Prince MR, Nordbeck P, Wanner C, Nagel E, et al. Minimizing Risk of Nephrogenic systemic fibrosis in Cardiovascular Magnetic Resonance. Journal of cardiovascular magnetic resonance : official journal of the Society for Cardiovascular Magnetic Resonance. 2012;14:31.
417. Kuo PH, Kanal E, Abu-Alfa AK, Cowper SE. Gadolinium-based MR contrast agents and nephrogenic systemic fibrosis. Radiology. 2007;242(3):647-9.
418. Kellman P, Arai AE, McVeigh ER, Aletras AH. Phase-sensitive inversion recovery for detecting myocardial infarction using gadolinium-delayed hyperenhancement. Magnetic resonance in medicine : official journal of the Society of Magnetic Resonance in Medicine / Society of Magnetic Resonance in Medicine. 2002;47(2):372-83.
419. Ferreira PF, Gatehouse PD, Mohiaddin RH, Firmin DN. Cardiovascular magnetic resonance artefacts. Journal of cardiovascular magnetic resonance : official journal of the Society for Cardiovascular Magnetic Resonance. 2013;15:41.
420. Spiewak M, Malek LA, Misko J, Chojnowska L, Milosz B, Klopotowski M, et al. Comparison of different quantification methods of late gadolinium enhancement in patients with hypertrophic cardiomyopathy. European journal of radiology. 2010;74(3):e149-53.
421. Amado LC, Gerber BL, Gupta SN, Rettmann DW, Szarf G, Schock R, et al. Accurate and objective infarct sizing by contrast-enhanced magnetic resonance imaging in a canine myocardial infarction model. Journal of the American College of Cardiology. 2004;44(12):2383-9.
422. McGill LA, Ismail TF, Nielles-Vallespin S, Ferreira P, Scott AD, Roughton M, et al. Reproducibility of in-vivo diffusion tensor cardiovascular magnetic resonance in hypertrophic cardiomyopathy. Journal of cardiovascular magnetic resonance : official journal of the Society for Cardiovascular Magnetic Resonance. 2012;14:86.
423. Streeter DD, Hanna WT. Engineering Mechanics for Successive States in Canine Left Ventricular Myocardium: II. Fiber Angle and Sarcomere Length. Circulation Research. 1973;33(6):656-64.
424. Bland JM, Altman DG. Statistical methods for assessing agreement between two methods of clinical measurement. The Lancet. 1986;1:307-10.
425. Tunnicliffe EM, Ferreira P, Scott AD, Ariga R, Mcgill L, Nielles-Vallespin S, et al. Intercentre reproducibility of second eigenvector orientation in cardiac diffusion tensor imaging. Journal of Cardiovascular Magnetic Resonance. 2016;18(Suppl 1):P35.
426. Nielles-Vallespin S, Mekkaoui C, Gatehouse P, Reese TG, Keegan J, Ferreira PF, et al. Erratum to In vivo diffusion tensor MRI of the human heart: Reproducibility of breath-hold and navigator based approaches (Magn Reson Med 2013;70:454-465). Magnetic Resonance in Medicine. 2014;72(2):599-.
427. McGill LA, Ferreira PF, Scott AD, Nielles-Vallespin S, Giannakidis A, Kilner PJ, et al. Relationship between cardiac diffusion tensor imaging parameters and anthropometrics in healthy volunteers. Journal of cardiovascular magnetic resonance : official journal of the Society for Cardiovascular Magnetic Resonance. 2016;18:2.
428. McGill L-A, Ferreira P, Scott AD, Nielles-Vallespin S, Ismail T, Silva R, et al. Influence of subject characteristics on DTI parameters in the normal heart. Journal of Cardiovascular Magnetic Resonance. 2014;16(Suppl 1):P7.
429. McGill L-A, Ferreira P, Scott AD, Nielles-Vallespin S, Silva R, Kilner PJ, et al. Comparison of cardiac DTI parameters between systole and diastole. Journal of Cardiovascular Magnetic Resonance. 2014;16(Suppl 1):P39.

430. Mansson A. Hypothesis and theory: mechanical instabilities and non-uniformities in hereditary sarcomere myopathies. Frontiers in physiology. 2014;5:350.
431. Dhillon A, Sweet W, Popovic ZB, Smedira NG, Thamilarasan M, Lytle BW, et al. Association of noninvasively measured left ventricular mechanics with in vitro muscle contractile performance: a prospective study in hypertrophic cardiomyopathy patients. Journal of the American Heart Association. 2014;3(6):e001269.
432. Fatkin D, McConnell BK, Mudd JO, Semsarian C, Moskowitz IG, Schoen FJ, et al. An abnormal Ca(2+) response in mutant sarcomere protein-mediated familial hypertrophic cardiomyopathy. The Journal of clinical investigation. 2000;106(11):1351-9.
433. Scollan DF, Holmes A, Zhang J, Winslow RL. Reconstruction of cardiac ventricular geometry and fiber orientation using magnetic resonance imaging. Annals of biomedical engineering. 2000;28(8):934-44.
434. McGill L, Ferreira P, Scott AD, Nielles-Vallespin S, Giannakidis A, Kilner P, et al. Diffusion Tensor Imaging: Comparison of Hypertrophic Cardiomyopathy, Hypertension and Healthy Cohorts. European heart journal cardiovascular Imaging. 2016;17 (suppl 1):i37-i84 (1615).
435. McGill L, Ferreira P, Scott AD, Nielles-Vallespin S, Kilner P, de Silva R, et al. Non-invasive Interrogation of Myocardial Disarray in Hypertrophic Cardiomyopathy. Heart. 2016;102(Suppl 6):A96.
436. Bhatheja S, Panchal HB, Ventura H, Paul TK. Obesity Cardiomyopathy: Pathophysiologic Factors and Nosologic Reevaluation. The American journal of the medical sciences. 2016;352(2):219-22.
437. Kim BJ, Kang HG, Kim HJ, Ahn SH, Kim NY, Warach S, et al. Magnetic resonance imaging in acute ischemic stroke treatment. Journal of stroke. 2014;16(3):131-45.
438. Callot V, Bennett E, Decking UK, Balaban RS, Wen H. In vivo study of microcirculation in canine myocardium using the IVIM method. Magnetic resonance in medicine : official journal of the Society of Magnetic Resonance in Medicine / Society of Magnetic Resonance in Medicine. 2003;50(3):531-40.
439. Scott AD, Ferreira PF, Nielles-Vallespin S, Gatehouse P, McGill LA, Kilner P, et al. Optimal diffusion weighting for in vivo cardiac diffusion tensor imaging. Magnetic resonance in medicine : official journal of the Society of Magnetic Resonance in Medicine / Society of Magnetic Resonance in Medicine. 2014.
440. Scott AD, Ferreira PF, Nielles-Vallespin S, Gatehouse P, McGill LA, Kilner P, et al. Optimal diffusion weighting for in vivo cardiac diffusion tensor imaging. Magnetic resonance in medicine : official journal of the Society of Magnetic Resonance in Medicine / Society of Magnetic Resonance in Medicine. 2014;74(2):420-30.
441. McGill LA, Scott AD, Ferreira PF, Nielles-Vallespin S, Ismail T, Kilner PJ, et al. Heterogeneity of Fractional Anisotropy and Mean Diffusivity Measurements by In Vivo Diffusion Tensor Imaging in Normal Human Hearts. PloS one. 2015;10(7):e0132360.
442. Reeder SB, Wintersperger BJ, Dietrich O, Lanz T, Greiser A, Reiser MF, et al. Practical approaches to the evaluation of signal-to-noise ratio performance with parallel imaging: application with cardiac imaging and a 32-channel cardiac coil. Magnetic resonance in medicine : official journal of the Society of Magnetic Resonance in Medicine / Society of Magnetic Resonance in Medicine. 2005;54(3):748-54.
443. Dibb R, Qi Y, Liu C. Magnetic susceptibility anisotropy of myocardium imaged by cardiovascular magnetic resonance reflects the anisotropy of myocardial filament alpha-helix polypeptide bonds. Journal of cardiovascular magnetic resonance : official journal of the Society for Cardiovascular Magnetic Resonance. 2015;17:60.

444. Scott AD, Nielles-Vallespin S, Ferreira PF, McGill LA, Pennell DJ, Firmin DN. The effects of noise in cardiac diffusion tensor imaging and the benefits of averaging complex data. NMR in biomedicine. 2016;29(5):588-99.
445. Froeling M, Leiner T, Vergoossen LWM, Hove EA, Nederveen AJ, Strijkers GJ, et al. Transmural heterogeneity of in-vivo whole heart diffusion parameters: architecture, physiology or artifact? Magnetic Resonance in Medicine. 2016.
446. Baehring JM, Fulbright RK. Diffusion-weighted MRI in neuro-oncology. CNS Oncol. 2012;1(2):155-67.
447. Ennis DB, Kindlmann G. Orthogonal tensor invariants and the analysis of diffusion tensor magnetic resonance images. Magnetic resonance in medicine : official journal of the Society of Magnetic Resonance in Medicine / Society of Magnetic Resonance in Medicine. 2006;55(1):136-46.
448. Strijkers GJ, Bouts A, Blankesteijn WM, Peeters TH, Vilanova A, van Prooijen MC, et al. Diffusion tensor imaging of left ventricular remodeling in response to myocardial infarction in the mouse. NMR in biomedicine. 2009;22(2):182-90.

Appendix

1. Prizes Awarded For This Work

1. Third prize Imperial College 3 Minute Thesis Competition

2. First prize NHLI 3 Minute Thesis Competition

3. Public Engagement Award Imperial College Graduate School Summer Research Symposium

4. Highly Commended Poster Presentation NHLI Postgraduate Research Day, London

5. Best Oral Presentation Institute of Cardiovascular Medicine and Science Symposium, London

2. First Author Publications Arising From This Research

1. McGill LA, Ismail TF, Nielles-Vallespin S, Ferreira P, Scott AD, Roughton M, et al. Reproducibility of in-vivo diffusion tensor cardiovascular magnetic resonance in hypertrophic cardiomyopathy. Journal of cardiovascular magnetic resonance : official journal of the Society for Cardiovascular Magnetic Resonance. 2012;14:86.

2. *Ferreira PF, *Kilner PJ, *McGill LA, Nielles-Vallespin S, Scott AD, Ho SY, et al. In vivo cardiovascular magnetic resonance diffusion tensor imaging shows evidence of abnormal myocardial laminar orientations and mobility in hypertrophic cardiomyopathy. Journal of cardiovascular magnetic resonance: official journal of the Society for Cardiovascular Magnetic Resonance. 2014;16:87 *Joint first author

3. McGill LA, Scott AD, Ferreira PF, Nielles-Vallespin S, Ismail T, Kilner PJ, et al. Heterogeneity of Fractional Anisotropy and Mean Diffusivity Measurements by In Vivo Diffusion Tensor Imaging in Normal Human Hearts. PloS one. 2015;10(7):e0132360.

4. McGill LA, Ferreira PF, Scott AD, Nielles-Vallespin S, Giannakidis A, Kilner PJ, et al. Relationship between cardiac diffusion tensor imaging parameters and anthropometrics in healthy volunteers. Journal of cardiovascular magnetic resonance : official journal of the Society for Cardiovascular Magnetic Resonance. 2016;18:2.

3. Additional Publications

1. Tunnicliffe EM, Scott AD, Ferreira P, Ariga R, M**cGill LA**, Nielles-Vallespin S, et al. Intercentre reproducibility of cardiac apparent diffusion coefficient and fractional anisotropy in healthy volunteers. Journal of cardiovascular magnetic resonance : official journal of the Society for Cardiovascular Magnetic Resonance. 2014;16:31.

2. Scott AD, Ferreira PF, Nielles-Vallespin S, Gatehouse P, **McGill LA**, Kilner P et al. Optimal diffusion weighting for in vivo cardiac diffusion tensor imaging. Magn Reson Med. 2015; 74: 420-430

3. Scott AD, Nielles-Vallespin S, Ferreira P, **McGill LA**, Pennell, DJ, Frimina, D. The effects of noise in cardiac diffusion tensor imaging and the benefits of averaging complex data. 2016; 29: 588-99

4. Abstracts

1. **McGill L-A**, Ferreira P, Scott AD, Nielles-Vallespin S, Ismail T, Silva R, et al. Influence of subject characteristics on DTI parameters in the normal heart. Journal of Cardiovascular Magnetic Resonance. 2014;16(Suppl 1):P7.

2. **McGill LA**, Ferreira P, Scott AD, Nielles-Vallespin S, Silva R, Kilner PJ, et al. Comparison of cardiac DTI parameters between systole and diastole. Journal of Cardiovascular Magnetic Resonance. 2014;16(Suppl 1):P39.

3. Tunnicliffe EM, Ferreira P, Scott AD, Ariga R, **McGill LA**, Nielles-Vallespin S, et al. Intercentre reproducibility of second eigenvector orientation in cardiac diffusion tensor imaging. Journal of Cardiovascular Magnetic Resonance. 2016;18(Suppl 1):P35.

4. **McGill LA**, Ferreira P, Scott AD, Nielles-Vallespin S, Kilner P, de Silva R, et al. Non-invasive Interrogation of Myocardial Disarray in Hypertrophic Cardiomyopathy. Heart. 2016;102(Suppl 6):A96

5. **McGill LA**, Ferreira P, Scott AD, Nielles-Vallespin S, Giannakidis A, Kilner P, et al. Diffusion Tensor Imaging: Comparison of Hypertrophic Cardiomyopathy, Hypertension and Healthy Cohorts. European heart journal cardiovascular Imaging. 2016;17 (suppl 1):i37-i84 (1615).

Personal Contribution to Thesis

I was employed by the Royal Brompton Hospital National Institutes of Health Research Biomedical Research Unit to lead this work on the evaluation of the monopolar diffusion weighted cardiovascular diffusion tensor imaging sequence. I set up a monthly departmental diffusion meeting to discuss results and strategise. I recruited and scanned all subjects presented in this work. I performed the initial post processing and statistical analysis for results chapters 10 to 13

and collaborated with Matthew Roughton for Chapter 9. I individually prepared the manuscripts and presentations for Chapters 9, 10, 12 and 13. In Chapter 11 I collaborated with Dr. Pedro Ferreira and Dr. Philip Kilner.

Supervision

Primary supervisory: Professor Dudley J Pennell

Secondary supervisor Professor David N Firmin

Tertiary supervisor Dr Sanjay Prasad

Acknowledgements

I would like to thank the following people for their assistance during this research period. Firstly Dr. Pedro Ferreira, Dr. Andrew Scott and Dr. Sonia Nielles-Vallespin for providing invaluable physics and illustrative support. Dr Sew Y Ho and Dr Karen P McCarthy for their insights into myocardial structure and function. Dr Philip Kilner for his direction, creativity and enthusiasm.

Funding

This research was funded by the National Institutes of Health Research Biomedical Research Unit Royal Brompton Hospital.

Permissions

Figure/ Table	Title	Source	Copy Right Holder	Date	Permission:	Reference
Figure 2.1	Left ventricular morphology of the giraffe heart examined by stereological methods	Anat Rec (Hoboken)	John Wiley and Sons	24-09-16	yes	3955551485415
Figure 2.2	Arrangement of the Muscular Fibres in the Ventricles of the Vertebrate Heart, with Physiological Remarks	Philosophical Transactions of the Royal Society of London	The Royal Society Publishing	25-09-16	awaited	
Figure 2.3	Spatial orientation of the ventricular muscle band: physiologic contribution and surgical implications	J Thorac Cardiovasc Surg	Elsevier	25-09-16	yes	3955891066044
Figure 2.4	Fiber Orientation in the Canine Left Ventricle during Diastole and Systole	Circulation Research	Wolters Kluwer Health, Inc	25-09-16	yes	3955891302747
Figure 2.5	A straightforward guide to the sarcomeric basis of cardiomyopathies.	Heart	BMJ Publishing Group Ltd.	25-09-16	yes	3955900049166
Figure 2.6	Myocyte cytoskeletal disorganization and right heart failure in hypoxia-induced neonatal pulmonary hypertension.	Am J Physiol- Heart and Circulatory Physiology	The American Physiological Society		yes – permission not required	
Figure 2.7	Laminar structure of the heart: ventricular myocyte arrangement and connective tissue architecture in the dog.	Am J Physiol- Heart and Circulatory Physiology	The American Physiological Society		yes – permission not required	
Figure 2.8	Three-dimensional transmural organisation of perimysial collagen in the heart.	Am J Physiol- Heart and Circulatory Physiology	The American Physiological Society		yes – permission not required	

Figure 2.9	The presence of two local myocardial sheet populations confirmed by diffusion tensor MRI and histological validation	Journal of Magnetic Resonance Imaging	John Wiley and Sons	25-09-16	yes	3955961154621
Figure 3.1	Transmural strain and rotation gradient in survivors of childhood cancers.	European Heart Journal - Cardiovascular Imaging	Oxford University Press	25-09-16	yes	3955961360612
Figure 3.2	Relation of regional cross-fiber shortening to wall thickening in the intact heart.	Circulation	Wolters Kluwer Health, Inc.	25-09-16	yes	3955970219417
Figure 3.3	The sliding filament theory of muscle contraction.	Nature Education	Nature Publishing Group		Yes – permission not required	
Table 3.1	Normalized left ventricular systolic and diastolic function by steady state free precession cardiovascular magnetic resonance	J Cardiovasc Magn Res	Informa Healthcare		Yes – permission not required	
Figure 4.1	Measuring and mapping cardiac fiber and laminar architecture using diffusion tensor MR imaging	Ann N Y Acad Sci	John Wiley and Sons	25-09-16	yes	3955980258017
Figure 4.2	Direct measurement of transmural laminar architecture in the anterolateral wall of the ovine left ventricle: new implications for wall thickening mechanics.	Am J Physiol- Heart and Circulatory Physiology	The American Physiological Society		Yes – permission not required	
Figure 4.3	Diffusion MRI tractography of the human heart In Vivo at end-diastole and end-systole.	J Cardiovasc Magn Res	Biomed Central		Yes – permission not required	
Figure 4.4	Direct measurement of transmural laminar architecture in the anterolateral wall of the ovine	Am J Physiol- Heart and Circulatory Physiology	The American Physiological Society		Yes – permission not required	

	left ventricle: new implications for wall thickening mechanics.					
Figure 5.1	A straightforward guide to the sarcomeric basis of cardiomyopathies.	Heart	BMJ Publishing Group Ltd.	25-09-16	yes	3955900049166
Figure 5.4	The pathology of hypertrophic cardiomyopathy.	Histopathology	John Wiley & Sons	25-09-16	yes	3955981471960
Figure 5.5	The pathology of hypertrophic cardiomyopathy.	Histopathology	John Wiley & Sons	25-09-16	yes	3955981471960
Figure 5.6	Histopahtological specificity of hypertrophic obstructive cardiomyopathy.	Heart	BMJ Publishing Group Ltd.	25-09-16	yes	3955990236415
Figure 5.7	Imaging myocardial fiber disarray and intramural strain hypokinesis in hypertrophic cardiomyopathy with MRI	J Mag Reson Imag	John Wiley & Sons	25-09-16	yes	3955990418216
Figure 6.1	Cardiovascular magnetic resonance physics for clinicians: part I	J Cardiovasc Magn Res	Biomed Central		Yes – permission not required	
Figure 6.6	Cardiovascular magnetic resonance physics for clinicians: part I	J Cardiovasc Magn Res	Biomed Central		Yes – permission not required	
Figure 6.13	Assessment of myocardial viability in contrast enhancement.	Cardiovascular MRI and MRA. Philadelphia	Lippincott Williams and Wilkins	25-09-16	awaited	
Figure 6.14	The prognostic role of late gadolinium enhancement magnetic resonance imaging in patients with cardiomyopathy	Can J Cardio	Elsevier	25-09-16	yes	3955991174905
Figure 7.3	Diffusion MRI: what water tells us about the brain	EMBO Mol Med	Open Access		Yes – not required	
Figure 7.6	Diffusion MRI: what water tells us about the brain	EMBO Mol Med	Open Access		Yes – not required	
Figure 7.7	Diffusion MRI: what water tells us about the brain	EMBO Mol Med	Open Access		Yes – not required	

Figure 7.9	Introduction to diffusion tensor imaging mathematics: Part I. Tensors, rotations, and eigenvectors.	Concepts in Magnetic Resonance: Part A, Bridging Education and Research	John Wiley & Sons	25-09-16	yes	3956000798636
Figure 7.13	Human Connectome Project	Human Connectome Project Data	LONI Image Data Archive	25-09-16	yes	
Figure 7.14	Human Connectome Project	Human Connectome Project Data	LONI Image Data Archive	25-09-16	yes	
Figure 7.15	Visualization of tensor fields using superquadric glyphs	Mag Reson Med	John Wiley & Sons	25-09-16	yes	3956001349115
Figure 7.16	In Vivo Measurement of Water Diffusion in the Human Heart	Mag Reson Med	John Wiley & Sons	25-09-16	yes	3956010019638
Figure 7.17	Anisotropy of water diffusion in the myocardium of the rat	Circulation Research	Wolters Kluwer Health, Inc.	25-09-16	yes	3956010208766
Figure 7.18	Imaging myocardial fibre architecture in vivo with magnetic resonance.	Mag Reson Med	John Wiley & Sons	25-09-16	yes	3956010464498
Figure 7.19	Measuring and mapping cardiac fiber and laminar architecture using diffusion tensor MR imaging	Ann N Y Acad Sci	John Wiley and Sons	25-09-16	yes	3955980258017
Figure 7.21	Regional ventricular wall thickening reflects changes in cardiac fibre and sheet structure during contraction: quantification with diffusion tensor MRI	Am J Physiol- Heart and Circulatory Physiology	The American Physiological Society		Yes – permission not required	
Figure 7.22	Histo-anatomical structure of the living isolated rat heart in two contraction states assessed by diffusion tensor MRI	Prog Biophys Mol Bio	Elsevier		Yes – permission not required	
Figure 7.23	Regional ventricular wall thickening reflects changes in cardiac fibre and sheet structure during contraction:	Am J Physiol- Heart and Circulatory Physiology	The American Physiological Society		Yes – permission not required	

	quantification with diffusion tensor MRI					
Figure 7.24	Histo-anatomical structure of the living isolated rat heart in two contraction states assessed by diffusion tensor MRI	Prog Biophys Mol Bio	Elsevier		Yes – permission not required	
Figure 7.25	Diffusion MR tractography of the heart.	J Cardiovasc Magn Res	Biomed Central		Yes – permission not required	
Figure 7.26	Diffusion MRI Tractography of the Developing Human Fetal Heart	PLOS One	Open Access		Yes – permission not required	
Figure 7.27	Diffusion Spectrum MRI Tractography Reveals the Presence of a Complex Network of Residual Myofibers in Infarcted Myocardium	Circ: Cardio Imag	Wolter Kluwer Health, Inc.	25-09-16	yes	3956011278588
Figure 7.28	Ex vivo diffusion tensor MRI reflects microscopic structural remodeling associated with aging and disease progression in normal and cardiomyopathic Syrian hamsters.	NMR in Biomedicine	John Wiley and Sons	25-09-16	yes	3956011445978
Figure 7.29	Three-dimensional alignment of the aggregated myocytes in the normal and hypertrophic heart	J Cardiovasc Magn Res	Biomed Central		Yes – permission not required	
Figure 7.30	Myocardial fibre shortening in humans: initial results of MR imaging	J Applied Physiol	The American Physiological Society		Yes – permission not required	
Figure 7.31	Combined diffusion and strain MRI reveals structure and function of human myocardial laminar sheets in vivo	Mag Reson Med	John Wiley and Sons	25-09-16	yes	3956020321009

Figure 7.32	Diffusion MRI tractography of the human heart In Vivo at end-diastole and end-systole	J Cardiovasc Magn Res	Biomed Central		Yes – permission not required	
Figure 7.33	Imaging myocardial fiber disarray and intramural strain hypokinesis in hypertrophic cardiomyopathy with MRI	J Mag Reson Imag	John Wiley & Sons	25-09-16	yes	3955990418216
Figure 7.39	Measuring Diffusion in the Presence of Material Strain. Journal of magnetic resonance Series B	Mag Reson Med	John Wiley & Sons	25-09-16	yes	3956020321009
Figure 7.40	Probing dynamic myocardial microstructure with cardiac magnetic resonance diffusion tensor imaging	J Cardiovasc Magn Res	Biomed Central		Yes – permission not required	
Figure 7.41	In vivo cardiovascular magnetic resonance diffusion tensor imaging shows evidence of abnormal myocardial laminar orientations and mobility in hypertrophic cardiomyopathy	J Cardiovasc Magn Res	Biomed Central		Yes – permission not required	
Figure 7.42	Cardiac diffusion tensor MRI in vivo without strain correction	Mag Reson Med	John Wiley & Sons	25-09-16	yes	3956020949858
Figure 7.43	"Squashing peanuts and smashing pumpkins": how noise distorts diffusion-weighted MR data	Mag Reson Med	John Wiley & Sons	25-09-16	yes	3956031257883
Figure 8.2	In vivo diffusion tensor MRI of the human heart: reproducibility of breath-hold and navigator-based approaches	Mag Reson Med	John Wiley & Sons	25-09-16	yes	3956031400205
Figure 8.3	In vivo diffusion tensor MRI of the human heart: reproducibility of breath-hold	Mag Reson Med	John Wiley & Sons	25-09-16	yes	3956031400205

	and navigator-based approaches					
Figure 8.12	In vivo cardiovascular magnetic resonance diffusion tensor imaging shows evidence of abnormal myocardial laminar orientations and mobility in hypertrophic cardiomyopathy	J Cardiovasc Magn Res	Biomed Central		Yes – permission not required	
Figure 8.14	Cardiovascular magnetic resonance artefacts	J Cardiovasc Magn Res	Biomed Central		Yes – permission not required	
Figure 8.16	Comparison of different quantification methods of late gadolinium enhancement in patients with hypertrophic cardiomyopathy	European J Radiol	Elsevier	25-09-16	yes	3956040111667
Figure 9.1	Reproducibility of in-vivo diffusion tensor cardiovascular magnetic resonance in hypertrophic cardiomyopathy	J Cardiovasc Magn Res	Biomed Central		Yes – permission not required	
Figure 9.2	Reproducibility of in-vivo diffusion tensor cardiovascular magnetic resonance in hypertrophic cardiomyopathy	J Cardiovasc Magn Res	Biomed Central		Yes – permission not required	
Figure 9.3	Reproducibility of in-vivo diffusion tensor cardiovascular magnetic resonance in hypertrophic cardiomyopathy	J Cardiovasc Magn Res	Biomed Central		Yes – permission not required	
Figure 9.4	Reproducibility of in-vivo diffusion tensor cardiovascular magnetic resonance in hypertrophic cardiomyopathy	J Cardiovasc Magn Res	Biomed Central		Yes – permission not required	
Figure 9.5	Reproducibility of in-vivo diffusion tensor cardiovascular	J Cardiovasc Magn Res	Biomed Central		Yes – permission not required	

	magnetic resonance in hypertrophic cardiomyopathy					
Figure 9.6	Imaging myocardial fiber disarray and intramural strain hypokinesis in hypertrophic cardiomyopathy with MRI	J Mag Reson Imag	John Wiley & Sons	25-09-16	yes	3955990418216
Figure 10.1	Intercentre reproducibility of cardiac apparent diffusion coefficient and fractional anisotropy in healthy volunteers	J Cardiovasc Magn Res	Biomed Central		Yes – permission not required	
Figure 10.2	Intercentre reproducibility of cardiac apparent diffusion coefficient and fractional anisotropy in healthy volunteers	J Cardiovasc Magn Res	Biomed Central		Yes – permission not required	
Figure 10.3	Relationship between cardiac diffusion tensor imaging parameters and anthropometrics in healthy volunteers	J Cardiovasc Magn Res	Biomed Central		Yes – permission not required	
Figure 10.4	Relationship between cardiac diffusion tensor imaging parameters and anthropometrics in healthy volunteers	J Cardiovasc Magn Res	Biomed Central		Yes – permission not required	
Figure 10.5	Relationship between cardiac diffusion tensor imaging parameters and anthropometrics in healthy volunteers	J Cardiovasc Magn Res	Biomed Central		Yes – permission not required	
Figure 10.6	Relationship between cardiac diffusion tensor imaging parameters and anthropometrics in healthy volunteers	J Cardiovasc Magn Res	Biomed Central		Yes – permission not required	

Table 10.1	Intercentre reproducibility of cardiac apparent diffusion coefficient and fractional anisotropy in healthy volunteers	J Cardiovasc Magn Res	Biomed Central		Yes – permission not required	
Table 10.7	Dual-phase cardiac diffusion tensor imaging with strain correction	PLOS One	Open Access		Yes – permission not required	
Figure 11.1	In vivo cardiovascular magnetic resonance diffusion tensor imaging shows evidence of abnormal myocardial laminar orientations and mobility in hypertrophic cardiomyopathy	J Cardiovasc Magn Res	Biomed Central		Yes – permission not required	
Figure 11.2	In vivo cardiovascular magnetic resonance diffusion tensor imaging shows evidence of abnormal myocardial laminar orientations and mobility in hypertrophic cardiomyopathy	J Cardiovasc Magn Res	Biomed Central		Yes – permission not required	
Figure 11.3	In vivo cardiovascular magnetic resonance diffusion tensor imaging shows evidence of abnormal myocardial laminar orientations and mobility in hypertrophic cardiomyopathy	J Cardiovasc Magn Res	Biomed Central		Yes – permission not required	
Figure 11.4	In vivo cardiovascular magnetic resonance diffusion tensor imaging shows evidence of abnormal myocardial laminar orientations and mobility in hypertrophic cardiomyopathy	J Cardiovasc Magn Res	Biomed Central		Yes – permission not required	

Figure 13.1	Optimal diffusion weighting for in vivo cardiac diffusion tensor imaging	Mag Reson Med	John Wiley & Sons	25-09-16	yes	3956040899269
Figure 13.2	In vivo study of microcirculation in canine myocardium using the IVIM method	Mag Reson Med	John Wiley & Sons	25-09-16	yes	3956040645111
Figure 13.3	Optimal diffusion weighting for in vivo cardiac diffusion tensor imaging	Mag Reson Med	John Wiley & Sons	25-09-16	yes	3956040899269
Figure 13.4	Optimal diffusion weighting for in vivo cardiac diffusion tensor imaging	Mag Reson Med	John Wiley & Sons	25-09-16	yes	3956040899269
Figure 13.6	Heterogeneity of Fractional Anisotropy and Mean Diffusivity Measurements by In Vivo Diffusion Tensor Imaging in Normal Human Hearts	PLOS One	Open Access		Yes – permission not required	
Figure 13.7	Heterogeneity of Fractional Anisotropy and Mean Diffusivity Measurements by In Vivo Diffusion Tensor Imaging in Normal Human Hearts	PLOS One	Open Access		Yes – permission not required	
Figure 13.8	Heterogeneity of Fractional Anisotropy and Mean Diffusivity Measurements by In Vivo Diffusion Tensor Imaging in Normal Human Hearts	PLOS One	Open Access		Yes – permission not required	
Figure 13.9	Heterogeneity of Fractional Anisotropy and Mean Diffusivity Measurements by In Vivo Diffusion Tensor Imaging in Normal Human Hearts	PLOS One	Open Access		Yes – permission not required	

Figure 13.10	Heterogeneity of Fractional Anisotropy and Mean Diffusivity Measurements by In Vivo Diffusion Tensor Imaging in Normal Human Hearts	PLOS One	Open Access		Yes – permission not required	
Figure 14.1	Orthogonal tensor invariants and the analysis of diffusion tensor magnetic resonance images	Mag Reson Med	John Wiley & Sons		yes	3956041197631